

# DEFENCE S&T TECHNICAL BULLETIN

VOL. 16 NUM. 2 YEAR 2023 ISSN 1985-6571

## CONTENTS

Image Quality Digital Industrial Radiography on Solid Propellant Using Digital Detector Array <i>Mohd Moesli Muhammad, Azmahani Sulaiman, Mohd Subhi Din Yati, Nik Hassanuddin Nik Yusoff &amp; Mahdi Che Isa</i>	98 - 104
Development of Vibration and Noise Measurement Procedure on Flexible Coupling for High-Speed Marine Diesel Engine <i>Y. Sinnasamy, R. Ramli &amp; A.A. Saifizul</i>	105 - 114
Overpressure Reduction by Hexagonal and Rectangular Portable Soil-Filled Barriers (PSB) Subjected to Surface Burst <i>Jestin Jelani, Mohd Zaid Othman &amp; Ahmad Mujahid Ahmad Zaidi</i>	115 - 124
Reduction of HCl Exhaust Products in AP / HTPB Propellants by Different Metal Additives Using Rocket Propulsion Analysis <i>Izzat Najmi Yaacob, Norkhairunnisa Mazlan, Kamarul Arifin Ahmad, Adi Azrif Basri, Ezanee Gires, Osmera Ismail, Norafiza Salleh &amp; Suraya Shahedi</i>	125 - 139
Results of Test Campaigns Comparing Some Field Instrumentations Used by First Responders During Radiological and Nuclear Emergencies <i>Claudio De Maio, Marco Beccaria, Guglielmo Manenti &amp; Andrea Malizia</i>	140 - 146
Analysis of Surrogate Marker Ricinine in Castor Beans Found in Malaysia: Optimisation Using Statistical Experimental Design <i>Mohamad Izharudin Che Amat &amp; Raja Subramaniam</i>	147 - 155
Effects of Volume Ratio of Citrate-Capped Gold Nanoparticles (cit-AuNPs) to Malathion, Concentrations of cit-AuNPs and DNA Aptamer on Malathion Colorimetric Detection <i>Mardhiahtul Iftiah Ariffin, Nor Laili-Azua Jamari, Norli Abdullah, Mohd Junaedy Osman, Ong Keat Khim, Wan Md Zin Wan Yunus, Nur Athirah Zulkifli, Siti Aminah Mohd Noor, Victor Feizal Knight, Ten Seng Teik, Mohd Nor Faiz Norrahim, Siti Hasnawati Jamal &amp; Syed Mohd Shafiq Syed Ahmad</i>	156 - 168
Preliminary Study on the Effects of Temperature and Ions on the Detection of Acephate <i>Mohd Junaedy Osman, Wan Md Zin Wan Yunus, Ong Keat Khim, Jahwarhar Izuan Abdul Rashid, Buong Woei Chieng, Noor Azilah Mohd Kassim, Norhana Abdul Halim, Siti Aminah Mohd Noor, Victor Feizal Knight &amp; Syed Mohd Shafiq Syed Ahmad</i>	169 - 184
Antimicrobial Properties for Textiles in Military and Defence <i>Ahmad Razi Mohamed Yunus, Izzat Farhan Shahrudin, Aznida Yusuf &amp; Nik Nur Ilyani Mohd Nazri</i>	185 - 193
Phenotypic and Molecular Identification of Tropic Fungal Strains Isolated from a Light Observation Helicopter <i>Siti Aminah Hassan, Wan Md Zin Wan Yunus, Nik Noorul Shakira Mohamed Shakrin, Nurnadia Andenan, Khairumajwa Md Said, Hana Tashyeva, Mohd Haniff Sofian, Nur Shazwani Abdul Latif &amp; Hidayati Hamdan</i>	194 - 205
Ground Based Synthetic Aperture Radar Advanced Simulator and Processor <i>Chee Siang Lim, Yee Kit Chan &amp; Voon Chet Koo</i>	206 - 219
Adaptation of Microwave Antenna to Confined Spaces <i>Chung Boon Kuan</i>	220 - 227
Evaluation of the Effect of Radio Frequency Interference (RFI) on Dual-Frequency Global Navigation Satellite System (GNSS) <i>Dinesh Sathyamoorthy, Hafizah Mohd Yusoff, Ahmad Firdaus Ahmad Kazmar, Mohd Zuryn Mohd Daud &amp; Maizurina Kifli</i>	228 - 237
Development of Framework for Quality Index Model of Defence Aerospace Products <i>Manmeet Singh &amp; Nilesh Ware</i>	238 - 253



Ministry of Defence  
Malaysia

SCIENCE & TECHNOLOGY RESEARCH INSTITUTE FOR DEFENCE (STRIDE)

## **EDITORIAL BOARD**

### **Chief Editor**

Gs. Dr. Dinesh Sathyamoorthy

### **Deputy Chief Editor**

Dr. Mahdi bin Che Isa

### **Associate Editors**

Dr. Ridwan bin Yahaya

Dr. Norliza bt Hussein

Dr. Rafidah bt Abd Malik

Ir. Dr. Shamsul Akmar bin Ab Aziz

Ts. Dr. Fadzli bin Ibrahim

Dr. Nik Hassanuddin bin Nik Yusoff

Ir. Dr. Nur Afande bin Ali Hussain

Nor Hafizah bt Mohamed

Kathryn Tham Bee Lin

Masliza bt Mustafar

Siti Rozanna bt Yusuf



## AIMS AND SCOPE

The Defence S&T Technical Bulletin is the official journal of the Science & Technology Research Institute for Defence (STRIDE). The journal, which is indexed in, among others, Scopus, Index Corpenicus, ProQuest and EBSCO, contains manuscripts on research findings in various fields of defence science & technology. The primary purpose of this journal is to act as a channel for the publication of defence-based research work undertaken by researchers both within and outside the country.

## WRITING FOR THE DEFENCE S&T TECHNICAL BULLETIN

Contributions to the journal should be based on original research in areas related to defence science & technology. All contributions should be in English.

## PUBLICATION

The editors' decision with regard to publication of any item is final. A manuscript is accepted on the understanding that it is an original piece of work that has not been accepted for publication elsewhere.

## PRESENTATION OF MANUSCRIPTS

The format of the manuscript is as follows:

- a) Page size A4
- b) MS Word format
- c) Single space
- d) Justified
- e) In Times New Roman, 11-point font
- f) Should not exceed 20 pages, including references
- g) Texts in charts and tables should be in 10-point font.

Please email the manuscript to:

- 1) Gs. Dr. Dinesh Sathyamoorthy (dinesh.sathyamoorthy@stride.gov.my)
- 2) Dr. Mahdi bin Che Isa (mahdi.cheisa@stride.gov.my)

The next edition of the journal (Vol. 17, Num. 1) is expected to be published in April 2024. The due date for submissions is 10 January 2024. **It is strongly iterated that authors are solely responsible for taking the necessary steps to ensure that the submitted manuscripts do not contain confidential or sensitive material.**

The template of the manuscript is as follows:

# TITLE OF MANUSCRIPT

Name(s) of author(s)

Affiliation(s)

Email:

## ABSTRACT

*Contents of abstract.*

**Keywords:** *Keyword 1; keyword 2; keyword 3; keyword 4; keyword 5.*

### 1. TOPIC 1

Paragraph 1.

Paragraph 2.

#### 1.1 Sub Topic 1

Paragraph 1.

Paragraph 2.

### 2. TOPIC 2

Paragraph 1.

Paragraph 2.

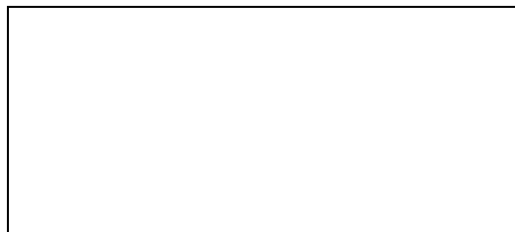


**Figure 1: Title of figure.**

**Table 1: Title of table.**

Content	Content	Content
Content	Content	Content
Content	Content	Content
Content	Content	Content

Equation 1 (1)  
Equation 2 (2)

## REFERENCES

Long lists of notes of bibliographical references are generally not required. The method of citing references in the text is 'name date' style, e.g. 'Hanis (1993) claimed that...', or '...including the lack of interoperability (Bohara *et al.*, 2003)'. End references should be in alphabetical order. The following reference style is to be adhered to:

### Books

Serra, J. (1982). *Image Analysis and Mathematical Morphology*. Academic Press, London.

### Book Chapters

Goodchild, M.F. & Quattrochi, D.A. (1997). Scale, multiscaling, remote sensing and GIS. In Quattrochi, D.A. & Goodchild, M.F. (Eds.), *Scale in Remote Sensing and GIS*. Lewis Publishers, Boca Raton, Florida, pp. 1-11.

### Journals / Serials

Jang, B.K. & Chin, R.T. (1990). Analysis of thinning algorithms using mathematical morphology. *IEEE T. Pattern Anal.*, **12**: 541-550.

### Online Sources

GTOPO30 (1996). *GTOPO30: Global 30 Arc Second Elevation Data Set*. Available online at: <http://edcwww.cr.usgs.gov/landdaac/gtopo30/gtopo30.html> (Last access date: 1 June 2009).

### Unpublished Materials (e.g. theses, reports and documents)

Wood, J. (1996). *The Geomorphological Characterization of Digital Elevation Models*. PhD Thesis, Department of Geography, University of Leicester, Leicester.

# IMAGE QUALITY DIGITAL INDUSTRIAL RADIOGRAPHY ON SOLID PROPELLANT USING DIGITAL DETECTOR ARRAY

Mohd Moesli Muhammad\*, Azmahani Sulaiman, Mohd Subhi Din Yati, Nik Hassanuddin Nik Yusoff & Mahdi Che Isa

Marine Technology Research Group, Maritime Technology Division (BTM), Science & Technology Research Institute for Defence (STRIDE), Ministry of Defence, Malaysia

\*Email: moesli.muhammad@stride.gov.my

## Abstract

*This paper presents the image quality of digital industrial radiography using findings from normalised signal to noise ratio ( $SNR_N$ ) results. The experiment was setup using double-based propellant as object, X-ray machine as radiation source, and digital detector array (DDA) as digital platform to convert radiation signal to digital image. Radiation energy and frame integration number were the study's variable parameters. The results showed that  $SNR_N$  value increased as radiation energy and frame integration number increased. The plotted graph for fixed radiation energy of 80 kV against different frame integration numbers demonstrated a linear trend, with the highest value obtained being 487 at frame integration number of 10. The same trends were shown for linear graphs plotted for radiation energies of 65, 70, 80 and 85 kV against different frame integration numbers. The increase of radiation energy significantly increased the  $SNR_N$  value as more radiation can penetrate the object. It was concluded that high radiation energy and frame integration number enhances the image quality of digital industrial radiography.*

**Keywords:** *Image quality; digital industrial radiography; digital detector array (DDA); normalised signal to noise ratio value ( $SNR_N$ ); double -based propellant.*

## 1. INTRODUCTION

Digital industrial radiography is a non-destructive testing technique that enables the examination of internal structures and flaws of propellant materials. It is favoured over conventional film-based radiography because it has a number of advantages, which makes it popular across a range of industries, including aerospace and defence (Robert *et al.*, 2000; Daniel, *et al.*, 2016). Digital detector array (DDA) is used in industrial radiography to capture x-ray images and convert those images into electrical signals that are processed and reconstructed to create digital images. Digital images can be improved, changed and analysed in real time, allowing for quick assessment and decision-making. Digital industrial radiography eliminates the need for film processing and speeds up inspection. Furthermore, it eliminates potentially harmful chemicals being used in traditional film processing, making it a safer and more environmentally friendly. Digital images from radiography provide a great deal of flexibility in terms of image settings such as brightness, contrast and magnification to enhance visibility and highlight specific areas of interest. This makes it easier to identify and characterise flaws in solid propellants, such as voids, cracks, inclusions or density (Stoey *et. al*, 2008; Luiz *et. al*, 2020).

In digital radiography, noise is defined as unwanted disturbances that refer to random variation in the radiographic image. Electronic noise in the detection system, fluctuations in radiation, scatter radiation and environmental factors all contribute to noise generation. Noise can degrade the image quality, reduce contrast and obscure important details, making it challenging to identify defects or abnormalities (Sapizah *et. al*, 2010; Shahidan & Suhaila, 2018). Noise level is measured by the signal to noise ratio (SNR), which is the quotient of mean value of the linearised signal intensity  $I_{mean}$  and standard deviation  $\sigma$  of the noise at the signal intensity. It can be calculated using the following equation:

$$SNR = \frac{I_{mean}}{\sigma} \quad (1)$$

The values of  $I_{mean}$  and  $\sigma$  should be computed from a region without shading or artifacts. Sampling of the  $SNR$  is gathered in different regions of the image area under test to ensure that the  $SNR$  value is stable and believable. The size of the region of interest (ROI) used to measure mean intensity and noise should be at least 20 by 55 pixels (Yahaghi & Movafeghi, 2019; Sy *et. al*, 2023).

$SNR$  in a DDA system should be normalised ( $SNR_N$ ) before it can be applied to measure the effect of different radiation energies and frame integration numbers. For this purpose, the duplex wire method (consists of 13 wire pairs from 1D with a wire of 0.80 mm to 13D with a wire of 0.050 mm) is used as an image quality indicator (IQI) to measure basic spatial resolution (effective pixel size) and to normalise  $SNR$ :

$$SNR_N = SNR_{measure} (88.6 \mu\text{m}/SR_b) \quad (2)$$

where  $SNR_{measure}$  is performed using specialised software tools that determine the average grey value (mean value) within the ROI, and  $SR_b$  is the basic spatial resolution.

A higher  $SNR_N$  implies that the signal is stronger as compared to the noise, resulting in a higher-quality image with improved visibility and enhanced ability to detect defects or irregularities (Bata *et. al*, 2023). Conversely, a lower  $SNR_N$  indicates that the noise level is relatively high as compared to the signal, leading to a lower-quality image with reduced clarity. In order to optimise  $SNR_N$  in industrial digital radiography, various techniques are employed. These include using appropriate exposure parameters, such as adjusting the X-ray or gamma ray energy, optimising the detector sensitivity, and employing noise reduction algorithms during image processing. Additionally, efforts are made to minimise external factors that contribute to noise such as shielding against ambient radiation or electromagnetic interference (Lutfi & Turan, 2016; Aline *et. al*, 2019). By maximising  $SNR_N$  in digital industrial radiography, inspectors and professionals can obtain high quality radiographic images that aid in the accurate assessment of materials, identification of defects and quality control processes (Topias *et. al*, 2022).

In this paper, a study was carried out on solid propellants using digital industrial radiography. Solid propellant is a type of fuel used to generate thrust in solid rocket motor. The objective of this paper to determine the  $SNR_N$  for various radiation energies and frames integration numbers.

## 2. METHODOLOGY

In this study, digital radiography images were captured using a NOVO DR NV22WNSRS03 DDA. The DDA is a flat panel with main structure made of gadolinium oxysulfide (Gd<sub>2</sub>O<sub>2</sub>S). The bit depth is 16 bits and the pixel size is 148  $\mu\text{m}$  with 426 mm x 355 mm effective imaging area. The DDA was calibrated to produce corrected images in accordance with the manufacturer's recommendation and ASTM (2022). The source of radiation was a Xylon XPO EVO 225D X-ray tube model with focal spot size of 3.0 mm. The maximum voltage and current were 225 kV and 10 mA respectively. A duplex IQI EN 462-5 was placed directly on the source side of the solid propellant to evaluate the total unsharpness of the DDA.

The sample was a solid propellant of size 50 mm diameter and 120 mm length. The solid propellant was double-base and the core was a hollow cylindrical shape (Figure 1). The experiment was performed with four different radiation energies of 65, 70, 80 and 85 kV. The current was set to 1 mA and frame integration number was limited to 10. The detector focal distance (DFD) was 700 mm and IQI duplex wire was placed at the source side of the object (Figure 2). The  $SNR_N$  value was determined using the ISee! software with ROI set to 20 by 55 pixels.



**Figure 1: Double-base solid propellant with hollow cylinder shape.**

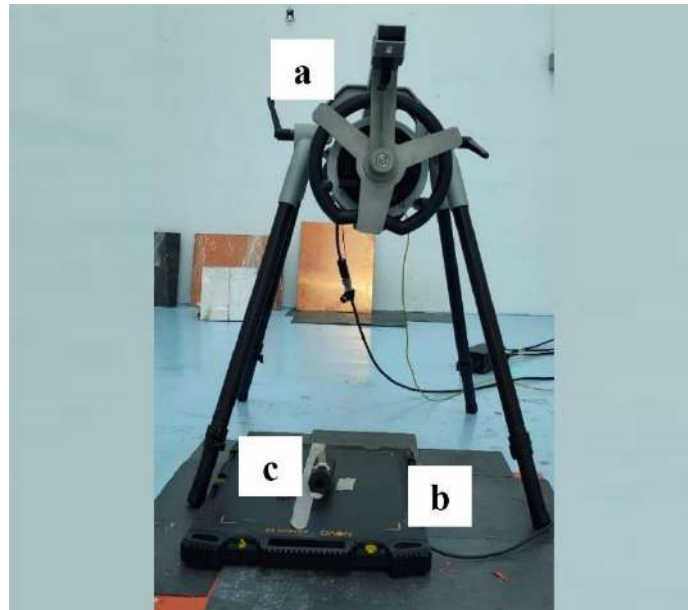


**Figure 2: Experimental setup: (a) Radiation source: x-ray (b) DDA (c) Object: solid propellant.**

### **3. RESULTS & DISCUSSION**

The digital radiography images were recorded and then analysed using ISee!. Figure 3 shows the digital radiographic images for radiation energy of 80 kV and frame integration number of 8. The image shows the duplex wire, ROI and identification of propellant sample during radiographic exposure. The duplex wire is placed 2 to 5° tilted from the centre of the sample for  $SR_b$  assessment in accordance to ISO (2013).  $SNR_N$  was measured with 20% spatial resolution, which is 0.2 mm. The measurements were carried out with window size of 20 pixels width (20 values per group in horizontal direction) and 55 pixels height (55 group for median in vertical direction). Tables 1 and 2 show the results of  $SNR_N$  values for various radiation energies and frame integration numbers. The unsharpness values were obtained at D8 and equivalent to 0.16 mm. This means that the effective pixel size and geometrical detail is 160  $\mu\text{m}$  (Junjie *et al.*, 2022).



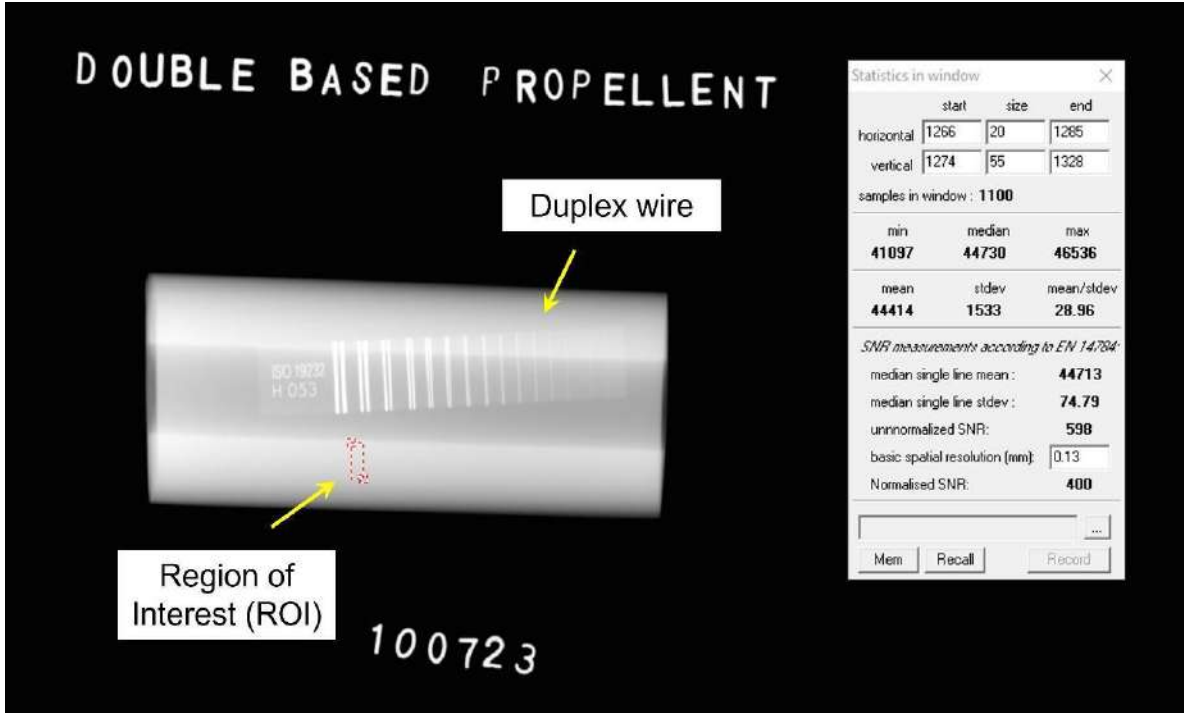


Figure 3: Digital radiography image of propellant for 80 kV and frame integration number of 8.

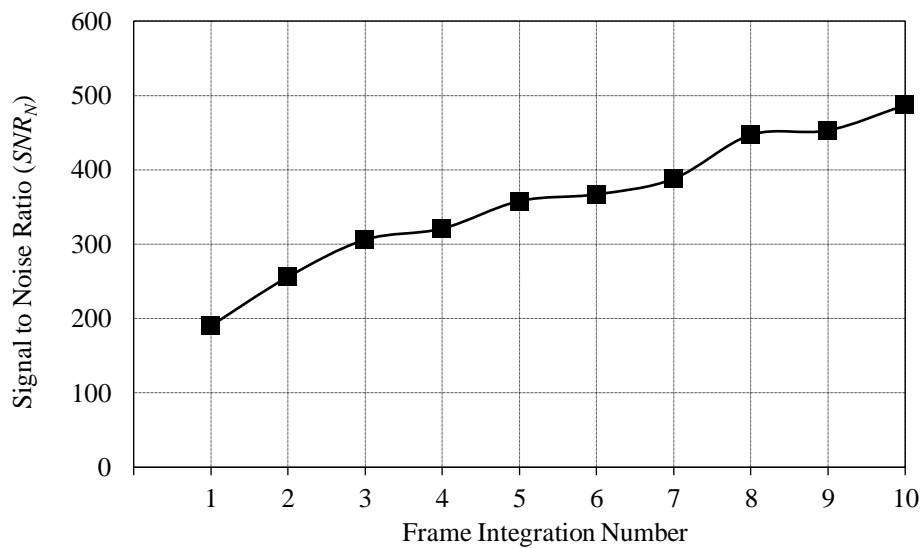
Table 1:  $SNR_N$  values of the solid propellant with fixed radiation energy of 80 kV and different frame integration numbers.

kV	mA	Frame Integration Number	Exposure Time (s)	Duplex Wire	$SR_b$ (mm)	$SNR_N$
80	1	1	0.5	D8	0.16	190
80	1	2	1.0	D8	0.16	256
80	1	3	1.5	D8	0.16	306
80	1	4	2.0	D8	0.16	345
80	1	5	2.5	D8	0.16	358
80	1	6	3.0	D8	0.16	367
80	1	7	3.5	D8	0.16	388
80	1	8	4.0	D8	0.16	447
80	1	9	4.5	D8	0.16	453
80	1	10	5.0	D8	0.16	487

**Table 2:  $SNR_N$  values of the solid propellant with radiation energies of 65, 70, 80 and 85 kV, and different of frame integration numbers.**

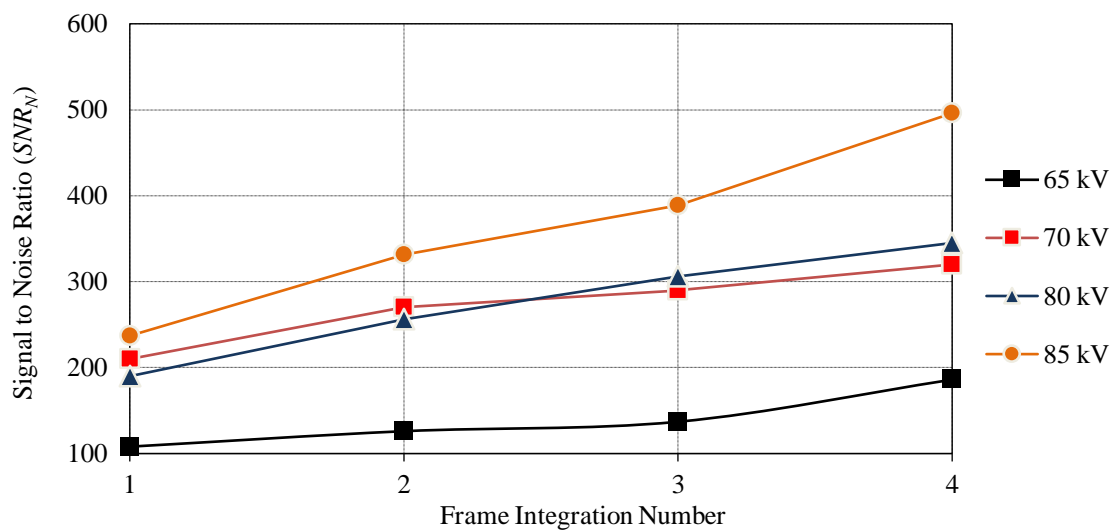
kV	mA	Frame Integration Number	Exposure Time (s)	Duplex Wire	$SR_b(\text{mm})$	$SNR_N$
65	1	1	0.5	D8	0.16	108
65	1	2	1.0	D8	0.16	126
65	1	3	1.5	D8	0.16	137
65	1	4	2.0	D8	0.16	186
70	1	1	0.5	D8	0.16	210
70	1	2	1.0	D8	0.16	270
70	1	3	1.5	D8	0.16	290
70	1	4	2.0	D8	0.16	320
80	1	1	0.5	D8	0.16	190
80	1	2	1.0	D8	0.16	256
80	1	3	1.5	D8	0.16	306
80	1	4	2.0	D8	0.16	345
85	1	1	0.5	D8	0.16	237
85	1	2	1.0	D8	0.16	331
85	1	3	1.5	D8	0.16	389
85	1	4	2.0	D8	0.16	496

Figure 4 shows the graph  $SNR_N$  against frame integration number for radiation energy of 80 kV. The plotted graph shows that the increase of frame integration number significantly improves the  $SNR_N$  values. This is as multiple images aid in the reduction of random noise present in individual images. When x-rays pass through an object being inspected, they are attenuated differently depending on density and thickness of materials. The resulting images may contain noise, artifacts and imperfection, which may obscure important details or flaws. Averaging multiple images smooths out these fluctuations and improves overall image quality because noise is a random variation in pixel values. However, increasing the frame integration number increases the exposure time, which means it takes longer exposure to inspect the object (Yang & Jiang, 2021).



**Figure 4: Graph of  $SNR_N$  against frame integration number for radiation energy of 80 kV.**

Further analysis was carried out using different radiation energies and frame integration numbers. Figure 5 shows the graph of  $SNR_N$  against frame integration numbers for radiation energies of 65, 70, 80 and 85 kV. All radiation energies indicate linear trend when the frame integration number is increased. This is clearly visible when the radiation energy is 85 kV and the value obtained at frames integration number of 4 is 496. High radiation energy generates a more intense signal that are better able to penetrate the object being inspected. As a result of the large number of photons, a stronger electrical signal is produced and more information is captured and recorded by the DDA. Furthermore, higher energy radiation tends to reduce the effects of scattering. Scattering occurs when x-rays deviate from their original path, which can obscure or reduce the clarity of the image. High energy radiation causes less scattering resulting in sharper images with better contrast. As a result, with a strong signal relative to noise, the impact of noise on the images can be reduced signally, resulting in higher  $SNR_N$  (Marshal *et al.*, 2017).



**Figure 5: Graph of  $SNR_N$  against frame integration numbers for voltages of 65, 70, 80 and 85 kV.**

## 5. CONCLUSION

This study concludes that increasing the radiation energy and frame integration number increases the  $SNR_N$  value. Frame integration number is used to combine multiple images into a single average image. Image averaging smooths out noise fluctuations and improves the overall image quality. Radiation energy increases the intensity of the signal's penetration through the object while decreasing the effects of scattering. As a result, the DDA captures and records a large amount of data.

## ACKNOWLEDGEMENT

The authors would like to thank the officers and staff from the various laboratories at the Maritime Technology Division (BTM), Science & Technology Research Institute for Defence (STRIDE), Ministry of Defence, Malaysia for their technical support during the experimental works.

## REFERENCES

- Aline, S.S., Davi, F.O., Celio, S.G., Soraia, R.A. & Ricardo, T.L. (2019). Evaluation of digital detector arrays system for industrial radiography. *Braz. J. Rad. Sci.* **12**: 1-13.
- ASTM (American Society Testing Method) (2022). *ASTM-E2597: Standard Practice for Manufacturing Characterization of Digital Detector Arrays*. American Society Testing Method (ASTM), Ohio, US.
- Bata, H., Ziang, W., Clemente, I.C. & Xavier, M. (2023). Deep learning neural network performance on NDT digital x-ray radiography images: analyzing the impact of image parameters- An experimental study. *Sensors*, **23**: 4324.
- Daniel, A.J., Robert, A. & Frederik, J. (2016). Overview of x-ray technique for solid rocket propellant regression measurements. 2016 *Propuls Ener Forum*, 24-27 July 2016, Salt Lake City, United State, pp 1-32.
- Euclid, S (2019) *Physical Principles and Quality Control*. Springer, Singapore
- Junjie, D., Tianpeng, L. & Zhaolong, X. (2022). Guided filter-based edge detection algorithm for ICT images of solid rocket motor propellant. *Elect*, **11**: 1-11.
- Luiz, F.S.H., Francisco, C.P.B. & Jose, W.P.B. (2020). Detection of linear surface defects in solid propellant motors using multilayer perceptron neural networks. *Poly. Test.* **88**: 106559.
- Lutfi, E. & Turan O. (2016). Investigation of noise sources for digital radiography systems. *Radiol. Phys. Technol.* **10**(2): 1-9.
- ISO (International Organization for Standardization) (2013). *ISO 19232:2013: Non-Destructive Testing: Image Quality of Radiographs-Part 1, Determination of the Quality Using Wire Type Image Quality Indicators*. International Organization for Standardization (ISO), Geneva, Switzerland.
- Marshall, R.C., Richard, A.G. & Dylan, F.B. (2017). X-ray scattering in the shielding of industrial irradiation facilities. *Phsy. Proc*, **90**:151-156.
- Robert, C., Donald, H. & Robert, F. (2000). Radiographic inspection of composite materials. *Compr. Compos. Mater.* **5**: 321-344.
- Sapizah, R., Khairul, A.M.S., Noorhazleena, A., Siti, M.M., Shaharudin, S., Arshad, Y. & Razak, H. (2010). Effecti of exposure time reduction towards sensitivity and SNR for computed radiography (CR) application in NDT. *2010 Seminar R&D Nuklear Malaysia*, Nuclear Malaysia Agency, Bangi, Malaysia, pp 1-6.
- Shahidan, M. & Suhaila, A.B. (2019). Image enhancement process on digital radiographic image with weld discontinuities. *J. Mech. Eng.* **5**(4):275-290.
- Stoey, K., Guerout, F.M., & Horn, D. (2008). A review of digital radiography technology for valve inspection. 2008 *Int. Conf. on Candu Maint.*, 16-18 November 2008, Metro Toronto Convention Centre, Toronto, Canada, pp 1-15.
- Sy, E., Samboju, v. & Mukhdomi, T. (2023). X-ray image production procedure. *In StatPearls*. StatPearls Publishin Treasure Island, Fl, USA.
- Topias, T., Likka, V., Peter, F., Anders, R. & Zuheir, B. (2022). Automated defect detection in digital radiography of aerospace welds using deep learning. *Weld. World.*, **66**: 643-671.
- Yahagi, E. & Movafeghi, A. (2019). Contrast enhancement of industrial radiography images by Gabor Filtering with automatic noise Thresholding. *J. Nondestruct Test.* **55**: 73-79.
- Yang, L. & Jiang, H. (2021). Weld defect classification in radiographic images using unified deep neural network with multi-level features. *J. Intell. Manuf.* **32**: 459-469

# IDENTIFICATION OF KNOCKING SYMPTOM ON FLEXIBLE COUPLING OF HIGH-SPEED MARINE DIESEL ENGINE BY UTILISING VIBRATION AND NOISE MEASUREMENT PROCEDURE

Yogeswaran Sinnasamy<sup>1,2</sup>, Rahizar Ramli<sup>2,3\*</sup> & Ahmad Saifizul Abdullah<sup>3</sup>

<sup>1</sup>Science and Technology Research Institute for Defence (STRIDE), Ministry of Defence, Malaysia

<sup>2</sup>Advanced Computational and Applied Mechanics (ACAM) Research Group, Department of Mechanical Engineering, Faculty of Engineering, University of Malaya, Malaysia

<sup>3</sup>Department of Mechanical Engineering, Faculty of Engineering, University of Malaya, Malaysia

\*Email: rahizar@um.edu.my

## ABSTRACT

*In reciprocating-rotating machines, flexible couplings are widely used in many applications, such as marine gearboxes and diesel engines. A flexible coupling is an element that transmits torque between two shafts while allowing for some misalignment between the shafts. Flexibility is introduced in couplings to minimise the effect of misalignment on vibration response. Vibration and noise monitoring are highly capable of detecting any abnormalities in flexible couplings before failure occurs. In this study, vibration and noise measurements are performed simultaneously on a real combination of marine diesel engine - gearbox flexible coupling at five different engine revolutions (400, 500, 600, 700 and 800 rpm) under two different conditions (before and after repair performed on flexible coupling). The measured data in time waveforms were analysed based on a comparative method to identify the existence of knocking symptom. It is found that the main diesel engine shows significant difference for before and after repair was performed, while the gearbox shows less significant difference.*

**Keywords:** Flexible coupling; vibration; noise; knocking symptom; engine revolution.

## 1. INTRODUCTION

A flexible coupling is an element that transmits torque between two shafts while allowing for some misalignment between the shafts. Flexibility is introduced in couplings to minimise the effect of misalignment on vibration response. Despite the fact that one may not consider gears to be flexible, gear couplings are particularly viewed as flexible couplings. A gear coupling is a mechanical device that is intended to transmit torque between two shafts that are not collinear. The coupling commonly comprises two flexible joints, one fixed to each shaft (Wei *et al.*, 2022).

Both diesel engine and gearbox are connected by flexible coupling. Therefore, any problem with the flexible coupling will badly affect the operation of the diesel engine and gearbox as well. Nevertheless, the main source of vibration coming from the diesel engine. Diesel engines are the most widely used power plant in the world with a wide range of applications. They convert the chemical energy of diesel fuel into mechanical energy, which is then used by drive ships, vehicles, power generators, etc. In the Royal Malaysian Navy (RMN), diesel engines are used for main and auxiliary propulsion systems with most of the diesel engines in RMN being high speed marine diesel engines. Diesel engines are mechanical devices, so defects in mechanical systems due to various reasons are general phenomena. Therefore, researchers are conducting continuous research to determine an optimal fault detection system for diesel engines in order to monitor the health condition of engines (Tharanga *et al.*, 2020).

Nowadays, diesel engines are widely used in many industrial sectors as compared to other types of engines such as gas and steam turbines. This is due to the diesel engine's heavy-duty capability and proven reliability especially in different weather conditions (Lamaris *et al.*, 2010). Diesel engines play an important part in major sectors, such as land and sea transportation, and power generation. The reliability of diesel engines in naval applications is crucial to maintaining maritime security and sovereignty (Arroyo *et al.*, 2013). Diesel engines are a critical and essential piece of equipment because its damage could potentially lead to costly repairs and ship down time. Therefore, it is essential to develop a sensitive condition monitoring system that is capable of detecting a fault in its early stages before a break-down occurs (Yousef *et al.*, 2015).

Condition monitoring could potentially detect abnormalities at an early stage and subsequently preclude catastrophic failure of the diesel engine jeopardising the ship's mission (Yan *et al.*, 2013, Vilas Boas *et al.*, 2021, Sinnasamy *et al.*, 2021). There are many types of defects or malfunctions on various components and subsystems of a diesel engine, which could affect the performance of the engine and potentially cause catastrophic failure (Flett & Bone, 2016). A diesel engine consists of various main components or systems and subsystems, such as combustion, cooling, lubrication, exhaust and fuel (Espadafor *et al.*, 2014). Several popular diagnosis methods have been applied over the years, such as oil analysis, vibration signal analysis, particle analysis, corrosion monitoring, noise signal analysis and wear debris analysis (Tharanga *et al.*, 2020). Among these methods, vibration and noise signal analysis has emerged as popular choices because many faults can be identified without stopping or disassembling the machine. The changes of these signals often indicate the presence of a fault (Kumar *et al.*, 2018; Sim *et al.*, 2019; de S'á S'ó *et al.*, 2021).

Most of previous studies employed experimental or research engines connected to flexible couplings. In this study, vibration and noise measurements are performed simultaneously on a real marine diesel engine - gearbox flexible coupling. Due to lack of lubrication oil, the flexible coupling was found under problematic conditions and continuous use of this flexible coupling could cause catastrophic failure. As shown in Figure 1, there were oil leak marks that came out from the internal portion of the flexible coupling. The study was conducted for five different engine revolutions (400, 500, 600, 700 and 800 rpm) under two different conditions (before and after repair was performed on the flexible coupling).



**Figure 1: The damaged flexible coupling investigated in this study.**

## 2. METHODOLOGY

In this measurement, four units of integrated charge piezoelectric (ICP) accelerometers manufactured by DYTRAN were used to measure the vibration signals. Meanwhile, noise signals measurement was performed using a prepolarised free field cartridge type microphone for general purpose acoustic measurements manufactured by G.R.A.S and a constant current powered (CCP) general purpose ½” preamplifier type 26CA. The resulting output of the free-field microphone is a signal proportional to the sound pressure, as it existed before the microphone was introduced into the sound field. The free-field microphone should always be pointed towards the sound source (0° incidence).

Figure 2 illustrates the measurement locations and directions on a 3D sketch of a ship propulsion system system. In this system, the main diesel engine and gearbox is connected by a flexible coupling. In this study, two accelerometers were mounted on the main diesel engine at two different directions, horizontal and vertical (Locations 1 and 2); and another two accelerometers were mounted on the input of the gearbox, also at horizontal and vertical directions (Locations 3 and 4).

In Ghaderi *et al.* (2017), engine sound signals were recorded using a microphone located 20 cm above the engine. Also, the investigated engine defect is in the ignition system, i.e., the engines are operating with only the first cylinder missing firing. However, for this study, by considering the positioning of the fuel supply piping and cooling system, the distance between the microphone and flexible coupling was set at 50 cm due to limited accessibility inside the engine room for noise measurement.

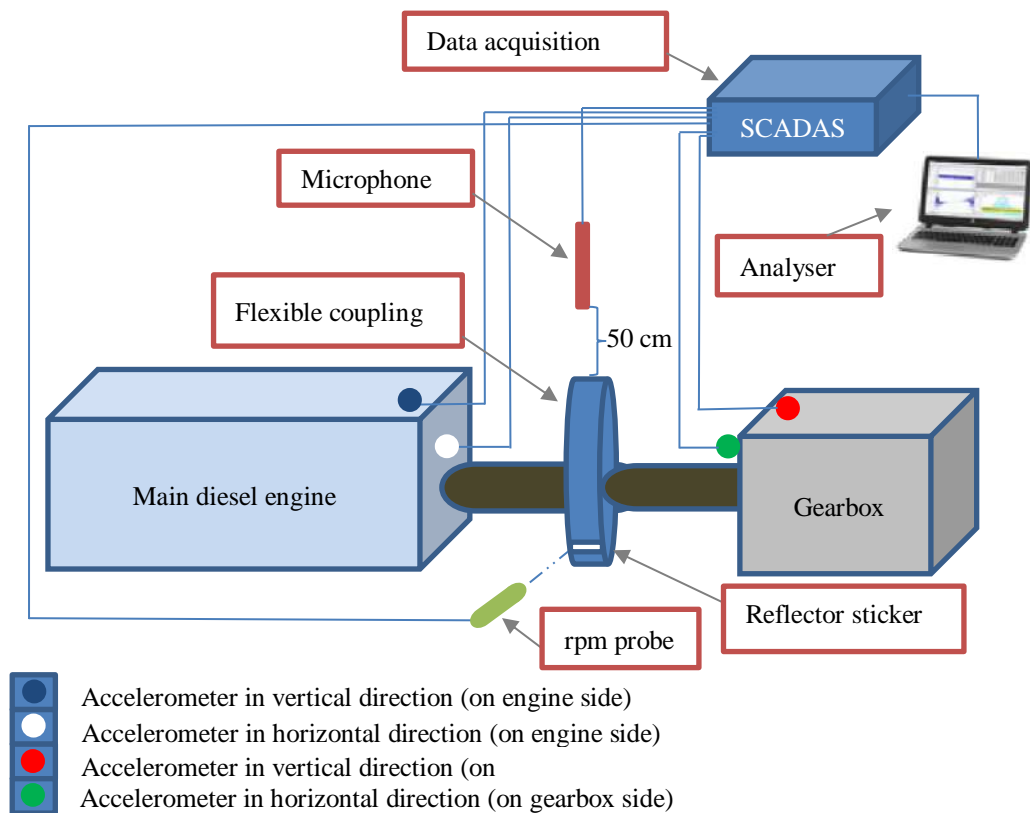


**Figure 2: The actual experimental setup.**

The noise signals are acquired in the near-field condition, which is the area of the sound field that is closest to the sound (noise) source. The vibration and noise signals are sampled at sampling frequency of 12,800 Hz. This frequency range is sufficient to disclose the frequency contents of noise data. Meanwhile, a tachometer probe was installed to record shaft revolutions per minute. The vibration, noise and rpm data were passed through a LMS signal conditioning and data acquisition system (LMS SCADAS) is a multichannel data acquisition system (DAQ), and raw data recording can be conducted in a data recorder and analyser system through the Simcenter Testlab software for further processing. The first step of the proposed algorithm is the preparation of input data such as sensitivity values of the accelerometers and microphone based on calibration prior to the measurement being conducted for before and after repair conditions. Average number of the signal sections was used to reduce the random signal error, while the Hanning window was used to inhibit the leakage of time domain signals. The lengths of time signals determine the spectral resolution of fast Fourier transform (FFT) and have an influence on accuracy of natural frequency detection (Ramteke *et al.*, 2020). As the proposed algorithm should be executed one time per hour, we proposed to use 10 min length time signals, whereby we recorded the signals (vibration and noise) for 10 min at each engine revolution. Table 1 shows the measurement matrix for this study, which covers five engine revolutions before and after repair on the flexible coupling. At each condition, measurements were conducted at five revolutions (engine revolutions in rpm), starting from the minimum revolution until it reached maximum.

**Table 1: Measurement matrix.**

Shaft speed (rpm)	Before repair	After repair
400	Section 1 - Runs 1, 2, 3	Section 2 - Runs 1, 2, 3
500	Section 1 - Runs 4, 5, 6	Section 2 - Runs 4, 5, 6
600	Section 1 - Runs 7, 8, 9	Section 2 - Runs 7, 8, 9
700	Section 1 - Runs 10, 11, 12	Section 2 - Runs 10, 11, 12
800	Section 1 - Runs 13, 14, 15	Section 2 - Runs 13, 14, 15

The second stage of measurements was conducted after the repaired flexible coupling was installed at the same position of the ship propulsion system. Once installed, the two-dial gauge method was used to check for proper alignment and balancing. The shaft was visually checked for any misalignment and unbalance. First, the rotor dynamic was run for a few minutes to settle down all minor vibrations. The vibration, noise and rpm data were recorded for the repaired flexible coupling by repeating the same measurement procedure.

For the measurements, all the accelerometers were installed using super glue as it was too easy to remove and suitable for this kind of measurement. This technique is used for temporary installation because the engine and gearbox surfaces are not adequately prepared for stud mounting. A temporary work station was installed outside of the engine room, which consisted of an analyser (for data recording and analysis) and SCADAS (for data acquisition). Normally two to three days is needed to set up the whole temporary work station, which could be conducted while the ship is harboured at the jetty. Once setting up is completed, the measurement can proceed at sea.

The measurements were performed for the well-balanced rotor systems at both the drive end (DE) of the engine and housing of the gearbox, with vibration signals recorded for five revolutions (engine revolutions in rpm). The measurement was started at 400 rpm, which is considered the minimum engine revolution. At this speed, vibration data was recorded for at least 10 min, which consisted of three consecutive runs. Each run consisted of measurement duration of 200 s. Once measurement at the minimum speed was completed, the engine revolution was increased to 500 rpm. Once again, the vibration data at this speed was recorded for at least 10 min and three runs were recorded as previously. This step was repeated at 600, 700 and 800 rpm.



During vibration measurement, rpm was also recorded using a tacho probe, which was connected to SCADAS. Table 2 shows the running rpm and frequency that was obtained by dividing the rpm value by 60 min, as shown in the following equation:

$$\text{fundamental frequency, } f = \frac{\text{shaft rpm}}{60} \quad (1)$$

**Table 2: Calculated fundamental frequencies using Equation 1.**

Shaft speed (rpm)	Calculated fundamental frequency (Hz)
400	6.67
500	8.33
600	10.00
700	11.67
800	13.33

### 3. RESULTS AND DISCUSSION

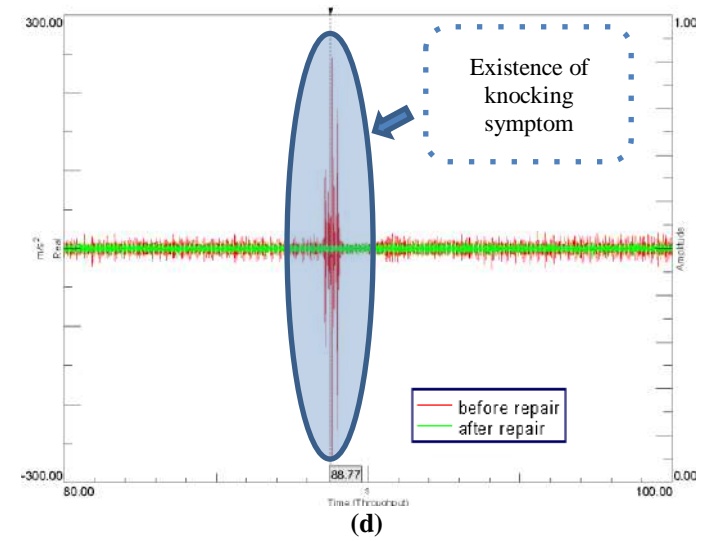
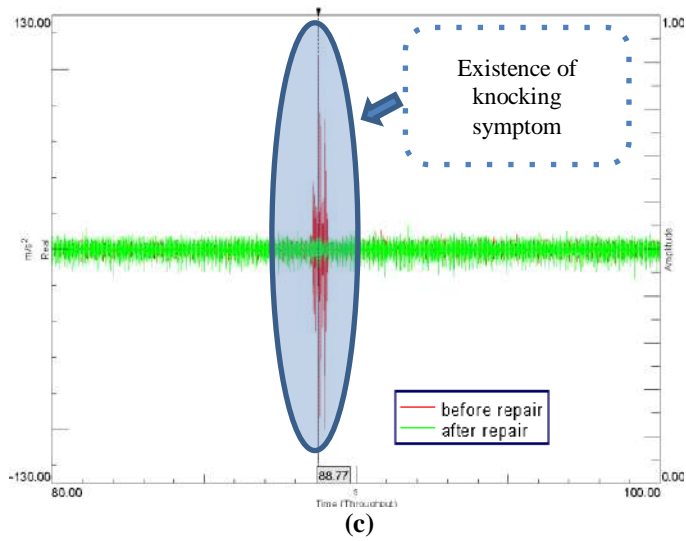
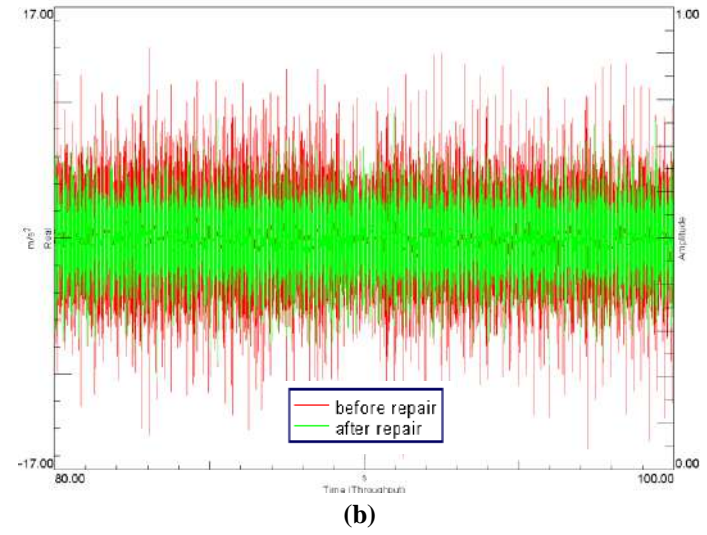
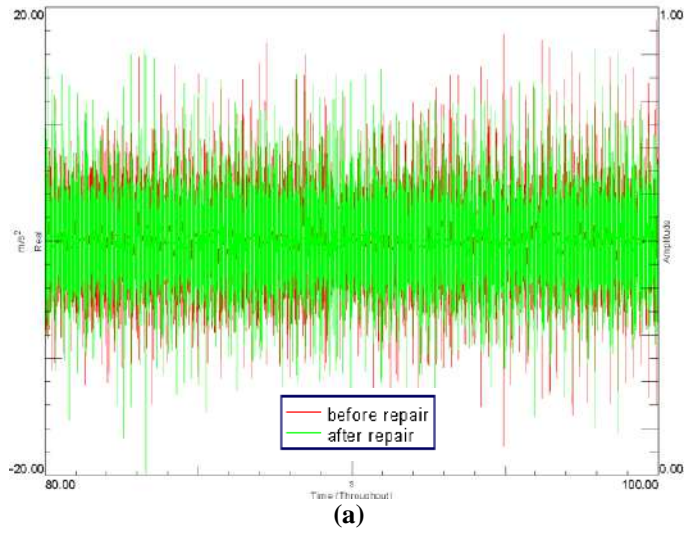
#### 3.1 Time-Domain Analysis

Figure 2 compares the vibration waveforms that were captured for before and after repair was performed for the flexible coupling under engine revolution of 400 rpm. As shown in Figure 2(a) and 2(b), for Locations 1 and 2 respectively, it was found that the vibration levels under both conditions were almost similar without any symptoms of abnormality. Locations 1 and 2 were located on the gearbox surface, in the vertical and horizontal directions respectively.

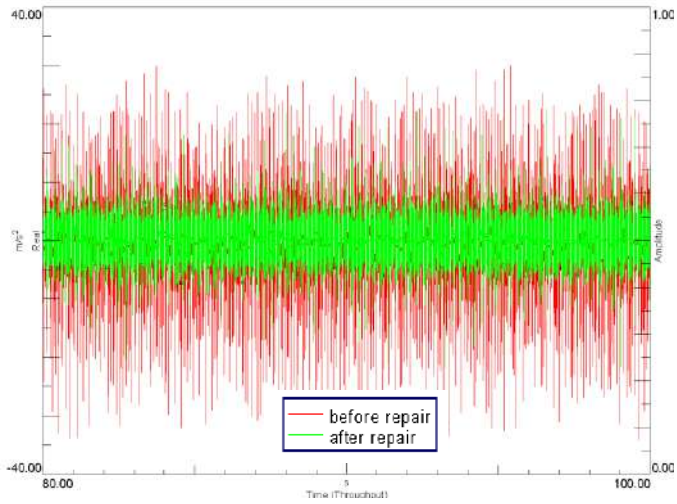
Meanwhile, for Locations 3 and 4 (Figures 2(c) and 2(d) respectively), the vibration levels before repair were higher than after repair was performed. In addition, it was found the vibration waveforms before repair showed the existence of knocking symptom. Knocking is one of the symptoms at lower speed of a machine that can identify the condition of a particular machinery periodically (Barszcz *et al.*, 2018). Basically, any delay in rectifying this symptom from the early stage can serious and catastrophic failure for the ship propulsion system. Based on the comparison between before and after repair conditions, this symptom could be identified based on the existence of higher spikes of vibration waveforms, which produced higher values of amplitude. The position of this symptom was observed at 88.77 s. Both Locations 3 and 4 were located on the main diesel engine surface, in the vertical and horizontal directions respectively. Meanwhile, based on interpretation conducted for Locations 1 and 2, which were located on surface of the gearbox, it was found there is no sign of knocking symptom. This shows that the source of knocking on the flexible coupling was nearer to the position of the diesel engine than gearbox and also, the surface of the gearbox is thicker and diametrically larger in comparison to the surface of the diesel engine.

Table 3 shows the vibration values between 87 and 90 s at the four locations for engine revolution of 400 rpm. Based on comparison for between before and after repair, it was found that the values at Locations 3 and 4 showed larger difference, while for Locations 1 and 2, the values for both conditions were almost similar.

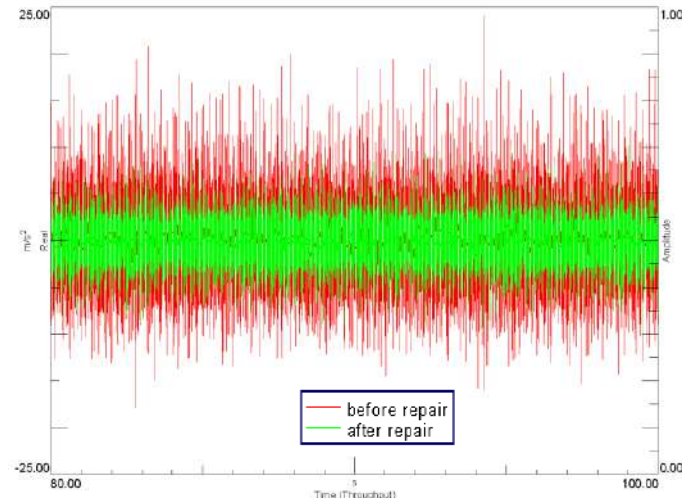
Meanwhile, for engine revolution of 500 rpm, at Location 1 (Figure 3(a)), it was found that the vibration level before repair was higher than after repair. However, the vibration waveforms under these conditions do not exhibit any symptoms of abnormality. These same findings are observed at other locations as well under 500 rpm, namely for Locations 2, 3 and 4, as shown in Figure 3(b), 3(c) and 3(d) respectively. Further analysis for the waveforms recorded under engine revolutions of 600, 700 and 800 rpm show the same results as 500 rpm at all the locations, under both conditions without any knocking symptom or abnormality. This shows that the knocking symptom only exists at minimum engine revolution and subsequently disappears when the engine revolution increases step by step.



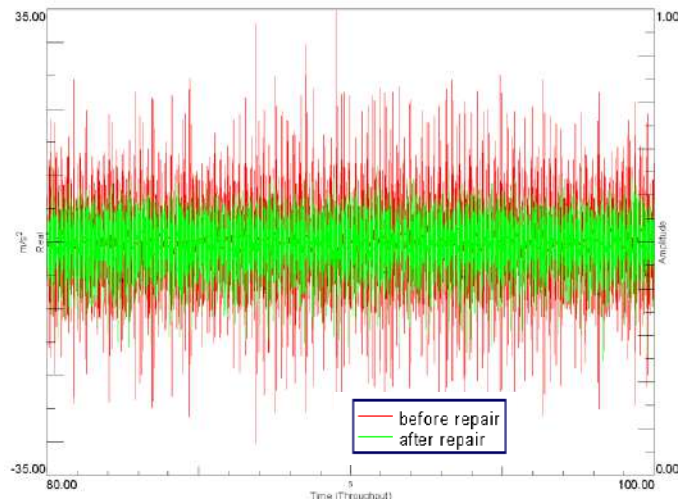
**Figure 3: Vibration waveforms for engine revolution of 500 rpm for: (a) Location 1 (b) Location 2 (c) Location 3 (d) Location 4.**



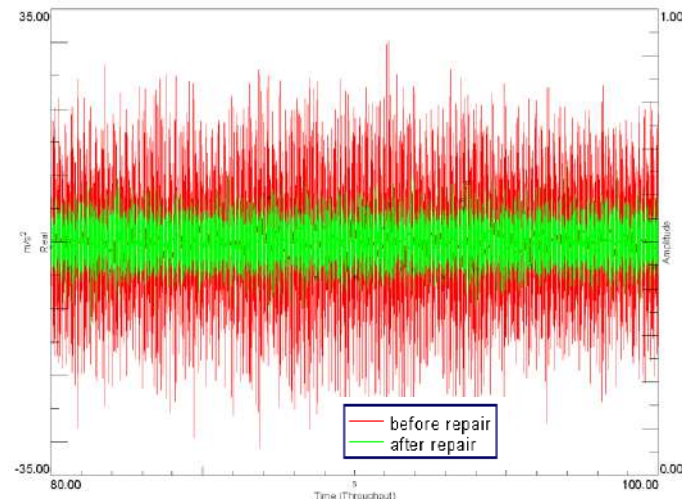
(a)



(b)



(c)



(d)

Figure 4: Vibration waveforms for engine revolution of 500 rpm for: (a) Location 1 (b) Location 2 (c) Location 3 (d) Location 4.

**Table 3: Vibration values in m/s<sup>2</sup> before and after repair was performed for engine revolution of 400 rpm.**

Location	1 <sup>st</sup> reading	2 <sup>nd</sup> reading	3 <sup>rd</sup> reading	4 <sup>th</sup> reading	5 <sup>th</sup> reading	6 <sup>th</sup> reading	7 <sup>th</sup> reading	8 <sup>th</sup> reading	9 <sup>th</sup> reading	10 <sup>th</sup> reading
Location 1	2.16	2.17	2.17	2.18	2.18	2.19	2.20	2.21	2.22	2.23
	2.14	2.14	2.13	2.13	2.12	2.10	2.07	2.04	2.02	1.99
Location 2	2.37	2.35	2.34	2.32	2.30	2.29	2.28	2.26	2.25	2.23
	1.28	1.27	1.27	1.27	1.27	1.27	1.27	1.27	1.27	1.27
Location 3	5.33	5.39	5.44	5.50	5.56	5.55	5.55	5.54	5.54	5.54
	1.40	1.40	1.39	1.39	1.39	1.39	1.39	1.39	1.39	1.39
Location 4	11.99	12.18	12.38	12.57	12.76	12.76	12.75	12.74	12.73	12.72
	1.42	1.42	1.43	1.43	1.44	1.45	1.46	1.47	1.48	1.49

**Red: before repair; Black: after repair**

**Table 4: Noise values (dB) before and after repair was performed for engine revolution of 400 rpm.**

Location	1 <sup>st</sup> reading	2 <sup>nd</sup> reading	3 <sup>rd</sup> reading	4 <sup>th</sup> reading	5 <sup>th</sup> reading	6 <sup>th</sup> reading	7 <sup>th</sup> reading	8 <sup>th</sup> reading	9 <sup>th</sup> reading	10 <sup>th</sup> reading
50 cm above flexible coupling surface	100.06	100.28	100.51	100.73	100.96	100.98	101.01	101.03	101.06	101.09
	96.97	96.98	96.98	96.99	96.99	96.98	96.96	96.95	96.94	96.92

**Red: before repair; Black: after repair**

### 3.2 Comparison Based on Noise Waveforms Before and After Repair Performed

For the noise measurement, only a single unit of microphone was used, which was installed 50 cm above the flexible coupling. These waveforms were recorded under various engine revolutions; 400, 500, 600, 700 and 800 rpm. These noise waveforms and vibration waveforms were recorded simultaneously. Figure 4(a) compares the noise waveforms between before and after repair for the flexible coupling for engine revolution of 400 rpm. It was found that the noise level in decibel (dB) before repair is slightly higher than after repair, as shown in Table 4. Basically, this reduction indicates that good improvement and better condition existed for this flexible coupling after repair. Nevertheless, further analysis of these waveforms shows the existence of knocking symptoms at 88.77 s, which can be seen clearly on the waveform for before repair. Similar comparison between before and after repair for the flexible coupling performed under engine revolutions of 500, 600, 700 and 800 rpm (Figure 4(b)). It was noticed that even though the noise level before repair is slightly higher than the noise level after repair, there was no existence of knocking symptom for these engine revolutions.

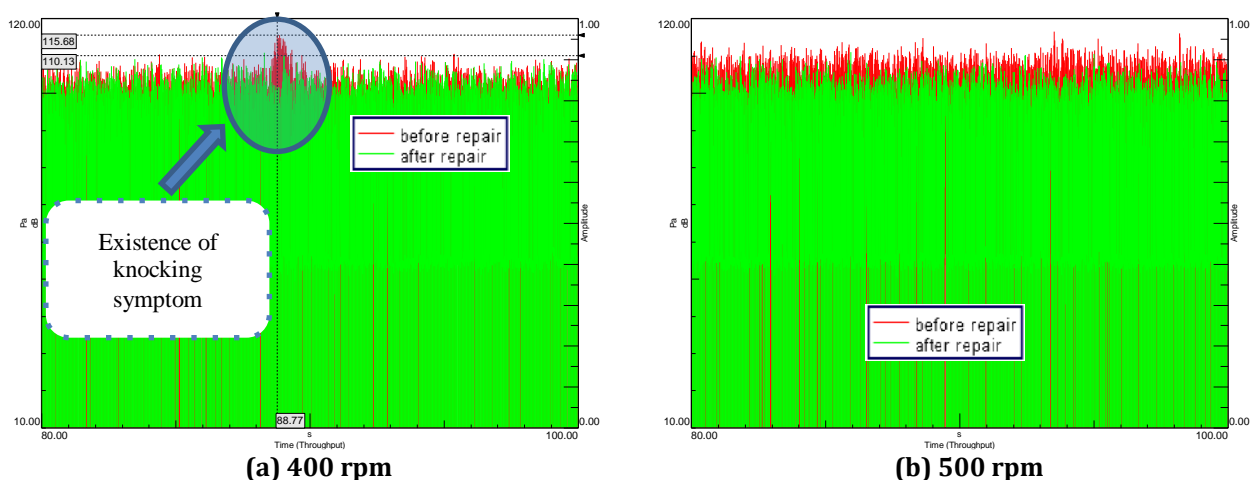


Figure 5: Noise waveforms before and after repair at (a) 400 rpm and (b) 500 rpm showing the existence and non-existence of knocking symptom respectively.

## 4. CONCLUSION

In this study, vibration and noise measurement was performed on a flexible coupling under two different conditions; before and after repair was performed. Vibration measurement was conducted at four different locations on the surface of the main diesel engine and gearbox. Meanwhile, noise measurement was conducted using a microphone at position of 50 cm above the surface of the flexible coupling. Based on analysis conducted for the vibration and noise data, it is concluded that the knocking symptom can be identified on engine surface before repair was performed for engine revolution of 400 rpm. At other engine revolutions, the knocking symptom did not exist for both vibration and noise data. Based on the results obtained in this study, it was found that the knocking symptom is an appropriate defect indicator for flexible couplings before catastrophic failure occurs. The methodology developed in this study can be optimised in order to develop condition-based monitoring programmes for flexible couplings and to conduct health checks periodically.

## 5. REFERENCES

- Alhouli, Y., Alkhaledi, A., Alzayedi, A., Alardhi, M. & Abed, A. I. (2015). Study of diesel engine vibration condition monitoring. *Global J. Res. Eng.*, **15**: 37-44.
- Arroyo, J., Muñoz, M., Moreno, F., Bernal, N. & Monné, C. (2013). Diagnostic method based on the analysis of the vibration and acoustic emission energy for emergency diesel generators in nuclear plants. *Appl. Acoust.*, **74**: 502-508.

- Barszcz, T., Gawarkiewicz, R., Jabłoński, A., Sękal, M. & Wasilczuk, M. (2018). Knocking sounds in the wind turbine gearbox during slowing down—case study. *5<sup>th</sup> Int. Conf. Condition Monitoring Machinery Non-Stationary Oper. (CMMNO'2016)*, 12–16 September 2016, Gliwice, Poland.
- de Sá Só Martins, D.H.C., Viana, D.P., de Lima, A.A., Pinto, M.F., Tarrataca, L., Lopes e Silva, F. & Haddad, D.B. (2021). Diagnostic and severity analysis of combined failures composed by imbalance and misalignment in rotating machines. *Int. J. Adv. Manuf. Tech.*, **114**: 3077-3092.
- Elamin, F. (2013). *Fault Detection and Diagnosis in Heavy Duty Diesel Engines Using Acoustic Emission*. Doctoral dissertation, University of Huddersfield, UK.
- Espadafor, F.J.J., Villanueva, J.A.B., Guerrero, D.P., García, M.T., Trujillo, E.C. & Vacas, F.F. (2014). Measurement and analysis of instantaneous torque and angular velocity variations of a low speed two stroke diesel engine. *Mech. Syst. Signal Proc.*, **49**: 135-153.
- Flett, J. & Bone, G.M. (2016). Fault detection and diagnosis of diesel engine valve trains. *Mech. Syst. Signal Proc.*, **72**: 316-327.
- Ghaderi, H. & Kabiri, P. (2017). Automobile engine condition monitoring using sound emission. *Turkish J. Electr. Eng. Comp Sci.*, **25**: 1807-1826.
- Wei, H., Wang, B., Wang, X., Wang, X. & Zhao, X. (2022). Analysis of fault coupling vibration and transmission characteristics of multistage gear transmission system. *J. Vibroeng.*, **24**: 871-884.
- Kumar, S., Loksha, M., Kumar, K. & Srinivas, K. R. (2018, June). Vibration based fault diagnosis techniques for rotating mechanical components. *Mater. Sci. Eng.*, **376**: 012109.
- Lamaris, V.T. & Hountalas, D.T. (2010). A general purpose diagnostic technique for marine diesel engines—Application on the main propulsion and auxiliary diesel units of a marine vessel. *Ener. Convers. Manage.*, **51**: 740-753.
- Ramteke, S.M., Chelladurai, H. & Amarnath, M. (2020). Diagnosis of liner scuffing fault of a diesel engine via vibration and acoustic emission analysis. *J. Vib. Eng. Tech.*, **8**: 815-833.
- Sim, H.Y., Ramli, R., Saifizul, A. & Soong, M.F. (2020). Detection and estimation of valve leakage losses in reciprocating compressor using acoustic emission technique. *Measurement*, **152**: 107315.
- Sinnasamy, Y., Ramli, R. & Saifizul, A.A. (2021). Statistical assessment on defect reporting system of high-speed marine diesel. *Naval Eng. J.*, **133**: 91-96.
- Song, M. H., Nam, T. K., & Lee, J. U. (2020). Self-excited torsional vibration in the flexible coupling of a marine propulsion shafting system employing Cardan shafts. *J. Marine Sci. Eng.*, **8**: 348.
- Tharanga, K. P., Liu, S., Zhang, S. & Wang, Y. (2020). Diesel engine fault diagnosis with vibration signal. *J. Appl. Math. Phys.*, **8**: 2031-2042.
- Vilas Boas, F.M., Borges-da-Silva, L.E., Villa-Nova, H.F., Bonaldi, E.L., Oliveira, L.E.L., Lambert-Torres, G. & da Silva, E.G. (2021). Condition monitoring of internal combustion engines in thermal power plants based on control charts and adapted nelson rules. *Ener.*, **14**: 4924.
- Yan, X., Li, Z., Yuan, C., Guo, Z., Tian, Z. & Sheng, C. (2013). On-line condition monitoring and remote fault diagnosis for marine diesel engines using tribological information. *Chem. Eng.*, **33**, 805-810.
- Yıldırım, H., Özsezen, A.N. & Çınar, A. Vibration and noise depending upon engine speed in diesel engine fueled with biodiesel. *6<sup>th</sup> Eur. Conf. Renew. Ener. Syst., Istanbul, Turkey*.

# OVERPRESSURE REDUCTION BY HEXAGONAL AND RECTANGULAR PORTABLE SOIL-FILLED BARRIERS (PSB) SUBJECTED TO SURFACE BURST

Jestin Jelani<sup>1\*</sup>, Mohd Zaid Othman<sup>2</sup> & Ahmad Mujahid Ahmad Zaidi<sup>3</sup>

<sup>1</sup>Department of Civil Engineering, Faculty of Engineering

<sup>2</sup>Department of Mechanical Engineering, Faculty of Engineering

<sup>3</sup>Department of Science and Technology Maritime, Faculty of Defence Science and Technology  
National Defence University of Malaysia (UPNM), Malaysia

\*Email: jestin@upnm.edu.my

## ABSTRACT

*Soil barriers protect humans and structures from blast overpressure induced by an explosion. Previous soil barriers in military applications include sandbags, Hesco Bastion and geosynthetic reinforced barriers such as geocell and geoblock. The soil barriers are typically rectangular walls with no void. This study uses hexagonal and rectangular portable soil-filled barriers (PSBs) to investigate the effect of barrier shape and arrangement in reducing blast overpressure behind the barriers. The experimental field blast test is scaled down to one-third of the actual size for safety reasons. The PSBs were subjected to 1 kg PE4 detonated on the ground surface. The blast overpressures were measured using PCB® Piezotronics pressure sensors and a high-speed data acquisition system (DAQ). The experimental field blast tests showed that the hexagonal PSB had more promising effectiveness,  $E_p$ , and showed 12 to 25% better overpressure reduction than the rectangular PSB. At greater distance behind the PSB, the ability of the rectangular PSB to attenuate blast overpressure decreased rapidly as compared to the hexagonal PSB.*

**Keywords:** *Portable soil-filled barrier (PSB); sand; surface burst; plastic explosive; blast overpressure reduction.*

## 1. INTRODUCTION

There are many advantages of using soil to construct above-ground protective structures, such as barricades, revetment walls, bunkers and retrofitting. Soil is an inexpensive, readily available material, and effective in mitigating blast overpressure, heat and fragment penetration (Hyde, 1988; Ng, Chew, Karunaratne, Tan, & Loh, 2000; Shamim, Ahmad Khan, & Ahmad, 2022). Soil barriers are purposely built in the direction of blast wave propagation to reduce the blast overpressure in the area immediately behind the soil barrier (Hussein, Heyliger, & Mahmoud, 2020; Zhou & Hao, 2008). Equation 1 is the formula for computing the effectiveness of a protective barrier in reducing blast overpressure,  $E_p$ , which is the ratio of the overpressure difference with and without soil barrier,  $O_d$  divided by the overpressure without soil barrier,  $O_{wb}$ .

$$E_p = \frac{O_d}{O_{wb}} \quad (1)$$

Soil has limited tensile strength and therefore is filled, wrapped or reinforced with synthetic materials with higher tensile strength to increase resistance against extreme blast load. The soil and synthetic material complement one another to produce a robust protective structure. Among its benefits, the ‘soft’ surface absorbs the impact of fragments and impedes the propagation of blast waves at the ground level (Andy, 2010; Jelani *et al.*, 2016; Tseng & Yang, 2023). As the soft material does not undergo brittle fractures that

occur with concrete or steel, there is no risk of harm from the dispersal of the generated debris (Li & Hao, 2014).

There is a dearth of research on the ‘reinforced soil’ barriers used for above-ground protective structures. The earliest study measuring sandbag soil barrier performance was conducted by the in (Department of Army, 1985). Chen *et al.* (2015) conducted a series of blast tests on a reinforced concrete structure protected by sandbags and subjected it to various high explosives. The sandbag demonstrated good protection capability with 80% overpressure reduction. Despite its effectiveness in protecting the structure from a direct hit, the barrier was susceptible to rot because its stability was primarily from the materials containing soil (Haris & Tan, 2020). Furthermore, it is laborious to fill the sandbags and time-consuming to stack them to form walls (Thawani *et al.*, 2021). For these reasons, sandbags are no longer popular as a vital protective structure.

He (2008) investigated the effectiveness of geosynthetic materials, such as geocell and geoblock, to reinforce backfill soil in a full-scale blast test. They arranged the barriers in a rectangle and subjected them to far- and close-range blast effects from varying charge weights. The reinforced soil barriers effectively mitigated the blast overpressure with at least 60% pressure reduction, depending on the scaled distance and amount of charge. The drawbacks of these soil barriers are high labour intensity, use of heavy construction equipment and long construction time.

In Scherbatiuk & Rattanawangcharoen (2008), a prefabricated container made of non-woven polypropylene and galvanised steel mesh, known as Hesco bastion (HB), was used to contain filled soil. HB is available in varying cubical sizes and is stacked to form a wall. The advantage of HB is its rapid construction with minimum use of heavy machinery. However, there is limited study on the performance of the HB barrier subjected to blast loading. The overpressure reduction behind the barrier is unknown because of safety reasons.

This paper studies a new soil barrier, known as portable soil-filled barrier (PSB), developed to investigate the ability of rectangular and hexagonal soil barrier geometries and arrangements to reduce overpressure behind them. The PSB was subjected to surface bursts in small-scale blast tests. This research is a continuation of previous works by the authors to study the effect of PSB shape and arrangement using numerical simulation software (Jestin *et al.*, 2014).

## **2. METHODOLOGY**

### **2.1 PSB Materials and Dimensions**

The PSBs for the blast test were fabricated from galvanised steel welded mesh frame lined with Geotube, as shown in Figure 1. The Geotube prevents the soil from draining out, while the steel mesh frame prevents the barrier from bulging outward during filling and compaction and retains the barrier shape. The PSBs were unpacked, filled with sand, compacted and used to construct a structure or wall. The galvanised steel mesh is a 3 mm diameter coated wire with tensile strength of 700 MPa and spaced at 83 mm. Geotube GT750M is a polypropylene woven fabric that is approximately 3 mm thick and has tensile strength of 120 kN/m in the machine and cross-machine direction.

Fabricated hexagonal and rectangular PSBs were fabricated for this study. Both PSBs have the same height and total volume of 1 m and 1.56 m<sup>3</sup> respectively to ensure comparable results. Figure 2 shows the configurations and arrangements of the hexagonal and rectangular PSBs. The blast test arrangements was based on a previous study conducted by the authors (Jestin, *et al.*, 2015).



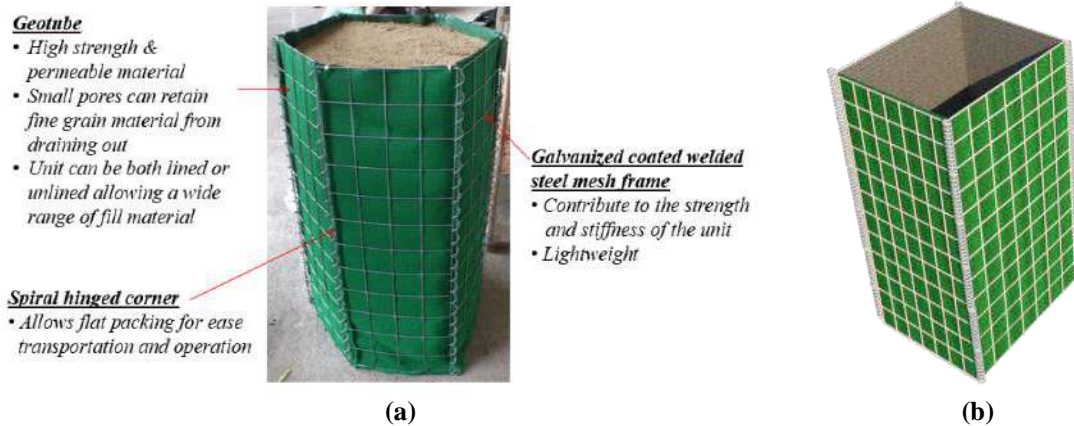


Figure 1: The PSBs in (a) hexagonal and (b) rectangular shapes.

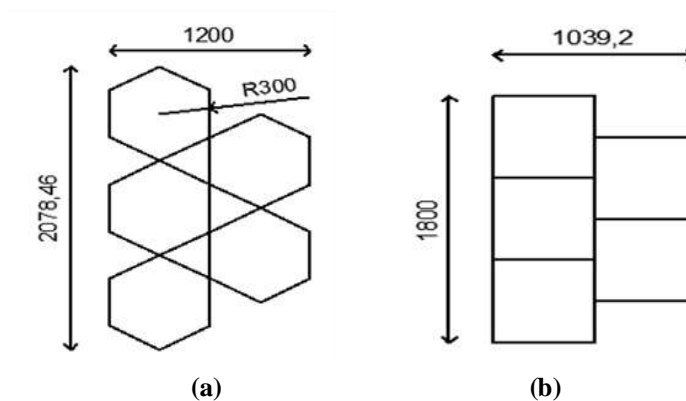


Figure 2: The dimensions and arrangements of the (a) hexagonal and (b) rectangular PSBs (in mm). Both PSBs have the same height and volume.

## 2.2 Small-Scale Field Blast Test and Instrument Setup

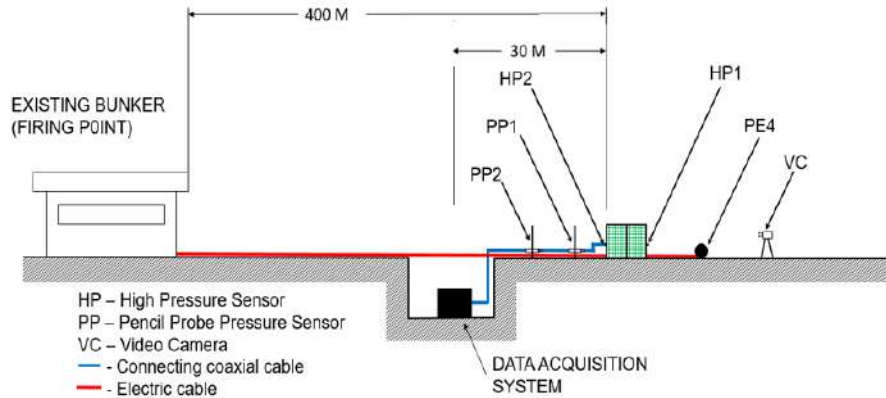
The experimental field blast test is the most realistic approach for replicating the actual condition of blast loading on a structure, but it is very costly, has high risk and requires tedious preparation. The alternative is small-scale blast test. A series of field blast tests were carried out at an undisclosed military facility in Malaysia. The charge weight and soil barrier size was scaled down to one-third of the actual size using the Hopkinson-Cranz scaling law (Baker *et al.*, 1991):

$$Z = \frac{R}{W^{1/3}} \quad (2)$$

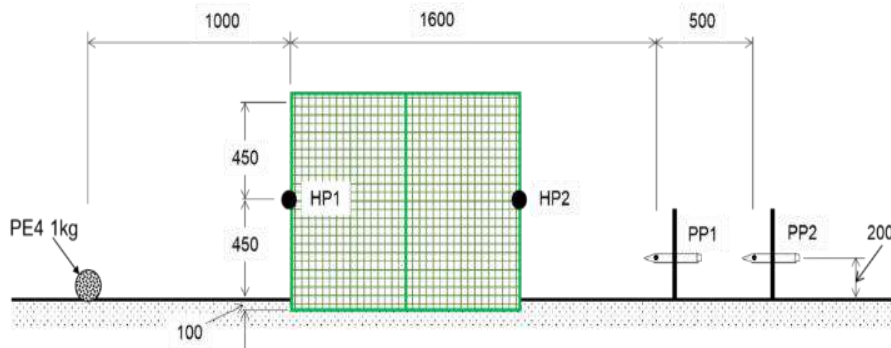
where  $Z$  is the scaled distance,  $R$  is the standoff distance from the centre of the explosive charge, and  $W$  is the weight of the explosive charges.

Figure 3 shows the general arrangement of the blast test setup. A 1 kg plastic explosive (PE4) moulded into a spherical shape was placed on the ground at a standoff distance of 1 m from the PSB. Two types of PCB® Piezotronics pressure sensors, namely Dynamic ICP® (HP) and Pencil Probe (PP), measured the reflected

and incident blast pressure respectively. The data acquisition system was placed in a trench 30 m behind the barrier to protect the unit from blast overpressure and any harmful flying debris during the blast event. The bunker was approximately 400 m from the blast site. Figures 4 and 5 show the close-up view of the sensor installation for the blast test with and without PSB. The position of each sensor was the same scaled distance to obtain comparable results.



**Figure 3: The cross-section view of the experimental field blast test and instrument setup.**



**Figure 4: The layout of the sensor installation with the PSB.**

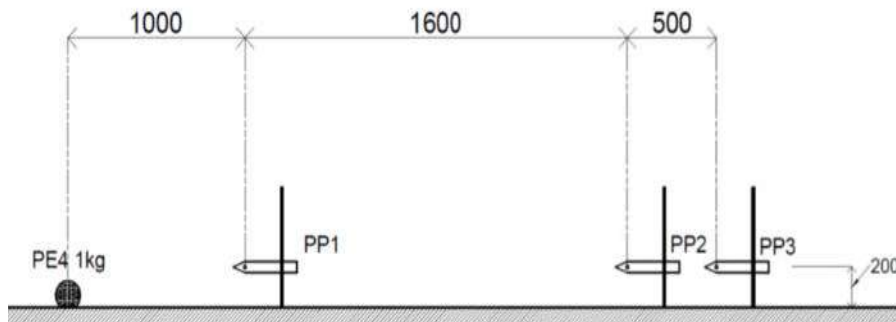


**Figure 5: The layout of the sensor installation without the PSB (free field).**

### 2.2.1 Dynamic ICP® Pressure Sensor (HP)

The HP sensors were mounted on the middle front and back of the soil barrier surface to measure the reflected and diffracted blast overpressure. The HP sensors were models 113B22 and 113B24 (Figure 6(a)) procured from PCB® Piezotronics. The maximum capacity for pressure measurement strength ranges between 7,000 and 34,500 kPa. Before filling the barrier with soil, a circular steel plate was attached between the HP sensor and Geotube to tighten the connection, as shown in Figure 6(b). The coaxial cable connecting the sensor to the data acquisition system was encased in a flexible pipe for protection and exited at the back of the soil barrier (Figure 6(c)).

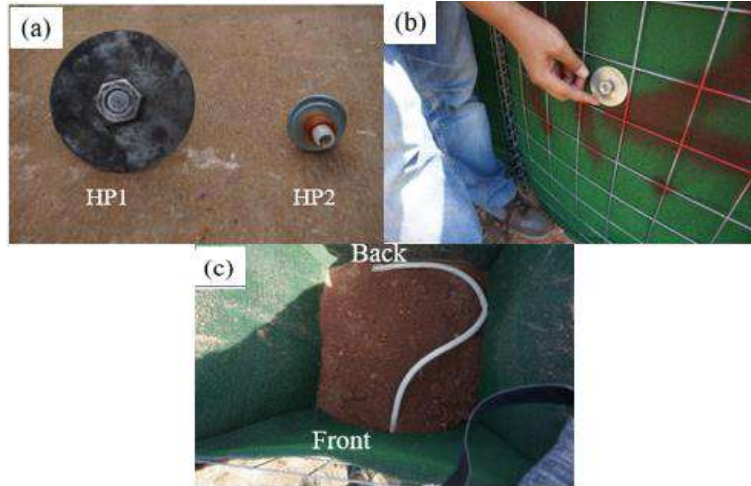


**Figure 6: The installation of the HP sensors. (a) HP1 and HP2 sensors. (b) The HP mounted on the front surface of PSB. (c) The coaxial cable encased in a flexible pipe.**

### 2.2.2 Pencil Probe Sensor (PP)

The PP sensors measured the intensity of the diffracted blast pressure behind the barrier. They were installed 0.2 m from the ground surface at a standoff distance of 2.6 and 3.1 m from the centre of the explosion, as shown in Figure 7(a). The procured models are 137B21A and 137B22A, with measurement strength ranging between 3,500 and 7,000 kPa. Figure 7(b) shows that the PP was studded with a customised holder and the tip installed pointing to the source of the explosion to obtain accurate measurements.

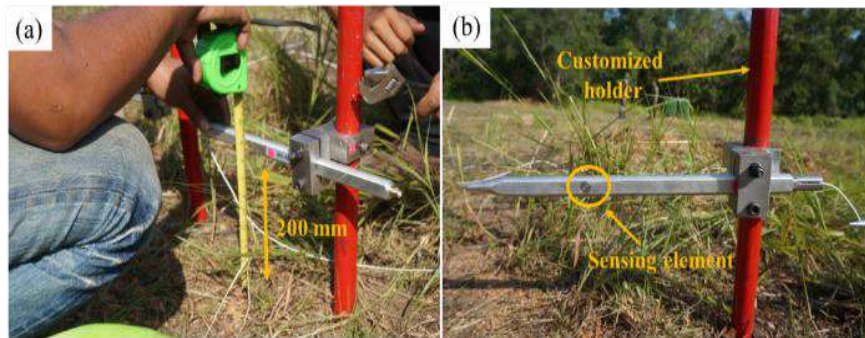


**Figure 7: Installation of the PP sensors. (a) The PP sensors were 200 mm from the ground surface. (b) The PP sensors were studded with customised holders to fix them firmly at the required position.**

### 2.2.3 Data Acquisition System (DAQ)

The high-speed data acquisition system (DAQ) used in this study was designed by National Instrument (NI) and has sampling rate capacity of 2 MHz. All pressure sensors, signal conditioner, software and cables were connected and monitored through this system, as shown in Figure 8. The signal conditioner modules were model NI SCXI-1000 and NI SCXI-1531, which have four-slot chassis and eight channels respectively. A high-performance shielded cable connected the signal conditioning module to the DAQ unit. The DAQ unit and generator set were placed in the trench to protect them from the blast load, thus preventing power failure and damage to the units. The data obtained by the DAQ unit was processed, filtered and displayed using LabView.

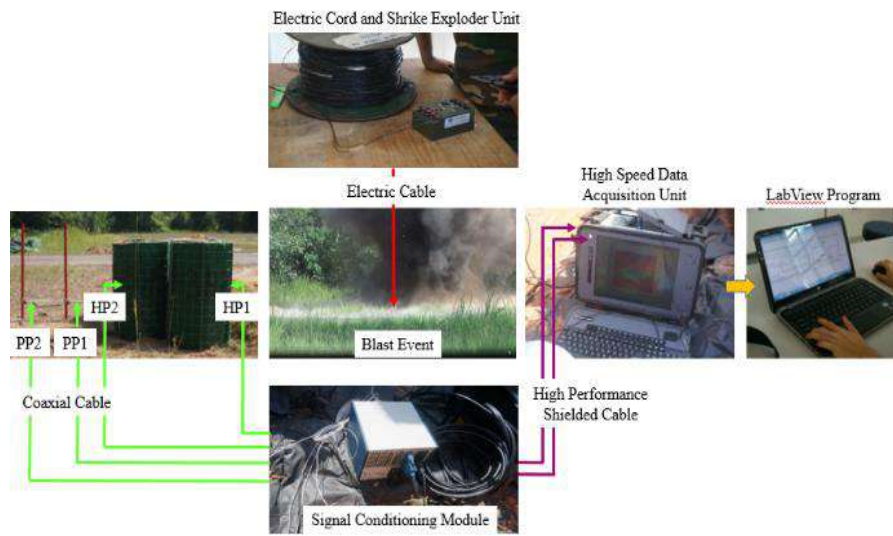


Figure 8: The schematic layout for connecting the DAQ unit.

## 3. RESULTS AND DISCUSSION

Figure 9 shows the overpressure-time history data from the HP and PP sensors for the hexagonal PSB. The pressure increased instantaneously from ambient, decayed exponentially to the negative phase, and then increased to ambient pressure. The highest value recorded by HP1 is 3,444 kPa. The next peak overpressures behind the hexagonal PSB were 61.7, 53.3 and 72.2 kPa recorded by HP2, PP1 and PP2 respectively. The peak values decreased significantly behind the barrier with a minimum of 98% pressure reduction. The higher pressure at the front is due to the interaction of the incident blast wave with the PSB surface, resulting in higher reflected blast pressure that superseded the incident blast wave manifold (Sochet *et al.*, 2017). The pressure decreased significantly as the blast wave continued to propagate over the PSB and away from the centre of the explosion. The propagation continued until the blast wave started to spill down towards the rear of the PSB and the ground, forming a vortex that caused lower pressure exerted behind the hexagonal PSB.

The rectangular PSB showed a similar trend of sudden onset of peak overpressure increase of up to 2,806 kPa and then decreased exponentially with a longer positive phase (Figure 10). The peak overpressure behind the rectangular PSB decreased by up to 98%, similar to the hexagonal PSB. Despite the similar percentage reduction, PP1 and PP2 for the rectangular PSB recorded higher peak overpressures behind the soil barrier of 69.9 and 97.3 kPa respectively, indicating that at the same distances of 2.6 and 3.1 m (or scaled distances of 2.3 and 2.8) behind the soil barrier, the mitigation effect of the rectangular PSB is 17% to 25% lower than the hexagonal PSB. The reduced overpressure was because of the shape and orientation

of the hexagonal PSB that disrupted the blast wave propagation over the top and back of the soil barrier. The void area between the first and second row in the arrangement of the hexagonal PSB created a strong air vortex impeding the blast wave propagation, thus reducing the overpressure behind the hexagonal PSB. This result is congruent with those of other researchers investigating different materials, shapes and arrangements (Smith, 2010; Sha *et al.* 2012; Hájek & Foglar, 2014).

The overpressure behind the hexagonal and rectangular PSB was compared to the free field data at the corresponding scaled distance (Figure 11) to determine the effectiveness of PSB in reducing blast overpressure,  $E_p$ . Table 1 presents the overpressure with and without the soil barrier. The overpressure values for the PSB are less than those for the free field, indicating a protective effect behind the PSB. The hexagonal PSB has the highest  $E_p$ , of 25% to 59% in reducing overpressure as compared to the rectangular PSB, which has  $E_p$  of 0.72% to 47%.

The results also showed that even though there was mitigation with increasing distance behind the barrier, the overpressure attenuation effect decreased. The overpressure differences between the hexagonal and rectangular PSBs were between 17% and 25%, demonstrating that the blast overpressure behind the rectangular PSB took less time to regain incident overpressure strength at the same distance behind the barrier. This result was similar to that of Hajek & Foglar (2015), which demonstrated that the effective mitigation area only existed a few metres behind the barrier, after which the blast overpressure intensity regained its normal strength. In cases where the person or asset being protected must be immediately behind the soil barrier, this zone provides the best mitigation.

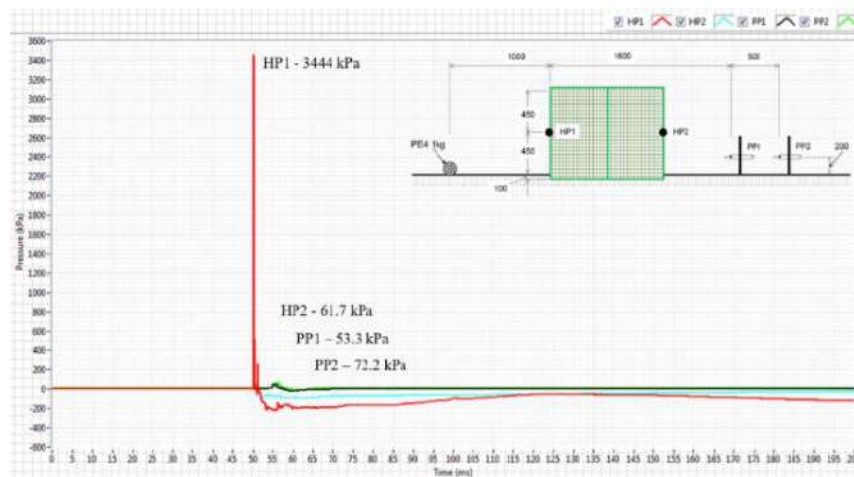


**Figure 9: Overpressure-time history for the hexagonal PSB.**

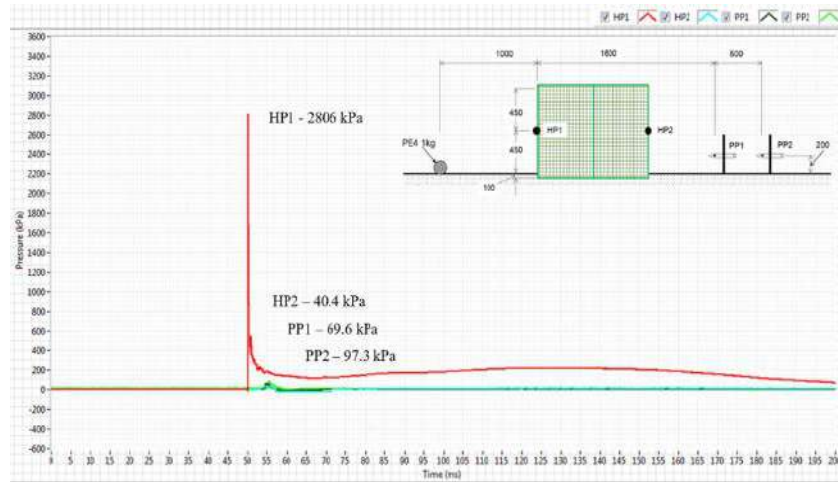


Figure 10: Overpressure-time history of the rectangular PSB.

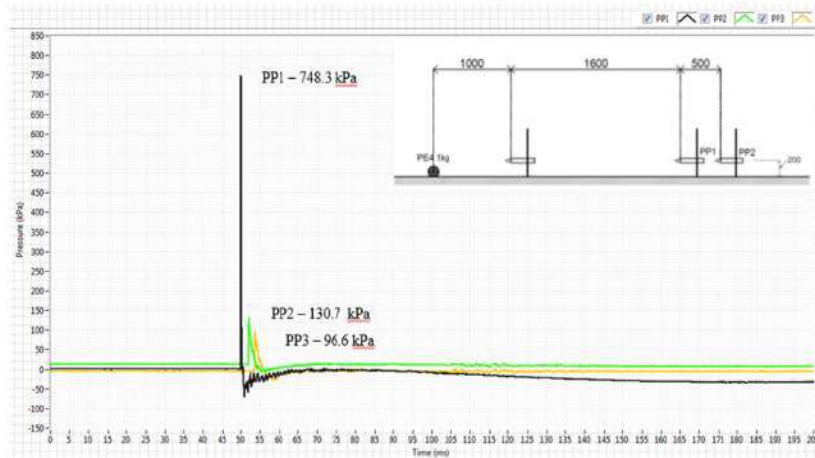


Figure 11: Overpressure-time history of the free field.

Table 1: Measured overpressure and percentage reduction.

	Measured overpressure behind the barrier (kPa)		The effectiveness of the barrier, $E_p$ (%)	
	Z=2.3	Z=2.8	Z=2.3	Z=2.8
Hexagonal	53.3	72.2	59	25
Rectangular	69.9	97.3	47	0.72
Free field	130.7	96.6	0	0

#### 4. CONCLUSION

This study investigated the overpressure reduction behind the hexagonal and rectangular PSBs in small-scale field blast testing. The hexagonal PSB with void showed 12 to 25% better overpressure reduction than the solid, rectangular PSB. The void space in the hexagonal arrangement caused the incident wave to spill down twice, thus creating a vortex flow that further attenuated the blast overpressure. At greater distances, the effectiveness of solid rectangular PSB in attenuating the blast overpressure decreased rapidly as compared to the hexagonal PSB.

#### ACKNOWLEDGEMENT

This research was funded by the ERGS grant, ERGS/1/2012/PK04/UPNM/01/2. The authors thank the Ministry of Higher Education (MOHE) and National Defence University of Malaysia (UPNM) for approving the fund, which made this research possible.

#### REFERENCES

- Hyde, D.W. (1988). *User's Guide for Microcomputer Program CONWEP and FUNPRO, Applications of TM 5-855-1, Fundamentals of Protective Design for Conventional Weapons*. Vicksburg, Mississippi, US.
- Jelani, J., Ali, F., Othman, M.Z., Zaidi, A.M.A. & Husen, H. (2016). Performance of small scale hexagonal portable soil-filled barrier subjected to blast load. *Electron. J. Geo. Eng.*, **21**: 1809–1817.
- Jestin, J., Ali, F., Mujahid, A., Zaidi, A., Koslan, F.S. & Othman, M.Z. (2014). Mesh sensitivity study of soil barrier subjected to blast loading: Numerical methods using AUTODYN 3D. *Modern Appl. Sci.*, **8**: 250–257.
- Jestin, J., Faisal, A., Ahmad Mujahid, A.Z. & Mohd Zaid, O. (2015). Comparative study of small scale soil barrier subjected to air blast load by using AUTODYN 2D and AUTODYN 3D. *Mater. Sci. Forum*, **819**: 417–422.
- Li, J. & Hao, H. (2014). Numerical study of concrete spall damage to blast loads. *Int. J. Impact Eng.*, **68**: 41–55.
- Ng, C.C., Chew, S.H., Karunaratne, G.P., Tan, S.A. & Loh, S.L. (2000). Flexible and rigid faced MSE walls subject to blasting. In Zornberg, J.C. & Christopher, B.R. (Eds.), *Advances in Transportation and Geoenvironmental Systems Using Geosynthetics*, ASCE Press, Reston, Virginia, US, pp. 322–336.
- Scherbatiuk, K. & Rattanawangcharoen, N. (2008). Experimental testing and numerical modeling of soil-filled concertainer walls. *Eng. Struct.*, **30**: 3545–3554.
- Sha, S., Chen, Z., Jiang, X. & Han, J. (2012). Numerical investigations on blast wave attenuation by obstacles. *Procedia Engineer.*, **45**: 453–457.
- Shamim, S., Ahmad Khan, R. & Ahmad, S. (2022). Fragility analysis of masonry wall subjected to blast loading. *Structures*, **39**: 1016–1030.
- Smith, P.D. (2010). Blast walls for structural protection against high explosive threats: A review. *Int. J. Protective Struct.*, **1**: 67–84.
- Sochet, I., Eveillard, S., Vinçont, J.Y., Piserchia, P.F. & Rocourt, X. (2017). Influence of the geometry of protective barriers on the propagation of shock waves. *Shock Waves*, **27**: 209–219.
- Thawani, B., Hazael, R. & Critchley, R. (2021). Numerical modelling study of a modified sandbag system for ballistic protection. *J. Comput. Sci.*, **53**: 101403.
- Tseng, S., Yang, K., Tsai, Y. & Teng, F. (2023). Investigation of the blast-resistance performance of geotextile-reinforced soil. *Geosynthetic Int.*, In press.
- US Army Corps of Engineers (1992). *Geosynthetic Reinforced Barricades for Ammunition Storage*.

Vicksburg, Mississippi, US.

Zhou, X.Q. & Hao, H. (2008). Prediction of airblast loads on structures behind a protective barrier. *Int. J. Impact Eng.*, **35**: 363–375.



# REDUCTION OF HCl EXHAUST PRODUCTS IN AP / HTPB PROPELLANTS BY DIFFERENT METAL ADDITIVES USING ROCKET PROPULSION ANALYSIS

Izzat Najmi Yaacob<sup>1,2</sup>, Norkhairunnisa Mazlan<sup>1,2,3\*</sup>, Kamarul Arifin Ahmad<sup>1,2</sup>, Adi Azrif Basri<sup>1,2</sup>, Ezanee Gires<sup>1,2</sup>, Osmera Ismail<sup>4</sup>, Norafiza Salleh<sup>4</sup> & Suraya Shahedi<sup>4</sup>

<sup>1</sup>Department of Aerospace Engineering

<sup>2</sup>Aerospace Malaysia Research Center (AMRC)

<sup>3</sup>Institute of Nanoscience and Nanotechnology (ION2)

Universiti Putra Malaysia (UPM), Malaysia

<sup>4</sup>Science & Technology Research Institute for Defence (STRIDE), Malaysia

\*Email: norkhairunnisa@upm.edu.my

## ABSTRACT

*Most conventional missiles and rocket boosters use solid propellant systems based on ammonium perchlorate (AP). However, combustion of AP during rocket launch produces toxic chloride emissions that increase in air pollution by 1 %. Researchers and engineers have developed several methods for transforming conventional AP-based propellant into green propellant, which is suitable for use in environmentally friendly rocket engines. These include neutralising, non-chlorine and scavenging propellants. The current study is aimed at investigating the properties of a neutralising propellant using various metal additives, including aluminium (Al), magnesium (Mg) and lithium (Li). Theoretical research has demonstrated that the addition of metal additives reduces the level of toxic hydrochloric acid (HCl) without compromising performance. By utilising the Rocket Propulsion Analysis (RPA) software with input on pressure conditions ranging from 100 to 2,000 psi, a simulation study of HCl reduction in propellant combustion products and ballistic performance was conducted. Pure metal additives of Mg with 15 % composition significantly increased the specific impulse ( $I_{sp}$ ) of solid propellant based on pure ammonium perchlorate / hydroxyl-terminated polybutadiene (AP / HTPB) by 24 % and the value of characteristic velocity ( $c^*$ ) by 22 %. Observations on the HCl reduction of AP-based propellant samples utilising rocket propulsion thermodynamics analysis indicate that adding Li-15 % to the basic propellant increases the HCl reduction by 99 %. Therefore, lithium metal mixtures in AP / HTPB-based solid propellant resulted in greater reduction of HCl mole fraction, whereas aluminium metal compositions resulted in superior ballistic performance.*

**Keywords:** *Aerospace materials; hydrochloric acid (HCl); composite solid propellant (CSP); rocket motor; propulsion.*

## 1. INTRODUCTION

Solid rocket motors are distinguished from other propulsion systems (nuclear, electric and radiant) in the way they discharge hot gases at high velocities to deliver a payload (e.g., a satellite or warhead) (Pradhan *et al.*, 2020). The fundamentals of solid propellants and historical summaries have been covered in many other publications. There are numerous applications for solid propellants, including tactical rockets, intercontinental and submarine-based ballistic missiles, space launch boosters, airline ejection seats, as well as recreational rockets. Solid propellants are preferred over liquid and hybrid propellants due to their reliability, simplicity, availability of ready-to-use systems, lower cost of propulsion systems and compactness (Kubota, 2015; DeLuca *et al.*, 2016). The two major classifications into which solid rocket propellants typically fall are homogenous (double-base) propellants, which combine the oxidiser and fuel into one molecule, and heterogeneous (composite)

propellants, which are composed of mixtures of different components. Due to the slow deflagrating characteristics of solid propellant, it can take a few seconds for these energetic materials to burn completely (Chaturvedi & Dave, 2019). Complete combustion of a composite propellant signifies that all chemical reactions have occurred and that the by-products of combustion must be released into the environment. The combustion products depend on the propellant's material composition and have a significant impact on performance and the environment, which is a crucial issue in the development of composite propellant technologies (Kubota, 2015; Trache *et al.*, 2017; Chaturvedi & Dave, 2019; Vara *et al.*, 2021).

Ammonium perchlorate (AP) serves as an oxidiser and aluminium serves as a metal fuel in composite propellants. Both have been widely used for military and non-military purposes for more than six decades (McClain *et al.*, 2019). AP is an inorganic compound with the formula  $\text{NH}_4\text{ClO}_4$  and is a strong oxidant used in solid propulsion systems. It is a white crystalline substance that dissolves quickly in water. The combination of ammonia and perchloric acid yields AP. AP is a prominent oxidiser due to its superior mechanical and ballistic properties relative to other oxidisers. According to several authors (Singh, 2017; Trache *et al.*, 2017; Dejeaifve *et al.*, 2020; Li *et al.*, 2021), the development of AP types of propellant poses environmental challenges in three important areas:

- Effects on the ground, such as pollution of groundwater or accidents caused by improper propellant handling and processing,
- Effects on the environment, usually caused by the interaction of waste products from combustion with the surrounding air, particularly the ozone layer,
- Biological effects, including toxicity and corrosiveness of propellants.

It is hypothesised that AP may interfere with the function of the human thyroid gland (AbdelGawad & Guozhu, 2022). This is because the combustion of propellants containing AP produces hydrochloric acid (HCl) as exhaust gas that pollutes the surrounding air. The hot gases discharged during rocket launches cause harmful emissions. In addition, toxic rocket emissions negatively impact the upper atmosphere as well as flora and fauna near the rocket launch site (Kumar *et al.*, 2018; Vellaisamy & Biswas, 2020). Based on the review by Abd-Elghany *et al.* (2018), the combustion of an AP-based solid propellant system releases approximately 100 T of HCl gas into the upper atmosphere. The build-up of these harmful substances in the atmosphere results in ozone depletion, acid rain, climate change, and adverse impacts on human health. Furthermore, each launch increases air pollution by 1 % due to the HCl gas emitted by rocket exhaust (Pellett *et al.*, 1983). According to Dennis & Bojko (2019), 60 T of HCl is present in the rocket exhaust from a rocket launch pad utilising composite propellant. It has been observed that the peak of HCl concentrations in eight Titan III rockets' exhaust plumes ranged from 25 to 0.5 mg/L or parts per million (ppm) for 3 to 300 min (Pellett *et al.*, 1983; Abd-Elghany *et al.*, 2018; Dennis & Bojko, 2019). In addition, the European Space Launcher Ariane-5, which contains 476 T of AP-based solid composite propellants and produces 270 T of concentrated HCl during combustion, exemplifies the hazardous nature of HCl. Despite the fact that aluminium compounds, such as aluminium oxide, are not thought to be poisonous to humans, plants or animals, the release of these compounds as microscopic particles in the form of aerosols could potentially harm all of these biological lives (Chalghoum *et al.*, 2020; Katsumi & Hori, 2021).

Researchers and rocketeers have developed various strategies to deal with toxic HCl emissions, including using green propellants. According to Hanafi *et al.* (2021), standard AP-based propellants can be converted into green propellants in three ways, which are by employing scavenging, neutralising and non-chlorine propellants. For scavenging propellants, sodium nitrate ( $\text{NaNO}_3$ ) is partially substituted for ammonium perchlorate ( $\text{NH}_4\text{ClO}_4$ ). This technique occurs in the combustion chamber, where sodium chloride (NaCl) is produced to eliminate HCl. Adding sodium nitrate, chlorine-free oxidants, and metal additives can cause 1-10 % of HCl to be scavenged or neutralised. Utilising  $\text{NaNO}_3$  as an HCl scavenger is advantageous due to its high density, wide availability and ease of use (Hanafi *et al.*, 2021; Katsumi & Hori, 2021; Lysien *et al.*, 2021). On the other hand, the addition of  $\text{NaNO}_3$  has been found to potentially lead to unfavourable mechanical and ballistic properties (Lysien *et al.*, 2021). Non-chlorine oxidisers, namely sodium nitrate ( $\text{NaNO}_3$ ), ammonium nitrate (AN), potassium dinitramide

(KDN) and ammonium dinitramide (AND), have been formulated as alternative substances to AP due to their ability to mitigate HCl emissions by neutralising HCl in the exhaust plume (Gettwert *et al.*, 2019; Ma *et al.*, 2022). Incorporating metal additives into the composite solid propellant formulation will complete the neutralisation process. The advantages of the neutralising propellant include high mechanical properties, durability, adaptability and reliability (Kumar, 2019). Multiple studies have indicated that the inclusion of metal additives in composite propellant leads to decrease in the percentage of HCl present in the combustion exhaust (Vara *et al.*, 2019; Paravan *et al.*, 2022). To date, there has been no extensive study on the effect of metal addition, and very few reports describe the augmentation of burn rate and decrease of HCl when metals are added to typical AP solid propellants. As stated by Chen *et al.* (2021), it is essential to effectively mitigate the issue of harmful exhaust emissions while simultaneously ensuring optimal rocket engine performance.

Terry *et al.* (2016) reported that the selection of metal alkali halophilic materials is based on their ability to efficiently remove chlorine ions and generate alkali metal chlorides (i.e., salts) during the combustion process. Hence, the utilisation of alkali metal nitrates, such as lithium nitrate ( $\text{LiNO}_3$ ) and sodium nitrate ( $\text{NaNO}_3$ ), has been employed as a substitute for a stoichiometric amount of AP to introduce strongly halophilic material in a stable manner (Chalghoum *et al.*, 2020). Although it has been established that these formulations significantly decrease the emission of HCl during the combustion process, they are also characterised by their cost-effectiveness in production and fabrication. Besides that, previous studies conducted by Terry *et al.* (2016) and Rodić *et al.* (2018) found that aluminium (Al), magnesium (Mg) and lithium (Li) metals are the most promising alkali metals to be used as scavenging agents in AP solid propellants. The primary objective of incorporating these metals is to mitigate the emission of HCl gases by facilitating the formation of aluminium chloride ( $\text{AlCl}_3$ ), magnesium chloride ( $\text{MgCl}_2$ ) and lithium chloride ( $\text{LiCl}_3$ ). In addition, it has been observed that Al, Mg and Li metals have the least toxicity, lower density and excellent safety characteristics compared to other metals such as boron, titanium and zirconium (Rodić *et al.*, 2018).

The study conducted by Vernacchia (2017) involved the manipulation of chamber pressures ( $P_c$ ) through simulation analysis to observe the corresponding pressure behaviour. It is known that elevation in pressure results in an increase in velocity, hence leading to a higher delta-v per unit of fuel. At elevated pressures, the density of the gas phase increases, leading to enhanced rates of reactions and diffusion. This phenomenon brings the flame's structure closer to the surface. Therefore, as the flame approaches the surface and the medium becomes denser, the heat transmission rate to the surface intensifies, thereby expediting the decomposition and combustion (Okniński *et al.*, 2020). Moreover, the combustion characteristics are influenced by both internal and external pressures within the combustion chamber. Therefore, it is necessary to analyse and test the propellant under varying  $P_c$  conditions, as it significantly impacts performance outcomes (Atwood *et al.*, 2013).

This study examines the simulation of the HCl mole fraction generated as AP / HTPB propellant combustion products. The investigation focuses on the effects of three different metal additives, Al, Mg and Li, with varying  $P_c$  conditions. By directly simulating combustion products utilising the Rocket Propulsion Analysis (RPA) software rather than manually calculating them using chemical molarity equations, this research can aid in developing a new promising additive for creating green solid propellants. In addition, through the utilisation of RPA, this study also aims to investigate the impact of metal additions and  $P_c$  on the HCl mole fraction, specific impulse ( $I_{sp}$ ) and characteristic velocity ( $c^*$ ). Additionally, the study seeks to investigate the ability of metal additives to mitigate the harmful effects of HCl.

## 2. EXPERIMENTAL PROCEDURE

### 2.1 Rocket Motor Design Specifications

The rocket motor used in the simulation of this research project conforms to the 2.75-inch standard design specification. This is due to the application of 2.75-inch rocket technologies using solid composite propellant and the K-class classification of rocket motor types (Atwood *et al.*, 2013). The design specifications and dimensions used throughout the simulation study, as depicted in Figure 1 and Table 1, were held constant.

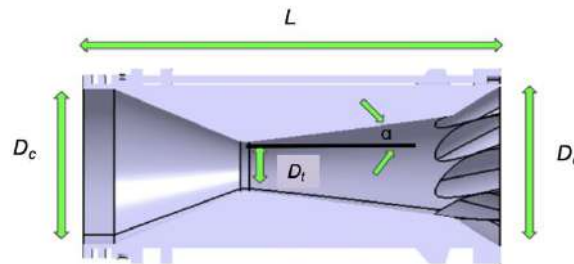


Figure 1: Cross section design of rocket motor nozzle.

Table 1: Specifications and dimensions of the rocket nozzle design.

Specification	Dimensions
Nozzle length ( $L$ )	140 mm
Nozzle divergence angle ( $\alpha$ )	48°
Nozzle throat diameter ( $D_t$ )	18 mm
Nozzle exit diameter ( $D_e$ )	58 mm
Chamber diameter ( $D_c$ )	56 mm
Nozzle expansion ratio ( $A_e / A_t$ )	10
Nozzle contraction ratio ( $A_c / A_t$ )	9

### 2.2 Propellant Composition and Formulation

Table 2 comprehensively depicts the composition and formulation of the materials utilised in the AP / HTPB composite propellant employed in this study. The simulation focused on the effect of the metal additives, specifically Al, Mg and Li. The remaining components, such as the curing agent and plasticisers, were held constant. At the same time, the oxidiser constituted the primary component, consistently accounting for 65 % of the overall weight percentage of the propellant. The binder employed in this study was hydroxyl-terminated polybutadiene (HTPB), whereas toluene diisocyanate (TDI) was used as the curing agent and dioctyl adipate (DOA) was employed as the plasticiser. In this work, the RPA software lite edition v.2.3.2 was utilised to establish the properties of each material, encompassing the comprehensive range of materials and chemicals needed for the simulation. This RPA software is a multi-platform analytical tool designed for the conceptual and preliminary design of chemical rocket engines. It also possesses the capacity to conduct rocket engine performance analysis. Additionally, the thermodynamic aspects of the simulation were established based on the material properties of the chemicals employed in the post-processing simulation.

**Table 2: Composition of AP based composite propellant samples.**

Formulation	Oxidiser (AP)	Fuel Binder (HTPB)	Aluminium (Al)	Magnesium (Mg)	Lithium (Li)
	In percentage (%)				
1	65	35	-	-	-
2	65	30	5	-	-
3	65	25	10	-	-
4	65	20	15	-	-
5	65	30	-	5	-
6	65	25	-	10	-
7	65	20	-	15	-
8	65	30	-	-	5
9	65	25	-	-	10
10	65	20	-	-	15

## 2.3 Theoretical Performance Parameter

### 2.3.1 Ballistic Performance

The investigation of theoretical performance characteristics resulted in the identification of metal additives for sample preparation. The research work involves the measurement of  $I_{sp}$ ,  $c^*$  and HCl mole fraction in solid propellants containing AP with and without the inclusion of metal additives. The HCl mole fraction can be determined by analysing the combustion products and evaluating the ballistic performance of the propellant.  $I_{sp}$  indicates how quickly the propellant is ejected from the rear of a rocket motor. In other words,  $I_{sp}$  refers to the duration during which the rocket engine generates a thrust equivalent to the mass of the propellant consumed.  $c^*$  is the ratio of the exhaust velocity to the thrust coefficient, representing a rocket engine's combustion efficiency in producing high temperatures and pressure. RPA calculates all propellant sample performance parameters and HCl mole fraction by shifting equilibrium conditions.  $I_{sp}$  and  $c^*$  were calculated using the theoretical rocket motor performance formula and applicable rocket motor conditions using RPA. The following equations depict the theoretical rocket motor performances of rocket motors derived by Terry *et al.* (2016):

$$c^* = \frac{P_c A_t}{\dot{m}} \quad (1)$$

where  $P_c$  is chamber pressure,  $A_t$  is throat area and  $\dot{m}$  is mass flow rate.

$$I_{sp} = \frac{F}{\dot{m}g} \quad (2)$$

where  $F$  is thrust,  $g$  is gravitational force and  $\dot{m}$  is mass flow rate.

The rocket motor input conditions in this simulation work using RPA are shown in Table 3.

**Table 3: RPA simulation setup parameters.**

Input conditions	Specifications
Rocket motor type	Composite AP / HTPB based solid propellant
Oxidiser-Fuel (O/F) mixture:	1.86 (65: 35)
Chamber pressure ( $P_c$ ):	100 – 2,000 psi
Expansion ratio ( $A_e / A_t$ ):	10
Combustion chamber condition	Equilibrium
Combustion temperature (Estimate):	3800 K
Ambient pressure	1 bar
Propellant system	Bipropellants

### 2.3.2 HCl Concentration in the Combustion Exhaust of AP Based Composite Solid Propellant

The theoretical HCl concentration in the combustion exhaust of solid composite propellant motors was computed using RPA. Besides that, the reduction percentage of HCl was calculated by determining the concentration of chloride ions through a molarity relationship. The following equations represent the calculation by RPA to determine the concentration of HCl in the exhaust emissions resulting from the combustion of a solid composite motor containing AP:

$$\text{Mole fraction} = \frac{(\text{No of moles of (HCl)})}{\text{Total number of moles of the mixture}} \quad (3)$$

$$\text{HCl percentage} = \frac{\text{HCl mole fraction of pure AP} - \text{HCl mole fraction of metallized AP}}{\text{HCl mole fraction of pure AP}} \times 100 \quad (4)$$

### 2.4 Flowchart of the Simulation Work

The simulation work was divided into multiple parts and phases due to the necessity of entering parameters and boundary conditions throughout the analysis setup. The flowchart presented in Figure 2 illustrates the progression of the simulation work from data collection to simulation of data analysis and interpretation.

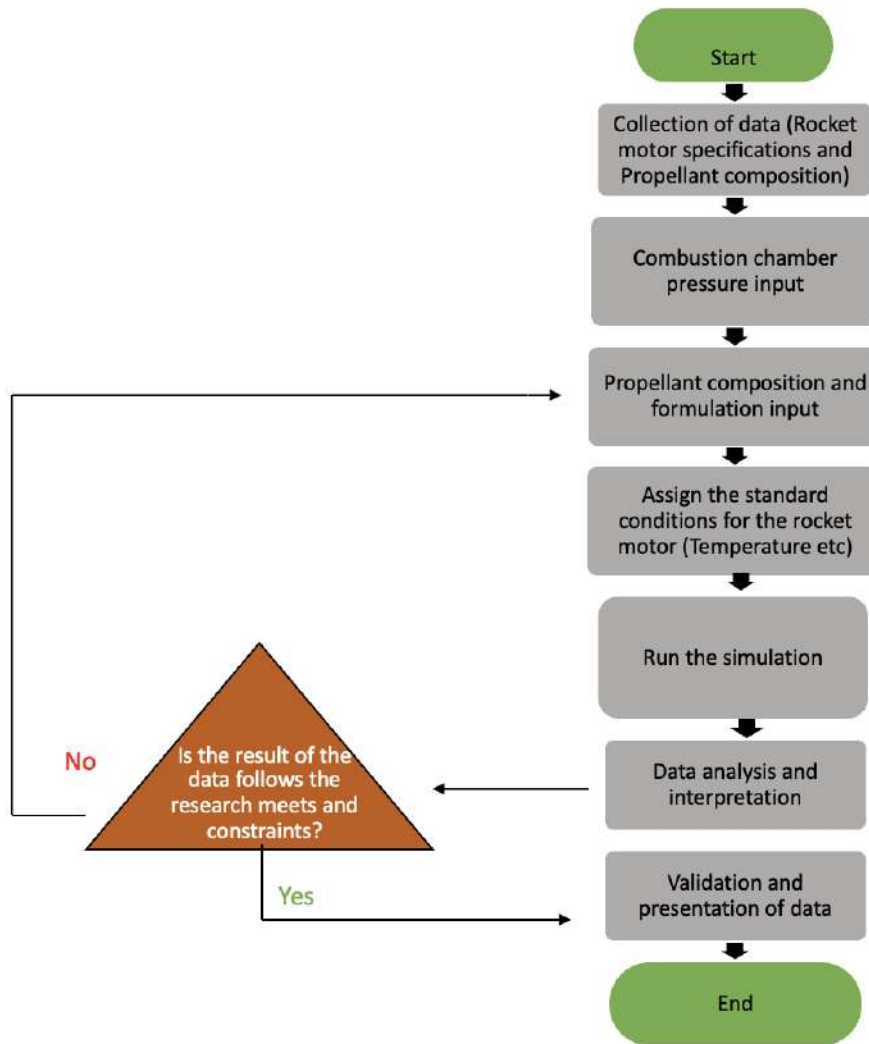


Figure 2: Flowchart of simulation process using RPA.

3.

## 4. RESULTS AND DISCUSSIONS

### 3.1 Theoretical Reaction of Metal Additives

The effect of metal additives on the neutralisation of HCl generated during the combustion of the AP / HTPB propellant in exhaust emissions and their influence on ballistic performance have been investigated. The percentage of HCl reduction was determined by using the molarity relationship to compute the concentration of chloride ions. The reactions of Al, Mg, and Li metals with AP are as follows (Rodić *et al.*, 2018):



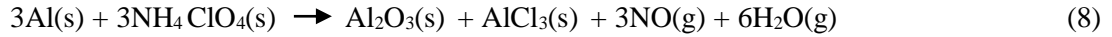
In the presence of humidity:



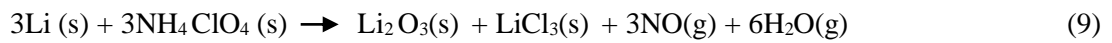
The hydroxide formed reacts with hydrogen chloride to give magnesium chloride ( $\text{MgCl}_2$ ) and water ( $\text{H}_2\text{O}$ ):



When Al is added to AP solid propellants, it reacts with the oxygen in the AP to form aluminium oxide ( $\text{Al}_2\text{O}_3$ ), aluminium chloride ( $\text{AlCl}_3$ ) and water vapour ( $\text{H}_2\text{O}$ ) (Vellaisamy & Biswas, 2020):



Li reacts with AP to produce lithium oxide ( $\text{Li}_2\text{O}_3$ ), lithium chloride ( $\text{LiCl}_3$ ), nitric oxide ( $\text{NO}$ ) and water vapour ( $\text{H}_2\text{O}$ ) (Blackman & Kuehl, 1961):



### 3.2 Ballistic Performance Analysis

The ballistic performance analysis aimed to determine the values of  $I_{sp}$  and  $c^*$  for unfilled AP / HTPB and AP / HTPB filled with metal additives under varying  $P_c$ . Figure 3 shows a graphical representation of the relationship between  $I_{sp}$  and  $P_c$  for each sample, while Table 4 lists the data values.

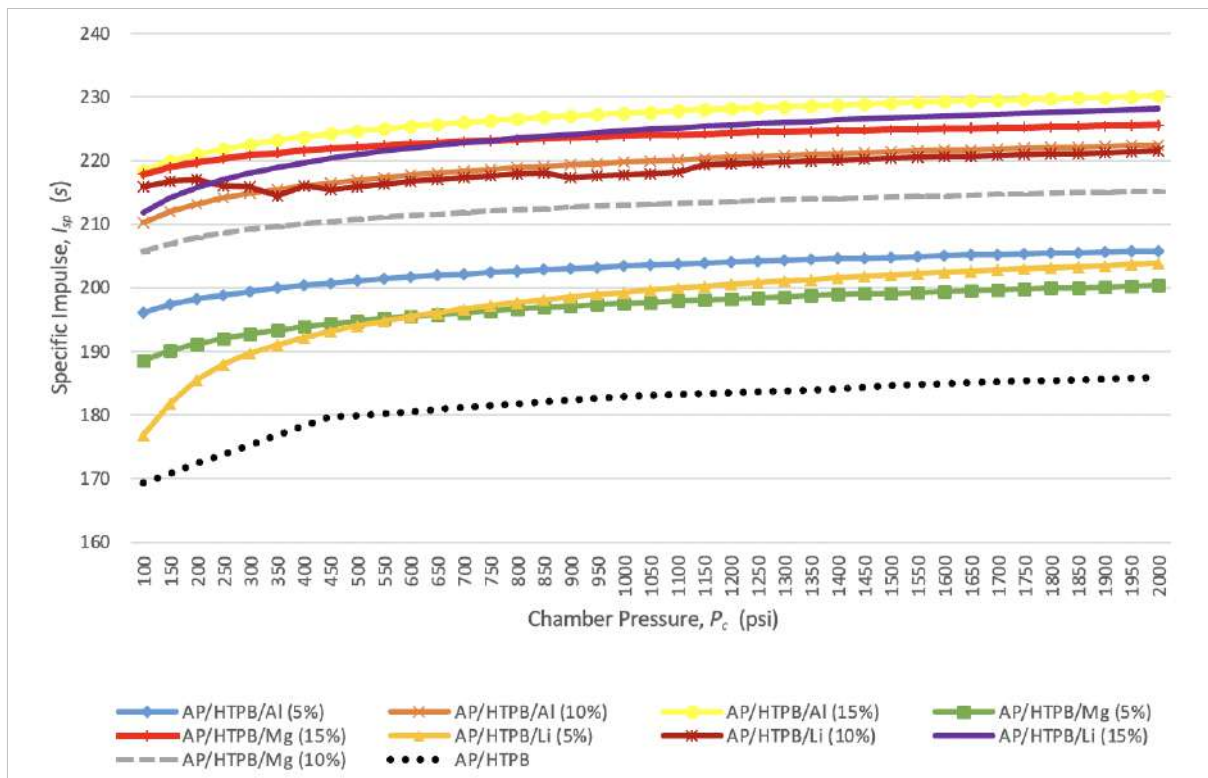


Figure 3: Specific impulse ( $I_{sp}$ ) vs chamber pressure ( $P_c$ ) for the propellant samples.



**Table 4: Effect of metal additives and pressure on specific impulse ( $I_{sp}$ ) of AP / HTPB based solid propellants.**

Samples	Specific impulse (s) at different pressures (psi)			
	500 psi	1,000 psi	1,500 psi	2,000 psi
AP / HTPB	179.94	182.96	184.73	185.98
AP / HTPB/ Al (5 %)	201.11	203.40	204.80	205.82
AP/HTPB/Al (10 %)	216.97	219.78	221.37	222.47
AP / HTPB / Al (15 %)	224.67	227.48	229.08	230.17
AP / HTPB / Mg (5 %)	194.79	197.56	199.20	200.36
AP / HTPB / Mg (10 %)	210.80	213.00	214.30	215.25
AP / HTPB / Mg (15 %)	222.13	223.89	224.90	225.60
AP / HTPB / Li (5 %)	194.10	199.32	202.03	203.84
AP / HTPB / Li (10 %)	215.97	217.78	220.37	221.47
AP / HTPB / Li (15 %)	220.99	224.70	226.76	228.15

As shown in Figure 3, it was found that the inclusion of metal additives in all samples resulted in higher  $I_{sp}$  values as compared to the unfilled AP / HTPB sample. It was observed that the higher  $P_c$  value, the faster the mass expands in the combustion chamber to exit through the rocket nozzle. In addition, the disparity in pressure between the combustion chamber and the surrounding environment results in the expulsion of hot air gases from the interior to the exterior, where the pressure is comparatively lower. This pressure variation dictates the mass acceleration (Blackman & Kuehl, 1961). Based on the data presented in Table 4, it can be observed that the sample AP / HTPB / Al (15 %) exhibits the highest  $I_{sp}$  of 230.17 s when subjected to  $P_c$  of 2,000 psi. This is followed by the samples AP / HTPB / Li (15 %) and AP / HTPB / Mg (15 %) with  $I_{sp}$  values of 228.15 and 225.60 s respectively. This finding illustrates that adding a 15 % aluminium additive into the rocket motor increases thrust while maintaining the same propellant consumption rate. Furthermore, comparing AP / HTPB with AP / HTPB / Al (15 %) propellant showed that  $I_{sp}$  increased by 24 %. The addition of metal additives to the propellant makes it fuel-rich, thereby increasing the reactivity of metals with oxidisers, which leads to higher  $I_{sp}$ . Similar findings have been observed by Rodić *et al.* (2018), who suggested that faster metal-oxidiser reactions could be another reason for the increase in  $I_{sp}$ .

$c^*$  represents the amount of energy available from the combustion process. It is dependent on the heat capacity of the exhaust gas and is inversely proportional to the molecular weight of the exhaust gas. Figure 4 illustrates the plot of the  $c^*$  versus  $P_c$  for all the samples and the data values were tabulated in Table 5.

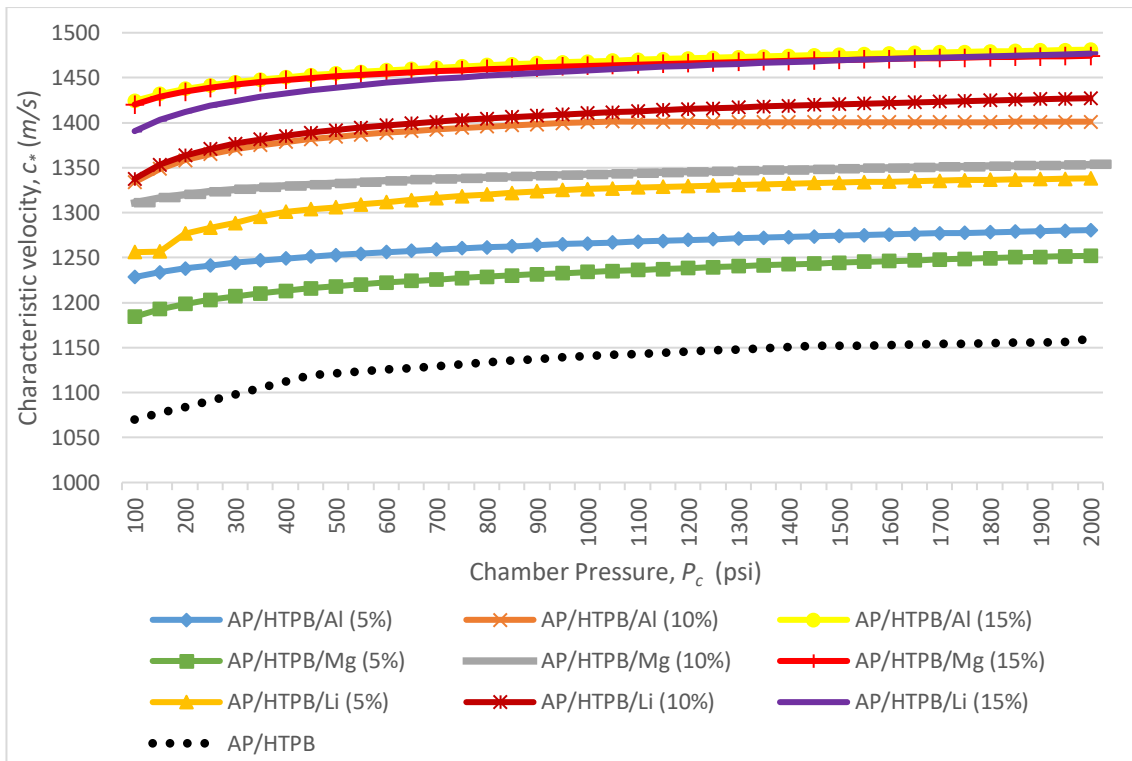


Figure 4: Characteristic velocity ( $c^*$ ) vs chamber pressure ( $P_c$ ) for the propellant samples.

Table 5: Effect of adding metal additives on characteristic velocity ( $c^*$ ) of AP / HTPB based solid propellants.

Samples	Characteristic velocity $c^*$ (m/s) at different pressures (psi)			
	500 psi	1,000 psi	1,500 psi	2,000 psi
AP / HTPB	1,121.34	1,140.60	1,151.85	1,159.80
AP / HTPB/ Al (5 %)	1,252.81	1,265.90	1,274.30	1,280.54
AP/HTPB/Al (10 %)	1,384.35	1,400.60	1,400.46	1,401.08
AP / HTPB / Al (15 %)	1,454.81	1,468.01	1,475.73	1,481.18
AP / HTPB / Mg (5 %)	1,218.07	1,233.89	1,244.37	1,251.88
AP / HTPB / Mg (10 %)	1,332.78	1,342.60	1,348.77	1,353.47
AP / HTPB / Mg (15 %)	1,451.42	1,463.21	1,469.80	1,474.37
AP / HTPB / Li (5 %)	1,306.11	1,326.23	1,333.40	1,338.13
AP / HTPB / Li (10 %)	1,391.78	1,410.44	1,420.49	1,427.22
AP / HTPB / Li (15 %)	1,439.06	1,458.38	1,469.26	1,476.83

The graph depicted in Figure 4 illustrates that all samples containing metal additives exhibit a consistent exponential growth pattern as compared to the unfilled AP / HTPB propellant. Table 5 presents the results of  $c^*$  measurements for several samples, including AP / HTPB / Al (15 %), AP/HTPB/Li (15 %), and AP / HTPB / Mg (15 %), at pressure of 2,000 psi. The AP / HTPB / Al (15 %) sample exhibits the highest  $c^*$  value of 1,481.18 m/s, followed by AP / HTPB / Li (15 %) and AP / HTPB / Mg (15 %) with values of 1,476.83 and 1,474.37 m/s respectively. The inclusion of metals in the system increases the

$c^*$  value, which may be due to the increased heat capacity of the exhaust gases resulting from incorporating these metals. The observed rise in  $c^*$  of propellants utilising metal additives could be attributed to reduction in the molecular weight of the exhaust gases produced during combustion. This is because  $c^*$  is inversely proportional to the molecular weight of the exhaust gas. On the other hand, the presence of metal oxides and metal chlorides in the exhaust gas leads to increase of molecular weight, which in turn increases the  $c^*$  value with decrease in heat capacity of the exhaust gases.

### 3.3 Reduction of HCl Concentration in Combustion Products

Mole fraction is important since it directly impacts the propulsion system's impulse. Even though the integration of metals results in the formation of products with high molecular weight, which lowers the  $I_{sp}$ , this drawback is compensated by the generation of products exhibiting high adiabatic flame temperature. The determination of the mole fraction is calculated based on the total mole fraction of the combustion products. Each metal additive's reactions with AP produces different products after fully completing the combustion process.

As the metals interact simultaneously with oxygen and halogen ions in the oxidiser, their affinity for the oxidiser and halogens affects the efficacy of propellants containing metal additives. Table 6 displays the HCl mole fraction and percentage of reduction in the HCl mole fraction in relation to the unfilled AP / HTPB-based propellant sample.

**Table 6: HCl mole fraction of the samples and percentage of reduction of HCl mole fraction.**

Samples	HCl mole fraction	Percentage (%) of reduction of HCl mole fraction as compared to pure AP / HTPB based propellant sample
AP / HTPB	0.12	-
AP / HTPB/ Al (5 %)	0.12	0
AP/HTPB/Al (10 %)	0.12	0
AP / HTPB / Al (15 %)	0.10	16
AP / HTPB / Mg (5 %)	0.03	75
AP / HTPB / Mg (10 %)	0.04	66
AP / HTPB / Mg (15 %)	0.04	66
AP / HTPB / Li (5 %)	0.00071	98.01
AP / HTPB / Li (10 %)	0.00033	99.72
AP / HTPB / Li (15 %)	0.00011	99.9

The addition of Mg and Li results in the formation of magnesium hydroxide ( $Mg(OH)_2$ ) and lithium hydroxide ( $LiOH$ ). These reactive bases have been found to promote the neutralisation of HCl to a greater extent when compared to the use of Al metal. Furthermore, it has been discovered that HCl molecules react with metal particles. Table 6 demonstrates that adding 15 % Li to the unfilled AP / HTPB sample results in the lowest HCl mole fraction among all the formulations, with recorded value of 0.00011. The maximum reduction of the HCl mole fraction observed by this sample was 99.9 %. The decrease in value implies that Li has the potential to act as a scavenger to reduce the concentration of HCl in the exhaust emissions of composite solid propellants. Complex metal hydrides are desirable as

aluminium replacements because they increase HCl emissions and  $I_{sp}$ , thereby contributing to low environmental impact (Chalghoum *et al.*, 2020). Although lithium-based propellant samples outperformed all others in terms of reducing HCl concentration, they cannot be considered green propellants due to the release of lithium chloride as one of the exhaust products, which is not only toxic but also challenging to handle with highly reactive lithium-based propellant.

### 3.4 Data Validation

Table 7 presents the theoretical ballistic data obtained from the study conducted by Vellaisamy & Biswas (2020) and the corresponding theoretical mole fraction of HCl concentration for each propellant sample. The findings illustrate the neutralising effect of metal additives on HCl. The HCl mole fraction is measured during the exhaust combustion of the rocket motor, where a state of complete combustion is achieved.

**Table 7: Theoretical performance parameters and simulation data for all propellant samples at 1,000 psi with oxidiser-fuel (O/F) ratio of 1.86.**

Propellant formulation	Theoretical				Simulation		
	$I_{sp}$ (s)	$c^*$ (m/s)	HCl mole fraction	References	$I_{sp}$ (s)	$c^*$ (m/s)	HCl mole fraction
AP / HTPB	221.78	1,426.2	0.20	Terry <i>et al.</i> (2016); Rodić <i>et al.</i> (2018); Vellaisamy & Biswas (2020)	182.96	1,140.60	0.12
AP / HTPB / Al (5 %)	244.07	1,576.10	0.2	Terry <i>et al.</i> (2016); Vellaisamy & Biswas (2020)	203.40	1,265.90	0.12
AP/HTPB/Al (10 %)	257.16	1,656.80	0.2	Blackman & Kuehl (1961); Kumar <i>et al.</i> (2018)	219.78	1,400.60	0.12
AP / HTPB / Al (15 %)	267.09	1,711.80	0.19	Rodić <i>et al.</i> (2018); Paravan <i>et al.</i> (2022)	227.48	1,468.01	0.10
AP / HTPB / Mg (5 %)	240.67	1,550.20	0.1	Rodić <i>et al.</i> (2018); Vellaisamy & Biswas (2020)	197.56	1,233.89	0.03
AP / HTPB / Mg (10 %)	260.46	1,665.20	0.95	Blackman & Kuehl (1961)	213.00	1,342.60	0.04
AP / HTPB / Mg (15 %)	263.93	1,691.40	0.94	Rodić <i>et al.</i> (2018); Vellaisamy & Biswas (2020)	223.89	1,463.21	0.04
AP / HTPB / Li (5 %)	246.07	1,573.70	0.01	Blackman & Kuehl (1961); Terry <i>et al.</i> (2016)	199.32	1,326.23	0.00071
AP / HTPB / Li (10 %)	255.71	1,615.50	0.01	Blackman & Kuehl (1961)	217.78	1,412.44	0.00033
AP / HTPB / Li (15 %)	258.44	1,627.30	0.0001	Blackman & Kuehl (1961); Vellaisamy & Biswas (2020)	223.70	1,458.38	0.00011

The simulation data was validated against the theoretical data to ensure its accuracy. The validation process is essential for comparing simulation data generated by the RPA software with actual or theoretical results. It demonstrates the software's relevance to the research being conducted. The data used for validation was collected at  $P_c$  of 1,000 psi. Equation 5 was used to calculate the percentage error by comparing simulation data with theoretical data. The resulting values are shown in Table 8.

$$\text{Error percent} = ((\text{Theoretical value} - \text{simulation value}) / \text{Theoretical value}) \times 100 \quad (5)$$

**Table 8: Error percentage of simulation result values based on theoretical values.**

Performance parameter at 1,000 psi	Value		Error (%)
	Theoretical	Simulation	
Specific impulse ( $I_{sp}$ ) of AP / HTPB / Al (15 %)	267.09 s	227.48 s	14.8
Characteristic velocity ( $c^*$ ) of AP / HTPB / Al (15 %)	1,711.8 m/s	1,468.01 m/s	14.2
HCl mole fraction of AP / HTPB / Li (15 %)	0.0001	0.00011	10

According to Zhang *et al.* (2007), simulation error percentage below 10 % is considered tolerable, while an acceptable value is below 20 %. Therefore, the error percentage values presented in Table 8 are acceptable. However, the allowable range of values for simulation works varies depending on the discipline of study. Certain projects involving very sensitive problems may require a precision of less than 1 %, while others may allow a margin of error of up to 20 %. The error percentage obtained in this study exceeded 10 % due to systematic errors in the simulation software, notably round-off error (Matuschek *et al.*, 2017). This error can be minimised by employing the same computational tools in simulations and theoretical studies.

## 5. CONCLUSION

The findings of this study demonstrated that the incorporation of metal additives significantly improves the performance of composite AP / HTPB propellants. The investigation of this parameter holds significant importance for developing green composite propellants since incorporating metal additions plays a crucial role in mitigating hazardous HCl levels while maintaining optimal performance. The impact of including metal additions such as Al, Mg and Li on HCl mole fraction in combustion end products and  $I_{sp}$  and  $c^*$  of the unfilled AP / HTPB propellant has been verified through simulations conducted using RPA. The metal additives act as a scavenger that effectively removes the HCl compound by forming metal oxide from the reaction between the metal and AP. For example, the simulation reveals that the formulation of AP / HTPB / Al (15 %) exhibits the highest  $I_{sp}$  and  $c^*$  at 2,000 psi with values of 230.17 s and 1,481.18 m/s, respectively. Besides that, the highest reduction of HCl mole fraction is shown by the formulation of AP / HTPB / Li (15 %) with value of 0.00011. Conversely, adding 15 % Al to an unfilled AP-based solid propellant increased  $I_{sp}$  by 24 %, while adding Li (15 %) decreased HCl mole fraction in the exhaust by 99.9 %.

Therefore, it can be concluded that the addition of metal additives to AP-based solid propellants can result in propellants that meet the performance criteria while emitting less toxic HCl. Furthermore, this research can contribute to the simulation of rocket motor performance in order to help in the development of green propellants for rocket applications.

## ACKNOWLEDGEMENT

The authors would like to express their gratitude to Universiti Putra Malaysia (UPM) for providing the assistance and resources necessary to conduct this study, as well as for the project support under Matching Grant UPM: UPM.RMC/800/2/2/4/GP-Matching/2021/UPM-LESTARIAERO/9300474.

## REFERENCES

- AbdelGawad, A.R. & Guozhu, L. (2022). A numerical simulation study for a dual thrust solid propellant rocket motor nozzle. *J. Phys. Conf. Ser.*, **2235**: 012010.
- Abd-Elghany, M., Klapötke, T.M. & Elbeih, A. (2018). Environmentally safe (chlorine-free): new green propellant formulation based on 2, 2, 2-trinitroethyl-formate and HTPB. *RSC Adv.*, **8**: 11771-11777.
- Atwood, A.I., Ford, K.P. & Wheeler, C.J. (2013). High-pressure burning rate studies of solid rocket propellants. *In Progress in Propulsion Physics*. EDP Sciences Web of Conferences, Les Ulis Cedex A, France, pp. 3-14.
- Blackman, A.W. & Kuehl, D.K. (1961). Use of binary light metal mixtures and alloys as additives for solid propellants. *ARS J.*, **31**: 1265-1272.
- Chalghoum, F., Trache, D., Maggi, F. & Benziane, M. (2020). Effect of complex metal hydrides on the elimination of hydrochloric acid exhaust products from high-performance composite solid propellants: a theoretical analysis. *Propell., Explos., Pyrot.*, **45**: 1204-1215.
- Chaturvedi, S. & Dave, P.N. (2019). Solid propellants: AP/HTPB composite propellants. *Arab. J. Chem.*, **12**: 2061-2068.
- Chen, T., Hu, Y. W., Zhang, C. & Gao, Z. J. (2021). Recent progress on transition metal oxides and carbon-supported transition metal oxides as catalysts for thermal decomposition of ammonium perchlorate. *Def. Technol.*, **17**: 1471-1485.
- Dejaifve, A., Sarbach, A., Roduit, B., Folly, P. & Dobson, R. (2020). Making progress towards» Green «propellants–Part II. *Propellants Explos. Pyrotech.*, **45**: 1185-1193.
- DeLuca, L. T. (2016). Innovative solid formulations for rocket propulsion. *Eurasian Chem.-Technol. J.*, **18**: 181-196.
- Dennis, C. & Bojko, B. (2019). On the combustion of heterogeneous AP/HTPB composite propellants: A review. *J. Fuels.*, **254**: 115646.
- Gettwert, V., Weiser, V., Tagliabue, C., Hafner, S. & Fischer, S. (2019). Environment-friendly composite propellants based on ammonium dinitramide. *Int. J. Energ. Mater.*, **18**: 1
- Hanafi, S., Trache, D., Meziani, R., Boukciat, H., Mezroua, A., Tarchoun, A. F. & Derradji, M. (2021). Synthesis, characterization and thermal decomposition behavior of a novel HNTO/AN co-crystal as a promising rocket propellant oxidizer. *Chem. Eng. J.*, **417**: 128010.
- Katsumi, T. & Hori, K. (2021). Successful development of HAN based green propellant. *Energ. Mater. Front.*, **2**: 228-237.
- Kubota, N. (2015). *Propellants and Explosives: Thermochemical Aspects of Combustion*. John Wiley & Sons, Hoboken, New Jersey, United States.
- Kumar, P. (2019). Advances in phase stabilization techniques of AN using KDN and other chemical compounds for preparing green oxidizers. *Def. Technol.*, **15**: 949-957.
- Kumar, P., Joshi, P. C., Kumar, R. & Biswas, S. (2018). Catalytic effects of Cu-Co\* on the thermal decomposition of AN and AN/KDN based green oxidizer and propellant samples. *Def. Technol.*, **14**: 250-260.
- Li, S. Y., Li, Y., Ding, Y. J., Liang, H. & Xiao, Z. L. (2021). One-step green method to prepare progressive burning gun propellant through gradient denitration strategy. *Def. Technol.*, **22**: 135-143.
- Lysien, K., Stolarczyk, A. & Jarosz, T. (2021). Solid propellant formulations: a review of recent progress and utilized components. *Mater.*, **14**: 6657.

- Ma, X., Jin, S., Xie, W., Liu, Y., Zhang, W. & Chen, Y. (2022). A novel green electrically controlled solid propellant with good electrical response and high energy performance. *Colloids Surf. A Physicochem. Eng. Asp.*, **641**: 128550.
- Matuschek, H., Kliegl, R., Vasisht, S., Baayen, H. & Bates, D. (2017). Balancing Type I error and power in linear mixed models. *J. Mem. Lang.*, **94**: 305-315.
- Okniński, A., Nowakowski, P. & Kasztankiewicz, A. (2020). Survey of low-burn-rate solid rocket propellants. In *Innovative Energetic Materials: Properties, Combustion Performance and Application*, pp. 313-349.
- Paravan, C., Dossi, S., Maggi, F., Galfetti, L., Vorozhtsov, A. B., Zhukov, I. & Sokolov, S. (2022). Reduction of solid propellants environmental impact: al-mg mechanically activated fuels and ap-psan blends. *9<sup>th</sup> Eur. Conf. Aerospace Sci. (EUCASS 2022)*, pp. 1-13.
- Pellett, G. L., Sebacher, D. I., Bendura, R. J. & Wornom, D. E. (1983). HCI in rocket exhaust clouds: atmospheric dispersion, acid aerosol characteristics, and acid rain deposition. *Air Pollut. Control.*, **33**: 304-311.
- Pang, W., Li, Y., DeLuca, L. T., Liang, D., Qin, Z., Liu, X. & Fan, X. (2021). Effect of metal nanopowders on the performance of solid rocket propellants: A review. *J. Nanomater.*, **11**: 2749.
- Pradhan, S. K., Kedia, V. & Kour, P. (2020). Review on different materials and their characterization as rocket propellant. *Mater. Today: Proc.*, **33**: 5269-5272.
- Rodić, V., Bogosavljević, M., Brzić, S. & Fidanovski, B. (2018). Possibility of aluminium/magnesium exchange in composite rocket propellants. *Sci. Tech. Rev.*, **68**: 40-49.
- Singh, H. (2017). Survey of new energetic and eco-friendly materials for propulsion of space vehicles. In *Chemical Rocket Propulsion: A Comprehensive Survey of Energetic Materials*. Springer, Berlin, Heidelberg, Germany, pp. 127-138.
- Terry, B. C., Sippel, T. R., Pfeil, M. A., Gunduz, I. E. & Son, S. F. (2016). Removing hydrochloric acid exhaust products from high performance solid rocket propellant using aluminum-lithium alloy. *J. Hazard. Mater.*, **317**: 259-266.
- Trache, D., Klapötke, T. M., Maiz, L., Abd-Elghany, M. & DeLuca, L.T. (2017). Recent advances in new oxidizers for solid rocket propulsion. *Green Chem.*, **19**: 4711-4736.
- Vara, J.A., Dave, P.N. & Chaturvedi, S. (2021). Investigating catalytic properties of nanoferrites for both AP and nano-AP based composite solid propellant. *Combust. Sci. Technol.*, **193**: 2290-2304.
- Vara, J.A., Dave, P.N. & Ram, V.R. (2019). Nanomaterials as modifier for composite solid propellants. *Nano-Struct. Nano-Objects.*, **20**: 100372.
- Vernacchia, M. T. (2017). *Development, Modeling and Testing of a Slow-Burning Solid Rocket Propulsion System*. Doctoral dissertation. Massachusetts, Boston, USA.
- Vellaisamy, U. & Biswas, S. (2020). Effect of metal additives on neutralization and characteristics of AP/HTPB solid propellants. *Combust. Flame.*, **221**: 326-337.
- Zhang, Z., Zhang, W., Zhai, Z. J. & Chen, Q. Y. (2007). Evaluation of various turbulence models in predicting airflow and turbulence in enclosed environments by CFD: Part 2—Comparison with experimental data from literature. *HVAC&R Res.*, **13**: 871-886.

# RESULTS OF TEST CAMPAIGNS COMPARING SOME FIELD INSTRUMENTATIONS USED BY FIRST RESPONDERS DURING RADIOLOGICAL AND NUCLEAR EMERGENCIES

Claudio De Maio<sup>\*1,2</sup>, Marco Beccaria<sup>2</sup>, Guglielmo Manenti<sup>3</sup> & Andrea Malizia<sup>3</sup>

<sup>1</sup>Department of Industrial Engineering, University of Rome Tor Vergata, Italy

<sup>2</sup>Italian Fire and Rescue Service, Italy

<sup>3</sup>Department of Biomedicine and Prevention, University of Rome Tor Vergata, Italy

\*Email: claudio.demaio@vigilfuoco.it

## ABSTRACT

*The authors in this work present the results of a comparison between field or portable instruments that can be used by first responders in case of a radiological or nuclear emergency. The comparison is performed through the use of four sources with different shapes and nature (a solid cylindrical shape of Am-241; a stone with copper matrix and extraction material of Th-232; a railway ballast stone of Cs-137; and a needle of Ra-226) and with four instruments with different detection technologies (HDS-101, FH-40, AutoMess 6150AD and XM-MIRA). The tests with the portable instruments are performed by placing the sources at 1 m distance and in contact with the instruments to report the difference in reaction, data collection and determining indications of the best solution for the emergency.*

**Keywords:** *Radiological and nuclear (RN) emergencies; detection; radioactive sources; first responder; fire & rescue service.*

## 1. INTRODUCTION

The urgency to test instrumentations that can be used in the case of radiological and nuclear (RN) emergencies is of paramount importance especially in this historical period due to several international contingencies (Malizia, *et al.*, 2012; Cavalieri d'Oro & Malizia, 2023). The authors have performed a series of tests using RN instrumentations and different radioactive sources. The test campaign was conducted in 2022 in the city of Milan, Italy with qualified and trained experts that carried out the phases of source manipulations, use of instrumentation and all software management activities (Ainsbury *et al.*, 2011). High safety levels of those experts were maintained with constant monitoring using thermoluminescent dosimeters (TLDs). The authors used “non-standard” sources to increase the affinity between those tests and real emergency interventions that usually involved sources with mixed matrices and irregular geometries (e.g., stones) (Discher *et al.*, 2021).

During RN emergencies, first responders can be called to respond without precise information about the scenario (Ferrari *et al.*, 2023). This leads them to decide in a short time range what type of instrument to choose and plan the intervention under unclear (sometimes unknown) circumstances. The aim of this work is to replicate some of the conditions expected in real events to test and choose the instruments that present the best compromise between precision, reliability and speed in performing the analysis and with a good level of transportability. The test campaigns are carried out in an environment that simulates some of the operative conditions of real intervention, with non-uniform sources and in a “non-sterile” situation, whereby the measurements cannot be considered as completely replicable (Werner *et al.*, 2017). This work can be considered as a starting point for developing valid support in terms of developing and performing training and procedures for first responders involved in RN emergencies.



## 2. MATERIALS AND METHODS

### 2.1 Equipment Used

The instruments used in the test campaigns are those most used by Italian first responders (such as firefighters) dealing with RN emergencies. The authors have considered the instrumentation used by civilians (and not military) first responders in order to set a reference in terms of international operational procedures (i.e., the Italian Fire and Rescue Service). Despite the technological progress of each instrument tested in this work (such as Bluetooth connection with tablets and cell phones; probes for a survey that protects the health of the operator; or new support to use those instruments on standard or unmanned vehicles), the authors have used the instruments' standard configurations for the tests and final comparison (ICRP, 2007). The instruments used were calibrated and passed through a periodical maintenance cycle. The following instruments were used for the tests:

- HDS 101 (Figure 1 and Table 1) is a versatile instrument with accessories that make it useful both as a portable scintillator and as a stationary scintillator (in combination with a PC). The last update includes a Bluetooth card for data transmission to allow for the visualization of data when the instruments must be placed in an uncomfortable location. The operator can perform the analysis in a safe condition even without direct access to the instrument display because of a sound alarm that is present.



Figure 1: HDS 101.

Table 1: Main technical features for HDS 101.

1. Detectors	# CsI (Tl) scintillator for spectrometry and low gamma dose rate measurement # Silicon Diode for high gamma dose rate measurement # LiI (Eu) scintillator for neutron measurement
2. Energy range	# 30 keV to 3 MeV (gamma and X-rays) # 0.025 eV to 15 MeV (neutrons)
3. Measurement and identification range (g rays)	# 1 $\mu$ Sv/h to 100 $\mu$ Sv/h
4. Continuous	# 0.1 mSv/h to 10 mSv/h

- FH-40 (Figure 2 and Table 2) is a Geiger–Müller counter that is considered by first responders as fast and with good performance for real operations with clear indications on the screen. It can also be used with commercial AA batteries, making it available for long periods of detection during operations. It is provided with large buttons that are easily accessible with rescuers' gloves. A case is available to protect the instrument from water drops (but does not make it waterproof). The instrument is also provided with a research probe, a probe for alpha and gamma particles and headphones to listen to the

sound of alarms. All the accessories can be mounted (one per time) with a connector placed at the base of the instrument with an extension cable to allow the first responder to read the data on the screen even in uncomfortable situations.



**Figure 2: FH-40.**

**Table 2: Main technical features for F4-H0.**

1. Detectors	# Wide range digital Geiger–Müller counter
2. Energy range	# 36 keV to 1.3 MeV
3. Dose range	# 100 nSv - 10 Sv

- Automess 6150AD (Figure 3 and Table 3) is a robust Geiger–Müller counter with an iron body, with both a long search probe and a smaller one available. Its sturdiness is related to the use of thick materials, but this also causes it to be a heavier instrument as compared to others, which can affect the performance of the operators in long-term operations.



**Figure 3: Automess 6150AD.**

**Table 3: Main technical features for Automess 6150AD.**

1. Detectors	# Geiger–Müller counter
2. Energy range	# 45 keV to 2.6 MeV
3. Dose range	# 100 nSv - 10 Sv

- XM-Mira (Figure 4 and Table 4) is the most recent instrument available in the market. It can be used both in a portable way, with its power supply and Bluetooth connection for wireless communication with Android applications, as well as a fixed station. As a fixed configuration, multiple XM-MIRA units can be used to form an instrument array to create a radiological detection network thanks to its capability to provide alarm, as well as store detected data that can be processed and used remotely by operators.



**Figure 4: Envinet XM-Mira.**

**Table 4: Main technical features for XM-Mira.**

1. Detectors	# 2 Geiger–Müller counter
2. Energy range	# 35 keV to 4.5 MeV
3. Dose range	# 100 nSv - 10 Sv

## 2.2 Radioactive Sources Used

The sources have been selected to replicate some of the unexpected scenarios that a first responder has to deal with during the real operations in case of radiological contamination. The authors used four different isotopes with different geometries and intensities:

- a) The source of Am-241 (Figure 5a) has cylindrical geometry with height of 1 cm and radius of 0.8 cm.
- b) The source of Th-232 (Figure 5b) is a 30 g stone. This source was exposed to air during the test.
- c) The source of Cs-137 (Figure 5c) is a railway embankment stone where Cs-137 was percolated. Smear tests gave negative results, so we considered as the entire stone of 1.2 kg as the source.
- d) The source of Ra-226 (Figure 5d) is a 5 cm long needle. As the source did not emit in an isometric way, the measurements were made by considering the long side.



Figure 5(a): Source of Am-241.



Figure 5(b): Source of Th-232.



Figure 5(c): Source of Cs-137.



Figure 5(d): Source of Ra-226.

### 3. TESTS PROTOCOL ADOPTED

The protocol used is the result of several tests carried out by the authors. The measurements were carried out in a closed environment with the following precautions:

- The source was placed in a position with no interference from other sources.
- The background signal was collected and considered during the tests.
- The instruments were always placed at a distance of 1 m from the source.
- The operator started to collect data only when the signal was stable.
- The instrument was taken away from this position and the data collected was saved.
- The instruments were placed in contact with the source, whereby the operator also waited for a stable signal.
- The instrument was taken away from this position and the data collected was saved.

This protocol was used for all the instruments and sources.

### 4. RESULTS & DISCUSSION

In this section, the authors report all the results obtained in the test campaigns. The test campaigns were performed in the same place that was sanitized every time to avoid cross-contamination that can affect the performance of the instruments and the reliability of the data collected. Tables 5 and 6 show the results of the test campaigns together with the standard deviation values at distance of 1 m from the source and at direct contact with the source respectively. The results are average of 10 replications of the same experiment (ICRP, 2010).

Table 5: Measurements at distance of 1 m from the source (average of 10 measurements, standard deviation in brackets).

Unit of Measure <i>nSv/h</i>	Am-241	Th-232	Cs-137	Ra-226
HDS101	200 (3.1)	180 (3.6)	200 (3.2)	270 (1.9)
FH-40	180 (4.6)	200 (4.0)	256 (3.8)	270 (4.1)
6150AD	170 (2.8)	230 (2.9)	200 (3.3)	250 (3.1)
XM-MIRA	170 (3.0)	210 (1.5)	220 (2.8)	280 (4.2)
HDS101	200 (3.1)	180 (3.6)	200 (3.2)	270 (1.9)

**Table 6: Measurements in contact with the source (average of 10 measurements, standard deviation in brackets).**

Unit of Measure <i>nSv/h</i>	Am-241	Th-232	Cs-137	Ra-226
HDS101	19 (1.1)	1.26 (0.1)	16 (1.4)	62 (2.1)
FH-40	23 (1.8)	1.20 (0.3)	16 (2.0)	72 (2.8)
6150AD	28 (0.4)	1.14 (0.1)	17 (0.8)	98 (2.3)
XM-MIRA	22 (0.7)	1.16 (0.2)	18 (0.9)	85 (1.8)
HDS101	19 (1.1)	1.26 (0.1)	16 (1.4)	62 (2.1)

The highest speed in reaching the stabilization time was reached by the XM-Mira, with average stabilization time of 2 s. The instrument with the lowest speed of stabilization time was the HSD-101 with average stabilization time of 5 s. Nevertheless, it must be specified that the detection technologies are different and that it is totally expected that a spectrometer has a longer response time rather than a Geiger–Müller detector (two detectors in the case of the XM-Mira), but that it can give more information such as the typing of the gamma-emitter element. However, all the instruments gave results in a range of time that is acceptable for a first responder involved in the identification of an unknown radioisotope.

Based on the results shown in Tables 5 and 6, there is not a single universal instrument for first responders. All the instruments analyzed can guarantee the safety of the first responders because of the capability to detect the presence of a radioactive source in few seconds, so having the instruments allows for CBRNe advisors to acquire more information, and through data analysis acquired with different techniques, can decrease the related errors. Therefore, the answer to the question of the radiological rescuer "which instrument should I bring?" does not have an unequivocal answer, but based on the type of scenario, the presumed evolutions and the principle of redundancy of the instruments, to evaluate the best choice.

## 5. CONCLUSION

In this study, the authors performed series of experimental campaigns to evaluate the performances of the instruments commonly used by Italian firefighters with different sources. The test campaigns were carried out in an environment that simulates some of the operative conditions of real intervention, therefore with non-uniform sources and in a "non-sterile" situation, the measurements cannot be considered completely replicable. The highest speed in reaching the stabilization time has been reached by the XM-Mira, with an average stabilization time of 2 s. The instrument with the lower speed of stabilization time was the HSD-101 with an average stabilization time of 5 s. However, all the instruments gave results in a range of time that is acceptable for a first responder involved in identifying of an unknown radioisotope.

Based on the results obtained, there is not a single universal instrument for first responders. All the instruments analyzed can guarantee the safety of the first responders because of the capability to detect the presence of a radioactive source in a few seconds. Therefore, having these instruments allows the CBRNe advisors to acquire more information and, through data analysis acquired with different techniques, can decrease the related errors.

## REFERENCES

- Ainsbury, E.A., Bakhanova, E. & Barquinero, J.F. *et al.* (2011). Review of retrospective dosimetry techniques for external ionising radiation exposures. *Radiat. Protect. Dosim.*, **147**: 573–592.
- Cavaliere d'Oro, E. & Malizia, A. (2023). Emergency management in the event of radiological dispersion in an urban environment. *Sensors*, **23**: 2029
- Discher, M., Woda, C., Ekendahl, D. Rojas-Palma, C. & Steinhäusler, F. (2021). Evaluation of physical retrospective dosimetry methods in a realistic accident scenario: results of the CATO field test. *Radiat. Meas.*, **142**: 106544.
- Ferrari, C., Manenti, G. & Malizia, A. (2023). Sievert or gray: Dose quantities and protection levels in emergency exposure. *Sensors*, **23**: 1918

- International Commission on Radiological Protection (ICRP) (2007). *The 2007 Recommendations of the International Commission on Radiological Protection*. ICRP Publication 103, Ann. ICRP, **37**: 2-4.
- International Commission on Radiological Protection (ICRP) (2010). *Conversion Coefficients for Radiological Protection Quantities for External Radiation Exposures*. International Commission on Radiological Protection (ICRP), Ontario, Canada
- Malizia, A., Lupelli, I., D'Amico, F. *et al.* (2012). Comparison of software for rescue operation planning during an accident in a nuclear power plant. *Defence S&T Bull.*, **5**: 36-45.
- Werner, C.J., Armstrong, J., Brown, F.B., *et al.* (2017). *MCNP User's Manual, Code Version 6.2*. Los Alamos National Security, New Mexico, US.

# ANALYSIS OF SURROGATE MARKER RICININE IN CASTOR BEANS FOUND IN MALAYSIA: OPTIMISATION USING STATISTICAL EXPERIMENTAL DESIGN

Mohamad Izharudin Che Amat\* & Raja Subramaniam

Research and Development Division, Department of Chemistry, Malaysia

\*Email: izharudin@kimia.gov.my

## ABSTRACT

*Ricin is listed as a Schedule 1 chemical under the Chemical Weapons Convention (CWC). It is derived from the seeds of the castor bean plant (*Ricinus communis*). Ricin is a large protein that requires a tedious extraction process and a sensitive method of detection. Instead, ricinine (3-cyano-4-methoxy-N-methyl-2-pyridone), a naturally occurring alkaloid found in the same beans, can be used as a surrogate marker for ricin exposure. In this study, we present a simple and optimised extraction method, as well as gas chromatography-mass spectrometry electron ionisation mode (GC-MS EI) analysis, for the identification of ricinine in castor bean seeds found in Malaysia. The study involved a comparison of three selected extraction methods from the literature. Subsequently, the extraction method with the highest ricinine recovery was optimised using statistical experimental design and multivariate data analysis. The optimisation of the extraction involved variables such as volume of deionised water, volume of extraction solvents (a mixture of diethyl ether, ethyl acetate and dichloromethane) and time of sonication. Ricinine was identified and quantified using GC-MS EI after extraction using commercial ricinine as an external standard. The limit of identification using EI full scan mode is 0.5 ppm, with approximately 1 g of seeds used. The seeds were sampled from castor bean plants found growing in the wild at a locality in Malaysia.*

**Keywords:** Ricinine; castor beans; extraction method; design of experiments (DOE); multivariate data analysis.

## 1. INTRODUCTION

The development of analytical methods for detecting chemical warfare agents has gained momentum since the establishment of the Chemical Weapons Convention (CWC) in 1997 (Vanninen, 2017). Some of the current works focus on ricin, one of only two protein toxins listed in Schedule 1 of the CWC. Recent global trends of ricin incidents have further justified the need for a rapid and sensitive method of identifying ricin (Audi *et al.*, 2005; Laura *et al.*, 2005; Roberto *et al.*, 2019).

Ricin is a deadly protein toxin found in the castor bean plant, *Ricinus communis*. The plant can be found in tropical and subtropical climates throughout the world, including Malaysia (Figure 1). The plant is also grown as a commercial source of castor oil, which is produced worldwide for industrial uses such as lubricants, pharmaceuticals and cosmetics. Furthermore, ricin itself has also been researched for its potential as anti-cancer treatment (Christopher *et al.*, 2013).

The ease with which the plant and seeds can be obtained as well as the simplicity of clandestine ricin extraction make ricin an attractive weapon for terrorists (Laura *et al.*, 2005; Roberto *et al.*, 2019). The recent exploitation of both intact seeds and extracted ricin, such as through white powder threats, assassinations, attempted poisonings, illegal production and storage by individuals, and even dirty bomb attempts, has raised security concerns (Christopher *et al.*, 2013; Feldberg *et al.*, 2021). Exposure to this poison can occur through inhalation, injection or ingestion. Currently, there is no antidote for ricin poisoning and treatment primarily focuses on symptomatic therapy (Audi *et al.*, 2005).



**Figure 1: Morphology and physical description of castor bean plant and seeds obtained from a locality in Malaysia**

Ricin is an approximately 65 kDa glycoprotein, and detecting intact ricin requires tedious sample preparation and analysis (Feldberg *et al*, 2021). In contrast, ricinine, a simple alkaloid found in castor bean seeds, can act as a unique surrogate marker in forensic investigations confirming the presence of castor beans or ricin (Christopher *et al*, 2013). The chemical structure of ricinine is presented in Figure 2. Analysing ricinine typically involves extracting ricinine from the seeds, urine or unpurified ricin followed by its identification using various analytical techniques, such as gas chromatography-mass spectrometry (GC-MS) (Christopher *et al*, 2013).

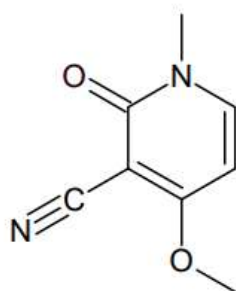


**Figure 2: Chemical structure of ricinine (3-cyano-4-methoxy-N-methyl-2-pyridone), CAS # 524-40-3.**

In this study, we present a simple liquid-liquid extraction and GC-MS electron ionisation mode (EI) analysis for the identification of ricinine in castor bean seeds. The extraction method was selected based on the recovery of ricinine from three methods found in the literature (Aziz, 1998; Thomas *et al.*, 2016; Marie *et al.*, 2020). Subsequently, the selected method was optimised using a statistical experimental design and multivariate data analysis tool (DOE - MoDDE). The optimised method was applied to identify ricinine extracted from a castor bean plant growing wild.



## 2. MATERIALS AND METHOD

### 2.1 Materials and Chemical Standards

Acetonitrile and methanol solvents were purchased from Merck (Darmstadt, Germany), while diethyl ether, ethyl acetate and dichloromethane solvents were purchased from Fisher (New Hampshire, USA). Deionised (DI) water with resistivity of  $18.2 \text{ M}\Omega \text{ cm}^{-1}$  was obtained from a Milli Q purification system (Woodridge, USA). The castor bean seeds were obtained from a wild castor bean plant found growing in the wild at a locality in Malaysia. The ricinine standard was purchased from Toronto Research Chemical (TRC, Toronto, Canada). Standard stock solutions of ricinine were prepared in methanol at concentrations ranging from 1 to 10 ppm.

### 2.2 Selection of Extraction Methods

Experiments were conducted to determine the most appropriate sample preparation method for ricinine. Based on the literature, three extraction methods were identified for their prevalence as simple extraction methods for ricinine and were selected for study on ricinine recovery comparatively (Method 1 - Aziz, 1998; Method 2 - Thomas *et al.*, 2016; Method 3 - Marie *et al.*, 2020). The methods and their extraction details are summarised in Table 1.

**Table 1: The selected extraction methods for ricinine study.**

Method 1	Method 2	Method 3
<ol style="list-style-type: none"><li>1. Remove castor bean seed coats (1 g seeds).</li><li>2. Soak pulp in 2 mL water and 2 mL NaOH for 2 min.</li><li>3. Mortar wet pulp to mash.</li><li>4. Separate mash from solvent using separating funnel.</li><li>5. Add 2 mL acetone to the separated mash to remove oil from the mash.</li><li>6. Add 2 mL mildly acidified deionised water (adjust pH of deionised water to pH 5-6 using acetic acid) to the mash and shake for 2 min. Extract the deionised water layer and</li></ol>	<ol style="list-style-type: none"><li>1. Remove castor bean seed coats (1 g seeds) and slice the pulp in half.</li><li>2. Add 2 mL toluene.</li><li>3. Add 2 mL Tris-buffered saline.</li><li>4. Homogenise in a tapered glass tissue.</li><li>5. Transfer into 10 mL screwcap tube.</li><li>6. Add 1 mL Tris-buffered saline.</li><li>7. Centrifuge at 1000 g for 30 min.</li><li>8. Collect the aqueous layer (bottom layer).</li><li>9. Evaporate the aqueous layer to dryness.</li><li>10. Add 50 <math>\mu\text{L}</math> MeOH.</li><li>11. Transfer for GC-MS analysis.</li></ol>	<ol style="list-style-type: none"><li>1. Ground castor bean seeds (1 g seeds) to powder using a mortar and pestle.</li><li>2. Mix the grounded seeds with 10 mL deionised water.</li><li>3. Boil mixture using hotplate at 100 °C for 10 min, cool at room temperature and filter using filter paper to remove castor seed particulates.</li><li>4. Basify the filtrate by adding 50 <math>\mu\text{L}</math>, 10M potassium hydroxide and vortex for 1 min.</li><li>5. Add 2 mL mix solvent (diethyl ether: ethyl acetate: dichloromethane) (20:20:5) and vortex the sample for 5 min and sonicate in ultrasonic bath for 15 min. Repeat this step twice.</li><li>6. Centrifuge the mixture for 3 min and collect the organic layer (upper layer) to</li></ol>

blow dry with N <sub>2</sub> gas. 7. Redissolve in 50 µL MeOH. 8. Transfer for GC-MS analysis.		a clean vial and blow dry with N <sub>2</sub> gas. 7. Add 50 µL methanol into the vial and vortex for 1 min. Transfer for GC-MS analysis.
--	--	--

### 2.3 Method Optimisation for Extraction of Ricinine using Statistical Experimental Design and Multivariate Data Analysis

The optimisation of the selected extraction method (Method 3) was conducted using design of experiments (DOE). The DOE software, MoDDE version 13, was sourced from Umetrics (Umeå, Sweden). A two-level full factorial design representing an interaction model was employed. Three critical parameters of the method were investigated: 5-15 mL of DI water, extraction solvent (diethyl ether: ethyl acetate: dichloromethane; 20:20:5) (ranging from 5 to 15 mL) and sonification time (ranging from 10 to 20 min). The selection of the parameters and their ranges were determined based on the authors' experiences with ricinine extraction and practical considerations. A total of eleven experiments were performed and their impact on the obtained results for a mixture of 1 g castor bean seeds was assessed.

### 2.4 Gas Chromatography Mass Spectrometry (GC-MS EI)

The samples were analysed using an Agilent 7890A gas chromatograph coupled to an Agilent 5975C inert XL mass selective detector (MSD) with a triple axis detector. Splitless injections (1 µL) were performed at injection temperature of 250 °C. The gas chromatograph was fitted with a 2 mm i.d. silanised linear for splitless injections and a DB5-MS capillary column (J&W, 30 m × 0.25 mm i.d., 0.25 µm film thickness). The carrier gas used was helium at a flow rate of 1 mL/ min. The transfer line temperature was set at 280 °C. The mass spectrometer operated in the EI mode with ion source temperature of 230 °C. The ions were acquired in scan mode (m/z 40-600). The GC oven temperature program was as follows: 40 °C for 1 min and then increased by 10 °C/min to 280 °C (held for 10 min), resulting in total run time of 35 min. Mass spectral data analysis was performed using the Agilent MSD ChemStation, NIST MS Search and deconvolution software (AMDIS) with the NIST14 Database.

### 2.5 Performance and Validation of the Method

Based on the optimised method, the identification of a 'real sample' was conducted to verify the performance of the method. The 'real sample' consisted of 1 g of seeds taken from the same plant. Additionally, the limit of identification of the method (GC-MS EI full scan) was determined for 1 g of seeds.

## 3. RESULTS AND DISCUSSION

### 3.1 Selection of Sample Preparation Method

Three different methods were investigated for ricinine extraction, and their yields were compared (Table 2). The amount of ricinine extracted using each method was estimated using standard ricinine from TRC, Canada. Experimental results revealed that Method 3 yielded the highest amount of ricinine as compared to Methods 1 and 2. Consequently, Method 3 was selected for optimisation to further enhance the ricinine yield.

**Table 2: Relative abundance of ricinine in 1 g of seeds.**

Method	Ricinine
Method 1	Not detected
Method 2	Not detected
Method 3	Detected (~19 ppm)

### 3.2 Optimisation of Methods Using DOE

The experimental design described in the study demonstrates how to effectively conduct and plan experiments to extract the maximum amount of information from the collected data, while minimising the number of experimental runs (Raja *et al.*, 2010). The underlying concept is to simultaneously vary all relevant factors over a set of planned experiments and establish connections between the results using an appropriate mathematical model. This model can subsequently be utilised for further interpretation, optimisation and making predictions.

In the optimisation of Method 3, three critical variables (factors) of the extraction process were investigated: a) volume of DI water, b) volume of extraction solvent (diethyl ether: ethyl acetate: dichloromethane; 20:20:5), and c) sonification time (Table 3). The experimental results were subjected to a multiple linear regression (MLR) least squares model using the projection method. MLR was chosen because it is suitable for the designed data sets that involve one response at a time, in this case, ricinine yield.

**Table 3: DOE worksheet containing factors setting to be optimised and response (GC-MS peak area of ricinine).**

Exp No	Exp Name	Variable (Factor)			Response
		DI water (mL)	Solvent (mL)	Sonication time (min)	GC-MS Peak Area (EIC m/z 164)
1	N1	5	1	10	-
2	N2	15	1	10	38,558
3	N3	5	3	10	299,375
4	N4	15	3	10	186,348
5	N5	5	1	20	18,224
6	N6	15	1	20	31,689
7	N7	5	3	20	239,289
8	N8	15	3	20	279,523
9	N9	10	2	15	121,965
10	N10	10	2	15	14,780
11	N11	10	2	15	122,017

It was observed during the selection of sample preparation method step earlier that the extraction solvents of ricinine, particularly the use of nonpolar and mid-polar organic solvents, resulted in improved yields. This observation was further confirmed during the optimisation, where the solvent was found to be the most significant factor influencing the yield of ricinine (Figure 3).

Data analysis of the results led to the development of a two-factor MLR model, with the following summary of fit: goodness of fit ( $R^2$ ) of 0.864, goodness of prediction ( $Q^2$ ) of -0.826, model validity of 0.80, and reproducibility of 0.70 (Figure 4). Based on the results, the optimised conditions for extraction to achieve maximum yield of ricinine are as follows: 5 mL of DI water, 3 mL of extraction solvent

(diethyl ether: ethyl acetate: dichloromethane; 20:20:5) and 10 min of sonification time (Figure 5, top left corner).

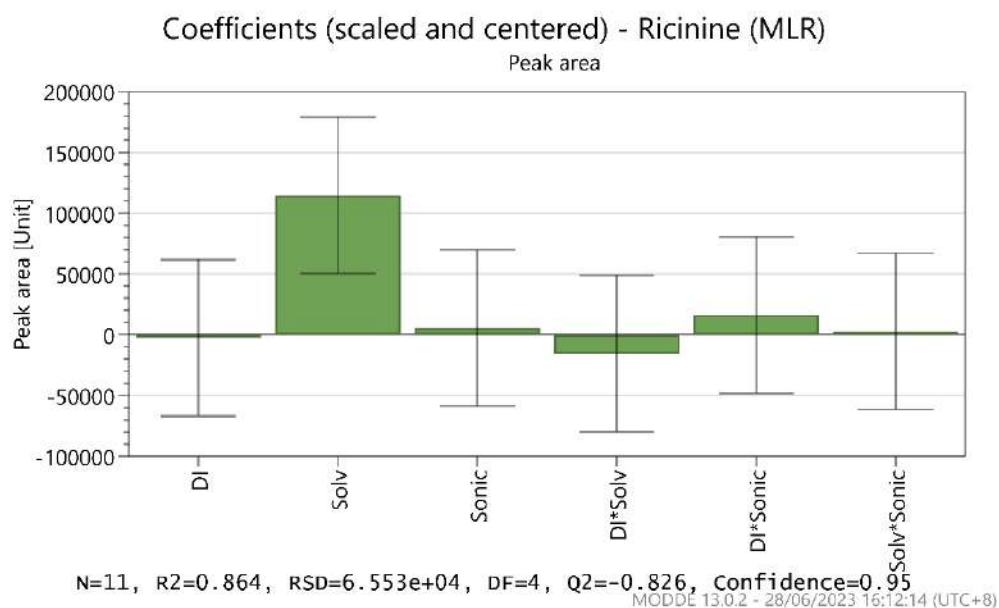


**Figure 3: Coefficient plot (scaled and centred, 95% confidence level). From the plot, the volume of solvent (Solv) represents the most significant factor in relation to response, where else factors of volume of deionised water (DI) and sonification time (Sonic) has minimal effect on response.**

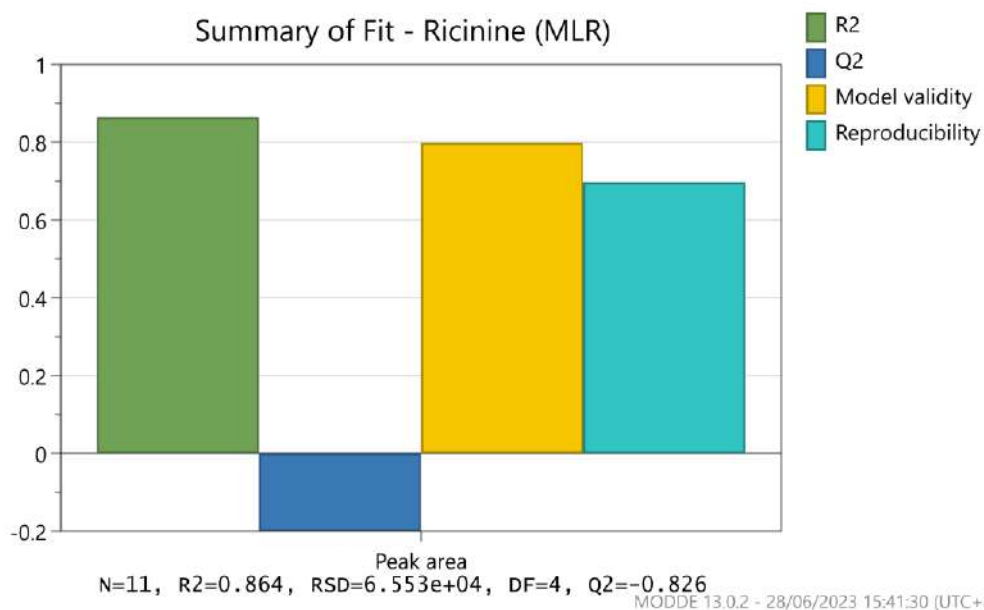


**Figure 4: The summary of fit plot demonstrates that the values of  $R^2$ ,  $Q^2$ , model validity and reproducibility are high, indicating a well-fitting mathematical model. This suggests that the model effectively explains the relationship between the variables and the response, and it can be used for further analysis and predictions.**

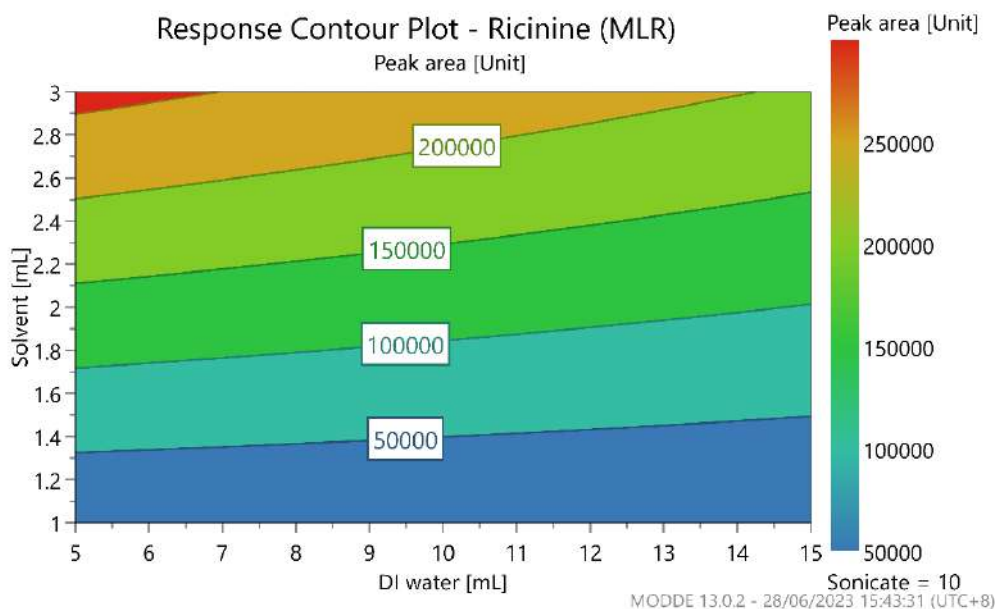


**Figure 5: The response contour plot of ricinine response indicating the influence of each factor term. The influence on response was measured in terms of the change in the area response from the GC-MS readout when the design factor was switched from its low to high level.**

### 3.3 Performance and Validation of the Method

Under the optimised conditions, the analysis of the real sample was conducted, and ricinine was conclusively identified with a high match factor (MS Search net match > 90) (Figure 6). All major ions of ricinine were clearly visible in the sample. However, there were also some background ions (marked as \*) observed, indicating the presence of matrix interference in the extracted ricinine sample. The limit of identification using GC-MS EI full scan was determined to be 0.5 ppm ricinine for 1 g of seeds.

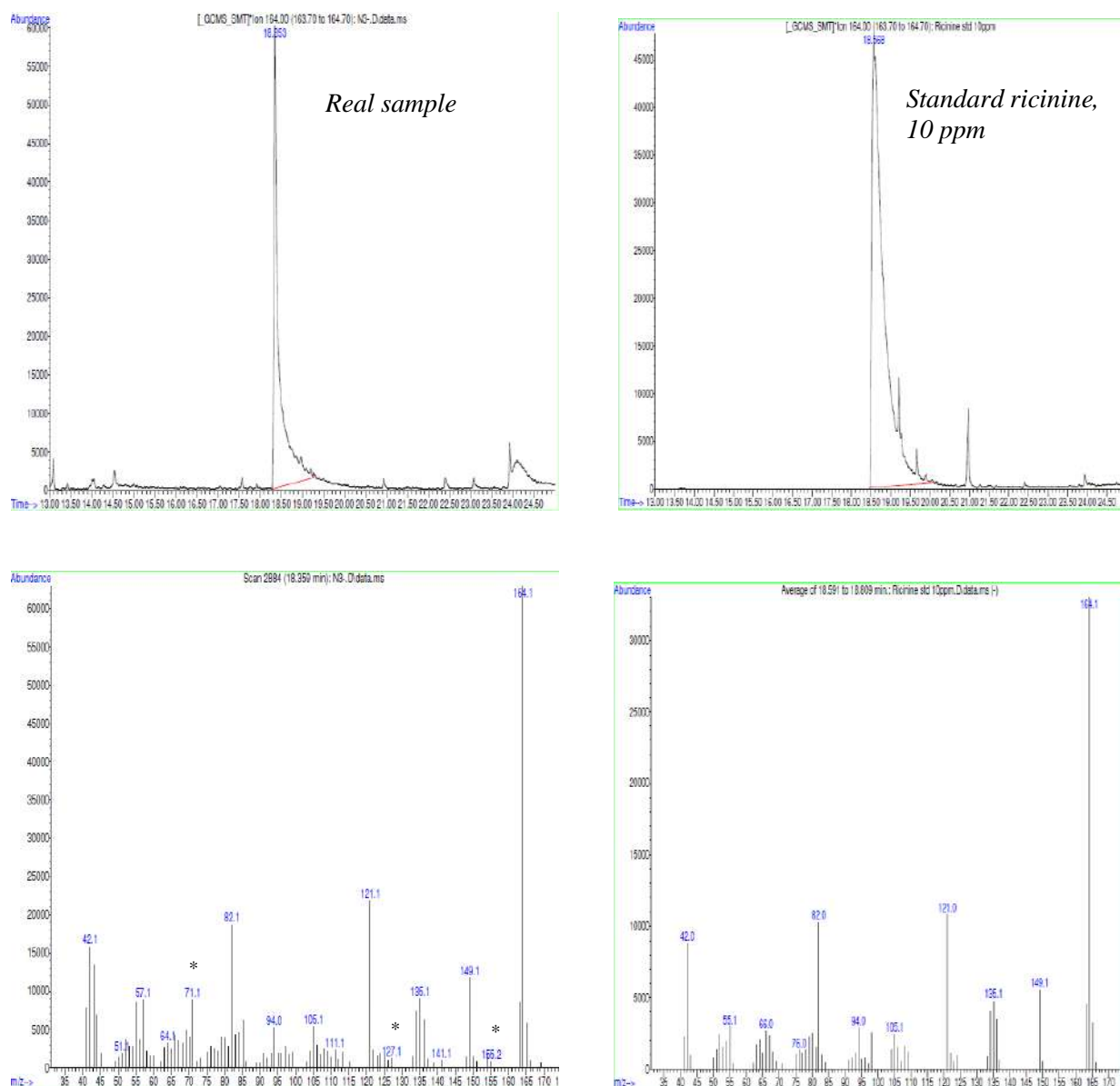


**Figure 6: Extracted ion chromatograms (m/z 164) and EI full scan spectra of ricinine from the real sample (left section) as compared to standard ricinine (right section).**

#### 4. CONCLUSION

In this study, an improved extraction method for the determination of the ricinine marker in 1 g of castor bean seeds (equivalent to approximately two seeds) has been demonstrated. The method achieved a limit of identification of 0.5 ppm using GC-MS EI full scan analysis. This optimised method can be utilised to screen multiple samples collected from castor bean seeds and ricin for the presence of ricinine.

Furthermore, this study represents the first investigation on the identification of ricinine in castor bean plants found in Malaysia. The findings contribute to the understanding of the presence and potential applications of ricinine as a surrogate marker for ricin exposure in the local context. The improved extraction method and identification of ricinine in castor bean plants hold significance for various fields, including forensic investigations, security measures and potential screening protocols for detecting ricin-related incidents.

## REFERENCES

- Audi, J., Belson, M., Patel, M., Schier J. & Osterloh, J. (2005). Ricin poisoning: A comprehensive review. *JAMA*, **294**: 2342-2351.
- Aziz, A. (1998). *The Mujahideen Poison Handbook*. Organisation for the Preparation of the Mujahideen, Afghanistan.
- Christopher, T.P., John, G., Elizabeth. I.H., Thomas, A.B. & Rudolph, C.J. (2013). Analysis of a ricin biomarker, ricinine, in 989 individual human urine sample. *J. Anal. Toxicol.*, **37**:237-240.
- Feldberg, L., Elhanany, E., Laskar, O. & Schuster, O. (2021). Rapid, sensitive and reliable ricin identification in serum samples using LC-MS/MS. *Toxins*, **13**: 79.
- Laura, S. & Robert, G.H. (2005). Ricin. *Crit. Care Clin.*, **21**:815-824.
- Marie, S., Petr, H., Martin, S. & Vitezslav, M. (2020). Fatal intoxication by intravenous injection of castor bean (*Ricinus Communis L.*) extract - A case study. *Int. J. Legal Med.*, **134**: 2133-2141.
- Raja, S., Crister, A., Lars, J., Calle, N. & Anders, O. (2010). Direct Derivatization and Rapid GC-MS Screening of Nerve Agent Markers in Aqueous Samples. *Anal. Chem.*, **82**:7452-9.
- Roberto, B.S., Keila, S.C.L., Caleb, G.M.S., Tanos, C.C.F., Eugenie, N., Kamil, K., Marcos, R.D. & Antonio, L.S.L. (2019). A new method for extraction and analysis of ricin samples through MALDI-TOF-MS/MS. *Toxins*, **11**: 201.
- Thomas, A.M., David, L.B. & Xiaohua H. (2016). Improved method for extraction of castor seed for toxin determination. *Biocatal. Agric. Biotech.*, **5**: 56-57.
- Vanninen, P. (Ed.) (2017). *Recommended Operating Procedures for Analysis in the Verification of Chemical Disarmament*. University of Helsinki, Finland.

# EFFECTS OF VOLUME RATIO OF CITRATE-CAPPED GOLD NANOPARTICLES (cit-AuNPs) TO MALATHION, CONCENTRATIONS OF cit-AuNPs AND DNA APTAMER ON MALATHION COLORIMETRIC DETECTION

Mardhiahtul Iftiah Ariffin<sup>1</sup>, Nor Laili-Azua Jamari<sup>2</sup>, Norli Abdullah<sup>2</sup>, Mohd Junaedy Osman<sup>2</sup>, Ong Keat Khim<sup>2\*</sup>, Wan Md Zin Wan Yunus<sup>1</sup>, Nur Athirah Zulkifli<sup>3</sup>, Siti Aminah Mohd Noor<sup>2</sup>, Victor Feizal Knight<sup>3</sup>, Ten Seng Teik<sup>4</sup>, Mohd Nor Faiz Norrahim<sup>3</sup>, Siti Hasnawati Jamal<sup>2</sup> & Syed Mohd Shafiq Syed Ahmad<sup>2</sup>

<sup>1</sup>Faculty of Defence Science and Technology

<sup>2</sup>Centre for Defence Foundation Studies

<sup>3</sup>Research Centre for Chemical Defence

National Defence University of Malaysia (UPNM), Malaysia

<sup>4</sup>Engineering Research Centre, Malaysian Agricultural Research and Development Institute (MARDI), 43400 Serdang, Selangor, Malaysia.

\*Email: ongkhim@upnm.edu.my

## ABSTRACT

*A simple, rapid and sensitive aptamer-gold nanoparticle-based colorimetric assay coupled with an image analysis technique was developed for quantitative determination of malathion (MLT) insecticide. The effects of volume ratio of citrate-capped gold nanoparticles (cit-AuNPs) to MLT, concentrations of cit-AuNPs and DNA aptamers on the sensing were investigated and optimised. The detection of MLT was based on colour change. Colour images of the mixtures were analysed to obtain red, green, and blue (RGB) values, where the response of the sensor was reported as  $\Delta RGB$ . The good linear relationship between the response and concentration of MLT proves that the developed aptasensor can be applied for quantitative determination of MLT.*

**Keywords:** Aptasensor; colorimetric; gold nanoparticles; image processing; malathion (MLT).

## 1. INTRODUCTION

Chemical warfare agents (CWA) are highly toxic and can be used in various ways (Ganesan *et al.*, 2010). Due to its lethality, the usage of CWA is restricted. Therefore, chemical warfare agent simulants (CWAS) often replace CWA for recent detectability investigation (Bikelytè *et al.*, 2020). Often CWAS structure resemble organophosphate (OP) and pesticides such as malathion (MLT) (James *et al.*, 2018). Pesticides are primarily used to prevent, control or eliminate pests and weeds for boosting agricultural productivity in modern agricultural practices. Currently, OP compounds are the most commercially favoured group of pesticides due to their high insecticidal activity and relatively low persistence, with large application areas all over the world (Liu *et al.*, 2019; Mdeni *et al.*, 2022). Most OPs are water-soluble and could enter the environment through dissolution, abrasion and volatilisation. Examples of OPs include MLT, parathion, diazinon, fenthion, dichlorvos, chlorpyrifos and ethion. MLT is one of the OP insecticides that is frequently utilised (Ojha & Srivastava, 2014). It is also known as diethyl 2-[(dimethoxyphosphorothioyl) sulfanyl] butanedioate and is one of the earliest insecticides developed. Furthermore, MLT is available in emulsifiable concentrate, wettable powder, dustable powder, and ultra-low volume (ULV) liquid formulations (Velkoska-Markovska & Petanovska-Ilievska, 2020). MLT is known for its high toxicity to insects, and low to moderate potency to humans and other mammals. Its toxicity has been associated with



the inhibition of acetylcholinesterase activity, leading to the interference with the transmission of nerve impulse, accumulation of acetylcholine at synaptic junctions, and subsequent induction of adverse health effects including headache, dizziness, nausea, vomiting, bradycardia and miosis (Li *et al.*, 2019; Sharma *et al.*, 2020).

Conventional analytical techniques, such as gas chromatography (GC) and high-performance liquid chromatography (HPLC), are typically coupled with mass spectrometry (MS) (Weissberg *et al.*, 2016) and used for pesticide detection and quantification. Although these instruments are effective, they are frequently highly priced and require complicated equipment. Methods that allow detection of OP pesticides in real-time using colorimetric methods that are visible through the naked-eye are distinctly needed for environmental applications. Various colorimetric sensors based on aptamers, enzymes and plasmonic nanoparticles have been developed (Lee *et al.*, 2018). Recently, colorimetric sensor based on plasmonic nanoparticles have gained more interest for environmental sensing functions due to their high extinction coefficients and potential to tune their properties with the aid of controlling their size, shape, composition and interparticle distance, and dielectric constant (refractive index) of the surrounding medium (Yu *et al.*, 2020). Gold and silver nanoparticles (AuNPs and AgNPs) have been widely investigated due to their unique optical, electrical and photothermal properties which are determined by their specific surface plasmon resonance (SPR) profiles (Che Sulaiman *et al.*, 2020).

Rapid colorimetric method utilising AuNPs was studied by Kohzadi & Roushani (2016) for detection of MLT. The calibration curve is linear over the concentration range of  $3.3 \times 10^7$  to  $3.3 \times 10^6$  mol/L of MLT with good precision and accuracy, and the detection limit was 0.15  $\mu$ M. Another previous research group developed a colorimetric probe based on AuNPs anti-aggregation effect for rapid, selective and high-sensitive detection of MLT pesticide residue with limit of detection (LOD) down to 11.8 nM (Li *et al.*, 2019). The probe also showed good specificity for MLT detection in the presence of other interfering pesticide residues. Furthermore, the probe was successfully employed to detect MLT in environmental samples, with recovery of 94 -107% and relative standard deviation (RSD) less than 8%.

The interest on introduction of thiol-modified aptamers on AuNPs has increased as aptamers are single-stranded nucleic acid (DNA) or peptide molecules that have high affinity and specificity for target analytes (Liu *et al.*, 2015; Osman *et al.*, 2020). Their specific recognition is based on the principle of explicit specificity of ligand molecules to the analyte molecule. Through the ligand exchange reactions and the formation of strong Au–S bonds, their surface can be functionalised with a broad variety of thiol- or disulfide-terminated organic ligands, resulting in stable colloidal suspensions in water or organic solvents (depending on the ligand) (Gaviña *et al.*, 2019; Che Sulaiman *et al.*, 2020). Thus, aptamers have received considerable attention as sensing elements for the development of biosensors (Sharma *et al.*, 2015).

Bala *et al.*, (2016) have demonstrated a novel sensing strategy for an OP pesticide, namely MLT. They employed unmodified AuNPs, aptamer, and positively charged and water-soluble polyelectrolyte polydiallyldimethylammonium chloride, where ultra-low limit of detection of 0.06 pM was obtained (Bala *et al.*, 2016). Later, Bala *et al.* (2018) reported a highly sensitive, rapid and low cost colorimetric monitoring of MLT employing a basic hexapeptide, MLT specific aptamer and AgNPs as a nanoprobe. The proposed methodology showed excellent selectivity and a very low limit of detection of 0.5 pM.

In this study, we developed an AuNPs-based colorimetric aptasensor for MLT detection, where we varied the volume ratio of MLT to cit-AuNPs (100  $\mu$ L: 900  $\mu$ L to 900  $\mu$ L: 100  $\mu$ L) and concentrations of cit-AuNPs (1-8 nM) and DNA aptamer (1-5 nM) to obtain the optimum response of the detection. This colorimetric detection was based on the colour change produced from the reaction of MLT and cit-AuNPs. The colour images obtained were digitised using ImageJ to obtain their red, green and blue (RGB) values.

## 2. MATERIALS AND METHOD

### 2.1 Reagents and Chemicals

Gold (III) chloride trihydrate ( $\text{HAuCl}_4 \cdot 3\text{H}_2\text{O}$ ; >49% Au basis), MLT and ethanol were obtained from Sigma-Aldrich (USA), while trisodium citrate dihydrate ( $\text{C}_6\text{H}_5\text{Na}_3\text{O}_7 \cdot 2\text{H}_2\text{O}$ ) were purchased from Merck KGaA, Germany. The thiolated DNA aptamer 72-mer oligo (5ThioMC6-D/ATC CGT CAC ACC TGC TCT TAT ACA CAA TTG TTT TTC TCT TAA CTT CTT GAC TGC TGG TGT TGG CTC CCG TAT) and IDTE solution (10 mM Tris, 0.1 mM EDTA) were obtained from Integrated DNA Technologies (Singapore). The sequence of the aptamer was customised according to a previous study (Abnous *et al.*, 2018). Mili-Q water (18.2 M $\Omega$ .cm resistivity, Millipore) was used throughout the experiments and all the chemicals were analytical grade.

### 2.2 Citrate Capped Gold Nanoparticles Synthesis

Citrate-capped gold nanoparticles (cit-AuNPs) was synthesised using the traditional trisodium citrate reduction method as described in previous study (Li *et al.*, 2018). Firstly, 250 mL of 0.5 mM of gold (III) chloride solution was stirred vigorously at 1,000 rpm and heated until 100 °C, followed by rapid addition of 25 mL of 38.8 mM of trisodium citrate solution. The solution was continuously stirred for another 15 min. Finally, the solution was cooled to room temperature and stored in a dark bottle at 4 °C for further use. This same procedure above was repeated for synthesis of different concentrations of gold (III) chloride (0.5, 1.0, 1.5, 2.0, 2.5 and 3.0 mM) solutions. The concentrations of synthesised cit-AuNPs were calculated using the following equation as reported by Zuber *et al.* (2016):

$$C_{AuNPs} = 6 \left( \frac{C_{Au} * M_{Au}}{\pi * \rho_{Au} * D_{AuNPs}^3 * N_A} \right) \quad (1)$$

where  $C_{AuNPs}$  is the molar concentration of cit-AuNPs (M),  $C_{Au}$  is the molar concentration of gold atoms/ions (M),  $M_{Au}$  is the molecular weight of gold ( $\text{g mol}^{-1}$ ),  $\rho_{Au}$  is the density of gold (which is  $19.3 \text{ g.cm}^{-3}$ ),  $D_{AuNPs}$  is the diameter of cit-AuNPs, and  $N_A$  is Avogadro constant ( $\text{mol}^{-1}$ ).

### 2.3 Preparation of Thiolated DNA Aptamer Solution

Briefly, 100  $\mu\text{M}$  of thiolated DNA aptamer stock solution was prepared by dissolving the aptamer in 734  $\mu\text{L}$  of IDTE solution. After that, 30  $\mu\text{M}$  of thiolated DNA aptamer solution was prepared by diluting the stock solution and finally diluted to various concentrations (1-5 nM) of thiolated DNA aptamer solutions. The prepared aptamer solutions were stored at 4 °C until further use.

### 2.4 Preparation of MLT Stock Solution

A stock solution of MLT (6.1 mM) was prepared by dissolving MLT in ethanol. Briefly, the desired amount of MLT was added to a 100 mL volumetric flask and dissolved with ethanol. Then, a series of dilutions from the stock solution were made to prepare various concentrations (2.5, 5.0, 10.0, 25.0, 50.0, 75.0 and 100.0 pM) of MLT working solutions.

## 2.5 Effect of Volume Ratio of cit-AuNPs to MLT on Detection

In order to determine the optimum volume ratio of cit-AuNPs to MLT for detection of 3  $\mu\text{M}$  of MLT, various volumes of MLT (100 to 900  $\mu\text{L}$ ) were mixed into different volumes of cit-AuNPs (100 to 900  $\mu\text{L}$ ) respectively, until its final volume was 1,000  $\mu\text{L}$  (Table 1). The final concentration of cit-AuNPs was fixed to 4 nM. The image of colour solution was captured after 15 s of detection in an image capturing box under constant conditions. Subsequently, the captured image was processed to gain red, green and blue (RGB) values as described in the image processing section (Section 2.8). This experiment was performed in triplicates to obtain average results. A similar experiment was applied for the blank.

**Table 1: Determination of optimum volume ratio of cit-AuNPs to MLT.**

Volume of cit-AuNPs ( $\mu\text{L}$ )	Volume of MLT ( $\mu\text{L}$ )
100	900
200	800
300	700
400	600
500	500
600	400
700	300
800	200
900	100

## 2.6 Effect of cit-AuNPs Concentration on Detection

The optimum concentration of cit-AuNPs was determined by mixing the optimum volume of different solutions of cit-AuNPs (final concentrations: 1-8 nM) into optimum volume of 3  $\mu\text{M}$  of MLT. The detection experiments were conducted in triplicates using the similar detection procedure for the effect of volume ratio of cit-AuNPs to MLT on the detection of MLT. Then, the same image processing technique was applied to process the images of the solutions captured after each detection.

## 2.7 Effect of DNA Aptamer Concentration on Detection

For optimisation of the DNA aptamer, 10  $\mu\text{L}$  of DNA aptamer (1- 5 nM) was mixed with the optimum volume and concentration of cit-AuNPs to obtain total volume of 1,000  $\mu\text{L}$ . After detection,  $\Delta\text{RGB}$  values of the solutions images were obtained using the procedure as mentioned in the image processing section.

## 2.8 Image Processing of Captured Images

For quantitative colorimetric analysis, all the images of the top view of the solutions were captured in a viewing box to ensure constant distant using a smartphone (iPhone 7) and the image was further digitised using ImageJ as follows: Firstly, the software's "oval" tool was used to highlight the desired area in each captured image. Then, the targeted area was carefully adjusted to remove the impact of backdrop brightness. Finally, the "RGB measure" tool was used to analyse the cropped image in order to get the mean RGB values. The response ( $\Delta\text{RGB}$ ) was calculated using the Equation 2 as mentioned in a previous study (Murdock *et al.*, 2013):

$$\Delta RGB = \sqrt{(R_n - R_o)^2 + (G_n - G_o)^2 + (B_n - B_o)^2} \quad (2)$$

where  $R_o$ ,  $G_o$  and  $B_o$  are mean values red, green and blue values of captured image of blank solution, while  $R_1$ ,  $G_1$  and  $B_1$  are mean values of red, green and blue values of captured image of the solution in the presence of MLT, respectively.

## 2.9 Ultra-Violet Visible (UV-Vis) Spectrophotometry

UV-Vis analysis was performed using a Genesys 6 UV-visible spectrophotometer at a scanning rate of 1 nm/sec from 450 to 750 nm.

## 2.10 High Resolution Transmission Electron Microscopy (HRTEM)

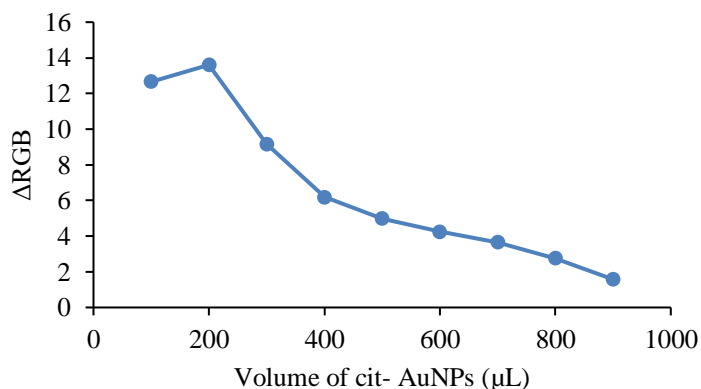
High resolution transmission electron microscopy (HRTEM) analysis was performed using a JEOL JEM 2100F high resolution transmission electron microscope with operating voltage of 200 kV. All the samples were deposited on the viewing grids and left overnight to dry. Next, the HRTEM images of each sample were captured and analysed.

## 3. RESULTS AND DISCUSSIONS

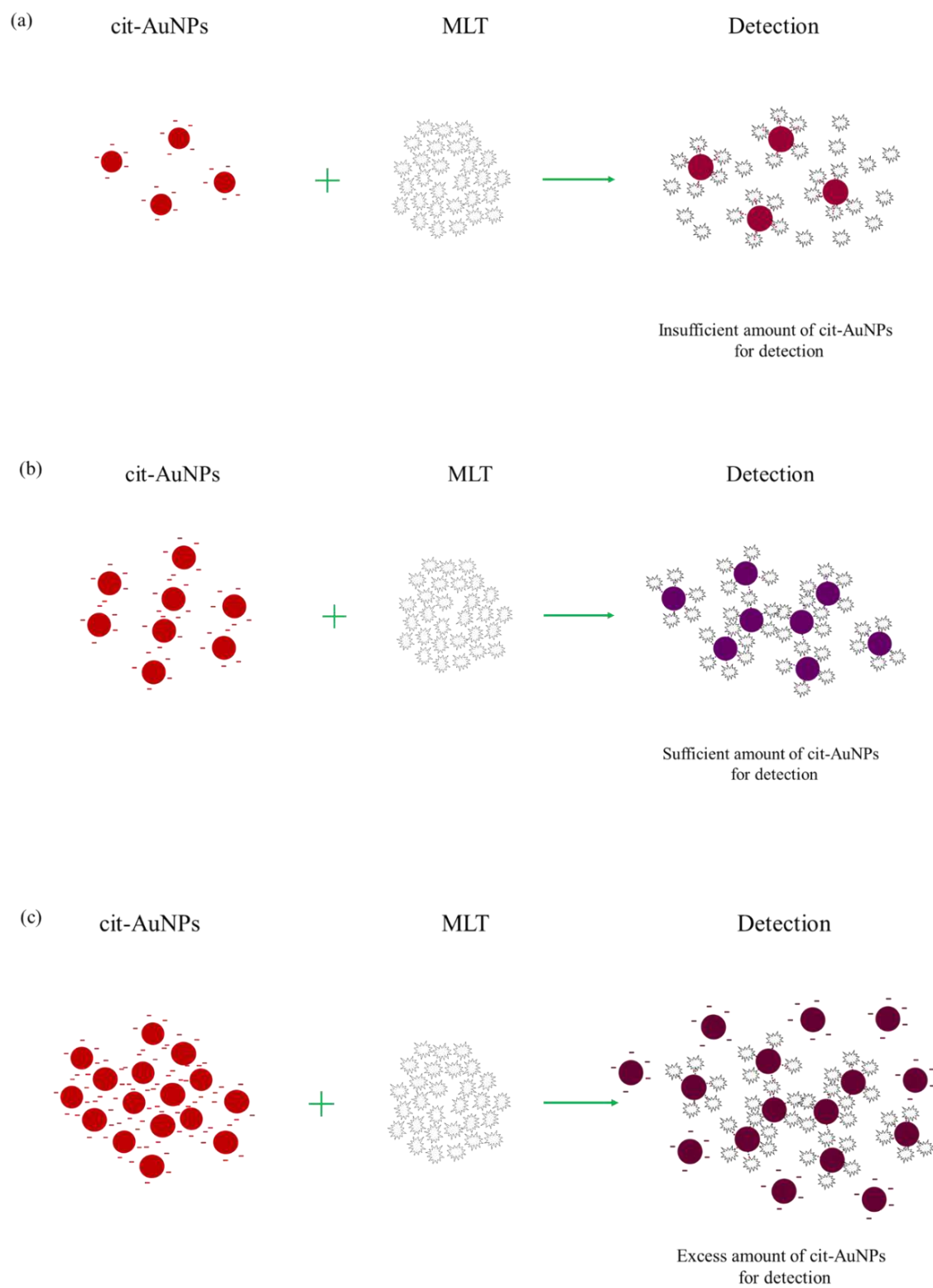
### 3.1 Optimisation of the Experimental Conditions

#### 3.1.1 Effect of Volume of cit-AuNPs

The influence of the volume of cit-AuNPs on MLT detection was investigated in the range of 100 - 900  $\mu$ L to obtain the optimum volume of cit-AuNPs for the detection of 3  $\mu$ M of MLT. As shown in Figure 1, the response ( $\Delta$ RGB values) increased when cit-AuNPs volume increased from 100 to 200  $\mu$ L. However, the response decreased when the volume of cit-AuNPs increased from 300 to 900  $\mu$ L. Thereby, 200  $\mu$ L of cit-AuNPs was selected as the optimum volume of cit-AuNPs. These results demonstrated that 200  $\mu$ L of cit-AuNPs was sufficient for the detection of 3  $\mu$ M of MLT, as illustrated in Figure 2 (b). Meanwhile, cit-AuNPs was insufficient for the detection when lower volume of cit-AuNPs (100  $\mu$ L) was applied (Figure 2 (a)). In contrast, when higher volumes of cit-AuNPs (> 200  $\mu$ L) were utilised, cit-AuNPs became excessive for the detection (Figure 2 (c)).



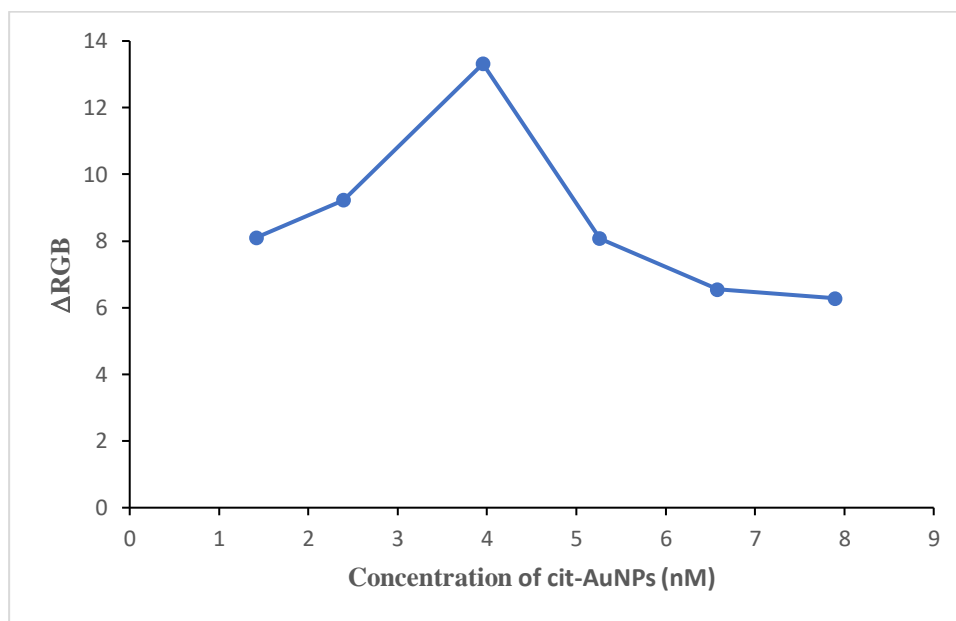
**Figure 1: Effect of volume of cit-AuNPs on MLT detection.**



**Figure 2: Schematic diagram of MLT detection mechanism using (a) insufficient volume of cit-AuNPs, (b) sufficient volume of cit-AuNPs, and (c) excess volume of cit-AuNPs.**

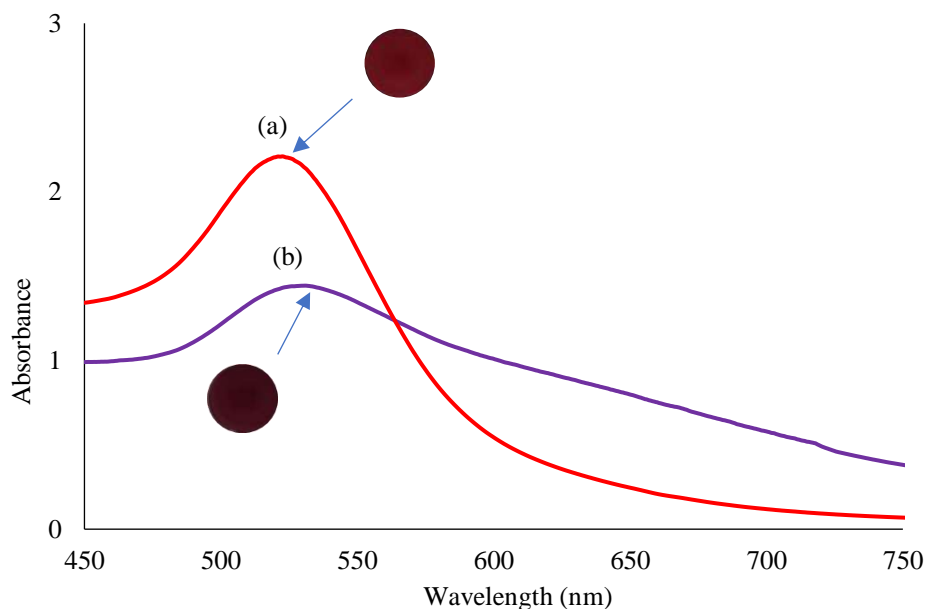
### 3.2.2 Effect of Concentration of cit-AuNPs

In order to optimise the detection method, the effect of cit-AuNPs concentration on the detection was investigated (Figure 3). The colloidal cit-AuNPs (final concentrations: 1 to 8 nM) were employed to determine the optimum concentration of cit-AuNPs used for detecting 3  $\mu$ M of MLT. The colorimetric responses ( $\Delta$ RGB) apparently increased as cit-AuNPs concentration increased from 1 to 4 nM. In addition, these results were supported by noticeable colour change in the solutions. The highest response was observed using 4 nM of cit-AuNPs. Thereafter,  $\Delta$ RGB values decreased when higher concentrations of cit-AuNPs were applied. A similar phenomenon as illustrated in Figure 2 can be used to explain these trends. Hence, 4 nM of cit-AuNPs was found to be the optimum cit-AuNPs concentration for MLT detection, which was then applied as the optimum concentration in the following MLT detection experiments.



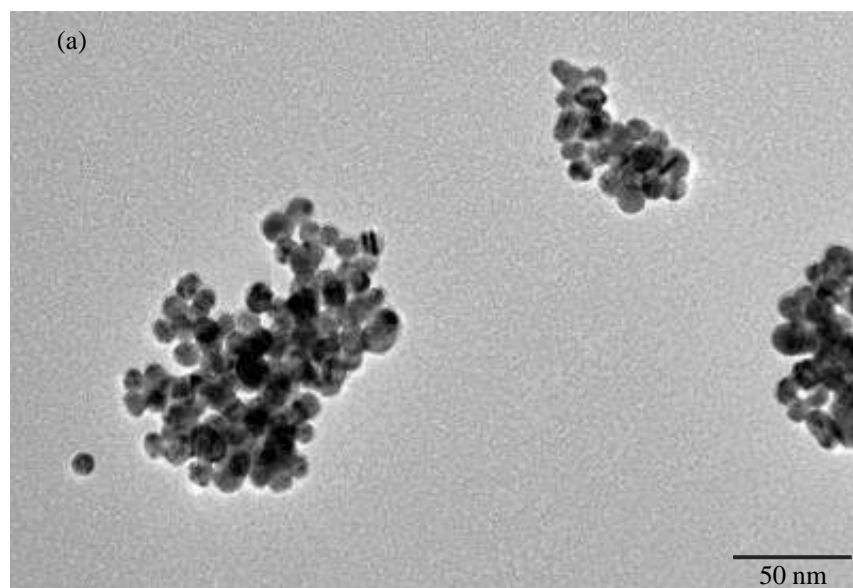
**Figure 3: Effect of cit-AuNPs concentration on MLT detection.**

In order to confirm successful synthesis of cit-AuNPs in this study, UV-Vis analysis was performed to measure the wavelength that exhibits the strongest photon absorption ( $\lambda_{max}$ ) of the surface plasmon resonance (SPR) characteristics peak of cit-AuNPs. The representative absorption spectrum of 4 nM of cit-AuNPs synthesised using 1.5 mM of gold (III) chloride is shown in Figure 4 (a). This characteristic SPR band of cit-AuNPs was observed at 520 nm, indicating the successful production of cit-AuNPs. However, the absorbance peak decreased in the presence of MLT (Figure 4 (b)). This phenomenon can be explained by the formation of a larger cluster due to aggregation of nanoparticles (Osman *et al.*, 2020).



**Figure 4:** UV-Vis absorption spectra of (a) synthesised cit-AuNPs using 1.5 mM gold (III) chloride (final concentration of cit-AuNPs: 4 nM) and (b) detection of 3  $\mu$ M of MLT using the synthesised cit-AuNPs.

HRTEM analysis was performed to visualise the morphology of cit-AuNPs synthesised using 1.5 mM gold (III) chloride (Figure 5(a)). In addition, the morphology of cit-AuNPs was also investigated after colorimetric detection of MLT as shown in Figure 5(b). The HRTEM image (Fig. 5(a)) shows that most of the cit-AuNPs have spherical shape with an average diameter of about 13 nm. Meanwhile, after detection of MLT, the HRTEM image (Figure 5(b)) demonstrates agglomeration of cit-AuNPs. This result was also supported with the UV-Vis findings, which demonstrated a slightly shift of  $\lambda_{\text{max}}$  from 523.5 nm to 528.5 nm (Figure 4 (b)). Furthermore, the analysis proved that the principle of sensing and detection is based on the aggregation of cit-AuNPs in the presence of MLT (Figure 5(b)).



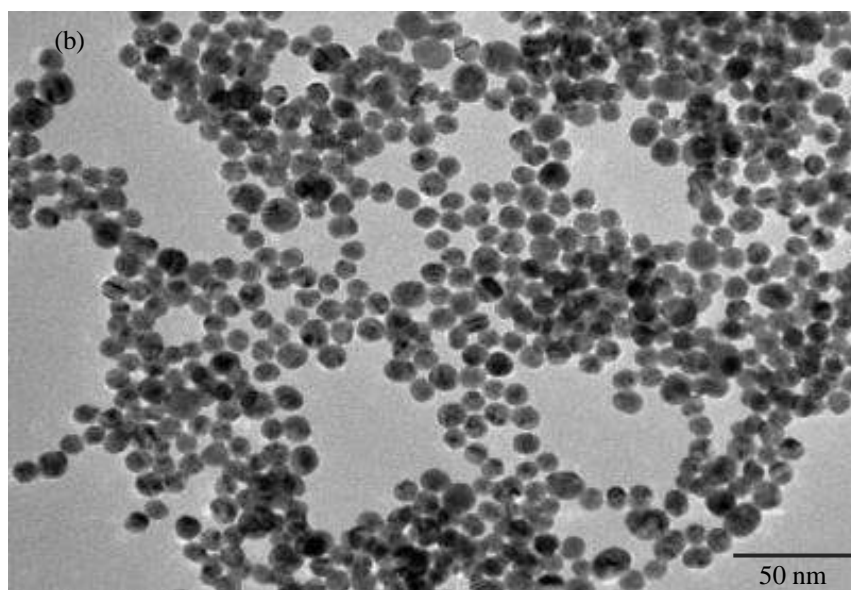


**Figure 5:** HRTEM images of (a) cit-AuNPs using 1.5 mM gold (III) chloride (final concentration of cit-AuNPs: 4 nM) and (b) detection of 3  $\mu$ M of MLT using the synthesised cit-AuNPs.

### 3.2 Effect of Concentration of DNA Aptamer

In this colorimetric assay, the effect of DNA aptamer concentration (in the range of 1 to 5 nM) was evaluated in order to determine the optimum concentration of the aptamer for the detection. As shown in Figure 6,  $\Delta$ RGB increased gradually with the increase of DNA aptamer concentrations (from 1 to 4 nM). The response of the aptasensor decreased slightly when the concentration of aptamer is higher than 4 nM. The results demonstrated that lower concentrations of DNA aptamers were insufficient to bind to the MLT. Nevertheless, the concentration of 4 nM of DNA aptamer is sufficient to bind with MLT, leading to greater aggregation of AuNPs, which caused colour change. In contrast, at higher concentration, excessive aptamers acted as electrostatic barriers (Divsar *et al.*, 2015) that caused lower response. Thus, DNA aptamer concentration of 4 nM was chosen as the optimum concentration. Colorimetric detection mechanism under optimum and excess concentrations of DNA aptamer is presented in Figure 7.

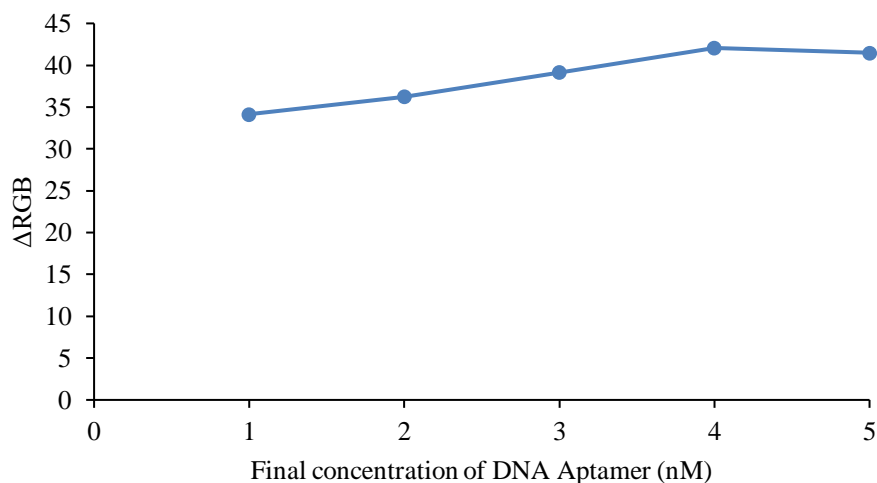


**Figure 6:** Effect of DNA aptamer concentration on MLT detection.



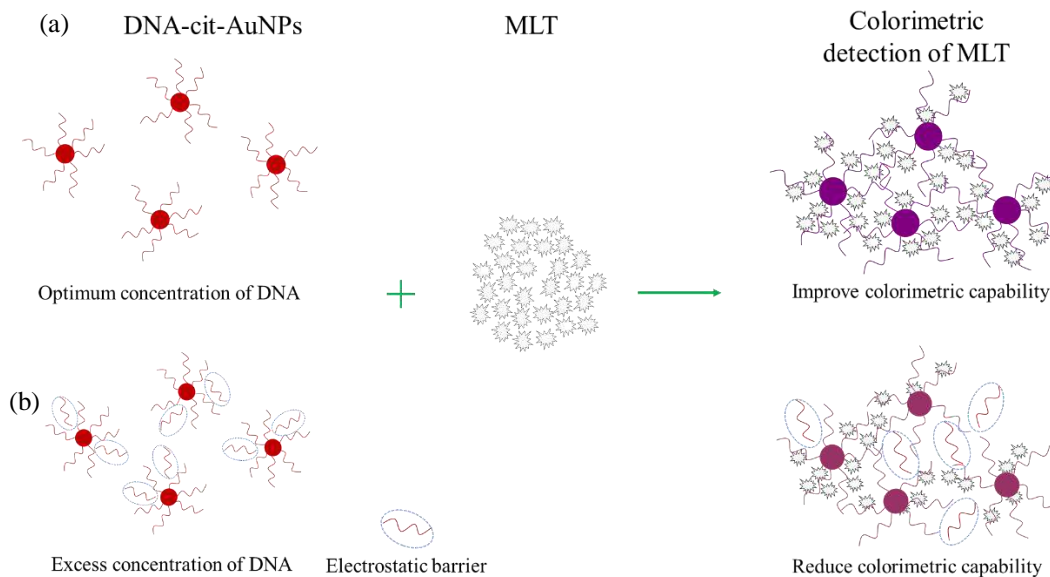


**Figure 7: Mechanism of colorimetric detection of MLT under (a) optimum and (b) excess concentrations of DNA aptamer.**

### 3.3 Colorimetric Detection of MLT Using Optimised DNA-AuNPs Sensor

The optimised values for the volume of cit-AuNPs, concentration of cit-AuNPs and concentration of DNA aptamer were found to be 200  $\mu\text{L}$ , 4 nM and 4 nM respectively for detection of 3  $\mu\text{M}$  of MLT. Under these optimal conditions, detection of MLT that produces the highest  $\Delta\text{RGB}$  represents the highest particle agglomeration of DNA-AuNPs colorimetric sensor. In this research, detection of MLT at different concentrations was conducted to confirm the capability of the optimised sensor. Figure 8 displays the  $\Delta\text{RGB}$  values for detection of MLT at different concentrations (2.5, 5.0, 10.0, 25.0, 50.0, 75.0 and 100.0  $\mu\text{M}$ ). The average values ( $\Delta\text{RGB}$ ) were used in developing a linear calibration model for the detection of MLT and was found to be fitted the following regression equation:  $Y = 0.1089 X + 36.005$  with regression coefficient ( $R^2$ ) of 0.903. Later, we employed the formula of  $3\sigma$  /slope for calculating the limit of detection (LOD) (Bala *et al.*, 2017; Shayesteh & Ghavami, 2019), where  $\sigma$  displays the standard deviation of the blank response and slope is derived from the linear calibration plot. Based on the mentioned formula, the LOD for MLT was found to be 1.4  $\mu\text{M}$ , which was lower than the previously reported method (Bala *et al.*, 2017).

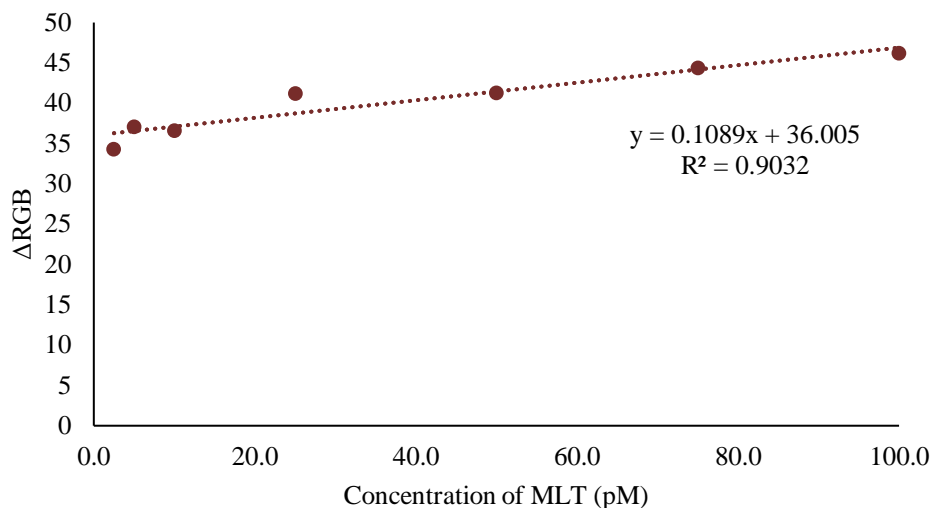


**Figure 8: Calibration curve of  $\Delta$ RGB for the detection of MLT.**

#### 4. CONCLUSION

In this work, an aptamer-gold nanoparticle-based colorimetric aptasensor coupled with an image processing technique was developed for easy-to-use, rapid and sensitive detection of MLT. In order to optimise the MLT detection, the effects of volume ratio of cit-AuNPs to MLT, concentrations of cit-AuNPs and concentrations of DNA aptamer were investigated. Under the optimum conditions, the developed aptasensor demonstrated a linear range from 2.5 to 100.0 pM and a LOD of 1.4 pM for determination of MLT. As a conclusion, a promising aptasensor for simple and rapid quantitative detection of MLT was successfully developed.

#### ACKNOWLEDGEMENT

The authors would like to thank the National Defence University of Malaysia (UPNM) for funding this project (PS0023-UPNM2022/GPPP/SG/8). The authors are also grateful for the research facilities supported from UPNM.

#### REFERENCES

- Abnous, K., Danesh, N. M., Ramezani, M., Alibolandi, M., Emrani, A. S., Lavaee, P. & Taghdisi, S. M. (2018). A colorimetric gold nanoparticle aggregation assay for malathion based on target-induced hairpin structure assembly of complementary strands of aptamer. *Microchim. Acta*, **185**: 216-223.
- Bala, R., Dhingra, S., Kumar, M., Bansal, K., Mittal, S., Sharma, R.K. & Wangoo, N. (2017). Detection of organophosphorus pesticide – Malathion in environmental samples using peptide and aptamer based nanoprobes. *Chem. Eng. J.*, **311**: 111–116.
- Bala, R., Kumar, M., Bansal, K., Sharma, R.K. & Wangoo, N. (2016). Ultrasensitive aptamer biosensor for malathion detection based on cationic polymer and gold nanoparticles. *Biosens. Bioelectron.*, **85**: 445–449.
- Bala, R., Mittal, S., Sharma, R.K. & Wangoo, N. (2018). A supersensitive silver nanoprobe based aptasensor for low cost detection of malathion residues in water and food samples. *Spectrochim.*

- Acta A Mol. Biomol. Spectrosc.*, **196**: 268–273.
- Bikelytė, F., Härtel, M.A.C., Klapötke, T.M., Krumm, B., & Sadaunykas, A. (2020). Experimental thermochemical data of CWA simulants: Triethyl phosphate, diethyl methylphosphonate, malathion and methyl salicylate. *J. Chem. Thermodynamics*, **143**: 1-9.
- Che Sulaiman, I.S., Chieng, B.W., Osman, M.J., Ong, K.K., Rashid, J.I.A., Wan Yunus, W.M.Z., Noor, S.A.M., Kasim, N.A.M., Halim, N.A. & Mohamad, A. (2020). A review on colorimetric methods for determination of organophosphate pesticides using gold and silver nanoparticles. *Microchim. Acta*, **187**: 1-22.
- Divsar, F., Habibzadeh, K., Shariati, S. & Shahriarinour, M. (2015). Aptamer conjugated silver nanoparticles for the colorimetric detection of arsenic ions using response surface methodology. *Anal. Methods*, **7**: 4568–4576.
- Gaviña, P., Parra, M., Gil, S. & Costero, A. (2019). Red or blue? Gold *Nanoparticles in Colorimetric Sensing*. In *Gold Nanoparticles - Reaching New Heights*. IntechOpen, London, UK.
- James, T., Wyke, S., Marczylo, T., Collins, S., Gaulton, T., Foxall, K., Amlôt, R., & Raquel Duarte-Davidson Chemical warfare agent simulants for human volunteer trials of emergency decontamination: A systematic review. *J Appl Toxicol.*, **38(1)**: 113–121.
- Kohzadi, T. & Roushani, M. (2016). Highly sensitive colorimetric determination of malathion using gold nanoparticles. *Water Sci. Technol. Water Supply*, **16**: 1214–1220.
- Lee, J.H., Cho, H.Y., Choi, H.K., Lee, J.Y. & Choi, J.W. (2018). Application of gold nanoparticle to plasmonic biosensors. *Int. J. Mol. Sci.* **19**: 1-14.
- Li, D., Wang, S., Wang, L., Zhang, H. & Hu, J. (2019). A simple colorimetric probe based on anti-aggregation of AuNPs for rapid and sensitive detection of malathion in environmental samples. *Anal. Bioanal. Chem.*, **411**: 2645–2652.
- Li, L., Liang, Y., Zhao, Y. & Chen, Z. (2018). Target binding and DNA hybridization-induced gold nanoparticle aggregation for colorimetric detection of thrombin. *Sens. Actuators B Chem.*, **262**: 733–738.
- Liu, D.L., Li, Y., Sun, R., Xu, J.Y., Chen, Y. & Sun, C.Y. (2019). colorimetric detection of organophosphorus pesticides based on the broad-spectrum aptamer. *J. Nanosci. Nanotechnol.*, **20**: 2114–2121.
- Liu, Q., Wang, J. & Boyd, B.J. (2015). Peptide-based biosensors. *Talanta*, **136**: 114–127.
- Mdeni, N.L., Adeniji, A.O., Okoh, A.I. & Okoh, O.O. (2022). Analytical evaluation of carbamate and organophosphate pesticides in human and environmental matrices: A review. *Molecules*, **27**: 1-21.
- Murdock, R.C., Shen, L., Griffin, D.K., Kelley-Loughnane, N., Papautsky, I. & Hagen, J.A. (2013). Optimization of a paper-based ELISA for a human performance biomarker. *Anal. Chem.*, **85**: 11634–11642.
- Ojha, A. & Srivastava, N. (2014). In vitro studies on organophosphate pesticides induced oxidative DNA damage in rat lymphocytes. *Mutat. Res. Genet. Toxicol. Environ. Mutagen.*, **761**: 10–17.
- Osman, M. J., Wan Yunus, W. M. Z., Ong, K. K., Chieng, B. W., Mohd Kassim, N. A., Mohd Noor, S. A., Knight, V. F., Abd Rashid, J. I., & Teoh, C. C. (2020). Image Digitization of Colorimetric Detection of Acephate Based on Its Complexation with Citrate-Capped Gold Nanoparticles. *J. Chem.*, **2020**: 1–10.
- Sharma, A., Shukla, A., Attri, K., Kumar, M., Kumar, P., Suttee, A., Singh, G., Barnwal, R.P. & Singla, N. (2020). Global trends in pesticides: A looming threat and viable alternatives. *Ecotoxicol. Environ. Saf.* **201**: 1-15.
- Sharma, R., Ragavan, K.V., Thakur, M.S. & Raghavarao, K.S. (2015). Recent advances in nanoparticle based aptasensors for food contaminants. *Biosens. Bioelectron.*, **74**: 612–627.
- Shayesteh, O.H. & Ghavami, R. (2019). Two colorimetric ampicillin sensing schemes based on the interaction of aptamers with gold nanoparticles. *Microchim. Acta*, **186**: 1-10.
- Velkoska-Markovska, L. & Petanovska-Ilievska, B. (2020). Rapid resolution liquid chromatography method for determination of malathion in pesticide formulation. *Acta Chromatogr.*, **32**: 256–259.
- Weissberg, A., Madmon, M. & Dagan, S. (2016). Determination of organophosphorus acids by liquid chromatography positive electrospray ionization tandem mass spectrometry after chemical

- derivatization. *Int. J. Mass Spectrom.*, **408**: 20–27.
- Yu, L., Song, Z., Peng, J., Yang, M., Zhi, H. & He, H. (2020). Progress of gold nanomaterials for colorimetric sensing based on different strategies. *TrAC, Trends Anal. Chem.* **127**: 1-18.
- Zuber, A., Purdey, M., Schartner, E., Forbes, C., van der Hoek, B., Giles, D., Abell, A., Monro, T. & Eben Ebendorff-Heidepriem, H. (2016). Detection of gold nanoparticles with different sizes using absorption and fluorescence based method. *Sens. Actuators B Chem.*, **227**: 117–127.

# PRELIMINARY STUDY ON THE EFFECTS OF TEMPERATURE AND IONS ON THE DETECTION OF ACEPHATE

Mohd Junaedy Osman<sup>1\*</sup>, Wan Md Zin Wan Yunus<sup>2</sup>, Ong Keat Khim<sup>1,4</sup>, Jahwarhar Izuan Abdul Rashid<sup>1</sup>, Buong Woei Chieng<sup>4</sup>, Noor Azilah Mohd Kassim<sup>1,4</sup>, Norhana Abdul Halim<sup>1</sup>, Siti Aminah Mohd Noor<sup>1,3</sup>, Victor Feizal Knight<sup>4</sup> & Syed Mohd Shafiq Syed Ahmad<sup>1</sup>

<sup>1</sup>Centre for Defence Foundation Studies

<sup>2</sup>Faculty of Defence Science and Technology

<sup>3</sup>Centre for Tropicalisation

<sup>4</sup>Research Centre for Chemical Defence

National Defence University of Malaysia (NUDM), Malaysia

\*Email: junaedy@upnm.edu.my

## ABSTRACT

*Acephate (Ac) is an organophosphate (OP) compound that is largely used to control pests in agriculture. It can produce toxic metabolite products, raising concern of uncontrollable effects towards humans, animals and environment. In this study, an DNA aptamer linked with citrate capped gold nanoparticles (TABA-Cit-AuNPs) was prepared and employed as a colorimetric sensor to detect Ac. Binding was conducted at three different temperatures, 5, 25 and 40 °C, to determine the optimum binding temperature. Room temperature was found to be optimal as it gives a significant reduction of mean red value (RV) measured with ImageJ. Different types of cations (Na<sup>+</sup>, Mg<sup>2+</sup>) and anions (Cl<sup>-</sup>, SO<sub>4</sub><sup>2-</sup>) were studied to improve the detection sensitivity. Introduction of Mg<sup>2+</sup> cations increased the sensitivity of the colorimetric sensor. This might be due to increment of the G-quadruplex (GQ) structure in the suspension, which led to specific binding towards Ac. Fourier transform infra-red (FTIR) analysis was conducted to identify the presence of hydrogen bonds for the Ac-TABA-Cit-AuNPs-Mg complex. Strong interparticle interaction was confirmed using high resolution transmission electron microscopy (HRTEM) and ultraviolet visible spectrophotometer (UV-Vis). In contrast, anions had no significant effect on the sensitivity of the colorimetric sensor.*

**Keywords:** *Acephate (Ac); binding temperature; aptamer-gold nanoparticles (Ac-TABA-Cit-AuNPs); cations and anions; detection sensitivity.*

## 1. INTRODUCTION

Acephate (N-[methoxy(methylsulfanyl)phosphoryl]acetamide) (Ac) (Figure 1) is an organophosphate (OP) pesticide that has been widely used to control pests in agricultural fields for decades. However, due to its methamidophos (amino(methylsulfanyl)phosphoryl)oxymethane) toxic metabolite product, its use has been partially restricted in many countries. Ac is classified in a class II “moderately hazardous” pesticide, while methamidophos is classified as a class Ib “highly hazardous” pesticide (WHO, 2019). The Department of Agriculture Malaysia stated that Ac is restricted only in coconut and oil palm plantations due to their high non-target toxicity (DOA, 2018).

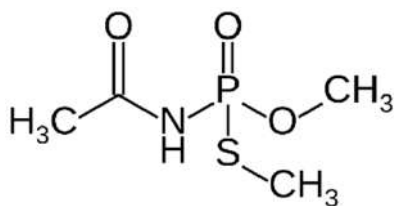


**Figure 1: Structural formula of acephate (Ac).**

The effectiveness of OP as insecticide is related with the inhibition of acetylcholinesterase (AChE) activity, causing increase of cholinergic hyperactivity (Songa & Okonkwo, 2016; Umar & Aisami, 2020), which results in blockage of neuromuscular junctions and blood (Songa & Okonkwo, 2016; Selvolini, *et al.*, 2018; Lin *et al.*, 2020). The inhibition of acetylcholinesterase enzyme occurs when OP binds with the hydroxyl group of the serine, leading to acetylcholine accumulation in the synaptic junctions and finally causing death (Colovic *et al.*, 2013; Sulaiman *et al.*, 2020).

Uncontrollable usage of Ac and methamidophos can result in severe poisonous effects after long term exposure (Lin *et al.*, 2020). Furthermore, Ac is hydrophilic and has low soil absorption, thus producing huge potential water contamination (Kumar *et al.*, 2015; Lin *et al.*, 2020). This has raised concerns and demands for the removal of Ac from the environment. Therefore, the development of robust detection techniques for pesticide residual analysis has become an important issue in recent years due to the widespread use of pesticides and the dangers related to their use leading to debilitating health effects (Jin *et al.*, 2012; Sekhon *et al.*, 2018).

Detection of OP is usually conducted using conventional techniques that use bulk instruments to provide sensitive and selective detection results, such as ion mobility spectrometry (Kalhor *et al.*, 2016; Zhou *et al.*, 2018; Aladaghlo *et al.*, 2020; Sadat *et al.*, 2020), surface-enhanced Raman scattering spectroscopy (Tite *et al.*, 2017; Xu *et al.*, 2017; Yaseen *et al.*, 2019; Xie *et al.*, 2020), combined mass spectrum detector Hu *et al.*, 2019; López-García *et al.*, 2019; Boneva *et al.*, 2021), high performance liquid chromatograph (Nezhadali *et al.*, 2015; Liu *et al.*, 2018) and enzyme-linked immunosorbent assay (Lee *et al.*, 2003; Tang *et al.*, 2008). However, these techniques are typically expensive (Osman *et al.*, 2019; Sulaiman *et al.*, 2020), require complex sample pre-treatment and long analysis time (Kaur & Prabhakar, 2017), as well as require the presence of trained personnel (Pundir & Chauhan, 2012; Bapat *et al.*, 2016; Pérez-Fernández *et al.*, 2020), all of which make their use as on-site screening of pesticide residues problematic (Bala *et al.*, 2015b). Therefore, the need for a sensor that is ready for in-situ and real-time detection that is simple and rapid, mobile, inexpensive, as well as user-friendly is highly needed. The development of aptasensors for the detection of OP has been of recent interest among scientists. Much research has been carried out to improve the sensitivity and selectivity of these aptasensors (Sikora *et al.*, 2011; Bala *et al.*, 2016, 2018; Kim *et al.*, 2018).

Colorimetric detection based on metal aptasensors is the most popular approach as it has been found to be cost effective and has the ability for detection at the lower limits of detection (LOD) (Mehrotra, 2016; Justino, 2017; Mondal *et al.*, 2018). Therefore, it has been proposed to be a promising method that can be exploited to overcome the conventional techniques' limitations (Bala *et al.*, 2015b; Wang *et al.*, 2016). Gold nanoparticles (AuNPs) based colorimetric were the most studied for detection of OP because of its unique characteristic, such as small particle size (1 to 100 nm) (Liu *et al.*, 2018) and easy readout because it provides distinct colour change (Yeh *et al.*, 2014). The colour change resulted from induced aggregation depending on their size and shape (Du *et al.*, 2014; Dheyab *et al.*, 2021). In addition, the aggregation corresponds with surface plasmon band shift in the visible region that is easily noticeable using an ultra-violet visible spectrophotometer (Yeh *et al.* 2014; Govindaraju *et al.* 2015; Yue *et al.* 2016; Kim *et al.* 2019). Furthermore, AuNP is an ideal nanoprobe for sensing due to high stability (Ma *et al.*, 2018), easy

preparation, surface modification and functionalisation (Jamkhande *et al.*, 2019), high molar extinction coefficient (Amanulla *et al.*, 2017; Xi *et al.*, 2017), good biocompatibility (Lee *et al.*, 2018), as well as low toxicity (Capek, 2017; Enea *et al.*, 2020).

However, AuNP based colorimetric detection suffers from the lack of selectivity towards analytes. The recognition element, such as an OP specific aptamer (Apt), is a good candidate to address this issue (Bala *et al.*, 2015b; Wang *et al.*, 2016; Liu *et al.*, 2019). Detection selectivity can be enhanced using Apt coil formation, which traps the specific analyte in it (Bala *et al.*, 2015b, 2017; Kumar, 2020; Phopin & Tantimongcolwat, 2020). Although it is effective to enhance detection selectivity, it is hard to maintain the highest binding affinity of Apt. Hianik *et al.* (2007) concluded that highest binding affinity depends on ionic strength. Furthermore, modifying ionic strength and temperature is suspected to improve Apt structural stability by undergoing reversible denaturing and regaining functionality upon returning of the binding conditions (McKeague & Derosa, 2012).

The human eye can easily catch the distinct colour change from colorimetric detection using AuNPs based sensors. Therefore, several studies utilised naked eye readout in their colorimetric detection (Bai *et al.*, 2015; Bala *et al.*, 2015a; Fahimi-Kashani & Hormozi-Nezhad, 2016). Despite that, naked eye readout can lead to inconsistencies from manual interpretation (Sankar *et al.*, 2020; Fan *et al.*, 2021) and unreliability as it only gives qualitative information (Dutta & Nath, 2017) as it is influenced by the observer. The use of image processing technique could replace naked eye read out as it can remove subjective error, and is able to precisely measure and quantify the resulting colour change of the AuNPs sensor. Recently, Osman *et al.* (2020) employed image processing technique to replace naked eye readout and was able to distinguish detection using AuNPs prepared using different techniques (Osman *et al.*, 2020).

Based on the above analysis, in this paper, we will study the effects of Apt binding temperature and ionic strength. With this knowledge, we hope to enhance and further develop colorimetric detection of Ac using an AuNPs enhanced aptasensor incorporated with image processing.

## **2. METHODOLOGY**

### **2.1 Materials**

Thiolated acephate binding aptamer (TABA) with a sequence of 5'-thiol-AAG CTT GCT TTA TAG CCT GCA GCG ATT CTT GAT CGG AAA AGG CTG AGA GCT ACG C-3' comparable to that employed by prior studies (Wang *et al.*, 2012; Bai *et al.*, 2015) with a change involving the inclusion of thiol group at the beginning of the TABA sequence (C5) was purchased from Integrated DNA Technologies, Singapore. Gold (III) chloride trihydrate (HAuCl<sub>4</sub>.3H<sub>2</sub>O; >49% Au basis) and acephate (Ac) (C<sub>4</sub>H<sub>10</sub>NO<sub>3</sub>PS) Pestanal analytical grade were purchased from Sigma Aldrich, USA. Tri-sodium citrate dihydrate (C<sub>6</sub>H<sub>5</sub>Na<sub>3</sub>O<sub>7</sub>.2H<sub>2</sub>O) (Na-Cit), sodium chloride (NaCl), magnesium sulphate (MgSO<sub>4</sub>) and sodium sulphate (Na<sub>2</sub>SO<sub>4</sub>) were purchased from Merck KGaA, Germany. All other chemicals were of analytical grade. All preparation and dilution of solutions were carried out using MilliQ water with resistivity of 18.2 MΩ.cm.

### **2.2 Preparation of TABA-Cit-AuNPs**

Citrate capped gold nanoparticles (Cit-AuNPs) were prepared by mixing 0.25 mM (100 mL) of HAuCl<sub>4</sub> and 2 mL 34 mM Na-Cit. The mixture was placed into a microwave oven chamber (Panasonic NN-CS599S) to react for 10 min at 300 W. The prepared suspension was stored in a dark amber glass bottle at 5.0 ± 0.5 °C.

### **2.3 Preparation of Thiolated Acephate Binding Aptamer-Based Citrate Capped Gold Nanoparticles (TABA-Cit-AuNPs).**

Thiolated acephate binding aptamer-based citrate capped gold nanoparticles (TABA-Cit-AuNPs) suspensions were freshly prepared for each detection. 100  $\mu\text{L}$  of TABA was incubated with the synthesised AuNPs (800  $\mu\text{L}$ ) at 25  $^{\circ}\text{C}$  for 3.0 h. The suspension was then centrifuged at 12,000 rpm for 10 min to remove the excess TABA and then redispersed using MilliQ water.

### **2.4 Detection of Acephate**

Different concentration of Ac was used to study the limit of detection of current TABA-Cit-AuNPs based colorimetric detection technique. Triplicate samples of 100  $\mu\text{L}$  of 15, 50, 70, 90, 100 and 200 ppm Ac were measured in a 3 mL glass vial containing 900  $\mu\text{L}$  of TABA-Cit-AuNPs. All colour changes were captured using a portable digital microscope at a fixed distance of 10.5 cm. From the image captured, the digitised red value (RV) was obtained using ImageJ. The detection of limit Ac was confirmed by the colour change from dark red colour suspension to dark purple colour complex (Ac-TABA-Cit-AUNPs).

### **2.5 Effect of Thiolated Acephate Binding Aptamer and Citrate Capped-Gold Nanoparticles Binding Temperature**

In order to study the effect of binding temperature, TABA and Cit-AuNPs were incubated at different temperatures. Generally, triplicate samples of 100  $\mu\text{L}$  of TABA were mixed with 800  $\mu\text{L}$  of Cit-AuNPs in three centrifuge tubes. Next the mixture was incubated at 25  $^{\circ}\text{C}$  for 3.0 h. The suspension was then centrifuged at 12,000 rpm for 10 min to remove excess TABA and then redispersed using MilliQ water. This procedure was repeated for binding temperatures of 5 and 40  $^{\circ}\text{C}$ . Next, 900  $\mu\text{L}$  of prepared TABA-Cit-AuNPs was transferred into a 3 mL glass vial. 100  $\mu\text{L}$  of 200 ppm Ac was added in the glass vial. All colour changes were captured using a portable digital microscope and the RV of image captured was obtained using ImageJ.

### **2.6 Effect of Ion Towards Detection of Acephate**

Improvement of detection can be achieved by varying the ionic strength (Wei *et al.*, 2007). Detection took place for 200 ppm Ac according to the procedure mentioned in Section 2.5. Next, 100  $\mu\text{L}$  of 100 mM NaCl was added to Ac-TABA-Cit-AuNPs complex in three glass vials. All colour changes were captured using a portable digital microscope and the RV of image captured was obtained using ImageJ. The procedure was repeated with the addition of  $\text{Na}_2\text{SO}_4$  and  $\text{MgSO}_4$

### **2.7 Digitising the Captured Images Using ImageJ**

The images captured were digitised using ImageJ. Firstly, each image was cropped to a constant area carefully. Then, the software cleared undesirable regions of the image. Eventually, the mean red, green and blue (RGB) values were extracted from the image and RV was used as reference value of colorimetric detection occurred.



## 2.8 Independent *t*-test

Minitab 18 software was used for all independent *t*-test analyses. The degree of confidence was set at 95%.

## 2.9 Ultra-violet Visible Spectrophotometer (UV-Vis)

UV-Vis analysis was performed using a Genesys 6 UV-visible spectrophotometer at a scanning rate of 1 nm/sec from 200 to 800 nm.

## 2.10 Fourier Transform Infrared analysis (FTIR)

FTIR analysis was performed using a Perkin Elmer Spectrum 100 equipped with Attenuated Total Reflection (ATR) accessory. The spectra were recorded from 4000 to 500  $\text{cm}^{-1}$  with a resolution of 4  $\text{cm}^{-1}$ .

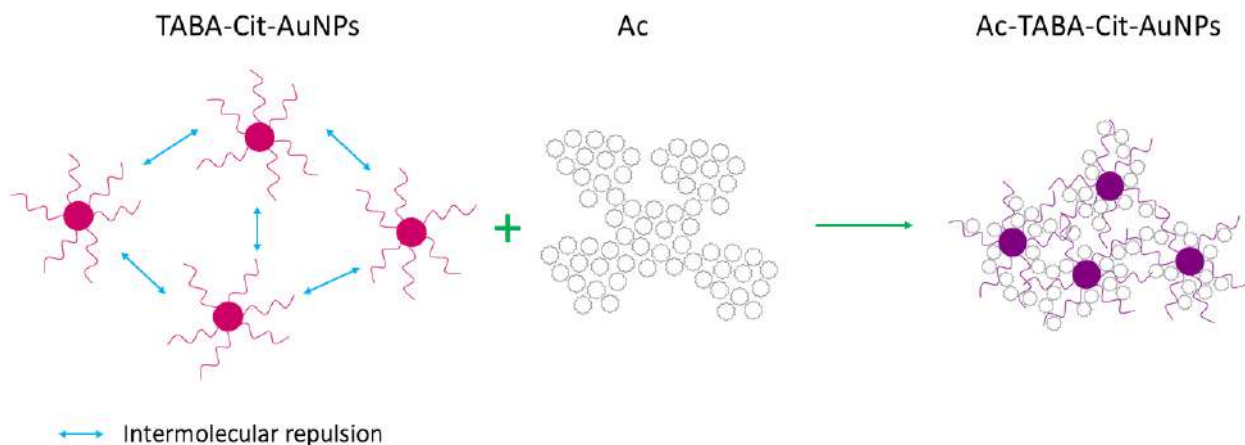
## 2.11 High Resolution Transmission Electron Microscope (HRTEM)

High resolution transmission electron microscope (HRTEM) analysis was performed using a JEOL JEM 2100F HRTEM with an operating voltage of 200 kV. All sample were dropped on the viewing grids and left overnight to dry. Next, the HRTEM images of each sample was captured and analysed.

# 3. RESULTS AND DISCUSSION








## 3.1 Detection of Acephate

Before the detection of Ac, TABA-Cit-AuNPs suspension was able to maintain its red colour due to intermolecular repulsion between negatively phosphate group charged ions of TABA with the counter-ions in the medium (Javier *et al.*, 2008). Upon detection of Ac, this repulsion was hindered, resulting in the colour change from dark red to dark purple (Chang *et al.*, 2019) as shown in Figure 2. All the samples were photographed and digitised as per Table 1. Observed at low concentration of Ac, there is no colour change as the colour of the sample was still red. On the other hand, the dark purple colour complex was observed for detection of Ac at higher concentration.



**Figure 2: Illustration of Ac-TABA-Cit-AuNPs formation.**

**Table 1: Photographed images and RVs for the detection of Ac.**

Concentration (ppm)	0	15	50	70	90	100	200
Captured image							
Mean RV	149.9	149.8	149.8	149.7	149.8	64.3	35.4
Standard deviation	0.15	0.20	0.17	0.27	0.20	0.10	0.20
Relative standard deviation RSD (%)	0.10	0.13	0.11	0.18	0.13	0.16	0.56

From this study, 100 ppm was found to be the lowest concentration detected. Sensitivity of the synthesised TABA-Cit-AuNPs was determined based on the RV of the captured image of each mixture. Independent *t*-test was used to identify any significant differences in the RV for all the captured images. The results are summarised in Table 2. The null hypothesis ( $H_0$ ): There is no significant difference in mean RVs for TABA-Cit-AuNPs and Ac-TABA-Cit-AuNPs. The results show significant difference in mean RVs for Ac-TABA-Cit-AuNPs as indicated by *p*-value < 0.05 for detection of higher concentration (100 and 200 ppm). In contrast, there is no significant difference in mean RVs for Ac-TABA-Cit-AuNPs as indicated by *p*-value > 0.05 for detection of lower concentration. At this point, the prepared sensor (TABA-Cit-AuNPs) was unable to detect Ac at lower concentrations (15, 50, 70 and 90 ppm) because there is no statistically significant difference in RV between the cropped images of blank (TABA-Cit-AuNPs) and detection (Ac-TABA-Cit-AuNPs).

**Table 2: Results of independent *t*-test for the detection of Ac at different concentrations.**

Concentration (ppm)	15	50	70	90	100	200
Mean RV	149.8	149.8	149.7	149.8	64.3	35.4
<i>p</i> -value	0.21	0.20	0.14	0.21	0.00	0.00

### 3.2 Effect of Aptamer Binding Temperature on the Detection of Acephate

Table 3 show the mean RV for the photographed images of 200 ppm Ac detected using TABA-Cit-AUNPs produced at different binding temperatures. As shown in the table, TABA-Cit-AuNPs binded at 25 °C was able to result in better detection of Ac as the lowest mean RV was obtained as compared with detection using TABA-Cit-AuNPs binded at 5 and 40 °C. This indicates that more Ac to TABA-Cit-AuNPs interaction occurs. In contrast, lower detection occurred for TABA-Cit-AuNPs binded at 5 and 40 °C due to less Ac to TABA-Cit-AuNPs interactions, which might be due to denaturation of TABA (Miodek *et al.*, 2015).

**Table 3: RVs for before and after detection of Ac at different binding temperatures.**





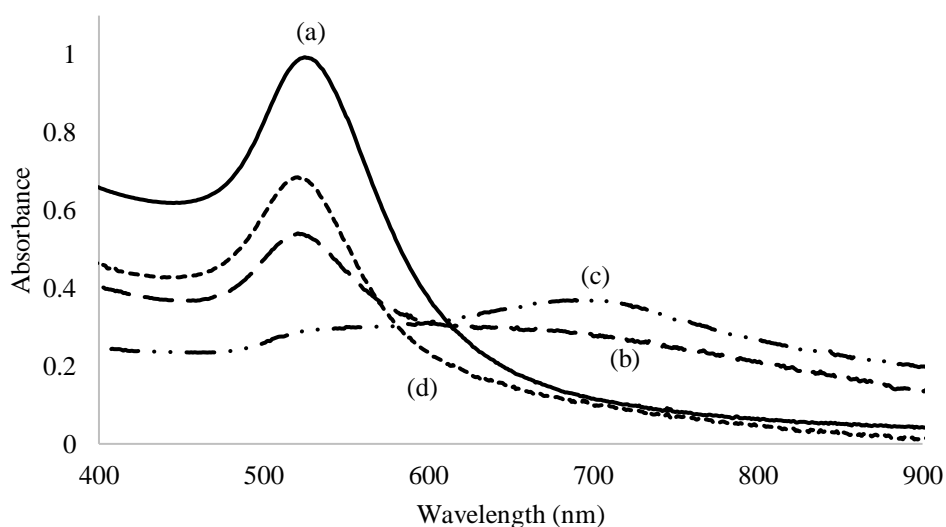
	Before detection / without Ac	After detection / with presence of Ac		
		TABA binding temperature (°C)		
		5	25	40
<b>Captured Image</b>				
<b>Mean RV</b>	149.9	77.1	35.4	124.8
<b>Standard deviation</b>	0.15	0.19	0.20	0.17
<b>Relative standard deviation RSD (%)</b>	0.10	0.25	0.56	0.14

Figure 3 shows the absorbance spectra of detected Ac using TABA-Cit-AuNPs binded at different binding temperatures. It is observed that absorbance intensity reduced for all binding temperatures. This is as Ac was trapped by TABA-Cit-AuNPs particles and hindered intermolecular repulsion, resulting in aggregation that was captured as the colour changed from dark red to dark purple (Osman *et al.*, 2020). This aggregation was in line with the UV-Vis spectra as the appearance of a new peak at longer wavelength (650 - 700 nm).








**Figure 3: UV-Vis absorbance spectra of (a) Cit-AuNPs, and Ac-TABA-Cit-AuNPs at different binding temperatures; (b) 5 °C (c) 25 °C and (d) 40 °C.**

### 3.3 Effect of Ions on the Detection of Acepate

Table 4 shows the effect of ions on the Ac-TABA-Cit-AuNPs complex. Two different salts, namely NaCl and Na<sub>2</sub>SO<sub>4</sub>, were used to evaluate the effect of adding anions (Cl<sup>-</sup> or SO<sub>4</sub><sup>2-</sup>) on detection of Ac. The results showed that there were small changes (0.4 and 0.2) in the RVs when the anions (Cl<sup>-</sup> and SO<sub>4</sub><sup>2-</sup>) were introduced respectively into Ac-TABA-Cit-AuNPs. On the other hand, two different salts, namely Na<sub>2</sub>SO<sub>4</sub> and MgSO<sub>4</sub>, were used to evaluate the effect of adding Na<sup>+</sup> or Mg<sup>2+</sup> cations on the detection of Ac. The results show that there was small change (0.2) in the RV when Na<sup>+</sup> was introduced into Ac-TABA-Cit-AuNPs and large change (1.2) in the RV when Mg<sup>2+</sup> was introduced.

The independent *t*-test was conducted to identify statistical significance between the mean RVs of Ac-TABA-Cit-AuNPs and mean RVs of Ac-TABA-Cit-AuNPs-anion/cation. The null hypothesis (*H*<sub>0</sub>): There is no significant difference in mean RVs for Ac-TABA-Cit-AuNPs and Ac-TABA-Cit-AuNPs-anion/cation. The results show that there is no significant difference in mean RVs of Ac-TABA-Cit-AuNPs-Cl<sup>-</sup>/SO<sub>4</sub><sup>2-</sup>/Na<sup>+</sup> as indicated by *p*-value > 0.05. In contrast, there is significant difference in mean RVs of Ac-TABA-Cit-AuNPs-Mg<sup>2+</sup> as indicated by *p*-value < 0.05. This was an indication of the improved sensitivity of TABA-Cit-AuNPs as lower RVs indicate that a higher degree of aggregation of particles occurred (Hu *et al.*, 2018; Yu & Li, 2019).

**Table 4: RV of colour change with the addition of different ion charges.**

Type of ion	Detection of 200 ppm Ac				
	No presence of salt	Anion		Cation	
		Cl <sup>-</sup>	SO <sub>4</sub> <sup>2-</sup>	Na <sup>+</sup>	Mg <sup>2+</sup>
<b>Cropped Image</b>					
<b>Mean red Value</b>	35.4	35.0	35.2	35.2	34.2
<b>Standard deviation</b>	0.20	0.12	0.15	0.15	0.21
<b>Relative standard deviation (RSD) (%)</b>	0.56	0.34	0.43	0.43	0.61
<b><i>p</i>-value</b>	-	0.131	0.103	0.103	<b><u>0.003</u></b>

These findings might be due to the existence of G-quadruplex (GQ) structure (Bhattacharyya *et al.*, 2016), whereby successive G-tetrads structure occurred from the addition of metal ions (Sannohe & Sugiyama, 2010; Zhu *et al.*, 2010) and reduced nonspecific binding between the TABA-Cit-AuNPs and Ac (Hianik *et al.*, 2007; Jeong & Paeng, 2012; Bhattacharyya *et al.*, 2016; Largy *et al.*, 2016).

The FTIR spectra of Ac-TABA-Cit-AuNPs and Ac-TABA-Cit-AuNPs-Mg are depicted in Figure 4. A broad intense peak around 3350 cm<sup>-1</sup> for both spectra belongs to O-H stretching from water, which was the solution used in this experiment. In addition, the large peak of around 1700 to 1600 cm<sup>-1</sup> was a combination peak of C=O asymmetric stretching and NH<sub>2</sub> scissoring (Lopes *et al.*, 2013). A peak representing symmetric

stretching of the C=O bond was found at 1400 to 1350  $\text{cm}^{-1}$ . The transmittance peak for  $\text{PO}^{2-}$  was found between 1300 to 1200  $\text{cm}^{-1}$  (Garidel *et al.*, 2000; Lopes *et al.*, 2013), while P-O stretching was found between 1000 to 900  $\text{cm}^{-1}$  (Garidel *et al.*, 2000; Lopes *et al.*, 2013), which is an indicative peak for nucleic acid of TABA (Andrushchenko *et al.*, 2015). The transmittance peak of C=O asymmetric stretching and  $\text{NH}_2$  scissoring FTIR spectrum for Ac-TABA-Cit-AuNPs-Mg shifted to a higher wavenumber and reduced in transmittance intensity. This indicated the presence of stronger bonds (hydrogen bond) (Garidel *et al.*, 2000; Andrushchenko *et al.*, 2015; Osman *et al.*, 2021) and the presence of hypochromic effect caused by  $\pi$ - $\pi$  electron interactions of the stacked guanine structure within the G-quadruplex structure (Andrushchenko *et al.*, 2015).

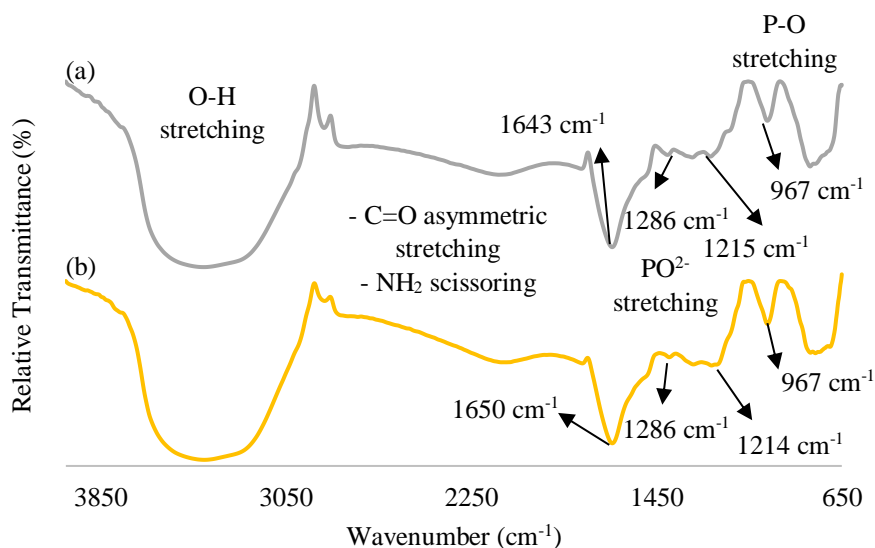


**Figure 4: FTIR spectra of (a) Ac-TABA-Cit-AuNPs and (b) Ac-TABA-Cit-AuNPs-Mg.**

Figures 5 and 6 show the surface plasmon resonance (SPR) of the Ac-TABA-Cit-AuNPs complex induced by different anions and cations. An easy way to determine whether there is any interaction between the GQ structure and the Ac is to analyse the shifting of the position of the maximum band from when TABA-Cit-AuNPs is free in the solution to when TABA-Cit-AuNPs was complexed with Ac (Tsai *et al.*, 2002). The maximum absorbance peak of Ac-TABA-Cit-AuNPs appeared at longer wavelength as compared to maximum absorbance peak of TABA-Cit-AuNPs suspension. The longest maximum absorbance peak shift can be seen for Ac-TABA-Cit-AuNPs induced with  $\text{Mg}^{2+}$  ion (760 nm). The magnitude of this shifting shows stronger interaction between the GQ of TABA-Cit-AuNPs and Ac (Murat & Defrancq, 2011; Jaumot & Gargallo, 2012) with presence of  $\text{Mg}^{2+}$ . The dramatic absorbance peak shift for acetate-TABA-Cit-AuNPs-Mg is an excellent indication of the interaction.

Figure 7 shows the HRTEM images of Ac-TABA-Cit-AuNPs and Ac-TABA-Cit-AuNPs-Mg complexation. The images show a higher degree of aggregation for Ac-TABA-Cit-AuNPs-Mg as the particles were arranged closer. This is due to Ac being effectively trapped by aptamer folding (stable GQ structure) (Zhengbo *et al.*, 2014; Rafati *et al.*, 2018) through  $\pi$ - $\pi$  stacking of guanine-quartet. In addition, the probable role of  $\text{Mg}^{2+}$  was to form complex coordinative bonds through Mg-O with the backbone phosphate oxygen atoms of TABA (J. Lin *et al.*, 2010) leading to improved sensitivity of the detection.

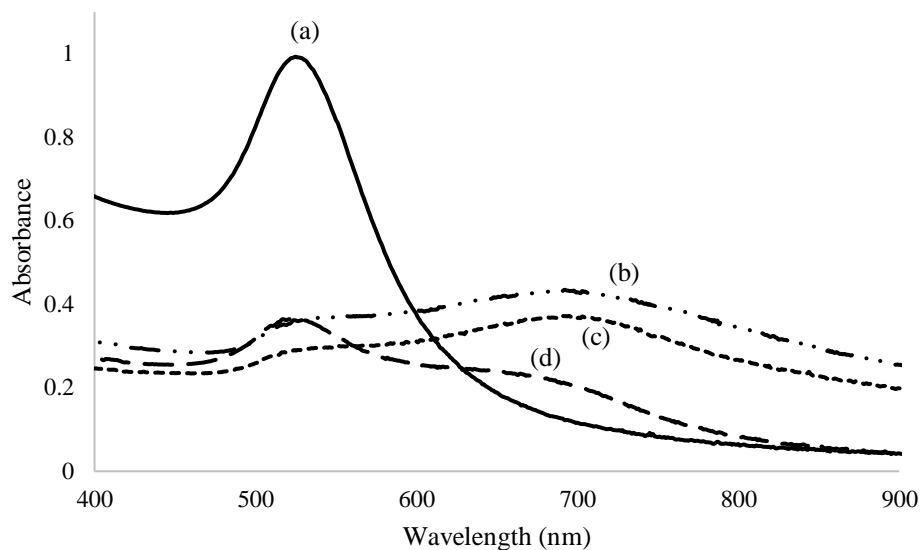


**Figure 5: UV-Vis absorbance spectra of (a) Cit-AuNPs, (b) Ac-TABA-Cit-AuNPs, (c) Ac-TABA-Cit-AuNPs-Cl and (d) Ac-TABA-Cit-AuNPs-SO<sub>4</sub>**

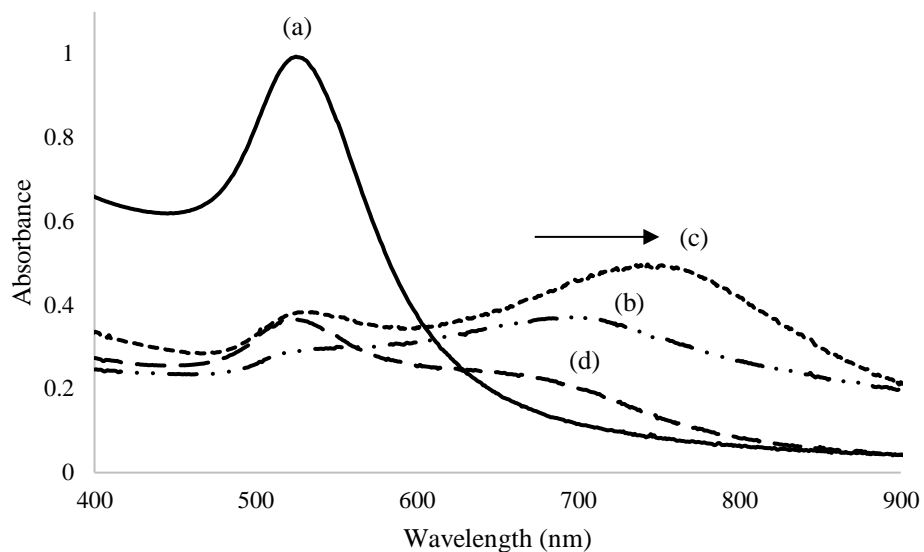


**Figure 6: UV-Vis absorbance spectra of (a) Cit-AuNPs, (b) Ac-TABA-Cit-AuNPs, (c) Ac-TABA-Cit-AuNPs-Mg and (d) Ac-TABA-Cit-AuNPs-Na**

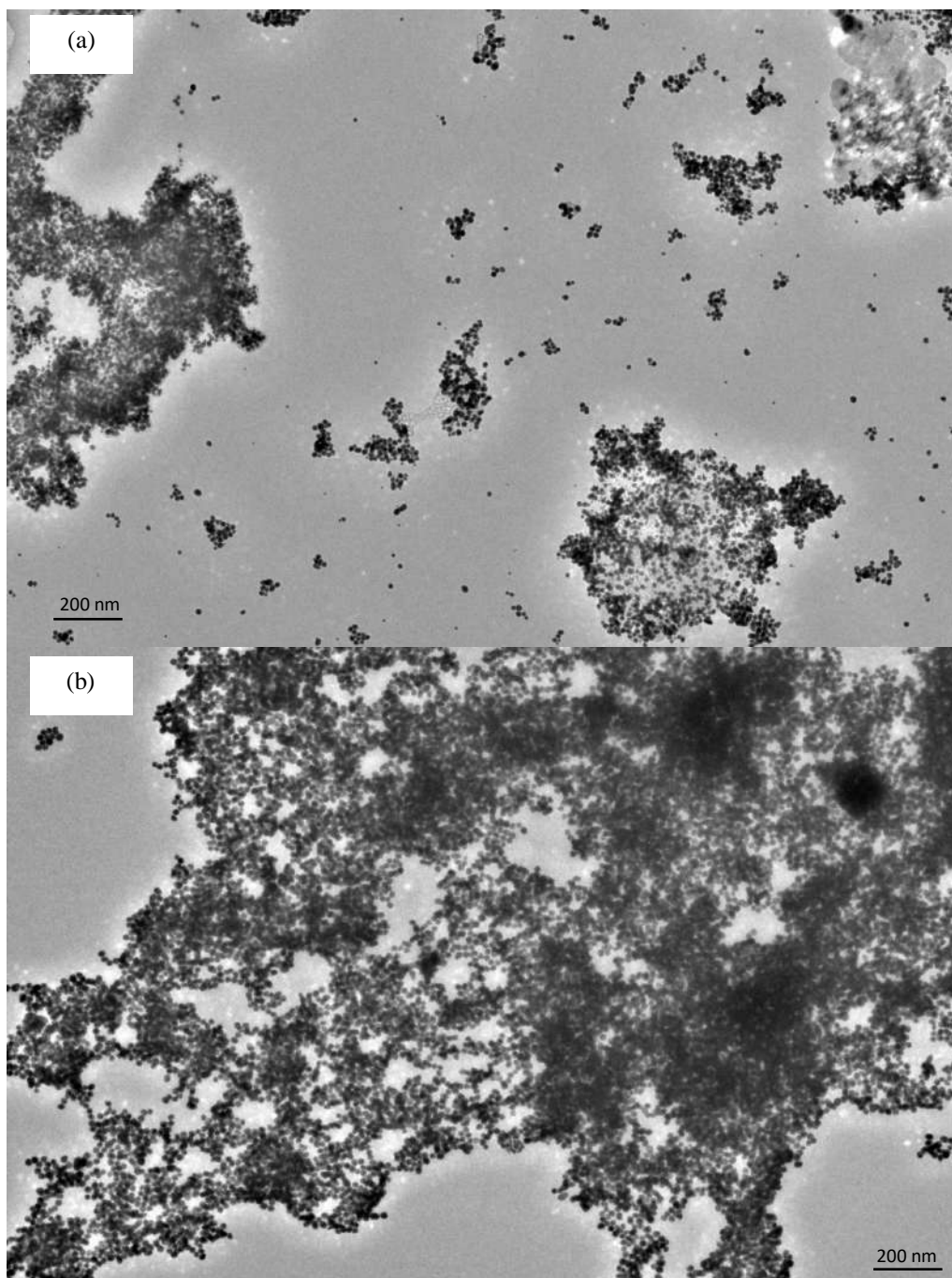


**Figure 7: HRTEM images of (a) Ac-TABA-Cit-AuNPs and (b) Ac-TABA-Cit-AuNPs-Mg complexation at 10,000x magnification**

#### **4. CONCLUSION**

The prepared TABA-Cit-AuNPs suspension was successfully utilised for detection of Ac. Initially, the suspension can detect up to 100 ppm Ac. In order to improve the detection sensitivity towards Ac, we studied the effect of Cit-AuNPs and TABA binding temperature and the effect of ions. Throughout this study, lower mean RVs were obtained when dark purple colour complex appeared as detection took place. The optimum TABA to Cit-AuNPs binding temperature was 25 °C, which indicated that lower mean RVs

were obtained when detection took place. The appearance of new maximum absorbance peaks at longer wavelength in the UV-Vis analysis indicated a higher degree of particle aggregation as compared to other binding temperatures as confirmed by the earlier observation. Detection of Ac improved after  $Mg^{2+}$  ion was introduced into the Ac-TABA-Cit-AuNPs complex as the lowest mean RVs were obtained as compared to the other ions. The FTIR transmittance peak of C=O asymmetric stretching and  $NH_2$  scissoring FTIR spectrum for Ac-TABA-Cit-AuNPs-Mg suggested a higher degree of aggregation of Ac-TABA-Cit-AuNPs-Mg particles, which was confirmed by its absorbance spectra and HRTEM images.

## ACKNOWLEDGEMENT

This project was funded (UPNM/2018/CHEMDEF/ST/2) by the Ministry of Education Malaysia. The authors also thank the National Defence University of Malaysia (NUDM) for providing the research facilities.

## REFERENCES

- Aladaghlo, Z., Fakhari, A.R., Alavioon, S.I. & Dabiri, M. (2020). A mesoporous nanosorbent composed of silica, graphene, and palladium (II) for ultrasound-assisted dispersive solid-phase extraction of organophosphorus pesticides prior to their quantitation by ion mobility spectrometry. *Microchim. Acta*, **187**: 1–11.
- Amanulla, B., Palanisamy, S., Chen, S.M., Chiu, T.W., Velusamy, V., Hall, J.M., Chen, T.W. & Ramaraj, S. K. (2017). Selective colorimetric detection of nitrite in water using chitosan stabilized gold nanoparticles decorated reduced graphene oxide. *Sci. Rep.*, **7**: 1–9.
- Andrushchenko, V., Benda, L., Páv, O., Dračinský, M. & Bouř, P. (2015). Vibrational properties of the phosphate group investigated by molecular dynamics and density functional theory. *J. Phy. Chem. B*, **119**: 10682–10692.
- Bai, W., Zhu, C., Liu, J., Yan, M., Yang, S. & Chen, A. (2015). Gold nanoparticle-based colorimetric aptasensor for rapid detection of six organophosphorous pesticides. *Environ. Toxicol. Chem.*, **34**: 2244–2249.
- Bala, R., Dhingra, S., Kumar, M., Bansal, K., Mittal, S., Sharma, R.K. & Wangoo, N. (2017). Detection of organophosphorus pesticide – Malathion in environmental samples using peptide and aptamer based nanoprobe. *Chem. Eng. J.*, **311**: 111–116.
- Bala, R., Kumar, M., Bansal, K., Sharma, R.K. & Wangoo, N. (2016). Ultrasensitive aptamer biosensor for malathion detection based on cationic polymer and gold nanoparticles. *Biosens. Bioelectron*, **85**: 445–449.
- Bala, R., Mittal, S., Sharma, R.K. & Wangoo, N. (2018). A supersensitive silver nanoprobe based aptasensor for low cost detection of malathion residues in water and food samples. *Spectrochim. Acta A Mol Biomol Spectrosc.*, **196**: 268–273.
- Bala, R., Sharma, R.K. & Wangoo, N. (2015a). Chemical Highly sensitive colorimetric detection of ethyl parathion using gold nanoprobe. *Sens. Actuators B Chem.*, **210**: 425–430.
- Bala, R., Sharma, R.K. & Wangoo, N. (2015b). Development of gold nanoparticles-based aptasensor for the colorimetric detection of organophosphorus pesticide phorate. *Anal. Bioanal. Chem.*, **408**: 333–338.
- Bapat, G., Labade, C., Chaudhari, A. & Zinjarde, S. (2016). Silica nanoparticle based techniques for extraction, detection, and degradation of pesticides. *Adv. Colloid. Interface Sci.*, **237**: 1–14.
- Bhattacharyya, D., Arachchilage, G.M. & Basu, S. (2016). Metal cations in G-quadruplex folding and stability. *Front. Chem.*, **4**: 1–14.



- Boneva, I., Yaneva, S. & Danalev, D. (2021). Development and validation of method for determination of organophosphorus pesticides traces in liver sample by GC-MS/MS-ion trap. *Acta Chromatogr.*, **33**: 188–194.
- Capek, I. (2017). Polymer decorated gold nanoparticles in nanomedicine conjugates. *Adv. Colloid. Interface Sci.*, **249**: 386–399.
- Chang, C.C., Chen, C.P., Wu, T.H., Yang, C.H., Lin, C.W. & Chen, C.Y. (2019). Gold nanoparticle-based colorimetric strategies for chemical and biological sensing applications. *Nanomaterials*, **9**: 1–24.
- Colovic, M.B., Krstic, D.Z., Lazarevic-Pasti, T.D., Bondzic, A.M. & Vasic, V. M. (2013). Acetylcholinesterase inhibitors : Pharmacology and toxicology. *Curr. Neuropharmacol.*, **11**: 315–335.
- Dheyab, M.A., Aziz, A.A., Khaniabadi, P.M., Jameel, M.S., Ahmed, N.M. & Ali, A.T. (2021). Distinct advantages of using sonochemical over laser ablation methods for a rapid-high quality gold nanoparticles production. *Mater. Res. Express*, **8**: 15009–15019.
- Du, J., Zhu, B., Peng, X. & Chen, X. (2014). Optical reading of contaminants in aqueous media based on gold nanoparticles. *Small*, 3461–3479.
- Dutta, S., & Nath, P. (2017). A fully automated colorimetric sensing device using smartphone for biomolecular quantification. *Optics and Biophotonics in Low-Resource Settings III*, **10055**: 1–6.
- Enea, M., Pereira, E., de Almeida, M. P., Araújo, A. M., Bastos, M. de L., & Carmo, H. (2020). Gold nanoparticles induce oxidative stress and apoptosis in human kidney cells. *Nanomaterials*, **10**: 1–17.
- Fahimi-Kashani, N., & Hormozi-Nezhad, M. R. (2016). Gold-nanoparticle-based colorimetric sensor array for discrimination of organophosphate pesticides. *Anal. Chem.*, **88**: 8099–8106.
- Fan, Y., Li, J., Guo, Y., Xie, L., & Zhang, G. (2021). Digital image colorimetry on smartphone for chemical analysis : A review. *Measurement*, **171**: 108829.
- Garidel, P., Blume, A., & Hübner, W. (2000). A Fourier transform infrared spectroscopic study of the interaction of alkaline earth cations with the negatively charged phospholipid 1,2-dimyristoyl-sn-glycero-3-phosphoglycerol. *Biochim. Biophys. Acta Biomembr.*, **1466**: 245–259.
- Govindaraju, S., Ramasamy, M., Baskaran, R., Ahn, S. J., & Yun, K. (2015). Ultraviolet light and laser irradiation enhances the antibacterial activity of glucosamine-functionalized gold nanoparticles. *Int J Nanomedicine*, **10**: 67–78.
- Hianik, T., Ostatná, V., Sonlajtnerova, M. & Grman, I. (2007). Influence of ionic strength, pH and aptamer configuration for binding affinity to thrombin. *Bioelectrochemistry*, **70**: 127–133.
- Hu, L., Tao, Y., Luo, D., Feng, J., Wang, L., Yu, M., Li, Y., Covaci, A. & Mei, S. (2019). Simultaneous biomonitoring of 15 organophosphate flame retardants metabolites in urine samples by solvent induced phase transition extraction coupled with ultra-performance liquid chromatography-tandem mass spectrometry. *Chemosphere*, **233**: 724–732.
- Hu, X., Chang, K., Wang, S., Sun, X., Hu, J. & Jiang, M. (2018). Aptamer-functionalized AuNPs for the high-sensitivity colorimetric detection of melamine in milk samples. *PLoS One*, **13**: 1–15.
- Jamkhande, P. G., Ghule, N.W., Bamer, A.H. & Kalaskar, M. G. (2019). Metal nanoparticles synthesis: An overview on methods of preparation, advantages and disadvantages, and applications. *J. Drug Deliv. Sci. Technol.*, **53**: 101174.
- Jaumot, J. & Gargallo, R. (2012). Experimental methods for studying the interactions between G-quadruplex structures and ligands. *Curr. Pharm. Des.*, **18**: 1900–1916.
- Javier, D. J., Nitin, N., Levy, M., Ellington, A. & Richards-Kortum, R. (2008). Aptamer-targeted gold nanoparticles as molecular-specific contrast agents for reflectance imaging. *Bioconjug Chem*, **19**: 1309–1312.
- Jeong, S. & Paeng, I.R. (2012). Sensitivity and selectivity on aptamer-based assay: the determination of tetracycline residue in bovine milk. *Sci. World J.*, **2012**: 1–10.
- Jin, B., Xie, L., Guo, Y. & Pang, G. (2012). Multi-residue detection of pesticides in juice and fruit wine : A review of extraction and detection methods. *Food Res. Int.*, **46**: 399–409.
- Justino, C.I.L. (2017). Recent progress in biosensors for environmental monitoring: A review. *Sensors*, **17**: 1–25.

- Kalhor, H., Hashemipour, S. & Yaftian, M. R. (2016). Ultrasound-assisted emulsification-microextraction/ion mobility spectrometry combination: Application for analysis of organophosphorus pesticide residues in rice samples. *Food Anal. Methods*, **9**: 3006–3014.
- Kaur, N. & Prabhakar, N. (2017). Current scenario in organophosphates detection using electrochemical biosensors. *TrAC - Trends Anal. Chem.*, **92**: 62–85.
- Kim, H.M., Hong Jeong, D., Lee, H.Y., Park, J.H. & Lee, S. K. (2019). Improved stability of gold nanoparticles on the optical fiber and their application to refractive index sensor based on localized surface plasmon resonance. *Opt. Laser Technol.*, **114**: 171–178.
- Kim, M., Kwon, J.E., Lee, K. & Koh, W. (2018). Signal-amplifying nanoparticle / hydrogel hybrid microarray biosensor for metal-enhanced fluorescence detection of organophosphorus compounds. Signal-amplifying nanoparticle / hydrogel hybrid microarray biosensor for metal-enhanced fluorescence detection. *Biofabrication*, **10**: 1–14.
- Kumar, V. (2020). Application of DNA-nanosensor for environmental monitoring: Recent advances and perspectives. *Curr. Pollut. Rep.*, 1–52.
- Kumar, V., Upadhyay, N., Kumar, V. & Sharma, S. (2015). A review on sample preparation and chromatographic determination of acephate and methamidophos in different samples. *Arab. J. Chem.*, **8**: 624–631.
- Largy, E., Mergny, J.L. & Gabelica, V. (2016). Role of alkali metal ions in G-quadruplex nucleic acid structure and stability. *The Alkali Metal Ions: Their Role for Life*. Springer Verlag Germany, pp 203–258.
- Lee, J.H., Cho, H.Y., Choi, H.K., Lee, J.Y. & Choi, J.W. (2018). Application of gold nanoparticle to plasmonic biosensors. *Int. J. Mol. Sci.*, **19**: 1–14.
- Lee, J. K., Ahn, K.C., Stoutamire, D.W., Gee, S.J. & Hammock, B.D. (2003). Development of an enzyme-linked immunosorbent assay for the detection of the organophosphorus insecticide acephate. *J. Agric. Food Chem.*, **51**: 3695–3703.
- Lin, J., Yan, Y., Ou, T., Tan, J., Huang, S., Li, D., & Gu, L.Q. (2010). Effective detection and separation method for G-quadruplex DNA based on its specific precipitation with Mg<sup>2+</sup>. *Biomacromolecules*, **11**: 3384–3389.
- Lin, Z., Pang, S., Zhang, W., Mishra, S., Bhatt, P. & Chen, S. (2020). Degradation of acephate and its intermediate methamidophos: mechanisms and biochemical pathways. *Front. Microbiol.*, **11**: 1–18.
- Liu, D.L., Li, Y., Sun, R., Xu, J.Y., Chen, Y. & Sun, C.-Y. (2019). Colorimetric detection of organophosphorus pesticides based on the broad-spectrum aptamer. *J. Nanosci. Nanotechnol.*, **20**: 2114–2121.
- Liu, G., Lu, M., Huang, X., Li, T. & Xu, D. (2018). Application of gold-nanoparticle colorimetric sensing to rapid food safety screening. *Sensors*, **18**: 1–16.
- Liu, W., Quan, J. & Hu, Z. (2018). Detection of organophosphorus pesticides in wheat by ionic liquid-based dispersive liquid-liquid microextraction combined with HPLC. *J. Anal. Methods Chem.*, **2018**: 1–11.
- Lopes, R.P., Marques, M.P. M., Valero, R., Tomkinson, J. & Batista De Carvalho, L.A.E. (2013). Guanine-A combined study using vibrational spectroscopy and theoretical methods. *Adv. Biomed. Spectrosc.*, **7**: 127–145.
- López-García, M., Romero-González, R. & Garrido Frenich, A. (2019). Monitoring of organophosphate and pyrethroid metabolites in human urine samples by an automated method (TurboFlow™) coupled to ultra-high performance liquid chromatography-Orbitrap mass spectrometry. *J. Pharm. Biomed. Anal.*, **173**: 31–39.
- Ma, X.M., Sun, M., Lin, Y., Liu, Y.J., Luo, F., Guo, L.H., Qiu, B., Lin, Z.Y. & Chen, G. N. (2018). Progress of visual biosensor based on gold nanoparticles. *Chinese J. Anal. Chem.*, **46**: 1–10.
- McKeague, M. & Derosa, M.C. (2012). Challenges and opportunities for small molecule aptamer development. *J Nucleic Acids*, **2012**: 1–20.
- Mehrotra, P. (2016). Biosensors and their applications – A review. *J. Oral. Biol. Craniofac. Res.*, **6**: 153–159.

- Miodek, A., Regan, E.M., Bhalla, N., Hopkins, N.A.E., Goodchild, S.A. & Estrela, P. (2015). Optimisation and characterisation of anti-fouling ternary SAM layers for impedance-based aptasensors. *Sensors*, **15**: 25015–25032.
- Mondal, B., Ramlal, S., Lavu, P.S., Bhavanashri, N. & Kingston, J. (2018). Highly sensitive colorimetric biosensor for Staphylococcal Enterotoxin B by a label-free aptamer and gold nanoparticles. *Front. Microbiol.*, **9**: 1–8.
- Murat, P. & Defrancq, E. (2011). Methods for investigating G-quadruplex DNA/ligand interactions. *Chem. Soc. Rev.*, **40**: 5293–5307.
- Nezhadali, A., Feizy, J. & Beheshti, H. R. (2015). A molecularly imprinted polymer for the selective extraction and determination of fenvalerate from food samples using high-performance liquid chromatography. *Food Anal. Methods*, **8**: 1225–1237.
- Osman, M.J., Abdul Rashid, J.I., Khim, O.K., Yunus Wan, W.M.Z., Mohd Noor, S.A., Mohd Kasim, N. A., Knight, V.F. & Chuang, T. C. (2021). Optimisation of a gold nanoparticle-based aptasensor integrated with image processing for the colorimetric detection of acephate using response surface methodology. *RSC Adv.*, **11**: 25933–25942.
- Osman, M.J., Wan Yunus, W.M.Z., Ong, K.K. & Abdul Rashid, J. (2019). Recent advances techniques for detection of organophosphates: A review. *J. Def. Sci. Eng. Technol.*, **2**: 49–70.
- Osman, M.J., Yunus Wan, W.M.Z., Ong, K.K., Chieng, B.W., Mohd Kassim, N.A., Mohd Noor, S.A., Knight, V.F., Abdul Rashid, J.I. & Teoh, C.C. (2020). Image digitization of colorimetric detection of acephate based on its complexation with citrate-capped gold nanoparticles. *J. Chem.*, **2020**: 1–10.
- Pérez-Fernández, B., Costa-García, A. & Alfredo, E.M. (2020). Electrochemical (bio) sensors for pesticides detection using screen-printed electrodes. *Biosensor*, **10**: 1–26.
- Phopin, K. & Tantimongcolwat, T. (2020). Pesticide aptasensors—State of the art and perspectives. *Sensors*, **20**: 6809–6849.
- Pundir, C.S. & Chauhan, N. (2012). Acetylcholinesterase inhibition-based biosensors for pesticide determination: A review. *Anal. Biochem.*, **429**: 19–31.
- Rafati, A., Zarrabi, A., Abediankenari, S., Aarabi, M. & Gill, P. (2018). Sensitive colorimetric assay using insulin g-quadruplex aptamer arrays on DNA nanotubes coupled with magnetic nanoparticles. *R. Soc. Open Sci.*, **5**: 171835–171845.
- Sadat, S.A.A., Ilbeigi, V., Valadbeigi, Y. & Soleimani, M. (2020). Determination of pesticides phosalone and diazinon in pistachio using ion mobility spectrometry. *Int. J. Ion Mobility Spectrom.*, **23**: 127–131.
- Sankar, K., Lenisha, D., Janaki, G., Juliana, J., Kumar, R.S., Selvi, M.C. & Srinivasan, G. (2020). Digital image-based quantification of chlorpyrifos in water samples using a lipase embedded paper based device. *Talanta*, **208**: 120408.
- Sannohe, Y. & Sugiyama, H. (2010). Overview of formation of G-quadruplex structures. *Curr. Protoc. Nucleic Acid Chem.*, **40**: 1–17.
- Sekhon, S.S., Park, G., Park, D., Kim, S.Y., Wee, J. & Ahn, J. (2018). Aptasensors for pesticide detection. *Toxicol. Environ. Health Sci.*, **10**: 229–236.
- Selvolini, G., Ioana, B., Hosu, O., Cristea, C., Sandulescu, R. & Marrazza, G. (2018). DNA-based sensor for the detection of an organophosphorus pesticide: Profenofos. *Sensors*, **18**: 1–12.
- Sikora, T., Istamboulie, G., Jubete, E., Ochoteco, E., Marty, J. & Noguer, T. (2011). Highly sensitive detection of organophosphate insecticides using biosensors based on genetically engineered acetylcholinesterase and poly (3,4-Ethylenedioxythiophene). *J. Sens.*, **2011**: 1–7.
- Songa, E.A. & Okonkwo, J. O. (2016). Recent approaches to improving selectivity and sensitivity of enzyme-based biosensors for organophosphorus pesticides: A review. *Talanta*, **155**: 289–304.
- Sulaiman, I.S.C., Chieng, B.W., Osman, M.J., Ong, K.K., Rashid, J.I.A., Yunus, W.M.Z.W. & Noor, S. A. M. (2020). A review on colorimetric methods for determination of organophosphate pesticides using gold and silver nanoparticles. *Microchim. Acta*, **187**: 1–22.
- Tang, J., Zhang, M., Cheng, G., Li, A. & Lu, Y. (2008). Development of IC-ELISA for detection of organophosphorus pesticides in water. *J. Environ. Sci. Health B*, **43**: 707–712.

- Tite, T., Ollier, N., Sow, M. C., Vocanson, F. & Goutaland, F. (2017). Ag nanoparticles in soda-lime glass grown by continuous wave laser irradiation as an efficient SERS platform for pesticides detection. *Sens. Actuators B Chem.*, **242**: 127–131.
- Tsai, C.J., Maizel, J.V. & Nussinov, R. (2002). The hydrophobic effect: A new insight from cold denaturation and a two-state water structure. *Crit. Rev. Biochem. Mol. Biol.*, **37**: 55–69.
- Umar, A. M. & Aisami, A. (2020). Acetylcholinesterase enzyme (AChE) as a biosensor and biomarker for pesticides : A mini review. *Bull. Environ. Sci. Sustain. Manage.*, **4**: 7–12.
- Wang, L., Liu, X., Zhang, Q., Zhang, C., Liu, Y., Tu, K. & Tu, J. (2012). Selection of DNA aptamers that bind to four organophosphorus pesticides. *Biotechnol. Lett.*, **34**: 869–874.
- Wang, P., Wan, Y., Ali, A., Deng, S., Su, Y., Fan, C. & Yang, S. (2016). Aptamer-wrapped gold nanoparticles for the colorimetric detection of omethoate. *Sci. China Chem.*, **59**: 237–242.
- Wei, H., Li, B., Li, J., Wang, E. & Dong, S. (2007). Simple and sensitive aptamer-based colorimetric sensing of protein using unmodified gold nanoparticle probes. *Chem. Comm.*, **36**: 3735–3737.
- WHO (World Health Organization) (2019). The WHO Recommended Classification of Pesticides by Hazard. World Health Organization (WHO), Geneva, Switzerland
- Xi, H., Cui, M., Li, W. & Chen, Z. (2017). Colorimetric detection of Ag<sup>+</sup> based on C–Ag<sup>+</sup>–C binding as a bridge between gold nanoparticles. *Sens. Actuators B Chem.*, **250**: 641–646.
- Xie, J., Li, L., Khan, I.M., Wang, Z. & Ma, X. (2020). Flexible paper-based SERS substrate strategy for rapid detection of methyl parathion on the surface of fruit. *Spectrochim. Acta A Mol. Biomol. Spectrosc.*, **231**: 1–8.
- Xu, Q., Guo, X., Xu, L., Ying, Y., Wu, Y., Wen, Y. & Yang, H. (2017). Template-free synthesis of SERS-active gold nanopopcorn for rapid detection of chlorpyrifos residues. *Sens. Actuators B Chem.*, **241**: 1008–1013.
- Yaseen, T., Pu, H. & Sun, D. W. (2019). Fabrication of silver-coated gold nanoparticles to simultaneously detect multi-class insecticide residues in peach with SERS technique. *Talanta*, **196**: 537–545.
- Yeh, Y.-C., Creran, B. & Rotello, V. M. (2014). Gold nanoparticles: Preparation, properties, and applications in bionanotechnology. *Nanoscale*, **4**: 1871–1880.
- Yu, L., & Li, N. (2019). Noble metal nanoparticles-based colorimetric biosensor for visual quantification : A mini review. *Chemosensors*, **7**: 1–23.
- Yue, G., Su, S., Li, N., Shuai, M., Lai, X., Astruc, D. & Zhao, P. (2016). Gold nanoparticles as sensors in the colorimetric and fluorescence detection of chemical warfare agents. *Coord. Chem. Rev.*, **311**: 75–84.
- Zhengbo, C., Junxia, G., He, M., Tong, Z. & Xiaoxiao, L. (2014). A simple colorimetric sensor for potassium ion based on DNA G-quadruplex conformation and salt-induced gold nanoparticles aggregation. *Anal. Methods*, **6**: 8018–8021.
- Zhou, Q., Wang, B., Li, J., Jin, Z., Li, H. & Chen, J. (2018). Improved analytical performance of photoionization ion mobility spectrometry for the rapid detection of organophosphorus pesticides using: K<sup>0</sup> patterns with multiple reactant ions. *RSC Adv.*, **8**: 18067–18073.
- Zhu, Z., Ravelet, C., Perrier, S., Perigaud, C. & Peyrin, E. (2010). Multiplexed detection of small analytes by structure-switching aptamer-based capillary electrophoresis. *Anal. Chem.*, **82**: 4613–4620.

# ANTIMICROBIAL PROPERTIES FOR TEXTILES IN MILITARY AND DEFENCE APPLICATIONS

Ahmad Razi Mohamed Yunus<sup>1</sup>, Izzat Farhan Shahrudin<sup>2</sup>, Aznida Yusuf<sup>1</sup> & Nik Nur Ilyani Mohd Nazri<sup>1</sup>

<sup>1</sup>Science and Technology Research Institute for Defence (STRIDE), Ministry of Defence, Malaysia

<sup>2</sup>Faculty of Biotechnology and Biomolecular Sciences, University Putra Malaysia (UPM), Malaysia

## ABSTRACT

*Textiles have been utilised in military and defence applications for various purposes, including clothing, gear and equipment. In recent years, there has been growing interest in developing textiles with antimicrobial properties to mitigate the spread of infectious diseases and protect military personnel from harmful pathogens. This paper reviews the current research on antimicrobial textiles, including types of antimicrobial agents used, methods for incorporating antimicrobial properties into textiles, and performance evaluation of antimicrobial textiles. This paper also discusses on the potential benefits and challenges associated with the use of antimicrobial textiles in military settings and identifies future research directions to further enhance antimicrobial properties of textiles for military and defence applications.*

**Keywords:** *Antimicrobial textiles; military and defence applications; antimicrobial agents; incorporation techniques; performance evaluation.*

## 1. INTRODUCTION

Textiles, including clothing, gear and equipment play a critical role in military and defence operations. Textiles are in close contact with the skin and can serve as potential reservoirs for microorganisms, such as bacteria, viruses and fungi, leading to the transmission of infectious diseases. Therefore, there has been a growing interest in developing textiles with antimicrobial properties to reduce the risk of infection transmission and protect military personnel from harmful pathogens (West *et al.*, 2019; Gupta *et al.*, 2022).

In recent years, significant progress has been made in the development of antimicrobial textiles for military and defence applications. This paper aims to provide an overview of the current research on antimicrobial textiles, including the types of antimicrobial agents used, methods of incorporating antimicrobial properties into textiles, and performance evaluation of antimicrobial textiles. The paper also discusses on the potential benefits and challenges associated with the use of antimicrobial textiles in military settings and identifies future research directions to further enhance antimicrobial properties of textiles for military and defence applications.

## 2. DEVELOPMENT OF ANTIMICROBIAL PROPERTIES ON TEXTILE

Throughout ancient history, people have been applying natural substances with antimicrobial properties to textiles and fabrics. This practice can be traced back to the time of the Egyptians, who would use spices and herbal coatings on cloth materials to preserve mummy wrappings (Gulati *et al.*, 2021). There was some evidence of ancient cultures utilising natural antimicrobial agents, such as garlic and onions, to treat wounds and prevent infections (Mahomoodally *et al.*, 2018). The idea of antimicrobial textiles in military context

emerged when researchers began exploring the use of silver and other metals as antimicrobial agents (Clement & Jarrett, 1994). However, the modern concept of antimicrobial textiles began to take shape in the 20<sup>th</sup> century with the discovery of the germ theory of disease and the role of microbes in infection (Gulati *et al.*, 2021).

Before the invention of antimicrobial textiles, armies faced significant problems with the spread of infections and diseases in military settings. Fungal infections such as athlete's foot and jock itch have been prevalent among military personnel for many years. Their feet were particularly susceptible to fungal growth, and the majority of cases were brought on by three distinct species: *Epidermophyton floccosum*, *Trichophyton mentagrophytes* and *Trichophyton rubrum* (Spitz *et al.*, 2016). Wounds and injuries sustained during battles were often susceptible to bacterial infections and soldiers living in close quarters were at risk of contracting contagious illnesses (Biselli *et al.*, 2022).

Antimicrobial textiles have become increasingly popular in military and defence settings in recent years due to advancements in technology and a greater understanding of the role of microorganisms in infections. These textiles offer numerous advantages including reducing the risk of infection transmission, improving hygiene, as well as promoting overall health and safety. In addition, antimicrobial textiles can also improve the durability of military equipment, such as uniforms and tents, by preventing the growth of microorganisms that can weaken and damage materials (Liyange *et al.*, 2021).

The development of antimicrobial properties in textiles for military and defence applications has undergone significant changes since World War I. During this war, there was limited comprehension regarding the function of microorganisms in diseases given that salvarsan synthesised by Ehrlich in 1910 marked the first antimicrobial substance in existence (Saga & Yamaguchi, 2009). In the years following the war, research into the role of microbes in infections increased leading to the development of antimicrobial textiles. Initially, these textiles were treated with chemicals such as mercury, silver and copper, which were effective at killing bacteria and preventing the spread of infections. The treatment of textiles with chemicals in the years following World War I had the purpose of preventing the spread of infections and improving the overall hygiene of textile materials. The function of these chemicals was to kill bacteria and prevent the growth of microorganisms on textile surfaces (Nadem *et al.*, 2020).

The advantages of chemical treatment of textiles included improved hygiene and reduced risk of infection transmission. It also allowed for the production of textiles that were more durable and long-lasting as the chemical treatments helped to protect the fibres from damage. However, there were also disadvantages to chemical treatment of textiles. Some of the chemicals used, such as mercury and arsenic, were toxic and posed health risks to workers involved in the production of these textiles. In addition, these chemicals were not always effective at killing all types of microorganisms and some strains developed resistance over time (Udhayamarthandan & Srinivasan, 2019).

Furthermore, the use of toxic chemicals in textile production led to environmental contamination as these chemicals were often released into the air and waterways during manufacturing and disposal. Despite these disadvantages, chemical treatment of textiles played an important role in improving hygiene and preventing the spread of infections during the years following World War I. However, as technology and research have advanced, there has been a shift towards the development of safer and more sustainable treatments, such as natural antimicrobial agents and non-toxic chemical treatments, that provide similar benefits without the negative environmental and health impacts (Dhir, 2021).

During World War II, the demand for antimicrobial textiles increased and researchers focused on developing more effective and safer treatments. In the 1950s, the development of synthetic antimicrobial agents such as triclosan and quaternary ammonium compounds allowed for the production of textiles that were both effective and safe for humans (Fouda, 2012).

In recent years, there has been increasing emphasis on developing antimicrobial textiles that are environmentally friendly and sustainable. This has led to the development of textiles treated with natural antimicrobial agents such as chitosan, which is derived from shellfish and is biodegradable. In addition to advancements in antimicrobial textiles, there have also been significant advancements in the production and use of protective gear in military and defence. For example, modern military uniforms are designed to be lightweight, breathable and resistant to chemical agents (Ren & Liang, 2016).

### **3. TYPES OF ANTIMICROBIAL AGENTS USED IN TEXTILES**

#### **3.1 Chemical Agents**

Chemical agents are synthetic antimicrobial compounds that are chemically incorporated into textiles during the manufacturing process. Examples of chemical agents commonly used in antimicrobial textiles include quaternary ammonium compounds (QAC) and triclosan. QACs are cationic surfactants that can disrupt the cell membranes of microorganisms leading to their death. These substances exhibit effectiveness against various microorganisms including both Gram positive bacteria such as *Staphylococcus aureus* and *Streptococcus pneumoniae*, as well as Gram negative bacteria such as *Escherichia coli* and *Pseudomonas aeruginosa* (Morais *et al.*, 2016). Furthermore, QACs have shown promise in combating specific categories of viruses. Some enveloped viruses, such as influenza viruses and coronaviruses, have lipid membranes that can be disrupted by QACs. The interaction between the positively charged QACs and the viral envelope can interfere with the viral structure rendering them unable to infect host cells (Lin *et al.*, 2021). Asri *et al.* (2013) suggested that immobilised QACs induce potent attractive forces between bacteria and the surface coated with QACs resulting in cell death.

Triclosan is a widely used antimicrobial agent that inhibits the growth of bacteria by disrupting their cellular membranes. The mechanism of action of triclosan involves its interaction with bacterial cell membranes. Triclosan is attracted to the phospholipid bilayer of bacterial cell membranes and infiltrates the membrane structure leading to leakage of cellular contents, thus inhibiting bacterial growth (Goldade & Vinidiktova, 2017). By utilising chemical agents for textiles in the military, they can have long lasting effectiveness, provide durable antimicrobial protection, and be engineered to have specific properties, such as being water, heat and ultraviolet (UV) resistant (Bhuiyan *et al.*, 2019).

#### **3.2 Natural Agents**

Natural agents are derived from natural sources, such as plants, animals and microorganisms, making them generally safe and environmentally friendly. They have been used for centuries in textiles due to their inherent antimicrobial properties. Some examples of natural antimicrobial agents used in military textiles are chitosan, tea tree oils and plant extracts (Ye *et al.*, 2020).

Chitosan is a biopolymer derived from chitin, which is a natural polymer abundantly found in the exoskeletons of crustaceans such as shrimp, crab and lobster, has gained considerable attention for its antimicrobial properties. Chitosan possesses a unique chemical structure that allows it to exhibit potent antimicrobial effects against a wide range of microorganisms including bacteria, fungi and viruses (Ye *et al.*, 2006). The antimicrobial activity of chitosan is attributed to its ability to disrupt the cell membranes of microorganisms. The positively charged amino groups present in chitosan interact with the negatively charged components of microbial cell membranes leading to membrane destabilisation and subsequent leakage of intracellular components. This disruption of cell membrane integrity ultimately results in cell death (Islam & Butola, 2019).

Tea tree oil is extracted from the leaves of tea trees (*Melaleuca alternifolia*). They have antibacterial, antifungal and antiviral properties that have been used in military textiles to inhibit the growth of microorganisms. Plant extracts contain bioactive compounds that possess antimicrobial activity against various microorganisms (Brun *et al.*, 2019). Tawiah *et al.* (2016) found that the final products extracted from the leaves of twinberry honeysuckle (*Lonicera involucrata*), vinyl hexylether and 2-methylnonane exhibited antimicrobial activity against *E. coli*. Despite their advantages, natural agents may have limited durability and effectiveness, and also require frequent reapplication or replacement. They can also be sensitive to environmental conditions such as pH, temperature and humidity, which can affect their performance. In addition, they may vary in effectiveness depending on the source and concentration of the natural antimicrobial agent (Higazy *et al.*, 2010).

### 3.3 Nanoagents

Nanoagents are a type of antimicrobial agent that is engineered at the nanoscale, typically ranging from 1 to 100 nm in size. Due to their small size, nanoagents have large surface area that allows them to have unique properties and interactions with microorganisms, making them highly effective in inhibiting their growth (Zhang *et al.*, 2022). There are several different types of nanoagents that have been utilised in military textiles, including silver, zinc oxide and copper nanoparticles. Silver nanoparticles are one of the most commonly used nanoagents in antimicrobial textiles, as it is known for its potent biocidal effects against numerous pathogenic bacteria (Shahidi *et al.*, 2010). It operates by releasing silver ions that can penetrate the cell walls of microorganisms (Sofi *et al.*, 2022). These nanoparticles possess the ability to hinder the early phases of virus attachment by altering the protein structures (Rahman *et al.*, 2021).

Zinc oxide nanoparticles are another type of nanoagent that has been used for antimicrobial textiles. It works by generating reactive oxygen species (ROS) upon exposure to moisture or UV light, which can damage cell membranes and metabolic processes of microorganisms (Dastjerdi & Montazer, 2010). In recent times, zinc oxide has garnered significant attention due to its immense potential in various fields, such as cosmetics and textiles. It has been investigated as an effective antimicrobial agent to provide a potential solution for combating microbial infections (Nourbakhsh *et al.*, 2016).

Copper nanoparticles have also shown promise in antimicrobial textiles. It operates by releasing copper ions that can disrupt cell membranes, leading to their inhibition. Nanocellulose is also an example of nanoagent that is utilised nowadays for military textiles (Ma *et al.*, 2022). According to Ahmed *et al.* (2021), carbon quantum dots (CQDs) generate oxygen that serves principally to trigger microbiological cell demise.

Although these nanoagents have higher efficiency against microbes, the release of ions into the environment and their effect on aquatic organisms is of concern. These nanoparticles require careful handling and application due to their potential toxicity to living things, including humans, animals and plants (Ozdal & Gurkok, 2022).

## 4. METHODS FOR INCORPORATING ANTIMICROBIAL PROPERTIES INTO TEXTILES

There are various techniques for incorporating antimicrobial properties into textiles depending on the type of antimicrobial agent used and the desired performance of the textile. Some common methods include coating, impregnation, in situ synthesis and blending. Coating involves the application of the antimicrobial agent onto the textile's surface via diverse techniques, such as dipping, spraying and padding. Through this process, a protective layer is formed on the textile, thereby impeding the growth of microorganisms (Gulati *et al.*, 2021).



On the other hand, impregnation occurs when the antimicrobial agent is infused into the fibres or yarns of the textile during the manufacturing phase. This approach ensures a homogeneous distribution of the antimicrobial agent throughout the textile leading to sustained antimicrobial activity (Koncar, 2016). In the case of in situ synthesis, nanoscale antimicrobial agents such as nanoparticles are synthesised directly onto the surface of the textile using chemical or physical methods. This technique enables precise control over the size, shape and distribution of the nanoparticles, enhancing the antimicrobial efficacy of the textile (Jadoun *et al.*, 2020).

Lastly, blending represents another viable method whereby the antimicrobial agent is combined with the textile fibres or yarns during the manufacturing process. This technique facilitates convenient customisation of antimicrobial properties by adjusting the concentration of the antimicrobial agent within the textile (Balouiri *et al.*, 2016).

## **5. PERFORMANCE EVALUATION OF ANTIMICROBIAL TEXTILES**

The performance of antimicrobial textiles in military and defence applications is typically evaluated through various tests and assessments to determine their effectiveness in inhibiting the growth of microorganisms. The antimicrobial activity of the textile against specific microorganisms is assessed through standard antimicrobial efficacy test methods. These tests measure the reduction in the number of microorganisms on the textile surface after a specified contact time (Gulati *et al.*, 2021).

The durability of the antimicrobial properties of the textile is also evaluated through repeated washing or abrasion tests to determine the effectiveness of the antimicrobial agent over time and under different conditions (Kowal *et al.*, 2016). Furthermore, toxicity testing is crucial for optimal performance. The toxicity of the antimicrobial agent used in the textile is assessed to ensure that it does not pose any health risks to the wearer or the environment. Functional performance testing is necessary to evaluate the performance of the textile in terms of breathability, water resistance and comfort to ensure that the antimicrobial treatment does not compromise its overall performance (Liyanage *et al.*, 2021).

## **6. POTENTIAL BENEFITS AND CHALLENGES OF ANTIMICROBIAL TEXTILES IN MILITARY AND DEFENCE APPLICATIONS**

The use of antimicrobial textiles in military and defence applications has the potential to offer significant benefits. One of the most crucial advantages is the reduction of infectious disease transmission. By effectively impeding the growth of microorganisms, antimicrobial textiles can aid in diminishing the spread of infectious diseases among military personnel, who often find themselves in close quarters or high-risk environments (Seelarbokus, 2021). Additionally, antimicrobial textiles can enhance hygiene and safety standards in military settings by preventing the growth of microorganisms on clothing, gear and equipment. This can lead to cost savings by extending the lifespan of textiles and reducing the need for frequent replacements. Moreover, antimicrobial treatments can help reduce odour on textiles, resulting in enhanced comfort for military personnel during prolonged deployments or missions (Saha *et al.*, 2021).

Nonetheless, the adoption of antimicrobial textiles in military and defence settings can also present several challenges that need to be addressed. One of the main challenges is selecting the appropriate antimicrobial agents to use in textiles. This requires careful consideration of factors such as durability, safety and environmental impact. It is crucial to select antimicrobial agents that are effective against microorganisms, durable under harsh conditions, safe for human use and environmentally friendly. Another challenge is complying with regulatory requirements. The use of antimicrobial textiles in military and defence

applications may be subject to various regulations, such as testing, labelling and registration. Compliance with these regulations can add complexity and cost to the development and implementation of antimicrobial textiles in military and defence settings (Madden *et al.*, 2018). Furthermore, prolonged use of antimicrobial textiles may potentially lead to the development of microbial resistance to antimicrobial agents, which reduces their effectiveness over time. Effective monitoring and management of microbial resistance are essential to ensuring the continued efficacy of antimicrobial textiles in military and defence applications. Finally, there are potential environmental concerns associated with the use of antimicrobial agents in textiles, such as the impact on aquatic ecosystems and potential toxicity to non-target organisms. Proper disposal and management of antimicrobial textiles are crucial to minimise environmental impact (Gulati *et al.*, 2021).

## **7. COUNTRIES THAT HAVE DEVELOPED ANTIMICROBIAL PROPERTIES FOR TEXTILES IN MILITARY AND DEFENCE APPLICATIONS**

### **7.1 United States of America**

The US was one of the first countries to develop antimicrobial textiles in the modern era. In 1914, Dr. Frederick J. Pierce developed a process to impregnate cotton with copper compounds that had antimicrobial properties (Hill & Brophy, 1961). The US military used this material for bandages, uniforms and other textile products during World War I. During World War II, the US military continued to develop antimicrobial textiles to protect soldiers from infections. In 1941, the US government established the Research and Development Board to coordinate the development of new technologies for military use. One of the board's main goals was to develop improved materials for military uniforms and other textile products. In 1943, the US Army Quartermaster Corps developed a new type of uniform that was treated with a silver based antimicrobial agent. The agent was designed to prevent the growth of bacteria and other microorganisms on the uniform. The new uniforms were used by soldiers in the Pacific region where bacterial infections were common (Galster & Nosch, 2010).

The revelation that treating body armour with shear thickening fluid could significantly improve its impact resistance was made by a team of US researchers from the University of Delaware and the Army Research Laboratory in 2003 (Mondal *et al.*, 2023). Since 2005, the Natick Soldier Research, Development and Engineering Center (NSRDEC) and Microban Products Company have worked together to incorporate antimicrobial properties in soldier clothings and manufactured products, such as army battle uniforms, green boot footwear and tan t-shirts (Spitz & Arcidiacono, 2016). According to Arcidiacono (2015), NSRDEC also examined the possible risks to health associated with antimicrobial treatments used in textile products, including socks, t-shirts and sleeping bag liners.

### **7.2 United Kingdom**

The UK actively employed antimicrobial textiles in its military operations during the World Wars. For instance, during World War I, the UK developed antibacterial woollen textiles treated with chemicals, such as mercuric chloride and copper salts. These treated fabrics were used for military uniforms such as those worn by soldiers on the front lines. British forces deployed in Afghanistan and Iraq were provided with antimicrobial underwear as part of a new desert uniform made from synthetic fibres integrated with silver particles interlaced into the textile. This initiative was part of the British Ministry of Defence's efforts to equip soldiers with suitable attire to deter perspiration (The Age, 2005).

## 8. CONCLUSION

The study of antimicrobial properties in textiles for military and defence applications has significant impact on the development of new materials and technologies that can enhance the safety and effectiveness of military personnel in various contexts. Some of the key impacts and conclusions that can be drawn from this research include improved protection, enhanced durability, increased comfort and environmental concerns. Antimicrobial textiles can provide enhanced protection against a range of harmful pathogens. This can help reduce the risk of infection and illness among military personnel in a variety of settings. Antimicrobial textiles can also help increase the durability and lifespan of military clothing and equipment by preventing the growth of harmful microorganisms that can degrade materials over time. In addition to their protective properties, antimicrobial textiles can also help improve the comfort and wearability of military clothing by reducing odour and moisture build-up. While antimicrobial textiles can provide important benefits for military personnel, there are also potential environmental concerns associated with the use of these materials. Some antimicrobial agents may have negative impacts on ecosystems and wildlife if they are released into the environment.

While significant progress has been made in the development of antimicrobial textiles for military use, there is still a need for further research to optimise these technologies and address any potential safety or environmental concerns. Ongoing research is required to explore new antimicrobial agents and textile treatments that can provide effective protection against a broader range of pathogens while minimising any potential negative impacts on the environment. In addition, further studies are required to evaluate the long-term safety and effectiveness of these materials in real world military settings and identify any potential unintended consequences of their use. Finally, continued efforts are needed to raise awareness among military personnel about the benefits and limitations of antimicrobial textiles, as well as promote responsible use and disposal of these materials.

## REFERENCES

- Ahmed, H.B., Abualnaja, K.M., Ghareeb, R.Y., Ibrahim, A.A., Abdelsalam, N.R. & Emam, H.E. (2021). Technical textiles modified with immobilized carbon dots synthesized with infrared assistance. *J. Colloid Interf. Sci.*, **604**: 15–29.
- Arcidiacono, S. (2015). *Antimicrobial Textile Treatments – A Literature Review of Risks, Benefits And Applications*. Natick Soldier Research, Development and Engineering Center (NSRDEC), Massachusetts, US.
- Asri, L.A., Crismaru, R.G., M., Roest, S., Chen, Y., Ivashenko, O., Rudolf, P., Tiller, J.C., van der Mei, H.C. Loontjens, T.J. & Busscher, H.J. (2013). A shape-adaptive, antibacterial-coating of immobilized quaternary-ammonium compounds tethered on hyperbranched polyurea and its mechanism of action. *Adv. Func. Mater.*, **24**: 346–355.
- Balouiri, M., Sadiki, M. & Ibsouda, S. K. (2016). Methods for in vitro evaluating antimicrobial activity: A review. *J. Pharmaceut. Anal.*, **6**: 71–79.
- Biselli, R., Nisini, R., Lista, F., Autore, A., Lastilla, M., De Lorenzo, G., Peragallo, M. S., Stroffolini, T., & D’Amelio, R. (2022). A historical review of military medical strategies for fighting infectious diseases: From battlefields to global health. *Biomed.*, **10**: 2050.
- Bhuiyan, M.A.R., Wang, L., Shaid, A., Shanks, R.A. & Ding, J. (2019). Advances and applications of chemical protective clothing. *J. Ind. Tex.*, **49**: 97-138.
- Brun, P., Bernabe, G., Filippini, R. & Piovan, A. (2019). In vitro antimicrobial activities of commercially available tea tree (*Melaleuca alternifolia*) essential oils. *Curr. Microbiol.*, **76**: 108-116.
- Clement, J. L., & Jarrett, P. S. (1994). Antibacterial Silver. *Metal-Based Drug.*, **1**: 467–482.
- Dastjerdi, R., & Montazer, M. (2010). A review on the application of inorganic nano-structured materials in the modification of textiles: Focus on antimicrobial properties. *Colloid. Surface B*, **79**: 5–18.

- Dhir, Y. J. (2021). Hazards of fashion and textile waste. In Nayak, R. & Patnaik, A. (Eds.), *Waste Management in the Fashion and Textile Industries*. Elsevier, Amsterdam, Netherlands, pp. 31-58.
- Fouda G. (2012). Antibacterial modification of textiles using nanotechnology. In Bobbarala, V. (2012), *A Search for Antibacterial Agents*. InTech, London, U.K.
- Galster, K & Nosch, M.L. (2010). Textile history and the military: an introduction. *Text. His. Mil.*, **41**: 1-5.
- Goldade, V.A. & Vinidiktova, N.S. (2017). Antimicrobial fibers for textile clothing and medicine: Current State. *Theor. Appl. Sci.*, **47**: 178–194.
- Gulati, R., Sharma, S. & Sharma, R. (2021). Antimicrobial textile: recent developments and functional perspective. *Polym. Bull.*, **79**: 5747–5771.
- Gupta, A., Simkovich, A.J. & Hall, D. (2022). The march against onychomycosis: a systematic review of the sanitization methods for shoes, socks, and textiles. *J. Am. Podiat. Med. Assoc.*, **112**: 21-223
- Higazy, A., Hashem, M., Elshafei, A.M., Shaker, N., & Hady, M.A. (2010). Development of anti-microbial jute fabrics via in situ formation of cellulose–tannic acid–metal ion complex. *Carbohydr. Polym.*, **79**: 890–897.
- Hill, S. & Brophy, L.P. (1961). The chemical warfare service: From laboratory to field. *Mil. Aff.*, **25**: 160.
- Islam, S. & Butola, B. S. (2019). Recent advances in chitosan polysaccharide and its derivatives in antimicrobial modification of textile materials. *Int. J. Biol. Macromol.*, **121**: 905–912.
- Jadoun, S., Verma, A. & Arif, R. (2020). Modification of textiles via nanomaterials and their applications. In Shabbir, M., Ahmed, S. & Sheikh, J.N. (Eds.), *Frontiers of Textile Materials*. Wiley, New Jersey, U.S., pp 135–152.
- Koncar, V. (2016). *Smart Textiles and Their Applications*. Elsevier, Amsterdam, Netherlands.
- Kowal, K.N., Cronin, P.K., Bauer, J., Tiernan, P., Podbielska, H. & Tofail, S.A.M. (2016). Durability of antimicrobial textiles. In Tofail, S.A.M. & Bauer, J. (Eds.), *Electrically Active Materials for Medical Devices*. World Scientific, Singapore, pp. 333-347.
- Lin, L., Haiying, C., Abdel-Samie, M.A. & Abdulla, G. (2021). Common, existing and future applications of antimicrobial textile materials. In Mondah, M.I.H. (Eds.), *Antimicrobial Textiles from Natural Resources*. Elsevier, Amsterdam, Netherlands, pp. 119–163.
- Liyanage, S., Parajuli, P., Hossain, M.T., Chaudhari, H. & Abidi, N. (2021). Antimicrobials for protective clothing. In Mondah, M.I.H. (Eds.), *Antimicrobial Textiles from Natural Resources*. Elsevier, Amsterdam, Netherlands, pp. 349–376.
- Ma, X., Zhou, S., Xu, X. & Du, Q. (2022). Copper-containing nanoparticles: mechanism of antibacterial effect and application in dentistry- a narrative review. *Front. Surg.*, **9**: 905892
- Madden, J., Henrichs, L., Ervin, M.D., Lospinoso, J., Beachkofsky, T.M. & Hardin, C.A. (2018). Preliminary efficacy testing of the disinfectant MicrobeCare XLP for potential use in military operational environments. *Mil. Med.*, **183**: 348–353.
- Mahomoodally, F., Ramcharun, S. & Zengin, G. (2018). Onion and garlic extracts potentiate the efficacy of conventional antibiotics against standard and clinical bacterial isolates. *Curr. Top. Med. Chem.*, **18**:787–796.
- Mondal, S., Adak, B. & Mukhopadhyay, S. (2023). Functional and smart textiles for military and defence applications. Adak, B. & Mukhopadhyay, S. (Eds.), *Smart and Functional Textiles*. De Gruyter Berlin, Germany, pp. 397-468.
- Morais, D., Guedes, R. & Lopes, M. (2016). Antimicrobial approaches for textiles: From research to market. *Mater.*, **9**: 498.
- Nadem, S.F., Gohar, U.F., Tahir, S.F., Mukhtar, H., Pornpukdeewattana, S., Nukthamna, P., Ali, A.M.M., Bavisetty, S.C.B. & Massa, S. (2020). Antimicrobial resistance: more than 70 years of war between humans and bacteria. *Crit. Rev. Microbiol.*, **46**: 578-599.
- Nourbakhsh, S., Montazer, M. & Khandaghabadi, Z. (2016). Zinc oxide nanoparticles coating on polyester fabric functionalized through alkali treatment. *J. Ind. Text.*, **47**: 1006–1023.
- Ozdam, M. & Gurkok, S. (2022). Recent advances in nanoparticles as antibacterial agents. *ADMET DMPK*, **10**: 115-129.

- Rahman, M.A., Saha J. & Mondal M.I.H. (2021). Silver nano materials coated textiles for antiviral protection. *Inte. Conf. Comp. Comm. Chem. Mater. Electr. Eng.*, 26-27 December 2021, Rajshahi, Bangladesh.
- Ren, X. & Liang, J. (2016). Smart anti-microbial composite coatings for textiles and plastics. In Montemor, M.F. (Ed.), *Smart Composite Coatings and Membranes*. Elsevier, Amsterdam, Netherlands, pp. 235–259.
- Saga, T. & Yamaguchi, K. (2009). History of antimicrobial agents and resistant bacteria. *Jpn. Med. Assoc. J.*, **52**: 103-108.
- Saha, N., Saha, N., Saha, T. & Saha, P. (2021). Antimicrobial textile materials: their healthcare benefits and management. In Mondah, M.I.H. (Eds.), *Antimicrobial Textiles from Natural Resources*. Elsevier, Amsterdam, Netherlands, pp. 377-396.
- Seelarbokus, C. B. (2021). The military and the environment: The neglected core barrier. In Seelarbokus, C.B. (Ed.) *International Environmental Cooperation and the Global Sustainability Capital Framework*, Elsevier, Amsterdam, Netherlands, pp. 349–434.
- Shahidi, S., Rashidi, A., Ghoranneviss, M., Anvari, A., Rahimi, M. K., Bameni Moghaddam, M. & Wiener, J. (2010). Investigation of metal absorption and antibacterial activity on cotton fabric modified by low temperature plasma. *Cellulose*, **17**: 627–634.
- Sofi, M.S., Sunitha, S., Sofi, M.A., Pasha, S.K.K. & Choi, D. (2022). An overview of antimicrobial and anticancer potential of silver nanoparticles. *J. King Saud Univ. Sci.*, **34**: 101791
- Spitz, M.G. & Arcidiacono, S. (2016). *Defining Antimicrobial Textile Requirements for Military Applications - A Gap Analysis*. U.S. Army Natick Soldier Center, Massachusetts, U.S.
- Spitz, M.G., Johnson, W., Leshner, L.L. & Arcidiacono, S. (2016). Soldier hygiene issues and use of antimicrobial textiles in the military. *AATCC J. Res.*, **3**: 27–37.
- Tawiah, B., Badoe, W. & Fu, S. (2016). Advances in the development of antimicrobial agents for textiles: The Quest for natural products. review. *Fiber Text. East. Eur.*, **24**: 136–149.
- The Age (2005). *British Soldiers to Get Germ-Fighting Underwear*. Available online at: <https://www.theage.com.au/world/british-soldiers-to-get-germ-fighting-underwear-20050819-ge0pyw.html> (Last access date: 26 July 2023).
- Udhayamarthandan, S. & Srinivasan, J. (2019). Integrated enzymatic and chemical treatment for single-stage preparation of cotton fabrics. *Text. Res. J.*, **89**: 3937–3948.
- West, G.F., Resendiz, M., Lustik, M.B., & Nahid, A. (2019). Bacterial contamination of military and civilian uniforms in an emergency department. *J. Emergen. Nur.*, **45**: 169-177.
- Ye, L., Zhang, J., Xiao, W. & Liu, S. (2020). Efficacy and mechanism of actions of natural antimicrobial drugs. *Pharmacol. Therapeut.*, **216**: 107671.
- Ye, W., Xin, J.H., Li, P., Lee, K.L.D. & Kwong, T.L. (2006). Durable antibacterial finish on cotton fabric by using chitosan-based polymeric core-shell particles. *J. Appl. Polym. Sci.*, **102**: 1787–1793.
- Zhang, L., Zhang, M., Mujumdar, A.S., Yu, D. & Wang, H. (2022). Potential nano bacteriostatic agents to be used in meat-based foods processing and storage: A critical review. *Trends Food Sci. Tech.*, **131**: 77–90.

## PHENOTYPIC AND MOLECULAR IDENTIFICATION OF TROPIC FUNGAL STRAINS ISOLATED FROM A LIGHT OBSERVATION HELICOPTER

Siti Aminah Hassan<sup>1</sup>, Wan Md Zin Wan Yunus<sup>2\*</sup>, Nik Noorul Shakira Mohamed Shakrin<sup>1,3</sup>, Nurnadia Andenan<sup>4</sup>, Khairunnajwa Md Said<sup>5</sup>, Hana Tashyreva<sup>1</sup>, Mohd Haniff Sofian<sup>6</sup>, Nur Shazwani Abdul Latif<sup>1</sup> & Hidayati Hamdan<sup>7</sup>

<sup>1</sup>Centre for Tropicalisation (CENTROP), National Defence University of Malaysia (UPNM), Malaysia

<sup>2</sup>Faculty of Defence Science and Technology, National Defence University of Malaysia (UPNM), Malaysia

<sup>3</sup>Faculty of Medicine and Defence Health, National Defence University of Malaysia (UPNM), Malaysia

<sup>4</sup>Centre for Research and Innovative Management, National Defence University of Malaysia (UPNM), Malaysia

<sup>5</sup>Science and Technology Research Institute for Defence (STRIDE), Ministry of Defence, Malaysia.

<sup>6</sup>Faculty of Defence Studies and Management, National Defence University of Malaysia (UPNM), Malaysia

<sup>7</sup>Centre for Defence Foundation Studies, National Defence University of Malaysia (UPNM), Malaysia

\*Email: wanmdzin@upnm.edu.my

### ABSTRACT

Fungi are ubiquitous in the environment and can be found in almost all the interiors and surfaces of a helicopter. They are responsible for the deterioration of materials such as polymers, glass and composites. Identification of fungal contaminants is crucial to avoid human health hazards and technical problems on helicopters and other military transports. This study was conducted to phenotypically and genotypically identify fungi species that inhabit a light observation helicopter (LOH). Swabs of various surfaces and components of the LOH were performed. Fungi were isolated from the samples using a culture method. Morphological identification of the fungi isolates was obtained by direct macroscopic observation and microscopic examination. In addition, molecular identification methods were utilised by targeting the internal transcribed spacer (ITS) region of ribosomal DNA (rDNA). *Cladosporium cladosporioides*, *Penicillium oxalicum*, *Aspergillus aculeatus*, *Aspergillus ochraceus*, *Nigrospora sphaerica*, *Arthrimum phaeospermum*, *Phoma herbarum*, *Trichoderma asperellum*, *Lasiodiplodia theobromae*, and *Curvularia lunata* were dominantly isolated from the various surfaces and components of the LOH. Future studies on possible metabolite compounds, including mycotoxins and organic acids, produced by each of these fungi, should be carried out to further understand the tropical fungal strains, particularly from LOH.

**Keywords:** *Fungi; light observation helicopter (LOH); tropical; molecular identification; internal transcribed spacer (ITS).*

### 1. INTRODUCTION

Fungi are dominant ecological participants in the forest ecosystems, which play a major role in recycling organic matter and channelling nutrients across trophic levels (Adnan *et al.*, 2022). In the region of South-East Asia, fungi play a major role in deteriorating equipment, fuel, guns, gunpowder and also clothes that are manufactured from natural and synthetic textiles (Upsher & Upsher, 1995). Over 200 deteriorating species of microscopic fungi were found on these damaged

materials. The most frequently isolated microfungi from deteriorated surfaces are affiliated with a few genera, including *Penicillium*, *Cladosporium*, *Aspergillus*, *Trichoderma*, and *Mucor*, with variation in taxonomic diversity depending on the type of damaged material (Lacey 1980; Upsher & Upsher, 1995; Oetari *et al.*, 2016). However, current molecular studies have suggested that the structure of tropical fungal communities can be much more diverse and complicated (Izuno *et al.*, 2016). Lopez-Gomez and Perez-Rivero (2019) also found that the high adaptability of *Aspergillus* allows it to survive within a broad range of environmental conditions.

There are at least 20 fungal genera detected on the surface of nylon and polyester textiles. Other studies of tropical environments have reported the presence of additional genera, including *Actinonema*, *Alternaria*, *Cladosporium*, *Culvularia*, *Gliomastix*, *Paecilomyces* and a few others (Upsher & Upsher, 1995). Due to their enormous enzymatic activity and moisture exposures, they may cause damage to protective layers and seals that prevent the corrosion of electronic components and instruments. Wirth *et al.* (2019) also reported on severe deterioration of the samples coated with acrylic paint and provided the development of the *Aspergillus* and *Aureobasidium* fungi, whereas the sample favoured the growth of the *Penicillium* and *Aspergillus* genera (Wirth *et al.*, 2019). Thus, there is a possibility of short-circuiting of electronic components that may cause technical problems. Moreover, tropical environments can be a source of fungal strains with high deteriorating activity towards synthetic polymer material, which are normally resistant to fungal attack (Amorim *et al.*, 2005). The review by Magnin *et al.* (2020) indicated that polyurethanes (PU) materials have been used for long-term applications to resist environmental factors including microbial degradation.

Macro- and micromorphology methods allow for identification of fungi isolate until the genus level based on similarity of fungal filaments. However, their taxonomical position cannot be identified using conventional morphological methods. Precise identification of fungi species is necessary to understand the biodegradation and colonisation of military materials. Nowadays, molecular methods such as polymerase chain reaction (PCR) targeting the internal transcribed spacer (ITS) regions of ribosomal DNA (rDNA) have been used for fast, specific and sensitive identification of fungal isolates (Bruns *et al.*, 1991; Larena *et al.*, 1999; Anderson & Parkin, 2007).

This study focuses on the isolation and identification of fungi with potential deteriorating activity from the affected areas of a light observation helicopter (LOH) by employing morphological and molecular methods. The findings of this study will contribute to evaluating the deteriorating potential of the tropical environment in Malaysia, in particular the deteriorating effect of fungal strains on military materials, and testing the fungal resistance of polymers and coatings.

## **2. MATERIALS AND METHODS**

### **2.1 SAMPLE COLLECTION AND ISOLATION**

Samples were collected using sterile cotton swab at selected infected surfaces and components of a military A109-LOH after it was used in tropical environment. Fungal growth on surfaces and components of the LOH was detected by the presence of brown spots, visible moulds and corroded areas. The selected surfaces and components consisted of the inner surface of the tail-cone constitution, port-L shaped bladder compartment, cabin roof interior surface (passenger side), tail rotor mechanism rubber, electronic connector (front bonnet and inside tail cone) and high ignition box, as well as corroded metal components, which were drum brake cover, bearings and bolt joints (big and small). The samples were taken to the laboratory and kept at 4 °C. The samples were then cultured onto potato dextrose agar (PDA) and incubated in the dark for 2 to 7 days at 27 °C. A small portion of emerging colony was transferred into a new PDA aseptically and incubated as mentioned above repeatedly until yielding pure culture. The culture of each fungal strain was prepared in triplicate.

## 2.2 MACROSCOPIC AND MICROSCOPIC IDENTIFICATION

Each of the fungi sample was identified based on morphological characteristics macro- and microscopically. In the macroscopic examination, features such as colony colour, texture, shape and size were observed. The microscopic features of fungus, such as reproductive and hyphae structure, were examined under a light microscope for genus identification.

## 2.3 MOLECULAR IDENTIFICATION

All the fungi culture samples were cut in size of 5 mm from the PDA and placed into a 1.5 ml sterile microcentrifuge tube. The samples were sent to First BASE Laboratories (Selangor, Malaysia) for molecular identification. They were disrupted using the bead-beating method and genomic DNA was extracted according to the manufacturer's protocol for the DNA extraction kit. The fungal ITS gene was then amplified using a set of primers, namely primers ITS1 and ITS4. The total reaction volume of 20  $\mu$ l contained fungal purified genomic DNA, 1 pmol of each primer, deoxynucleotides triphosphates (dNTPs, 200  $\mu$ M each), 0.4 U Taq DNA polymerase, and reaction buffer. The PCR was performed as follows: 1 cycle (98 °C for 2 min) for initial denaturation; 25 cycles (98 °C for 15 sec; 60 °C for 30 sec; 72 °C for 30 sec) for annealing and extension, and 1 cycle (72 °C for 10 min) for the final extension of the amplified DNA. The PCR products were purified using standard molecular methods and directly sequenced using BigDye® Terminator v3.1 cycle sequencing kit (Applied Biosystems). The amino acid sequences data were analysed using the Basic Local Alignment Search Tool (BLAST) program (NIH, 2023).

## 3. RESULTS

Fungi were observed at all of the sampling sites for the A109-LOH. It is indicated by the presence of visible moulds, brown spots and corroded areas at the selected surfaces or components (Figure 1). Out of 30 swab sites, 10 different fungi species were isolated; *C. cladosporioides*, *P. oxalicum*, *A. aculeatus*, *A. ochraceus*, *N. sphaerica*, *A. pheospermum*, *P. herbarum*, *T. asperellum*, *L. theobromae* and *C. lunata*. Details of fungi growth based on the sites of sampling are shown in Table 1. Each of the surfaces and components of the LOH was found to be contaminated by at least one fungi strain. There were four fungi strains that were most frequently isolated from the selected sampling surfaces and components. The *C. cladosporioides* was the most frequently isolated fungus from the corroded components. The least frequent fungi to be found from the sampling surfaces and components were *A. aculeatus*, *A. ochraceus* and *L. theobromae*.

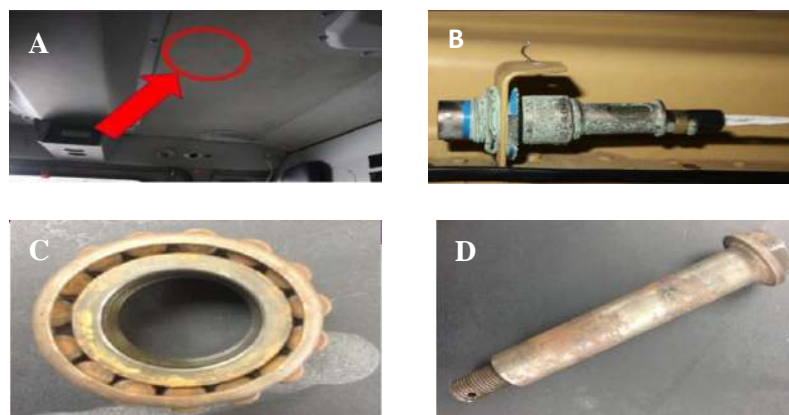




**Figure 1: Deteriorated surfaces and components of the A109-LOH: (A) Brown spots on the cockpit interior roof (B) Corroded electronic connector (C) Bearing (D) Bolt joint.**

**Table 1: Details of fungi growth based on the sampling sites.**

Surfaces and components	Fungi growth									
	<i>C. cladosporioides</i>	<i>P. oxalicum</i>	<i>A. aculaetus</i>	<i>A. ochraceus</i>	<i>N. sphearica</i>	<i>A. pheospermum</i>	<i>P. herbarum</i>	<i>T. asperellum</i>	<i>L. theobromae</i>	<i>C. Lunata</i>
Tail cone constitution inner surface							+			+
Port L-shaped bladder compartment surface	+	+			+	+		+	+	+
Cabin roof interior surface (passenger side)	+				+	+		+		
Tail rotor mechanism rubber	+				+	+		+		+
Electronic connector				+	+			+		
High ignition box		+	+			+		+		+
*Metal bar inside tail cone	+									
*Drum brake cover	+									
*Bearing	+							+		
*Bolt joint A					+	+				+
*Small bolt joint B						+				+

+ : Growth of fungi

\*: Corroded components

### 3.1 MORPHOLOGICAL ANALYSIS OF FUNGAL ISOLATES

Macroscopic analysis of the 10 isolated fungi from the LOH showed that there was variation in the colony front and reverse colours, texture, and shape (Figure 2). Microscopic observation of the fungi revealed different reproduction structures and conidiophores as shown in Figure 3.

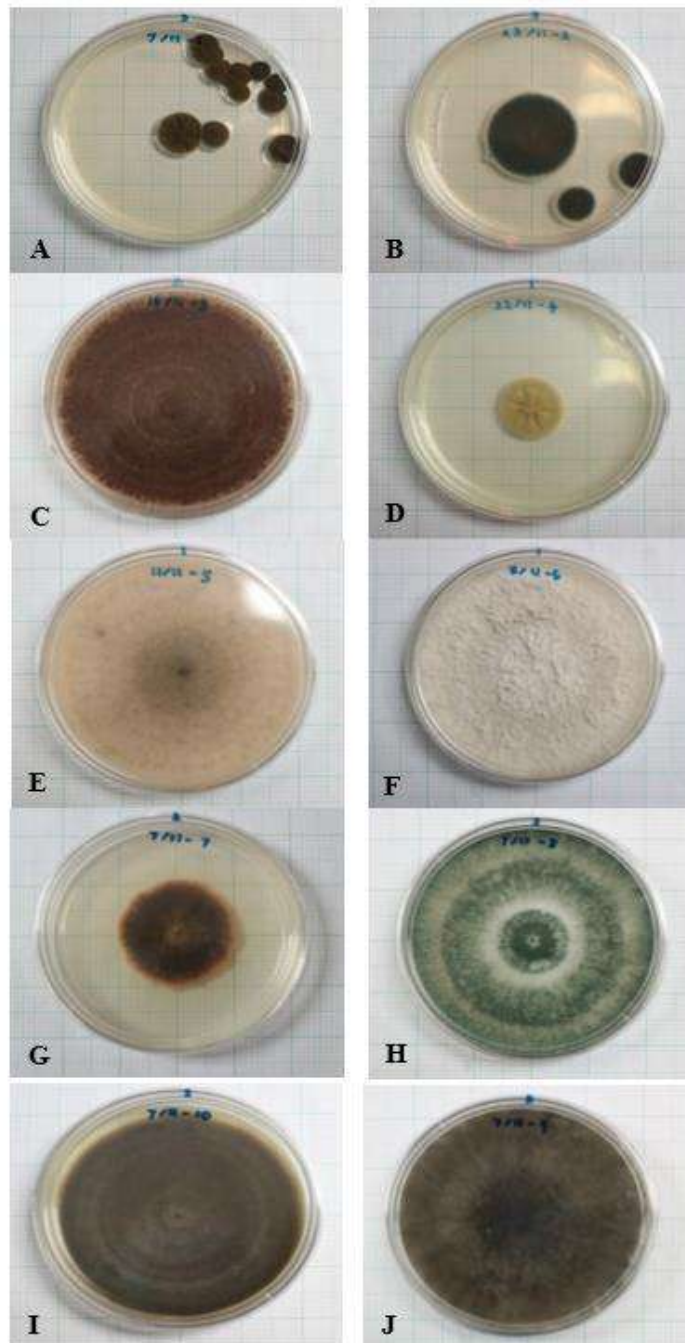


**Figure 2: Morphological characteristics of different fungi strains on PDA plates: (A) *Cladosporium* (B) *Penicillium* (C, D) *Aspergillus* (E) *Nigrospora* (F) *Arthrinium* (G) *Phoma* (H) *Trichoderma* (I) *Lasiodiplodia* (J) *Curvularia*.**

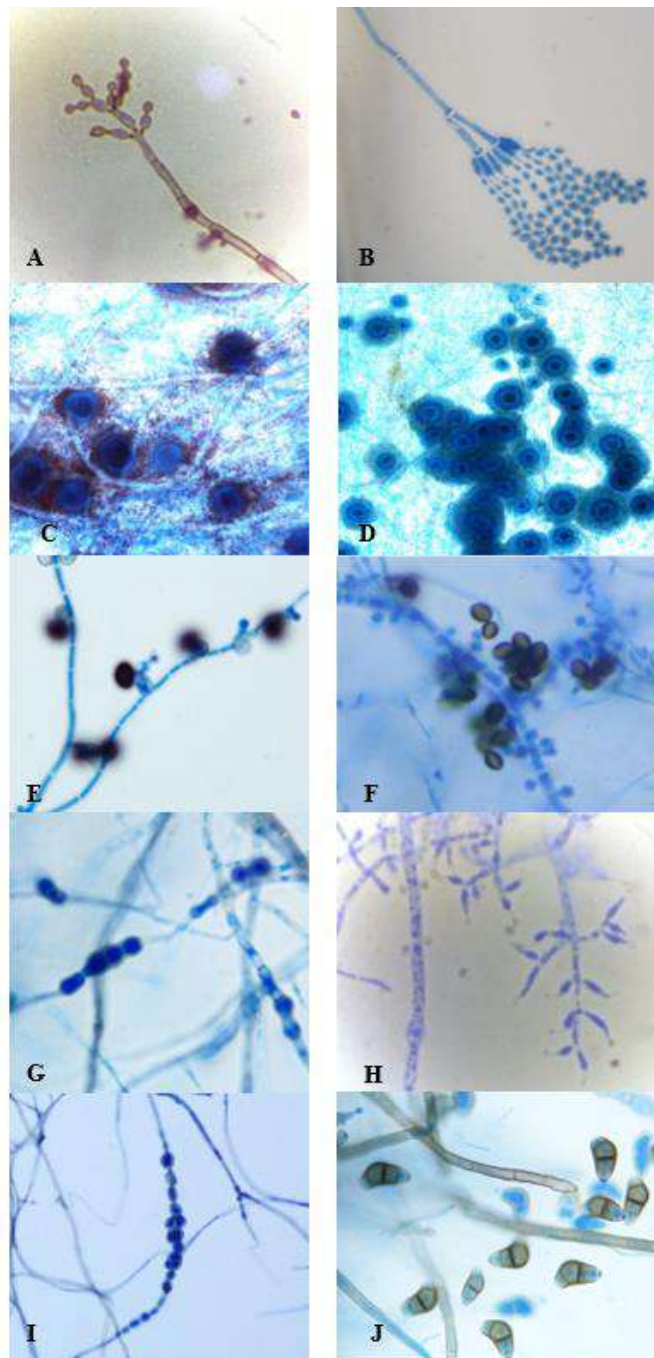


**Figure 3: Different reproduction structures of fungi isolated from the LOH: (A) *Cladosporium* (B) *Penicillium* (C,D) *Aspergillus* (E) *Nigrospora* (F) *Arthrinium* (G) *Phoma* (H) *Trichoderma* (I) *Lasiodiplodia* (J) *Curvularia***

### 3.2 MOLECULAR ANALYSIS

PCR amplification of the ITS region of the 10 fungal isolates obtained from the surfaces and components of the LOH yielded a single fragment of approximately 500 and 600 base pairs (bp) respectively. The BLAST analysis showed 100% similarities with *C. cladosporioides*, *P. oxalicum* and *A. aculeatus* for isolates F1 to F3 and with *P. herbarum*, *T. asperellum* and *L. theobromae* for isolates F7 to F9 respectively. As for the remaining isolates, the homology search hit 98% for

*Nigrospora sphaerica* (F5), and 99% for *Aspergillus ochraceus* (F4), *Arthrinium phaeospermum* (F6) and *Curvularia lunata* (F10). Fungal species names based on PCR regions of rDNA are listed in Table 2.

**Table 2: Identification of fungal isolates from the LOH based on ITS region by PCR.**

Isolate no.	BLAST result	Homology (%)	Accession number
F1	<i>Cladosporium cladosporioides</i>	100	KJ767065.1
F2	<i>Penicillium oxalicum</i>	100	KY352035.1
F3	<i>Aspergillus aculeatus</i>	100	JX501358.1
F4	<i>Aspergillus ochraceus</i>	99	KY378947.1
F5	<i>Nigrospora sphaerica</i>	98	KC505176.1
F6	<i>Arthrinium phaeospermum</i>	99	KT385742.1
F7	<i>Phoma herbarum</i>	100	KY780194.1
F8	<i>Trichoderma asperellum</i>	100	MG657259.1
F9	<i>Lasiodiplodia theobromae</i>	100	MF114110.1
F10	<i>Curvularia lunata</i>	99	KX013220.1

#### 4. DISCUSSION

Fungi are ubiquitous in the environment and can be found in almost all interiors and surfaces of a helicopter (Chawla *et al.*, 2014). They assimilate organic materials producing organic acids, including oxalic, lactic, acetic and citric, through metabolic processes (Little *et al.*, 1997a). Their deteriorating activity has been associated with the degradation of protective coatings, corrosion of underlying metal and high-cost maintenance (Little *et al.*, 1997b). Previous studies revealed the corrosion behaviour of anodised and non-anodised aluminium alloy 6061 in the presence of *Aspergillus niger* fungus using electrochemical noise, recurrence plots and electrochemical impedance spectroscopy techniques. Based on the findings, fungus generated organic acids causing microbially induced corrosion of the specimens (Jirón *et al.*, 2018).

Mycotoxin is one of the defence mechanisms produced by fungi as secondary metabolites that may also affect human and animal health depending on the amount of toxicity produced (Guo *et al.*, 2014; Ab Majid *et al.*, 2015). In most fungal studies, only macro- and micromorphology examinations were used to assist in the identification of isolates for up to the genus level based on the similarity of fungal filaments. However, with the various species isolated, their taxonomic position was difficult to be identified. On the other hand, molecular identification using ITS region is specific, sensitive and reliable. The PCR method was able to distinguish fungi with similar morphology characteristics until the species level. Therefore, the molecular identification method was utilised in the present study to identify ten isolates of fungi (*C. cladosporioides*, *P. oxalicum*, *A. aculeatus*, *A. ochraceus*, *N. sphaerica*, *A. phaeospermum*, *P. herbarum*, *T. asperellum*, *L. theobromae*, and *C. lunata*) using fungal universal primers ITS-1 and ITS-4.

In this study, based on the microscopic, macroscopic and molecular identification, the LOH surfaces and components were found to be predominantly affected by *C. cladosporioides*, *P. oxalicum*, *A. aculeatus*, *A. ochraceus*, *N. sphaerica*, *A. phaeospermum*, *P. herbarum*, *T. asperellum*, *L. theobromae* and *C. lunata*. The species of *Trichoderma*, *Aspergillus*, *Penicillium*, *Phoma*, *Cladosporium* (*Hormodendrum*), *Nigrospora*, *Arthrinium*, and *Curvularia*, which are commonly found on the interiors and surfaces of helicopters (Little *et al.*, 1997a; Chawla *et al.*, 2014) and aircrafts (McKernan *et al.*, 2007). However, the occurrence of *Lasiodiplodia sp.* on a helicopter or aircraft has never been reported. There is extensive evidence of fungal degradation of metal (Geesey & Cragnolino, 1995; Lavoie *et al.*, 1997; Little *et al.*, 1997a, b; Little & Ray, 2002; Gu *et al.*, 2011) and polymeric materials (Lavoie *et al.*, 1997; Little *et al.*, 1997a; Little & Ray, 2002). The production of organic acids is widely accepted as having a relevant role in direct material degradation despite the use of unapproved cleaning agents and procedures that may lead to this problem. A study by Belov *et al.* (2008) reported that fungal mycelia and fungal bodies played a fundamental role in the process of the material degradation mechanism. In addition, deterioration processes are also influenced by microorganisms attributed to their ability to form biofilms when in contact with surfaces in aqueous media (Morton & Surman, 1994; Gu, 2003; Beech *et al.*, 2005; Gu *et al.*, 2011).

Exposure to spores from fungi has been reported to affect human health (Samson, 2011; Houbraken *et al.*, 2014). While the health effects attained from spore exposure are primarily allergic responses, immunocompromised individuals may get infections and toxic responses from intensive exposure (Rogers, 2003). *Penicillium*, *Aspergillus*, and *Cladosporium* are the common species that have higher incidence of air contamination in tropical regions (Flannigan *et al.*, 2011, Dijksterhuis, 2011). Ahmad Razi *et al.* (2021) also found that *Penicillium* is widely dispersed in air samples, with its spores frequently found. *Aspergillus* species are widely distributed, grow on almost all humid substrates, and threaten public health in indoor environments (Navale *et al.*, 2021). McKernan *et al.* (2007) reported that *A. ochraceus* and *C. lunata* isolated in their study were found to contaminate the air environment of aircrafts despite their presence on the aircraft surface not being observed. Kim & Kim (2022) observed the exposure levels of disease-causing bacteria and germs on aircraft cleaning workers on multiple different aircrafts. Based on their findings, the concentration levels of airborne bacteria and fungi in the aircraft surveyed were lower than the indoor environmental standards. However, average concentrations of bacteria and fungi in the air were highest in small aircrafts. Besides that, Zhao *et al.* (2019) found that the aircraft interior surfaces in seat areas (tray tables, armrests and seat covers) and lavatories (doorknob handles and toilet flush buttons) were generally colonised by various types of potentially hazardous microorganisms. The interior surfaces in seat and lavatory areas pose higher health risks by causing infections due to their relatively high microbial contamination as compared with other interior surfaces.

*Curvularia lunata* can be mostly found in subtropical and tropical countries. It can be isolated from soil, air, various plants and some grain cereals. Various studies (Masratul *et al.*, 2009; Cui & Sun, 2012; Majeed *et al.*, 2016; Gupta *et al.*, 2017; Bussaban *et al.*, 2017) found that this fungus is also a leaf pathogen that is commonly isolated from various plants displaying spotted leaves. On the other hand, *Penicillium oxalicum* has been found to cause corrosiveness on aluminium alloys with the exposure of marine environments (Lee *et al.*, 2014). However, in this study, the fungus did not affect its origin surface and component due to different nature of the environment. *Cladosporium Cladosporioides* is one of the most common of all outdoor airborne fungi that colonises plant materials and soil. It is known to be a pathogen to many kinds of crops, such as grapes (Bensch *et al.*, 2010), strawberries (Latorre *et al.*, 2011), wheat (Gubler *et al.*, 1999), pecan (Walker *et al.*, 2016) and spinach (Bensch *et al.*, 2010). This fungus also grows in indoor environments (Deshmukh & Rai, 2005), whereby it can be isolated in many sources of soils, textiles, air and several other substrates (Bensch *et al.*, 2010), found on wet building materials, paint and wallpaper (Flannigan *et al.*, 2011), as well as paper and pulp (Sampedro *et al.*, 2015). This species produces antifungal compounds that are effective against plant pathogens fungi, making it one of the important species for the potential control of various plant-infecting fungi (Wang *et al.*, 2013).

Moreover, Little *et al.* (1997a) found that species from *Cladosporium* (reported as *Cladosporium resinae*) causes corrosion on aluminium alloy through the production of organic acids.

This study is the first instance of *Nigrospora sphearica*, *Arthrimum phaeospermum*, *Phoma herbarum*, *Trichoderma asperellum* and *Lasiodiplodia theobromae* being isolated from a military helicopter in Malaysia. These species are commonly isolated from soil, air, various plant and fruits. In our study, *Nigrospora sphearica*, and *Arthrimum phaeospermum* were found on corroded components, but there is no previous study that reported the deteriorating activity of these species on metal or polymeric materials. Fouda *et al.* (2023) indicated that the most deterioration aspects were represented by the dust, dirt, erosion, stains, bores, weakness, missed parts, as well as change of colour and pH. Therefore, investigations on bio-deteriorating activities and utilisation of fungal species on protective coatings, metals and synthetic materials should be further studied.

## 5. CONCLUSION

Detection and identification of fungal contaminants are crucial to avoid their health hazardous risks and technical problems for helicopters and other military transports. Additional works on possible metabolite compounds including mycotoxins and organic acids produced by each of these fungi should be carried out prior to selecting fungal resistance for polymer and protective coatings.

## ACKNOWLEDGEMENT

The authors wish to acknowledge the financial support funded by Ministry of Higher Education, Malaysia through the Fundamental Research Grant Scheme (Grant No. FRGS/1/2018/STG07/UPNM/01/2) and the National Defence University of Malaysia (UPNM) for providing research facilities. This study would not have been possible without the cooperation of the staff and students of the Centre for Tropicalisation (CENTROP), UPNM.

## REFERENCES

- Ab Majid, A.H., Zahran, Z., Rahim, A.H.A., Ismail, N.A., Rahman, W.A., Zubairi, K.S.M., Dieng, H. & Satho, T. (2015). Morphological and molecular characterization of fungus isolated from tropical bed bugs in Northern Peninsular Malaysia, *Cimex hemipterus* (Hemiptera: Cimicidae). *Asian Pac. J. Trop. Biomed.*, **5**: 707-713.
- Adnan, M., Islam, W. & Gang, L. (2022). Advanced research tools for fungal diversity and its impact on forest ecosystem. *Enviro SciPollut. R.*, **29**:45044-45062.
- Ahmad Razi, M.Y., Noorliza, H., Mohd Badrolnizam, J., Asmariah, J. & Noor Hafifi, Z.A.R. (2021). Identification of harmful fungal contamination in moisture damaged laboratories. *Defence S&T Tech. Bul.*, **14**: 154-163.
- Amorim, R.V.S., Ledingham, W.M., Fukushima, K. & Campos-Takaki G. M. (2005). Screening of chitin deacetylase from Mucoralean strains (Zygomycetes) and its relationship to cell growth rate *J. Microb. Biotechnol.*, **32**:19-23.
- Anderson, I.C. & Parkin, P.I. (2007). Detection of active soil fungi by RT-PCR amplification of precursor rRNA molecules. *J Microbiol Method.*, **68**(2): 248-253.
- Beech, I.B., Sunner, J.A. & Hiraoka, K. (2005). Microbe–surface interactions in biofouling and biocorrosion processes. *Int. Microbiol.*, **8**: p. 157-168.
- Belov, D.V., Sokolova, T.N., Smirnov, V.F., Kuzina, O.V., Kostyokova, L.V. & Karstashov, V.R. (2008). Corrosion of aluminum and its alloys under the effect of microscopic fungi. *Prot. Met.*, **44**: 737-742

- Bensch, K., Groenewald, J.Z., Dijksterhuis, J., Starink-Willemse, M., Andersen, B., Summerell, B.A., Shin, H.D., Dugan, F.M., Schroer, H.J., Braun, U. & Crous, P.W. (2010). Species and ecological diversity within the *Cladosporium cladosporioides* complex (Davidiellaceae, Capnodiales). *Stud Mycol.*, **67**:1-94.
- Bruns, T.D., White, T.J. & Taylor, J.W. (1991). Annual review of ecology and systematics. *Fungal Mol. Syst.*, **22**: 525-564.
- Bussaban, B., Kodchasee, P., Apinyanuwat, S., Kosawang, C. & Jonglaekha, N. (2017). First report of *Curvularia lunata* causing leaf blight on Mulberry (*Morus* sp.) in Thailand. *Plant Dis.*, **101**:1951.
- Chawla, S., Payer, J. & Gai, C. (2014). Fault tree analysis for fungal corrosion of coated aluminium. *Corrosion.*, **70**: 1101-1113.
- Cui, R.Q. & Sun, X.T. (2012). First report of *Curvularia lunata* causing leaf spot on lotus in China. *Plant Dis.*, **96**: 1068.
- Deshmukh, S.K. & Rai, M.K. (2005). *Biodiversity of Fungi: Their Role in Human Life*. Science Publishers, Enfield, New Hampshire, US.
- Dijksterhuis, J. (2011). The fungal cell. In Adan, O.C.G., Samson, R.A. (Eds.), *Fundamentals of Mold Growth in Indoor Environments and Strategies for Healthy Living*. Academic Publishers, Wageningen, Netherlands, pp. 83-100.
- Flannigan, B., Samson, R.A. & Miller, J.D. (Eds.). (2011). *Microorganisms in Home and Indoor Work Environments: Diversity, Health Impacts, Investigation and Control, 2<sup>nd</sup> Ed.*, CRC Press, Boca Raton, Florida, US.
- Fouda, A., Abdel-Nasser, M. & Khalil, A.M.A. (2023). Investigate the role of fungal communities associated with a historical manuscript from the 17th century in biodegradation. *Mater Degrad.*, **6**:88.
- Geesey, G. & Cragolino, G.A. (1995). A review of the potential for microbial corrosion of high-level nuclear waste containers in an unsaturated repository site. *Int. Conf. Microbially Influenced Corr.*, Houston, Texas, US.
- Gu, J.D. (2003). Microbiological deterioration and degradation of synthetic polymeric materials: recent research advances, *Int. Biodeterior. Biodegrad.*, **52**: 69-91.
- Gu, J.D., Ford, T.E. & Mitchell, R. (2011). Microbiological corrosion of metallic materials. In Revie, R.W. (Ed.), *Uhlig's Corrosion Handbook*. John Wiley and Sons, Hoboken, New Jersey, US.
- Gubler, W. D., Feliciano, A. J., Bordas, A. C., Civerolo, E. C., Melvin, J. A. & Welch, N. C. (1999). First report of blossom blight of strawberry caused by *Xanthomonas fragariae* and *Cladosporium cladosporioides* in California. *Plant Dis.*, **83**: 400.
- Guo, Z., Doll, K., Dastjerdi, R., Karlovsky, P., Dehne, H.W. & Altincicek, B. (2014). Effect of fungal colonization of wheat grains with *Fusarium* spp. on food choice, weight gain and mortality of meal beetle larvae (*Tenebrio molitor*). *PloS One.*, **9**: e100112.
- Gupta, S., Dubey, A. & Singh, T. (2017). *Curvularia lunata* as a dominant seed-borne pathogen in *Dalbergia sissoo* Roxb: Its location in seed and its phytopathological effects. *Afr. J. Plant Sci.*, **11**: 203-208.
- Houbraken, J.A.M.P., de Vries, R.P. & Samson, R.A. (2014). Modern taxonomy of biotechnologically important *Aspergillus* and *Penicillium* species. *Adv. Appl. Microbiol.*, **86**, 199e249.
- Izuno, A., Tanabe, A.S., Toju, H., Yamasaki, M., Indrioko, S. & Isagi, Y. (2016). Structure of phyllosphere fungal communities in a tropical dipterocarp plantation: A massively parallel next-generation sequencing analysis. *Mycosci.*, **57**: 171-180.
- Jirón-Lazos, U., Corvo, F., De la Rosa, S. C., García-Ochoa, E. M., Bastidas, D. M. & Bastidas, J. M. (2018). Localized corrosion of aluminum alloy 6061 in the presence of *Aspergillus niger*. *Int. Biodeter. Biodeg.*, **133**:17 – 25.
- Kim, D.Y. & Kim, K.Y. (2022). Exposure assessment of airborne bacteria and fungi in the aircraft. *Saf. Health Work*, **13**: 487-492.
- Lacey, J. (1980). Fungal deterioration of gunpowder, *T. Brit. Mycol. Soc.*, **74**:195-197.

- Larena, I., Salazar, O., Gonzalez, V., Julian, M.C. & Rubio, V. (1999). Design of a primer for ribosomal DNA internal transcribed spacer with enhanced specificity for ascomycetes. *J. Biotechnol.*, **75**:187-194.
- Latorre, B.A., Briceño, E.X. & Torres, R. (2011). Increase in *Cladosporium spp.* populations and rot of wine grapes associated with leaf removal. *Crop Prot.*, **30**: 5256.
- Lavoie, D.M., Little, B.J., Ray, R.I., Hart, K.R. & Wagner, P.A. (1997). Microfungal degradation of polyurethane paint and corrosion of aluminum alloy in military helicopters. *Corr.* 1997, March 1997, New Orleans, Louisiana, US.
- Lee, J.S., Ray, R.I. & Little, B.J. (2014). Corrosion susceptibility of Aa5083-H116 in biologically active atmospheric marine environments. *Corr.* 2014, March 2014, San Antonio, Texas, UK.
- Little, B.J. & Ray, R.I. (2002). The role of fungi in microbiologically influenced corrosion. *15<sup>th</sup> Int Corr. C. (ICC) Congr.*, Curran Associated Inc, Red Hook, New York, US.
- Little, B.J. Ray, R.I. & Lee, J.S. (1997a). *An Overview of Microbiologically Influenced Corrosion in Aircrafts*. Naval Research Laboratory, Stennis Space Center, Mississippi, US.
- Little, B.J. Wagner, P., Lavoie, D. & Ray, R.I. (1997b). Fungal degradation of military assets. *1997 TriService Corr. Conf.*, Office of Naval Research, North Carolina, US.
- López-Gómez, J. P. & Pérez-Rivero, C. (2019). Cellular systems. In Moo-Young, M. (Ed.), *Comprehensive Biotechnology, 3<sup>rd</sup> Ed.*, Pergamon, Oxford, UK, pp 9-21.
- Magnin, A., Pollet, E., Phalip, V. & Avérous, L. (2020). Evaluation of biological degradation of polyurethanes. *Biotechnol. Adv.*, **39**: 107457.
- Majeed, R.A., Shahid, A. A., Ashfaq, M., Saleem, M.Z. & Haider, M.S. (2016). First report of *Curvularia lunata* causing brown leaf spots of rice in Punjab, Pakistan. *Plant Dis.*, **100**: 219.
- Martín-Sampedro, R., Fillat, U., Ibarra, D. & Eugenio, M.E. (2015). Towards the improvement of *Eucalyptus globulus* chemical and mechanical pulping using endophytic fungi. *Int. Biodet. Biodegr.*, **105**: 120-126.
- Masratul, H.M., Salleh, B. & Latiffah, Z. (2009). First report of *Curvularia lunata* on red-fleshed dragon fruit (*Hylocereus polyrhizus*) in Malaysia. *Plant Dis.*, **93**: 971.
- McKernan, L.T., Burge, H., Wallingford, K.M., Hein, M.J. & Herrick, R. (2007). Evaluating fungal populations by genera/species on wide body commercial passenger aircraft and in airport terminals. *Ann. Occup. Hyg.*, **51**: 281–291.
- Morton, L.H.G. & Surman, S.B. (1994). Biofilms in biodeterioration — a review, *Int. Biodet. Biodegr.*, **34**: 203-221.
- Navale, V., Vamkudoth, K.R., Ajmera, S. & Dhuri, V. (2021) *Aspergillus* derived mycotoxins in food and the environment: Prevalence, detection, and toxicity. *Toxicol. Rep.*, **8**: 1008-1030.
- NIH (2023). *Basic Local Alignment Search Tool*. Available online at: <https://blast.ncbi.nlm.nih.gov/Blast.cgi> (Last access date: 22 March 2023).
- Oetari, A., Susetyo-Salim, T., Sjamsuridzal, W., Suherman, E.A., Monica, M., Wongso, R., Fitri, R., Nurlaili, D.G., Ayu, D.C., & Teja, T.P. (2016). Occurrence of fungi on deteriorated old dluwang manuscripts from Indonesia. *Int. Biodet. Biodegr.*, **114**: 94-103.
- Rogers, C.A. (2003) Indoor fungal exposure. *Immunol. Allergy. Clin.*, **23**: 501-518.
- Samson, R.A. (2011). Ecology and general characteristics of indoor fungi. In Adan, O.C.G., Samson, R.A. (Eds.), *Fundamentals of mold growth in indoor environments and strategies for healthy living*. Wageningen Academic Publishers, Netherlands, pp. 101-116.
- Upsher, J. & Upsher, C. (1995). Catalogue of the Australian National Collection of Biodeterioration Microfungi, Defence Science and Technology Organisation (DSTO), Australia.
- Walker, C., Muniz, M.F.B., Martins, R.R.O., Mezzomo, R. Rolim J.M. & Blume, E. (2016). First report of species in the *Cladosporium cladosporioides* complex causing pecan leaf spot in Brazil. *J. Plant Pathol.*, **98**(2):369-377.
- Wang, X., Radwan, M.M., Taráwneh, A.H., Gao, J. Wedge, D.E., Rosa, L.H., Cutler, H.G. & Cutler, S.J. (2013). Antifungal Activity against plant pathogens of metabolites from the endophytic fungus *Cladosporium cladosporioides*. *J. Agr. Food Chem.*, **61**: 4551–4555.



- Wirth, A., Pacheco, F., Toma, N., Tutikian, B., Valiati, V. & Gomes., L. (2019). Analysis of fungal growth on different coatings applied to lightweight systems. *Revista Ingenieria de Construccion*, **34**:5-14.
- Zhao, B., Dewald, C., Hennig, M., Jörg B., Michael B., Pletz, M.W. & Jandt, K.D. (2019). Microorganisms @ materials surfaces in aircraft: Potential risks for public health? – A systematic review. *Travel Med. Infec. D.*, **28**: 6-14.

# GROUND BASED SYNTHETIC APERTURE RADAR ADVANCED SIMULATOR AND PROCESSOR

Chee Siong Lim, Yee Kit Chan\* & Voon Chet Koo

Centre for Remote Sensing & Surveillance Technologies, Faculty of Engineering & Technology,  
Multimedia University, Malaysia

\*Email: ykchan@mmu.edu.my

## ABSTRACT

*Ground-based synthetic aperture radar (GBSAR) is a great example of the extended applications of synthetic aperture radar (SAR). SAR is well-known for its capability of producing highly-detailed images. A set of SAR images taken from the same scene can be further processed and analysed to measure the displacement or deformation that took place in the scene if any. This technique is extremely useful in surface deformation monitoring for human-made structures, landslides, avalanches and many more. The process of designing and developing a GBSAR system is rather costly and time-consuming. It would be a great advantage for the system designer to have a realistic simulation and designing tool to anticipate the results before the implementation of the final design. In this work, an advanced simulation and processing tools was developed for GBSAR. The program is developed in MATLAB and is equipped with various tools to assist the system designer at different stages in GBSAR design, development, system simulation, data processing and interferometric SAR (InSAR) analysis. This paper documents the developed GBSAR simulator, which includes the GBSAR system designer, GBSAR raw signal generator, GBSAR signal processing tool as well as InSAR processing tool.*

**Keywords:** *Ground-based synthetic aperture radar (GBSAR); system design and simulator tool; virtual scene creator; raw signal generator; SAR signal processing.*

## 1. INTRODUCTION

Hazards due to ground movements and instability in human-made structures can potentially lead to considerable human and economic losses. Conventional ground and structural movement monitoring systems use geodetic methods such as total stations, levelling and Global Navigation Satellite System (GNSS), which are very limited to observations at distinct points. Laser scanning and photogrammetric techniques, on the other hand, cover wider areas, but they can only be operated during day time and under good weather conditions. With the recent development of interferometric synthetic aperture radar (InSAR), it is possible to monitor the displacements in large areas remotely with high spatial resolution regardless of the weather conditions. Many research works have been conducted for ground displacements monitoring such as ground displacements at a regional scale due to subsidence (Ferretti, *et al.*, 2007), earthquakes and volcanoes (Massonnet & Rabaute, 1993; Lanari *et al.*, 2004; Yun, 2008), landslides (Goldstein, *et al.*, 1993; Crosetto, *et al.*, 2005; Carlà, *et al.*, 2019; Shao, *et al.*, 2019;), and glacier motion (Zebker, *et al.*, 1994; Kenyi, *et al.*, 2003). However, most of the InSAR systems are satellite-based and therefore limit the response time of the radar systems. Comparatively, the use of a fixed and dedicated radar imaging system at the site for continuous monitoring would be a good alternative solution.

In recent years, there has been many ground-based synthetic aperture radar (GBSAR) related development and experiment works conducted by researchers around the world. For instance, researchers from China University of Mining and Technology jointly collaborated with researchers from China Academy of Safety Science and Technology to develop a GBSAR system integrated with the terrestrial laser scanner (TLS) and corner reflector (CR). The system operates at 17.25 GHz with bandwidth of 500 MHz. It is built on a high precision linear rail with an accurate positioning resolution

of 0.1 mm. It is capable of validating GBSAR interferometric measurements with micro-displacement detection. The CR is used as the ground control point (GCP) for both the SAR images from GBSAR sensor as well as the point cloud data from the TLS. The fusion of the 2D SAR interferogram with the matched 3D point cloud from the TLS yields an intuitive 3D displacement model. A close range (< 50 m) controlled field experiment was conducted by the team. A CR built on a motorised linear rail simulating linear deformation was used together with three others small CRs in the experiment. The experiment demonstrated successful results with the merging of GBSAR and TLS systems. However, the team has pointed out some slight anomaly occurred in the GBSAR displacement data due to the phase discontinuity of the CR, which led to the error in the phase unwrapping (Zheng *et al.*, 2018).

Another joint research group from Kangwon National University (Korea) and Korea Polar Research Institute (KOPRI) developed a ground-based tomographic SAR (GB-TomoSAR) system. The GB-TomoSAR operates in C-band at 5.3 GHz with 600 MHz bandwidth. The rated range resolution and azimuth angular resolution of the system are 0.25 m and  $0.65^\circ$  respectively. The sensor is built on a rack with 2.3 m-long motorised linear rail in the  $x$ -direction and vertical manual uplift in the  $z$ -direction. Unlike conventional GBSAR, which normally deals only with the range-azimuth domain data, GB-TomoSAR on the hand has to process the signal in both the range-azimuth and range-vertical domains. The group developed a new two-dimensional deramp-FFT algorithm to accommodate third dimension data from the range-vertical domain, which produces 3D tomographic SAR images. The focusing algorithm was verified using simulated data with  $3 \times 3 \times 3$  point targets. The GB-TomoSAR system and algorithm were then further tested with a field experiment that was conducted on the rooftop of a building at Kangwon National University, whereby the sensor beam was directed to buildings, roads and trees. The output SAR images showed clear and distinct features that overlaid perfectly to Google Maps. Nevertheless, the team has revealed that the slow scanning speed of the system had caused the temporal decorrelation in the output, which caused it to be relatively weak in detecting the trees as compared to buildings and roads (Lee *et al.*, 2016).

Researchers from IDS GeoRadar (Italy) developed the IBIS - Arc-scanning SAR (ArcSAR) system. ArcSAR is another variation of GBSAR, whereby it has adopted the arc-scanning motion using a rotating arm instead of the conventional linear-scanning motion using a linear rail. This has led to the broadening of the horizontal coverage of the sensor as wide as  $360^\circ$ , which is particularly useful in open-pit mine monitoring (Viviani *et al.*, 2018).

Research groups from North China University of Technology (NCUT) and Chinese Academy of Science (IECAS) have also collaborated in working on the research of ArcSAR, particularly for the imaging algorithm. The typical imaging algorithm of ArcSAR relies heavily on the reference plane. The error between the reference plane and the targeted scene deteriorates the imaging quality significantly. The group developed an interferometric digital elevation model (DEM)-assisted high precision imaging method to address the issue. The results from the simulation showed that the use of interferometric DEM can improve the accuracy of ArcSAR imaging as compared to the reference plane (Wang *et al.*, 2019).

A GBSAR has been successfully designed and developed by iRadar, Malaysia. A series of indoor and outdoor experiments were conducted to verify the performance of the radar system, which includes the phase stability test conducted in an anechoic chamber, long-term test at the fixed cabin station, and surface deformation detection test at Gunung Pass, Malaysia. The experiments' results showed that the developed system is suitable to be deployed for surface deformation monitoring, such as landslide monitoring, avalanche detection and open-pit mine monitoring (Heddallikar *et al.*, 2022; Govil *et al.*, 2022). It is also a useful monitoring system for man-made structures, such as water dams (Qiu *et al.*, 2020) long bridges (Pieraccini *et al.*, 2019), power transmission towers and high-rise buildings (Chan *et al.*, 2021; Lim *et al.*, 2019).

However, the process of designing and developing a GBSAR system is rather costly and time-consuming. It would be a great advantage for the system designer to have a realistic simulation and designing tool to anticipate the result before the implementation of the final design. Besides, point target

simulations are specifically designed to test and confirm the accuracy of SAR processing algorithms. GBSAR systems are mainly employed for measuring and monitoring deformations, which necessitate InSAR processing. Point target signal simulations that lack terrain surface information make the data less valuable for testing and verifying GBSAR systems. In this work, a GBSAR advanced simulator and processor (GBSAR-ASP) is developed. The program is developed in MATLAB and is equipped with various tools to assist the system designer at different stages in GBSAR design, development, system simulation, data processing and interferometric SAR (InSAR) analysis, as a timely tool to monitor earth environments, especially for landslides and terrain subsidence.

## 2. SYNTHETIC APERTURE RADAR (SAR) AND GROUND BASED SYNTHETIC APERTURE RADAR (GBSAR)

Synthetic aperture radar (SAR) is a side-looking radar capable of producing high-resolution 2D radar images. The SAR concept was initiated by Carl Wiley of Goodyear Aircraft Corporation in 1951 (Wiley, 1985). Since then, SAR has been recognised as an essential component for the future surveillance systems. SAR and real aperture radar (RAR) share many aspects in common. As far as the range resolution is concerned, RAR (Figure 1) and SAR (Figure 2) are very much identical. One of the elements that differentiate between the two is the cross-range resolution. In a typical RAR system, it requires a considerably large antenna to achieve a very fine cross-range resolution. It is not practical for any airborne or spaceborne to carry a radar system with a huge antenna. This limitation led to the invention of SAR. SAR has the capability to achieve better cross-range resolution simulating a long antenna array by utilising the forward motion of a moving platform where the system is mounted (Sullivan, 2004).

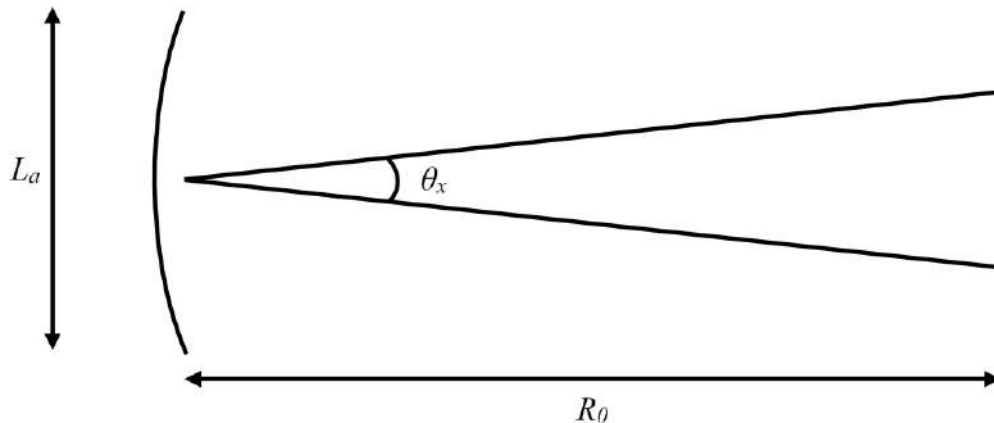


Figure 1: RAR system (Chan & Koo, 2008).

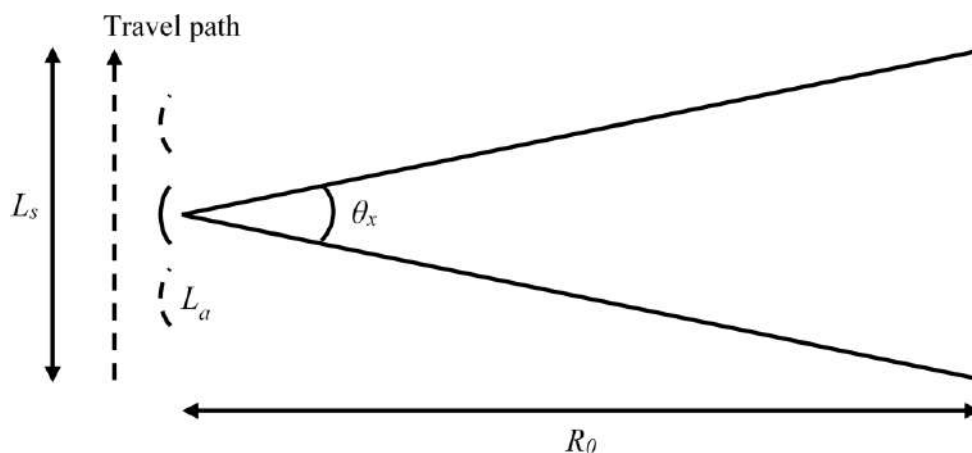
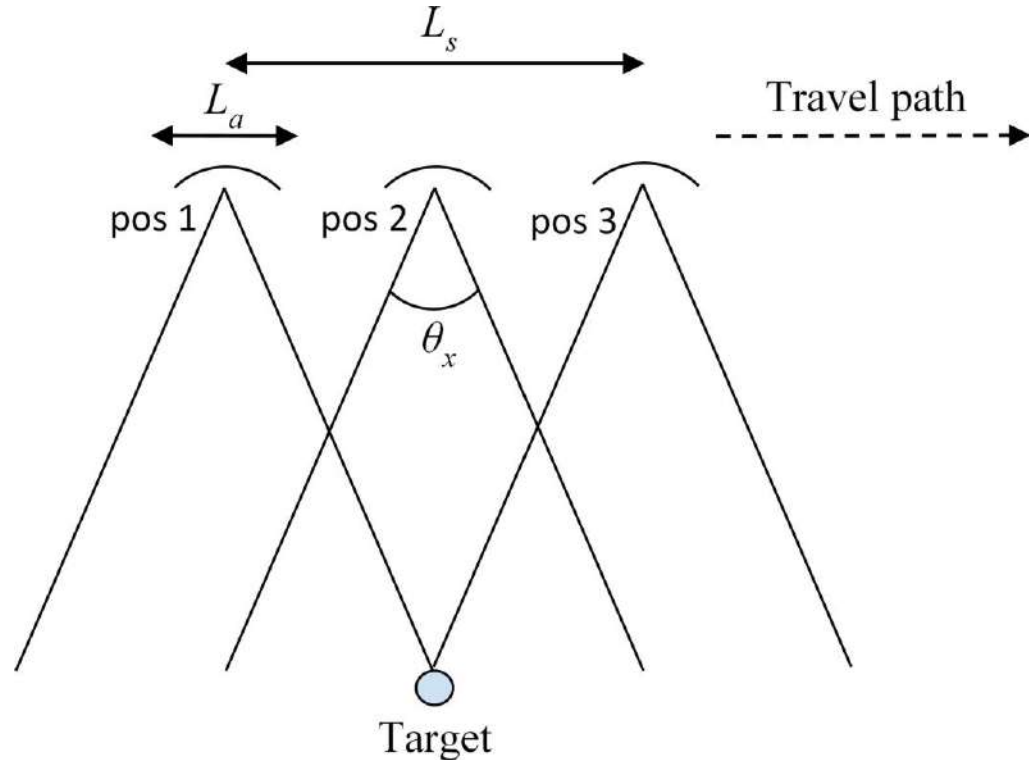


Figure 2: SAR system (Chan & Koo, 2008).

The working principle of SAR is shown in Figure 3. As the carrying platform moves, the SAR system illuminates the area of interest. The backscattered echoes are received and recorded at a fixed temporal interval. The echo from the target enters the radar beam when the moving platform is at Position 1 and leaves when the moving platform is at Position 3. The distance from Positions 1 to 3 defines the length of the synthesised antenna (*Chan & Koo, 2008*).



**Figure 3: The concept of SAR (*Chan & Koo, 2008*).**

GBSAR is a SAR system that is operated on a ground-based platform. A GBSAR repeatedly emits and receives a burst of electromagnetic waves while moving at a fixed step along a rail track (As shown in Figure 4) (*Bernardini et al., 2007*). It was designed mainly for ground movement activities monitoring. There are three fundamental components in a GBSAR system. The first component is the pulse compression technique to resolve the resolution in range. It is then followed by SAR, the technique to resolve the resolution in cross-range. Last but not least is InSAR, which exploits the coherent phase of the SAR image to determine the object displacement. The idea of GBSAR technique was first proposed by the Joint Research Center (JRC) in the late 1990s, and the first GBSAR system was named as Linear Synthetic Aperture Radar (LiSA) (*Tarchi et al., 2000*).

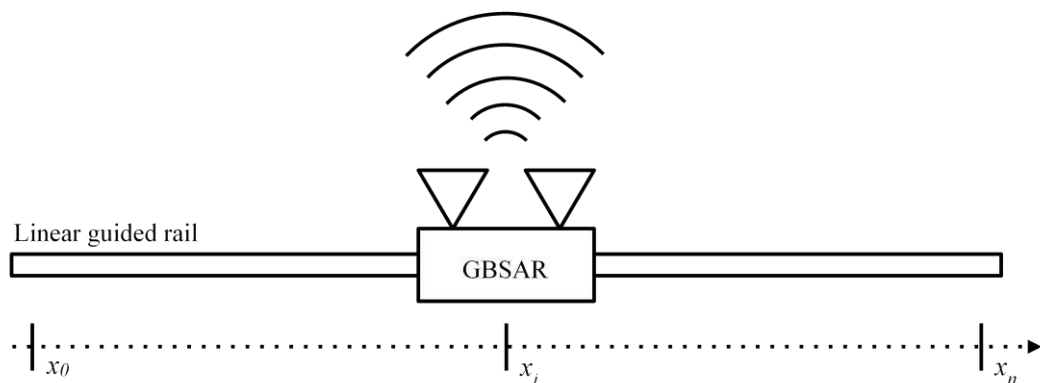


**Figure 4: The concept of GBSAR (*Chan et al., 2021*).**

A GBSAR system travels on a fixed-length linear guide rail in order to perform the scanning process. Figure 5 shows the geometry of the GBSAR system, whereby the azimuth (or cross-range) resolution of the output SAR images is directly proportional to the length of the linear guide rail. Increasing the length of the track will result in higher resolution SAR images in the azimuth direction. The bandwidth of the transmitted radio frequency, on the other hand, determines the fineness of the output SAR images in the range direction. The following equations show the maximum achievable resolution in both slant range  $\delta r$  and azimuth  $\delta\theta_{az}$ . The azimuth resolution  $\delta x$  is expressed in the term of radians and can be translated into the unit of meter by multiplying it with the distance to beam centre  $R_0$ .

$$\delta r = \frac{c}{2B} \quad (1)$$

$$\delta\theta_{az} = \frac{\lambda}{2L_s} \quad (2)$$

$$\delta x = \frac{\lambda R_0}{2L_s} \quad (3)$$

where  $c$  is the speed of light approximated at  $3 \times 10^8$  m/s,  $B$  is the transmitted signal bandwidth,  $\lambda$  is the signal wavelength, and  $L_s$  is the synthetic aperture length.

These essential specifications need thorough consideration when designing a GBSAR system as they will determine the data volume, maximum reachable range (Equation 4) and resolution of the output SAR image.

$$R_{max} = \frac{cN_r}{2B} \quad (4)$$

where  $N_r$  is the frequency step count.

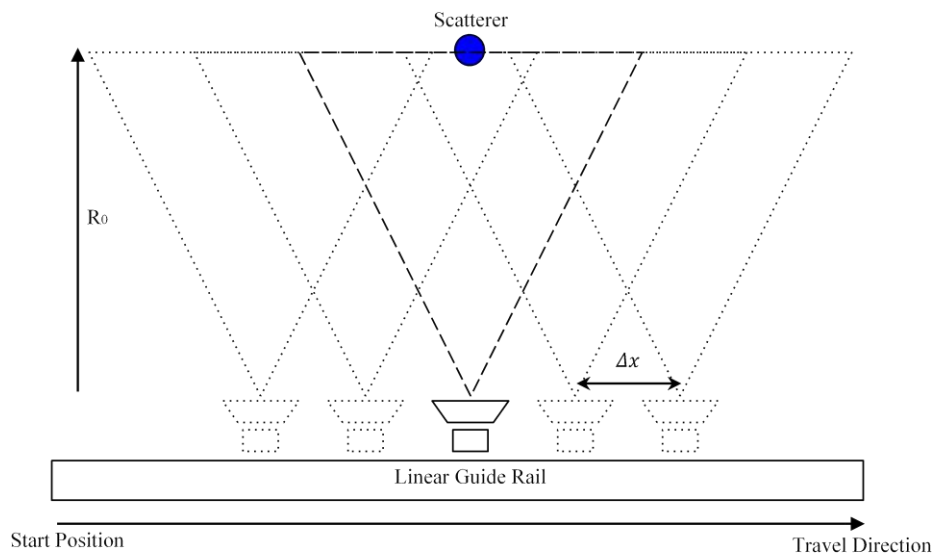


**Figure 5: Illustration of a GBSAR system.**

The trade-off between SAR image quality and the data processing load requires some in-depth analysis. Therefore, a system design and simulator tool is useful for the system designer to save time and cost.

### 3. GROUND BASED SYNTHETIC APERTURE RADAR ADVANCED SIMULATOR AND PROCESSOR (GBSAR-ASP)

GBSAR-ASP is developed in MATLAB and covers the entire GBSAR development process ranging from system designing, signal simulation, signal processing, output analysis and system validation. The program has embedded various tools to assist the system designer at different stages in GBSAR design and development. Table 1 and Figure 6 shows the list of GBSAR-ASP modules and the overall process flowchart.

**Table 1: List of GBSAR-ASP Modules.**

No.	Module Name
1	System Designer
2	Scene Simulator
3	Raw Signal Generator
4	Noise Generator
5	GBSAR Processor
6	InSAR Processor

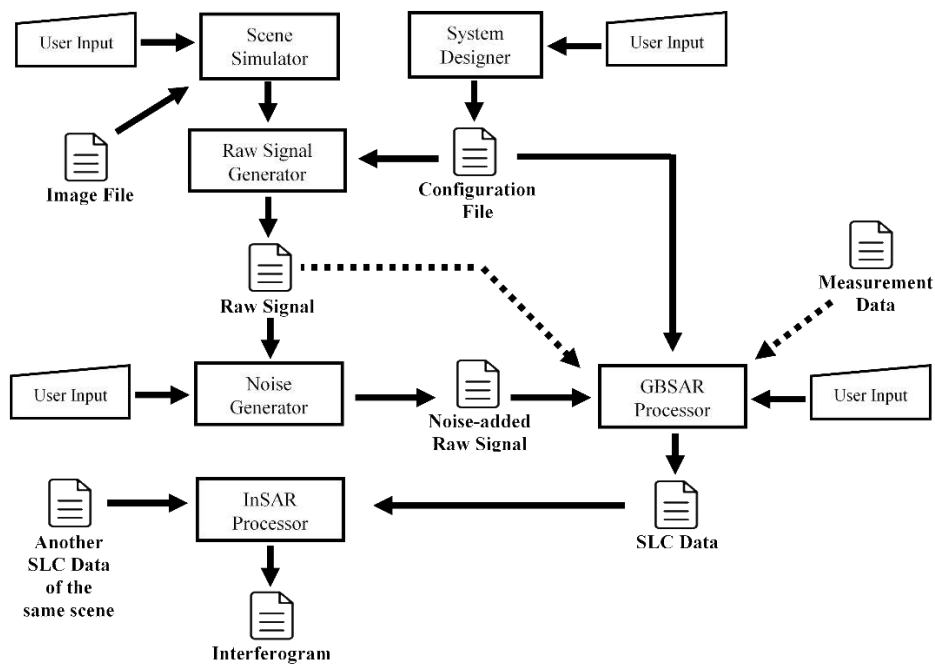


**Figure 6: Overall flowchart of GBSAR-ASP.**

#### 3.1 GBSAR System Designer

The GBSAR-ASP's first tool is the SAR system designer (Figure 7), which enables the user to create the desired GBSAR design specifications. The user can input various parameters, such as start frequency  $f_1$ , stop frequency  $f_2$ , frequency step count  $N_r$ , azimuth linear step count  $N_x$ , linear guide azimuth step size  $\Delta x$  and antenna length  $L_a$ . Using these settings, the system designer module calculates values such as wavelength  $\lambda$ , slant range resolution  $\delta r$ , azimuth resolution  $\delta_x$ , maximum reachable range  $R_{max}$ , antenna beam width  $\theta_x$ , and maximum azimuth coverage  $X_{max}$ . These system parameters are then saved in the system configuration file for future use in the subsequent stages.

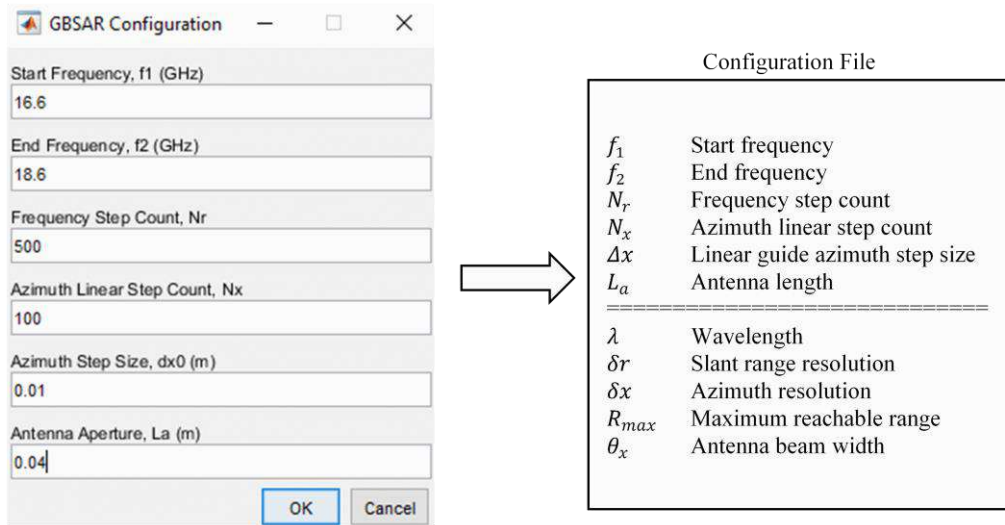


Figure 7: GBSAR-ASP system designer GUI.

### 3.2 Raw Signal Generator

GBSAR-ASP also includes a scene designer and raw signal generator. Using the scene designer, users can create a personalised virtual terrain scene, as illustrated in Figure 8 (a). Additionally, users have the option of adding point reflectors on the top of the terrain surface. The sub-module allows users to input reflector target coordinates manually or import an image file (Figure 8 (b)) and translate it into point targets (Figure 8 (c)). The emulated virtual scene with known targets is then generated, as depicted in Figure 8 (d) (top view of the virtual scene) and Figure 8 (e) (3D view of the virtual scene).

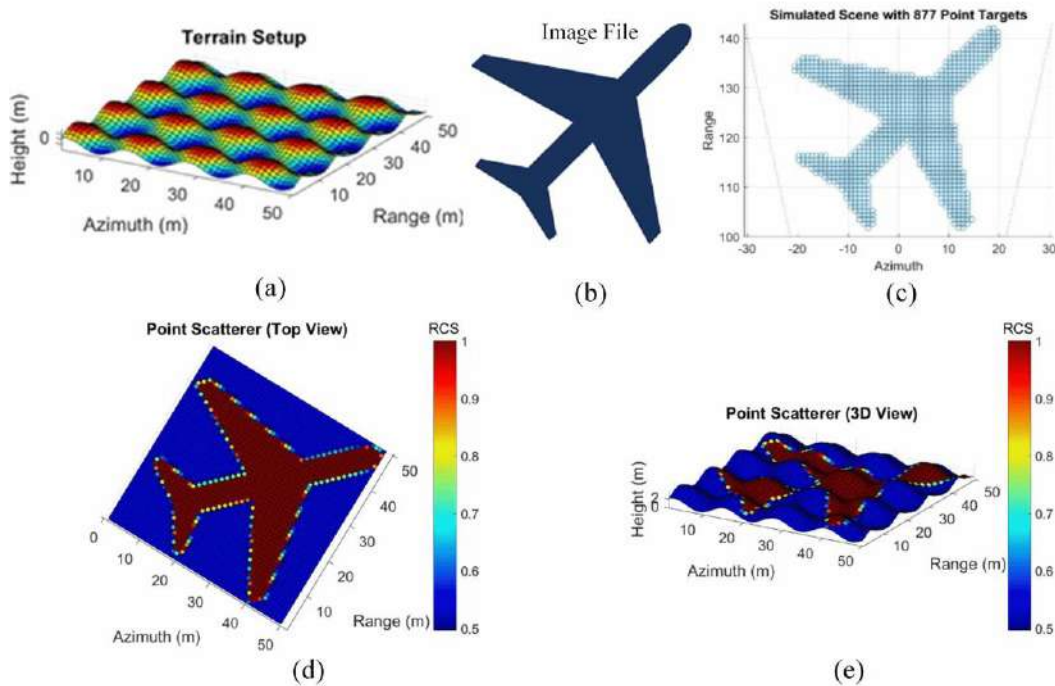


Figure 8: Virtual scene simulation.



The return signal from  $N$  number of scatterers at coordinate  $(x_i, y_i, z_i)$  can be expressed in the form of range frequency domain (range profile) as shown in the following equation:

$$S(x_n, w(t)) = \sum_{i=1}^N a_i e^{-j2w(t)\sqrt{(x_n-x_i)^2+(y_a-y_i)^2+(z_a-z_i)^2}} \quad (5)$$

where  $a_i$  is the radar cross section (RCS) of the scatterer and  $w(t)$  is the instantaneous radial frequency of the received signal. The antenna's coordinate is given as  $(x_n, y_a, z_a)$ , where  $x_n$  is the  $n^{\text{th}}$  azimuth position of the antenna on the linear guide rail.

The variables  $y_a$  and  $z_a$  are the fixed position of the antenna in range and height direction respectively. Figure 9 (a) illustrates part of the ten instantaneous simulated return signals from  $x_n = -0.04$  m to  $x_n = 0.05$  m, with the distance of 1 cm apart. Plotting the entire matrix of the simulated return signal of  $S(x_n, w(t))$  will produce a raw image (unfocused) as depicted in Figure 9 (b).

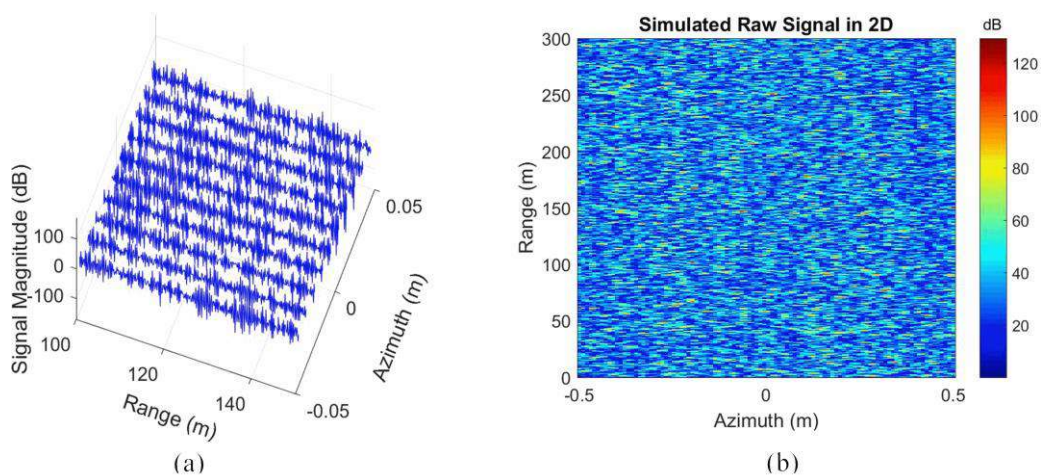


**Figure 9: GBSAR raw signal simulation.**

The simulated signal produced by the GBSAR raw signal generator module is excessively idealised, making it almost impossible to replicate in real-world scenarios due to the presence of noise in the radio-frequency (RF) components. Therefore, it is vital to investigate the level of noise immunity of the system. In order to achieve this, White Gaussian noise can be added to the simulated raw signal. The user can then test and analyse the output image quality of the system using varying power levels of White Gaussian noise. Figure 10 provides a comparison between the original simulated return signal and the signal with White Gaussian noise with signal-to-noise ratio (SNR) of 20, 10, 5 and -5 dB.

Generating the raw signal can be a time-consuming process, particularly depending on the size of the virtual scene and number of simulated point targets. In order to save time, White Gaussian noise is added to the raw signal after the simulation process, rather than during it. The noise-added raw signal is saved separately from the original (theoretical) return signal file. This means that a new noise-added raw signal with different noise power levels can be easily generated without repeating the entire simulation process.

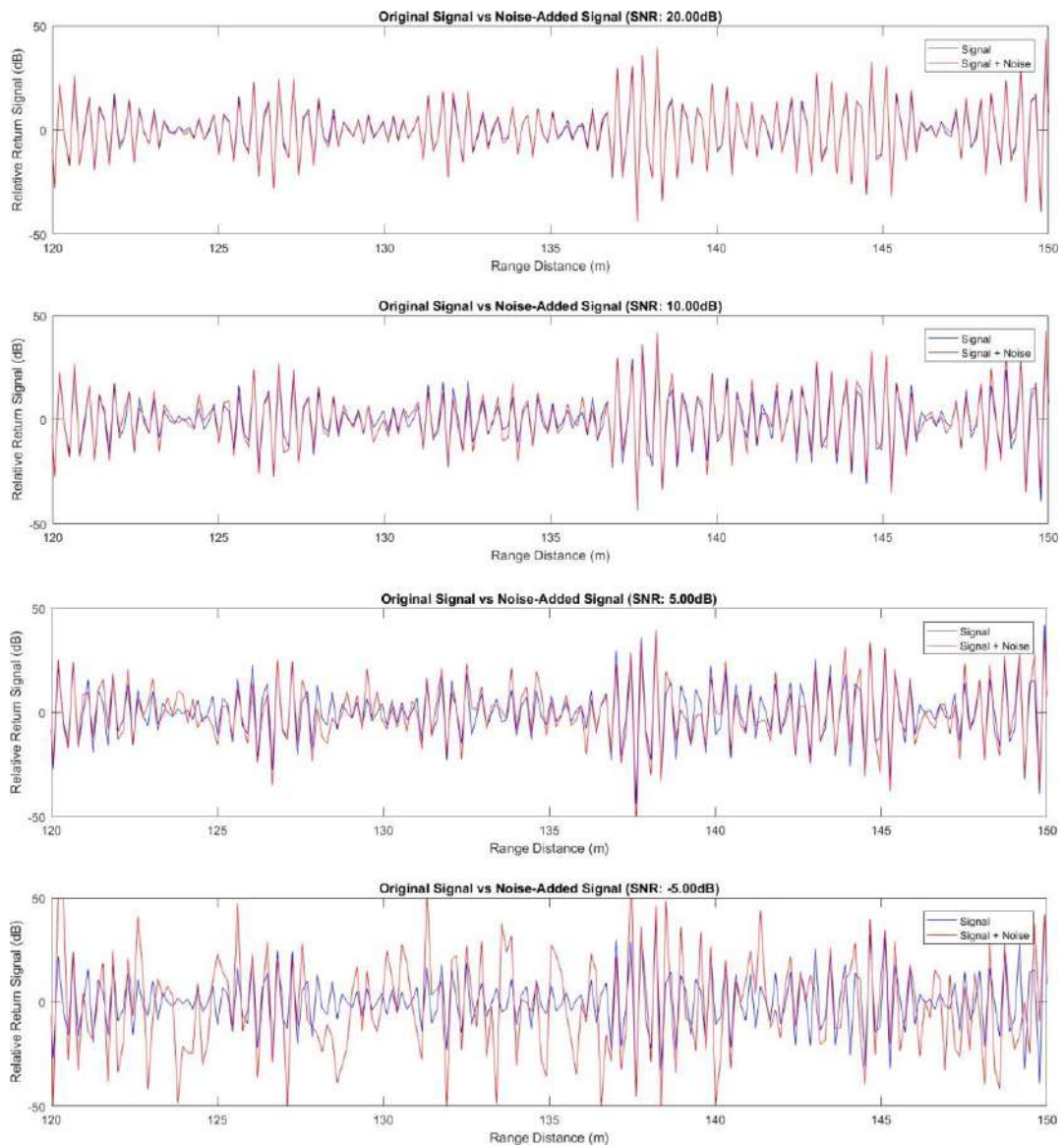


**Figure 10: Noise signal generation.**

### 3.3 Signal Processing Tool

The GBSAR-ASP includes a signal processing tool that processes the raw signal to create a single look complex (SLC) file. Processing GBSAR datasets can be computationally intensive due to their large volume and trimming the dataset can help to reduce the processing load. This tool supports data trimming and upon importing the raw signal, the program displays the range profile generated from the raw signal. The range profile provides valuable information for determining the distance range of interest for GBSAR processing. In Figure 11 (a), for example, some strong returns appear between the range of 100 and 150 m, which corresponds to the distance from the sensor to the simulated targets. Thus, processing time can be reduced by cropping the data from the range of 100 to 150 m.

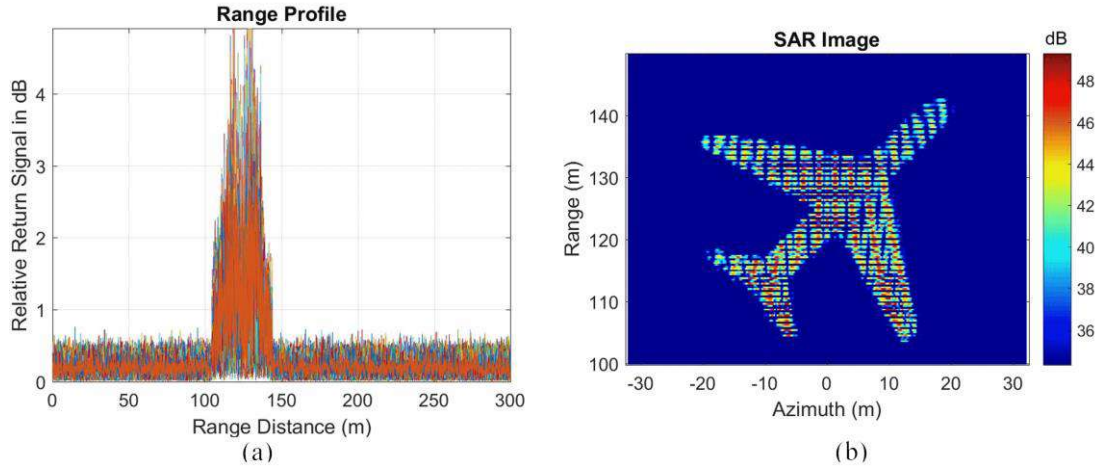


**Figure 11: SAR signal processing.**

The GBSAR-ASP employs the range migration algorithm (RMA) for its signal processing tool. The RMA process, illustrated in Figure 12, starts with Fourier transforming the raw data into the  $(k_x, k_r)$  domain in the azimuth direction. Then, the data undergoes matched filtering with the  $S_m f(k_x, k_r)$  filter as per Equation 6. Before transforming back into the time domain, it is essential to correct the range curvature of the data matrix through Stolt interpolation, where the data is interpolated in the  $k_r$  axis. Next, the data is mapped into the spatial wavenumber domain  $k_y$  using Equation 7. Finally, the Stolt interpolated matrix is inverse Fourier transformed to the time domain to produce a SAR image (Figure 11(b)) (Chan, *et al.*, 2020).

$$S_m f(k_x, k_r) = e^{jR_c \sqrt{(k_r)^2 - (k_x)^2}} \quad (6)$$

$$k_y = \sqrt{(k_r)^2 - (k_x)^2} \quad (7)$$

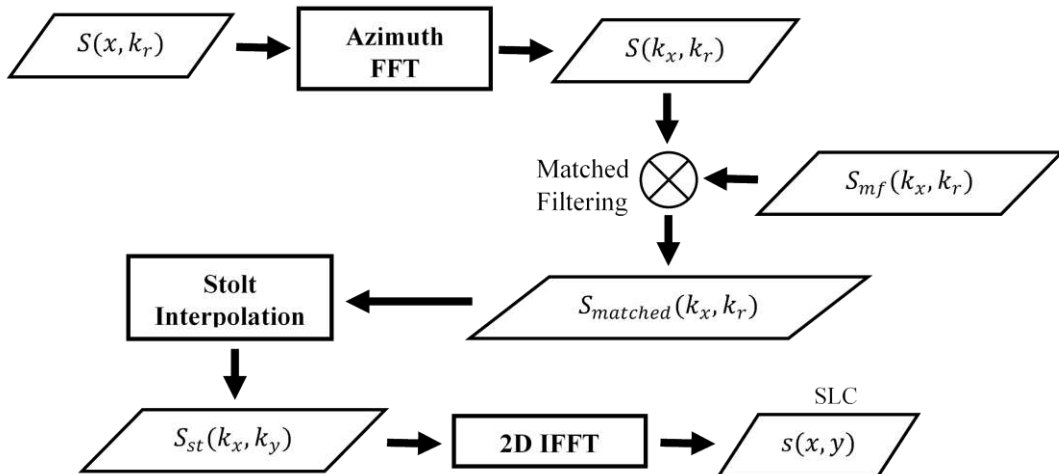


**Figure 12: Overview of RMA focusing process.**

### 3.4 Interferometric SAR (InSAR) Processing Tool

InSAR is indeed a powerful technique in GBSAR for generating DEMs. The interferogram is formed by computing the complex conjugate of one SAR image and multiplying it with another SAR image. The baseline  $b$  is defined as the separation between two antennas in the direction of the radar line of sight (Figure 13,  $A_1$  and  $A_2$  being the observation points). The resulting interferogram contains phase information that is proportional to the displacement of the scatterers in range  $\Delta r$  for each pixel between the datasets in the scene. The phase shift  $\Delta\phi$  between the two SAR images is given by Equation 8. The phase shift  $\Delta\phi$  is useful in determining the pixel's elevation to generate the DEM of the scene. One can calculate the pixel's elevation  $z_p$  using Equation 9, in which  $H$  is the height of the antenna,  $b_z$  is the vertical baseline in height direction, and  $b_y$  is the horizontal baseline in the ground range direction. For the case of a GBSAR mounted at  $H = 0$  with no horizontal baseline  $b_y = 0$ , Equation 9 can be simplified into Equation (10) (Martinez & Fortuny, 2008).

$$\Delta r = \frac{\lambda}{4\pi} \Delta\phi \quad (8)$$

$$z_p = H - \frac{r_1(\Delta r + b_y)}{b_z} \quad (9)$$

$$z_p = -\frac{r_1}{b_z} \frac{\lambda}{4\pi} \Delta\phi \quad (10)$$

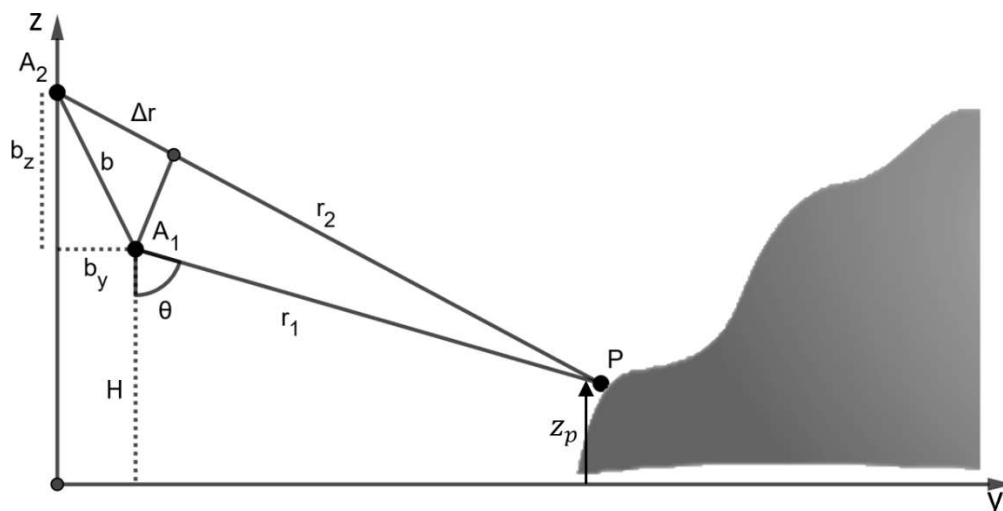


Figure 13: Interferometric SAR geometry.

The process flow of InSAR processing is depicted in Figure 14. It begins by multiplying the Master SLC and the conjugate of the Slave SLC, which are obtained from observation points  $A_1$  and  $A_2$  respectively. It is important to note that the phase value extracted from the complex interferogram can have a discontinuity. Due to the periodic nature of the phase values, a phase jump can occur when the phase exceeds the range of  $-\pi$  to  $+\pi$ , resulting in the phase being wrapped (as seen in Figure 15 (a)) in between  $-\pi$  and  $+\pi$ . In order to obtain the full interferometric phase, the phase must undergo phase-unwrapping to correct the phase jumps. Only then can the phase values be used to calculate displacement information accurately.

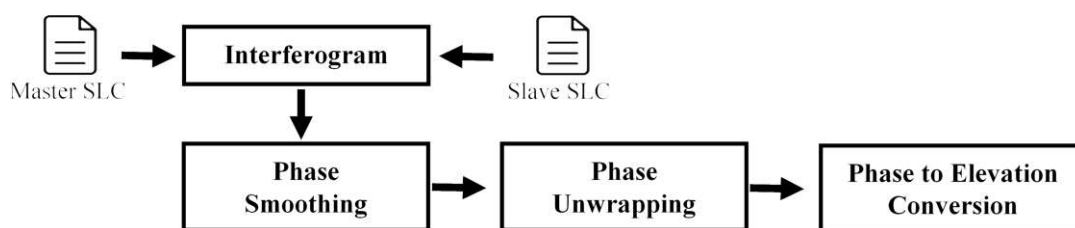
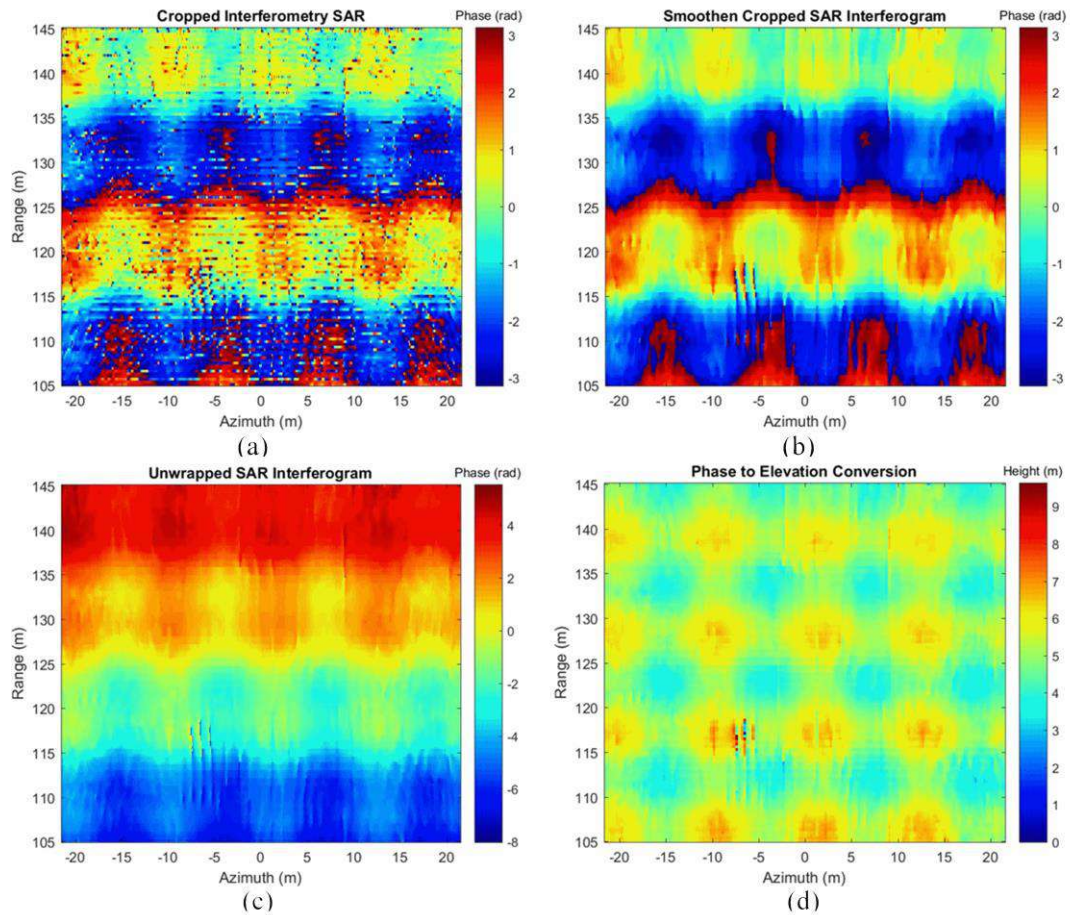
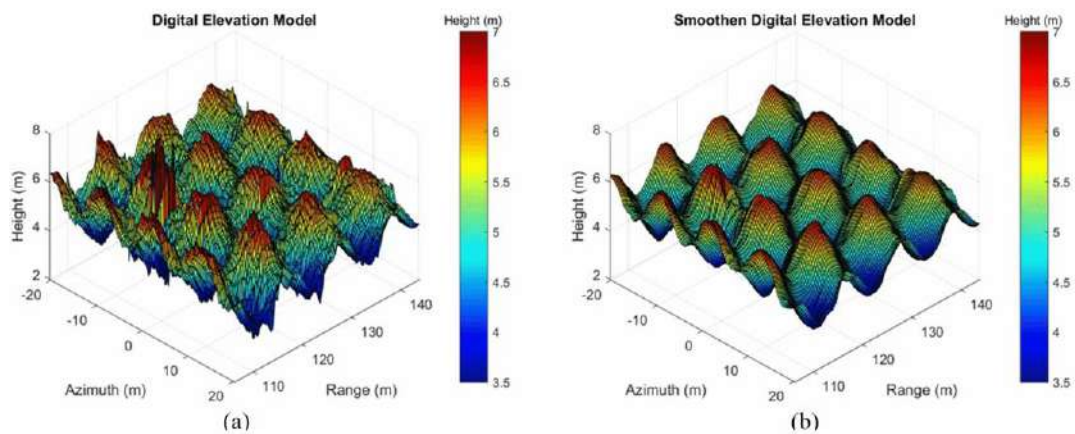


Figure 14: InSAR processing.

It is important to note that the interferogram in Figure 15 (a) exhibits apparent speckles that need to be reduced before the phase-unwrapping process. These speckles can negatively impact the quality of the unwrapped interferogram. A common method to reduce speckles is to perform 2D convolution on the data using 3-by-3 kernels, with the size of the kernels being adjustable to achieve the desired smoothing. Figure 15 (b) displays the output after the smoothing process. After smoothing, the interferogram is subjected to phase-unwrapping to produce a full interferometric phase, which is shown in Figure 15 (c). The final step of InSAR involves translating the phase information into the DEM using Equation (10), resulting in the output shown in Figure 15 (d). The height information from the translated output can be presented in a 3D terrain view, as demonstrated in Figure 16(a). A subsequent round of smoothing is carried out to produce a smoother terrain view, as depicted in Figure 16(b).



**Figure 15: SAR interferogram.**



**Figure 16: Generated DEM.**

## 4. CONCLUSION

This paper showcases GBSAR-ASP, an integrated simulation and processing tool for GBSAR systems. Typically, point target simulations are created solely for testing and verifying SAR processing algorithms. However, GBSAR systems are primarily used for deformation measurement and monitoring, which involves InSAR processing. The absence of terrain surface information in point target signal simulation renders the data less useful for GBSAR system testing and verification. GBSAR-ASP, on the other hand, is specifically designed for GBSAR and generates GBSAR return signals based on both point targets and terrain surface information. The program comprises several submodules, including the virtual scene creator, SAR raw signal simulation, noise generator, SAR processing and InSAR processing, with each workflow presented in detail. The submodules underwent testing and verification, with the preliminary results indicating success. The next stage of the project involves validating the program using field measurement data.

## REFERENCES

- Bernardini, G., De Pasquale, G., Gallino, N. & Gentile, C. (2007). Microwave interferometer for ambient vibration measurements on civil engineering structures: 2. application to full-scale bridges. *Exp. Vib. Anal. Civil Eng. Struct. (EVACES '07)*, pp. 153–162.
- Carlà, T., Tofani, V., Lombardi, L., Raspini, F., Bianchini, S., Bertolo, D., Thuegaz, P. & Casagli, N. (2019). Combination of GNSS, satellite InSAR, and GBInSAR remote sensing monitoring to improve the understanding of a large landslide in high alpine environment. *Geomorphology*, **335**: 62–75.
- Chan, Y.K., Lee, Y.C. & Koo, V.C. (2020). Synthetic aperture radar (SAR) signal simulation using range Doppler algorithm (RDA). *Def. S T Tech. Bull.*, **13**: 295–315.
- Chan, Y.K. & Koo, V.C. (2008). An introduction to synthetic aperture radar (SAR). *Prog. Electromagn. Res. B*, **2**: 27-60.
- Chan, Y.K., Koo, V.C., Hii, W.H.H. & Lim, C.S. (2021). A ground-based interferometric synthetic aperture radar design and experimental study for surface deformation monitoring. *IEEE Aero. El. Syst. Mag*, **36**: 4-15.
- Crosetto, M., Crippa, B. & Biescas, E. (2005). Early detection and in-depth analysis of deformation phenomena by radar interferometry. *Engineering Geology*, **79** (1-2): 81–91.
- Ferretti, A., Monti-Guarnieri, A., Prati, C., Rocca, F., & Massonet, D. (2007). *INSAR Principles-Guidelines for SAR Interferometry Processing and Interpretation, TM-19*. ESA Publications, The Netherlands.
- Goldstein, R.M., Engelhardt, H., Kamb, B. & Frolich, R.M. (1993). Satellite radar interferometry for monitoring ice sheet motion: application to an Antarctic ice stream. *Science*, **262**, 1525–1530.
- Govil, H., Chatterjee, R.S., Bhaumik, P. & Vishwakarma, B. (2022). Deformation monitoring of Surakachhar underground Coal mines of Korba India using SAR interferometry. *Adv. Space Res.*, **70**: 3905-3916.
- Heddallikar, A., Pinto, R., Kothari, H., James, J., Rao, Y.S. & Sajjad., T. (2022). Initial results of ground based SAR experiment in an opencast coal mine for slope stability monitoring. *IEEE Microw., Antennas, and Propag. Conf. (MAPCON) 2022*, pp. 1720-1725
- Kenyi, L.W., & Kaufmann, V. (2003). Estimation of rock glacier surface deformation using SAR interferometry data. *IEEE Trans. Geosci Remote Sens.*, **41**: 1512–1515.
- Lanari, R., Mora, O., Manunta, M., Mallorquí, J. J., Berardino, P. & Sansosti, E. (2004). A small-baseline approach for investigating deformations on full-resolution differential SAR interferograms. *IEEE Trans. Geosci Remote Sens.*, **42**: 1377–1386.
- Lee, H., Ji, Y. & Han, H. (2016). Experiments on a ground-based tomographic synthetic aperture radar. *Remote Sens.*, **8**: 667.
- Lim, C. S., Chan, Y. K., Koo, V. C. & Hii, W. H.-H. (2019). Phase statistical model and correction in imagery of ground based synthetic aperture radar (GBSAR) for land deformation monitoring. *Prog. Electromagn. Res.*, **97**: 189–200.

- Martinez-Vazquez, A. & Fortuny-Guasch, J. (2008). Averaging and formulation impact on GBSAR topographic mapping. *IEEE Geosci. Remote Sens. Lett.*, **5**: 635–639.
- Massonnet, D. & Rabaute, T. (1993). Radar interferometry: limits and potential. *IEEE Trans. Geosci. Remote Sens.*, **31**: 455–464.
- Pieraccini, M. & Miccinesi, L. (2019). An Interferometric MIMO Radar for Bridge Monitoring. *IEEE Geosci. Remote Sens. Lett.*, **16**: 1383–1387.
- Qiu, Z., Jiao, M., Jiang, T., & Zhou, L. (2022). Dam structure deformation monitoring by GB-InSAR approach. *IEEE Access*, **8**: 123287–123296.
- Shao, Z., Zhang, X. & Li, Y. (2019). Landslides monitoring with a squint angle based on GBSAR. *Prog. Electromagn. Res.*, **80**: 13–22.
- Sullivan, R. (2004). *Radar Foundations for Imaging and Advanced Concepts*. Institution of Engineering and Technology (IET), UK.
- Tarchi, D., Rudolf, H., Pieraccini, M. & Atzeni, C. (2000). Remote monitoring of buildings using a ground-based sar: application to cultural heritage survey. *Int. J. Remote Sens.*, **21**: 3545–3551.
- Viviani, F., Michelini, A., Mayer, L. & Conni, F. (2018). IBIS-ARCSAR: An innovative ground-based SAR system for slope monitoring. *Proceeding 2018 IEEE Int. Geosci. Remote Sens. Symp. (IGARSS 2018)*, pp. 1348–1351.
- Wang, Y., Song, Y., Lin, Y., Li, Y., Zhang, Y. & Hong, W. (2019). Interferometric DEM-assisted high precision imaging method for ARCSAR. *Sensors*, **19**, 2921.
- Wiley, C.A. (1985). Synthetic aperture radars. *IEEE Trans. Aerosp. Electr. Syst.*, **3**: 440–443.
- Yun, S.H. (2008). *Volcano Deformation Modeling Using Radar Interferometry*. VDM Verlag, Bonn, Germany.
- Zebker, H.A., Rosen, P.A., Goldstein, R. M., Gabriel, A. & Werner, C. L. (1994). On the derivation of coseismic displacement fields using differential radar interferometry: The landers earthquake. *J. Geophys. Res.: Sol. Ea.*, **99**: 19617–19634.
- Zheng, X., Yang, X., Ma, H., Ren, G., Zhang, K., Yang, F. & Li, C. (2018). Integrated ground-based SAR interferometry, terrestrial laser scanner, and corner reflector deformation experiments. *Sensors*, **18**: 4401.

# ADAPTATION OF MICROWAVE ANTENNA TO CONFINED SPACES

Chung Boon Kuan

Department of Electrical and Electronic Engineering, Universiti Tunku Abdul Rahman, Malaysia

Email: chungbk@utar.edu.my

## ABSTRACT

*Autonomous mobile robots are used for exploration, routine inspections and surveillance tasks in confined and subterranean spaces for safety reasons by reducing the presence of humans in those environments. One of the challenges to overcome for confined and subterranean robot operations is unreliable wireless transmission due to changes of radiation efficiency of the microwave antenna. Impedance mismatch can vary significantly with operating conditions, such as the proximity of the antenna to different surrounding metal objects or dielectric material. This paper proposes an integrated adaptive single-stub impedance matching system using phase shifters to transform dynamically varying complex load impedances for conjugate matching of microwave antennas. The system comprises of mismatch detector, control circuit and variable elements. Variable phase shifter is much easier to make as compared to variable inductor and capacitor. It has low parasitic, high  $Q$ -factor, highly linear, and can be made to have wide tuning range. It is also superior than variable inductor / capacitor at ultra-high microwave frequencies. The equations and design methodologies for the adaptive impedance matching system are presented, including a few methods to automatically control the phase shifters. A few simulation examples are presented, with the results confirming the effectiveness of the system.*

**Keywords:** *Circuit analysis; impedance matching; microwave amplifiers; antennas; transmission line theory; filter*

## 1. INTRODUCTION

Many civilian and industrial sites have confined and subterranean spaces that are hazardous for humans given the presence of narrow spaces, poisonous gases, flooding, extreme temperatures and collapsing structures. Autonomous mobile robots are commonly used for exploration, routine inspections, and surveillance tasks in these confined and subterranean spaces in order to reduce the presence of humans in those environments. The challenges of such robots include the incorporation of robust and reliable map generation, precise localisation, obstacle avoidance, and efficient path planning (Azpúrua *et al.*, 2023). Wireless communication with the host controller is a vital part of the system. The challenge is increased for confined and subterranean robot operations due to unreliable wireless transmission, which is mainly caused by changes of radiation efficiency of the microwave antenna. Impedance mismatch can vary significantly with operating conditions, such as the proximity of the antenna to different surrounding metal objects or dielectric material (Thirappa *et al.*, 2021).

Monolithic microwave integrated circuits (MMIC) and radio frequency system-on-a-chip (RFSoc) are widely used in many electronic products to provide wireless communications. Impedance matching network is essential to achieve maximum power transfer, minimum reflection and adequate harmonic rejection (Chung, 2022). Although various solutions are available, the practical considerations in selecting the suitable solution for different applications include simplicity, form factor, bandwidth, manufacturing feasibility and ease of tuning (Chung, 2006; Li *et al.*, 2019; Alibakhshikenari *et al.*, 2020; Fan *et al.*, 2019; Qingping *et al.*, 2020). In many applications, such as transmitting / receiving antennas, gain- and band-switchable power amplifiers, power line communications, radio wave energy harvesting circuits and noise measurement systems, the load impedance to be transformed is usually variable (Simons & Lee, 1998; McIntosh *et al.*, 1999; Zhang *et al.*, 2005; Neo *et al.*, 2006; Lauder & Sun, 2020).



Adaptive impedance matching network can be used to provide optimum performances under the operating environment with dynamically varying impedances (Li *et al.*, 2019). For example, performance of the antenna is sensitive to its proximity to nearby objects. The time-varying shifts in impedance require an integrated, low power, effective and robust adaptive matching network to maintain power efficiency. An adaptive matching network comprises three main parts: mismatch detector, control circuit, and variable elements.

A few different methods have been proposed for the implementation of the mismatch detector (Fanfan *et al.*, 2006; Li & Cheng, 2010; Bezooijen *et al.*, 2010; Jang *et al.*, 2013; Li *et al.*, 2019). The mismatch detector measures the reflection coefficient of the load in real-time. The main approaches include: detection of the reflected power using a coupler, detection of the phase shift using voltage and current probes, and comparison with a reference signal. For the control circuit, there are mainly two approaches: using processors and algorithms, and using a feedback circuit (Thompson & Fidler, 2001; Gu *et al.*, 2011; Gu & Morris, 2013; Sjoblom & Sjöland, 2005; Robichaud *et al.*, 2013). The main considerations are accuracy, required space, power and difficulty to integrate.

The variable matching elements can be inductors, capacitor, varactors or a combination of them in continuously tunable form or digitally switchable array of elements (as illustrated in Figure 1). These elements need to have low parasitic, high tuning ratio and be highly linear. Generally, integrated components have low quality factors and have small values, which make it difficult for achieving high tuning ratio.

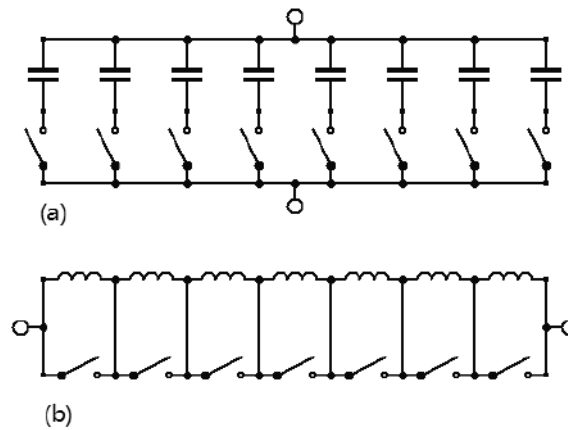


**Figure 1: Digitally switchable array of (a) capacitors and (b) inductors (Alibakhshikenari *et al.*, 2020).**

In MMIC design, inductances can be implemented using thin microstrip lines (i.e., high characteristic impedance), loop, spiral (square, hexagonal, octagonal or circular shape) and bond-wire (Chung, 2022). Two main problems with using integrated inductors are: lack of accurate modelling tools and relatively low Q-factors due to associated metallisation and dielectric losses. Typical inductance values for monolithic circuits are in the range of 0.2 to 10 nH. Higher values are difficult to achieve in strictly lumped form due to inter-segment fringing capacitance.

Capacitances can be implemented using wide microstrip lines (i.e., low characteristic impedance), metal-insulator-metal (MIM) capacitor and interdigital capacitor. MIM capacitors are formed by sandwiching a dielectric layer between two layers of metal, resulting in a simple parallel-plate capacitor. Interdigital capacitor is realised by arranging coupled transmission line sections in an interlaced manner. The resulting capacitance is mainly due to the fringe fields between the fingers. Interdigital capacitors are usually for values in the range of 0.05 to 0.5 pF, whereas MIM techniques are for values of 0.1 to 25 pF (to minimise the overall size). Problems with using integrated capacitors are: capacitors with high Q-value usually have relatively loose tolerance (approximately 20% or worse), and capacitors with the most area-efficiency tend to have high loss and poor voltage coefficients.

The conventional L, Pi or T networks are commonly used in the designs of adaptive impedance matching circuits. In the L-network, a variable inductor and a variable capacitor are typically required. The domain of impedance matching can only cover half of the Smith Chart. For normalised load resistance  $r$  larger than 1, a shunt element must first be connected to the load followed by a series element, as illustrated in Figure 2(a).

For normalised load conductance  $g$  larger than 1, a series element must first be connected to the load followed by a shunt element, as illustrated in Figure 2(b).

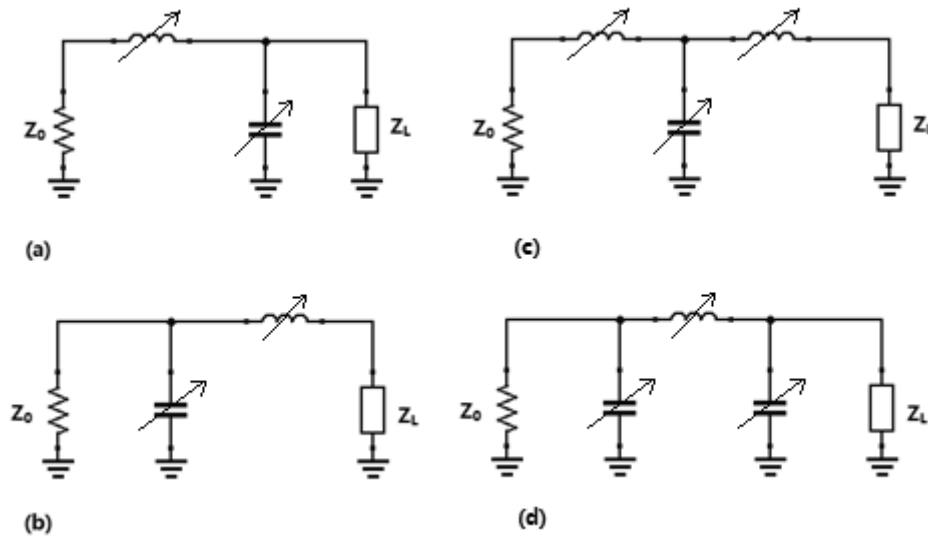


Figure 2: L-, Pi- and T-networks impedance matching (Chung, 2022).

In the T-network in Figure 2(c), two variable inductors and one variable capacitor are needed. In the Pi-network in Figure 2(d), one variable inductor and two variable capacitors are needed. Theoretically, the domain of impedance matching can cover the whole Smith Chart provided the tuning ratio is high enough. However, the need for three variable matching elements makes the circuit more complicated to implement.

Discrete variable inductors and capacitors have a few practical limitations in RFIC / MMIC designs of L, Pi or T network impedance matching. Firstly, parasitic elements give rise to parallel / series resonances and set a limit to the upper operating frequency of the inductors / capacitors. Secondly, the form factor may be too large when larger inductance / capacitance is needed. Thirdly, the required size is difficult to determine due to inaccurate closed-form expressions. Therefore, single- or double-stub impedance matching are usually used at higher microwave frequencies. Microstrip transmission lines and stub lines can be used at ultra-high microwave frequencies. However, longer transmission lines and stub lines increase the required area on the semiconductor substrate. Furthermore, these elements are difficult to tune in an integrated adaptive impedance matching system.

This paper proposes an adaptive stub matching system using phase shifters to transform dynamically varying complex load impedances for conjugate matching. The equations and design methodologies are presented. Variable phase shifter is much easier to make as compared to variable inductor and capacitor. The simplest phase shifter is just a transmission line with a predefined electrical length  $\theta = \beta l$ . That means it has low parasitic, high Q-factor, highly linear, and can be made to have wide tuning range. It can be used at ultra-high microwave frequencies. Variable phase shifter is widely used in the design of phased array antennas. An example of a low-loss and compact six-bit distributed microelectromechanical systems (MEMS) transmission line phase shifter for phased array antenna applications can be found in Teymoori *et al.* (2020). A digital phase shifter configuration is illustrated in Figure 3. By controlling the switch position of the single-pole-double-throw (SPDT) switches, the phase shift of  $M \times 2.8125^\circ$ , where  $M + 1 = 2^0 - 2^6$ , can be obtained; i.e., from 0 - 180°.

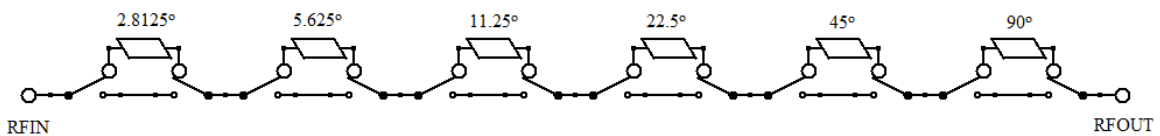


Figure 3: Digital 6-bit phase shifter configuration (Analog Devices, 2023).

To the best of the author's knowledge, this is a new method of adaptive impedance matching method incorporating tunable phase shifters to vary the electrical length of the transmission line, instead of tunable inductors / capacitors in the existing designs of adaptive impedance matching networks. Other papers on single- or double-stub tuning use stub lines with multiple short-circuit points to select (Unlu *et al.*, 2006; Zhang *et al.*, 2018), or stub lines with variable capacitors (Lu *et al.*, 2003; Vaha-Heikkila *et al.*, 2004, 2005; Whatley *et al.*, 2006) instead of a phase shifter to vary the electrical length and use only one short / open circuit at the other end of the phase shifter. In those papers, the electrical length of the transmission line connecting the load to the stub line cannot be varied. Hence, there is a forbidden region within which the impedance mismatch cannot be resolved.

## 2. ADAPTIVE IMPEDANCE MATCHING TECHNIQUE

Figure 4 shows the configuration of the adaptive stub matching system. From the RF source, the mismatch measurement block uses a directional coupler to sample a fraction of the incident and reflected signals. The signals are measured and analysed by the microprocessor to determine the reflection coefficient. The  $N$ -bit Phase Shifter 1 comprises of transmission lines with characteristic impedance  $Z_0$  to provide variable phase shift of up to  $180^\circ$ . The  $N$ -bit Phase Shifter 2 comprises of transmission lines with characteristic impedance  $Z_0$  to provide variable phase shift of up to  $90^\circ$ . Larger number of bits  $N$  can provide better phase shift resolution and accuracy of impedance matching.

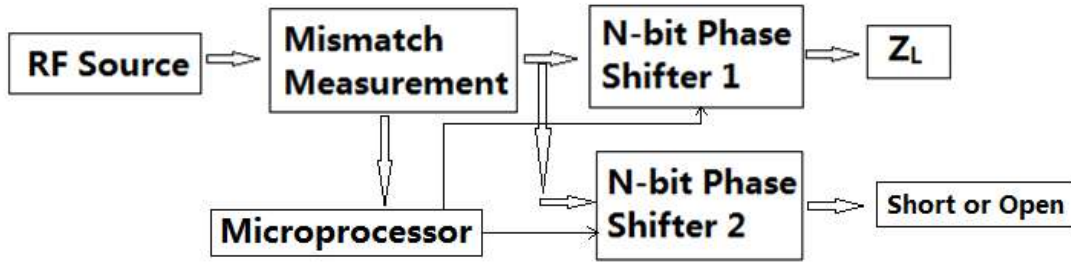


Figure 4: The adaptive stub matching system.

Consider the  $N$ -bit Phase Shifter 1 as a transmission line of length  $l$  with characteristic impedance  $Z_0$  and phase constant  $\beta$  connected to a complex load impedance  $Z_L$ . The input impedance  $Z_{in}$  at the input of the transmission line is given by the following equation:

$$Z_{in} = Z_0 \left[ \frac{Z_L + jZ_0 \tan \beta l}{Z_0 + jZ_L \tan \beta l} \right] = R_{in} + jX_{in} \quad (1)$$

$$\rho_{in} = \frac{Z_{in} - Z_0}{Z_{in} + Z_0} \quad (2)$$

For reference impedance  $Z_0 = 50 \Omega$ , the reflection coefficient  $\rho_{in}$  is given by Equation 2. As the electrical length  $\theta = \beta l$  increases from 0 to  $180^\circ$ ,  $\rho_{in}$  will trace out a concentric circle at the centre of the Smith Chart according to Equation 3, as shown in Figure 5. It is called a voltage standing wave ratio (VSWR) circle or constant-mismatch circle. It starts from the reflection coefficient of the load  $\rho_L$ .

$$\rho_{in} = \frac{Z_{in} - Z_0}{Z_{in} + Z_0} = \frac{Z_L - Z_0}{Z_L + Z_0} e^{-j2\beta l} = \rho_L e^{-j2\beta l} \quad (3)$$

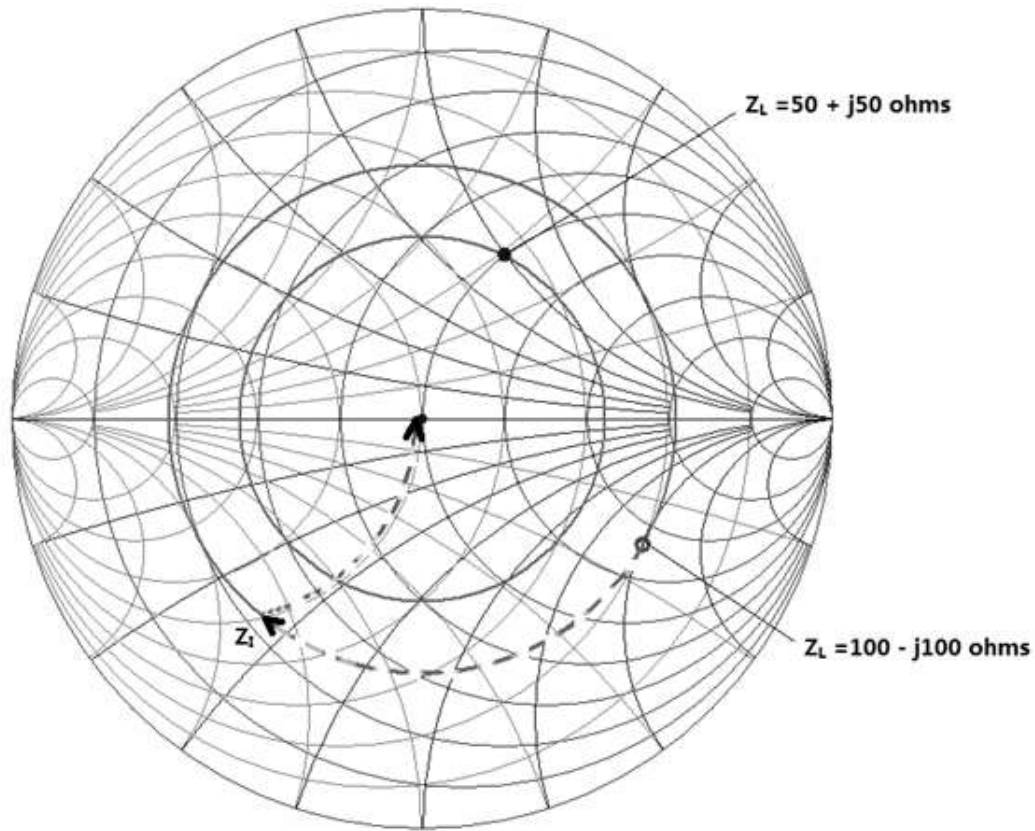


**Figure 5: VSWR circles for different values of  $Z_L$ .**

The complex load impedance  $Z_L$  is first transformed to an intermediate complex impedance  $Z_I = R_I + jX_I$  at the intersection point between the VSWR circle and the unit conductance circle, as illustrated in Figure 5 for  $Z_L = 100 - j100 \Omega$ . The required electrical length or phase shift  $\theta_1$  is provided by the  $N$ -bit Phase Shifter 1. It would be less than  $180^\circ$ . The  $N$ -bit Phase Shifter 2 (short-circuited at one end) acts as a variable length stub line with electrical length  $\theta_2$  to transform  $Z_I$  to  $50 \Omega$ . It would be less than  $90^\circ$ . This single-stub impedance matching system can also transform any complex impedance  $Z_L$  to another complex impedance  $Z_S$  for conjugate matching applications. The impedance matching domain covers the whole Smith Chart.

The reflection coefficients  $\rho_I$  of all possible intersection points between the VSWR circle and the unit conductance circle can be calculated and stored in the microprocessor memory as a lookup table. These points are simply the bottom half of the unit conductance circle in Figure 5, given by Equations 4 and 5. An automatic control system can be implemented in such a way that the phase shift  $\theta_1$  of the  $N$ -bit Phase Shifter 1 is varied until the measured reflection coefficient  $\rho_I$  (based on the system configuration in Figure 4) is near to any one point in the lookup table. The required phase shift  $\theta_2$  of  $N$ -bit Phase Shifter 2 (given by Equations 6 and 7) can be set accordingly in the real-time adaptive impedance matching operation. Alternatively, based on the initial measurement of load reflection coefficient  $\rho_L$ , the VSWR circle can be plotted on the Smith Chart. The intersection point with the unit conductance circle can be determined. Then, the required phase shifts  $\theta_1$  and  $\theta_2$  can be calculated. Thereafter, both phase shifters can be directly switched to the required settings to achieve adaptive impedance matching.

$$\rho_I = |\rho_I|e^{j\theta} = \frac{Z_I - Z_0}{Z_I + Z_0} \quad (4)$$

$$|\rho_I| = \cos \theta \quad 90^\circ < \theta < 270^\circ \quad (5)$$

$$Y_I = \frac{1}{Z_I} = \frac{1}{Z_0} \cdot \frac{1 + \rho_I}{1 - \rho_I} = \frac{1}{Z_0} + jB_I \quad (6)$$

$$\tan \theta_2 = \frac{1}{Z_0 B_I} \quad (7)$$

For  $Z_L = 100 - j100 \Omega$ , the required phase shifts are  $\theta_1 = 49^\circ$  and  $\theta_2 = 32^\circ$ . For  $Z_L = 50 + j50 \Omega$ , the required phase shifts are  $\theta_1 = 90^\circ$  and  $\theta_2 = 44^\circ$ .

If the  $N$ -bit Phase Shifter 2 is left open circuited at one end, it will act as an open-circuited stub line. In this case, the reflection coefficients  $\rho_I$  along the upper half of the unit conductance circle in Figure 5 are to be calculated and stored in the microprocessor memory as a lookup table. These points are also given by Equations 4 and 5. The following equations give the required phase shift  $\theta_2$  of  $N$ -bit Phase Shifter 2:

$$Y_I = \frac{1}{Z_I} = \frac{1}{Z_0} \cdot \frac{1+\rho_I}{1-\rho_I} = \frac{1}{Z_0} - jB_I \quad (8)$$

$$\tan \theta_2 = Z_0 B_I \quad (9)$$

For  $Z_L = 100 - j100 \Omega$ , the required phase shifts are  $\theta_1 = 101^\circ$  and  $\theta_2 = 58^\circ$ . For  $Z_L = 50 + j50 \Omega$ , the required phase shifts are  $\theta_1 = 154^\circ$  and  $\theta_2 = 46^\circ$ .

### 3. SIMULATION RESULTS

Based on the calculated phase shifts of  $\theta_1$  and  $\theta_2$  for each case above, the simulation results are shown in Figure 6. When short-circuited stub solution is chosen, the impedance matching bandwidth is slightly wider for  $Z_L = 100 - j100 \Omega$  as compared to the case for  $Z_L = 50 + j50 \Omega$ . This is because the loaded  $Q$ -factor is slightly lower for  $Z_L = 100 - j100 \Omega$ . The required phase shifts for  $\theta_1$  are 49 and  $90^\circ$  respectively.

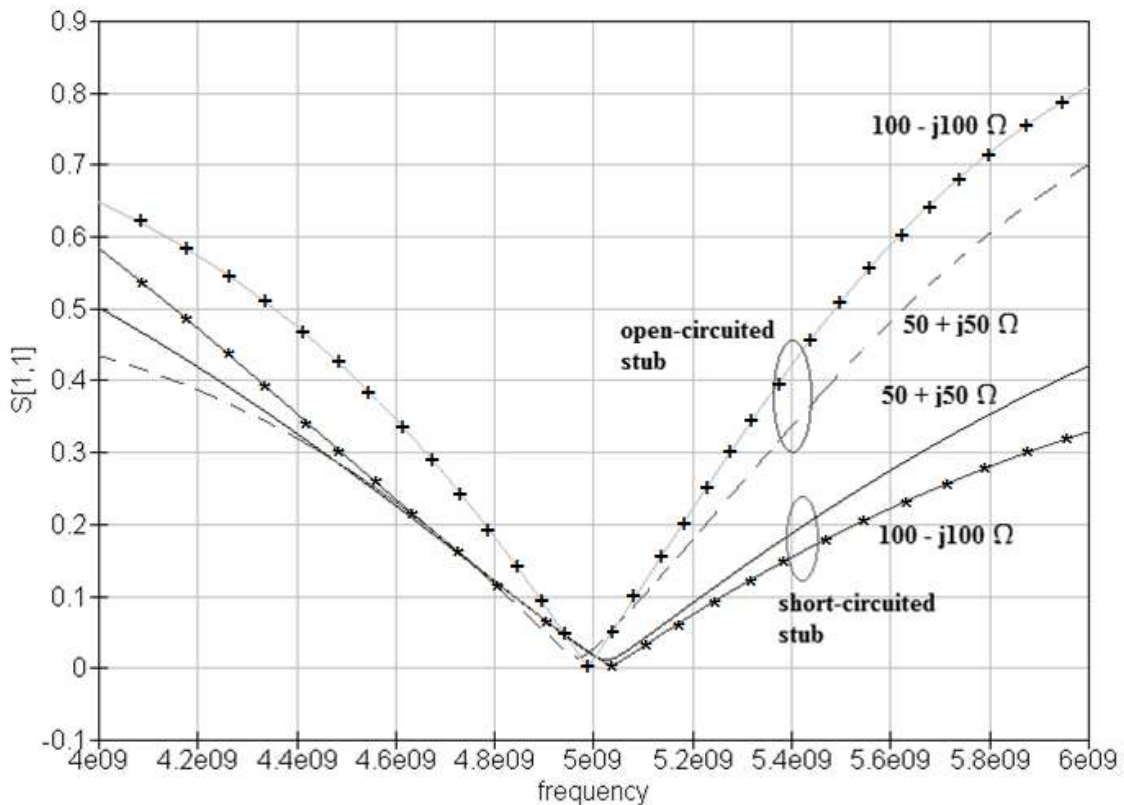


Figure 6: Simulation results for different load impedances.

Notice that the impedance matching bandwidth is narrower when the open-circuited stub solution is chosen. It is due to the larger phase shift  $\theta_l$  required when open-circuited stubs are used, resulting in higher Q-factor. The required phase shifts are  $\theta_l = 101^\circ$  for  $Z_L = 100 - j100 \Omega$ , and  $\theta_l = 154^\circ$  for  $Z_L = 50 + j50 \Omega$ . Larger phase shift has the same effect as longer transmission line, which causes the increase of Q-factor. The method to calculate the resulting Q-factor can be found in Chung (2022).

Short-circuited stub solution does not always produce wider impedance matching bandwidth but depends on the load impedance. When the load impedance is on the left-hand side of the Smith Chart (for example,  $Z_L = 25 - j25 \Omega$ ), the required phase shift  $\theta_l$  will be smaller if open-circuited stub is used. That means open-circuited stub solution would potentially produce wider impedance matching bandwidth. Conversely, the required phase shift  $\theta_l$  will be larger if short-circuited stub is used and the bandwidth would be narrower.

When the load impedance is on the right-hand side of the Smith Chart, the required phase shifts  $\theta_l$  would be smaller if short-circuited stub is used. That means short-circuited stub solution would potentially produce wider impedance matching bandwidth, as demonstrated by the simulation results in Figure 6.

#### 4. CONCLUSION

Recent research interest in the open literature is the design of adaptive impedance matching networks. Impedance of antennas can vary significantly with frequency as well as with operating conditions such as the proximity of the antenna to surrounding metal objects or dielectric material. Thus, use of tunable inductors / capacitors in L-network or Pi / T-network impedance matching are necessary for realisation of adaptive matching dynamically. This paper proposed a new method of adaptive impedance matching system using phase shifters to overcome the problems associated with the use of tunable inductors / capacitors. The complex impedance transformation using transmission lines can potentially be used at high microwave frequencies. Due to its simpler structure compared to digitally switchable array of inductors / capacitors, phase shifter can also reduce the substrate area for fabrication of impedance matching network. The equations and design methodologies for the adaptive impedance matching system are presented, including a few methods to automatically control the phase shifters. A few simulation examples are presented. The simulation results confirm the effectiveness of the system.

#### REFERENCES

- Alibakhshikenari, M., Virdee, B.S., Shukla, P., *et al.* (2020) Improved adaptive impedance matching for RF front-end systems of wireless transceivers. *Sci. Rep.*, **10**: 14065.
- Analog Devices (2023). *HMC936ALP6E GaAs MMIC 6 Bit Digital Phase Shifters Datasheet*. Analog Devices, Norwood, Massachusetts, US.
- Azpúrua, H., Saboia, M., Freitas, G.M. *et al.* (2023) A survey on the autonomous exploration of confined subterranean spaces: Perspectives from real-word and industrial robotic deployments. *Robotics Auton., Syst.*, **160**: 104304.
- Bezooijen, A., de Jongh, M.A., van Straten, F. *et al.* (2010) Adaptive impedance-matching techniques for controlling L networks. *IEEE Trans. Circ. Syst. I*, **57**: 495-505.
- Chung, B.K. (2006) Q-based design method for T network impedance matching. *Microelectron. J.*, **37**: 1007-1011.
- Chung, B.K. (2022) Integrated adaptive impedance matching using phase shifters. *J. Commun. Tech. Electron.*, **66**: 185–193.
- Fan, S., Yuan, Z. Gou, W. *et al.* (2019) A 2.45-GHz rectifier-booster regulator with impedance matching converters for wireless energy harvesting. *IEEE Trans. Microw. Theory Techni.*, **67**: 3833-3843.
- Fanfan, M., Bezooijen, A. & Mahmoudi, R. (2006) A mismatch detector for adaptive antenna impedance matching. *36<sup>th</sup> Eur. Microw. Conf.*, 10-15 September 2006, Manchester, UK
- Gu, Q., De Luis, J.R., Morris, A.S. & Hilbert, J. (2011) An analytical algorithm for Pi-network impedance tuners. *IEEE Trans. Circ. Syst. I*, **58**: 2894-2905.
- Gu, Q. & Morris, A.S. (2013) A new method for matching network adaptive control. *IEEE Trans. Microw. Theory Tech.*, **61**: 587-595.

- Jang, H., Lee, W., Yeo, T. & Yu, J. (2013) Adaptive load impedance matching using 5-port reflectometer with computationally simple measurement. *2013 Asia Pac. Microw. Conf. Proc. (APMC 2013)*, 5-8 November 2013, Seoul, South Korea.
- Lauder, D. & Sun, Y. (2020) Design considerations of antennas and adaptive impedance matching networks for RF Energy Harvesting. *2020 Eur. Conf. Circ. Theory Design (ECCTD 2020)*, 7-10 September 2020, Sofia, Bulgaria.
- Li, H., Ahmed, M. & Andrea, A. (2019) Beyond Chu's limit with Floquet impedance matching. *Phys. Rev. Lett.*, **123**: 164102.
- Li, Y., Dong, W., Yang, Q., Zhao, J., Liu, L. & Feng, S. (2019) An automatic impedance matching method based on the feedforward-backpropagation neural network for a WPT system. *IEEE Trans. Ind. Electron.*, **66**: 3963-3972.
- Li, Y. & Cheng, D. (2010) Adaptive impedance matching system. *2010 Int. Forum Inform. Tech. Appl.*, 16-18 July 2010, Kunming, China
- Lu, Y., Peroulis, D., Mohammadi, S. & Katehi, L.P.B (2003) A MEMS reconfigurable matching network for a class AB amplifier. *IEEE Microw. Wirel. Compon. Lett.*, **13**: 437-439.
- McIntosh, C. E., Pollard, R.D. & Miles, R.E. (1999) Novel MMIC source impedance tuners for on-wafer microwave noise-parameter measurements. *IEEE Trans. Microw. Theory Tech.*, **47**: 125–131.
- Neo, W.C.E., Lin, Y., Liu, X.D. etc. (2006). Adaptive multi-band multi-mode power amplifier using integrated varactor-based tunable matching networks. *IEEE J. Solid- State Circ.*, **41**: 2166-2176.
- Qingping, W., Sha, L., Jin, A.S.O. & Tian, W. (2020) Electrical impedance matching based on piezoelectric ceramics for energy harvesting application. *Mater. Tech.*, **35**: 650-655.
- Robichaud, A., Alameh, A. H., Nabki, F. & Deslandes, D. (2013) An agile matching network using phase detection for antenna tuning. *IEEE 20<sup>th</sup> Int. Conf. Circ. Syst. (ICECS 2022)*. 24-26 Oct. 2022, Glasgow, UK
- Simons, R. N. & Lee, R. Q. (1998) Impedance matching of tapered slot antenna using a dielectric transformer. *Electron. Lett.*, **34**: 2287–2289.
- Sjoblom, P. & Sjöland, H. (2005) An adaptive impedance tuning CMOS circuit for ISM 2.4-GHz band. *IEEE Trans. Circ. Syst. I*, **52**: 1115-1124.
- Teymoori, M.M., Dousti, M. & Afrang,, S. (2020) A low-loss compact six-bit DMTL phase shifter for phased array antenna applications. *Int. J. Circ. Theory Appl.*, **48**: 2111– 2129.
- Thirappa, K., Lim, E.H., Bong, F.L. & Chung, B.K. (2021) Slim RFID tag antenna for metallic tools with narrow footprint. *IEEE J. Radio Freq. Identification*, **5**: 182-190.
- Thompson, M. & Fidler, J. F. (2001) Application of the genetic algorithm and simulated annealing to LC filter tuning. *Proc. Inst. Elect. Eng. Circ. Devices Syst.*, **148**: 177–182.
- Unlu, M., Topalli, K., Atasoy, H.I. *et al.* (2006) A reconfigurable RF MEMS triple stub impedance matching network. *2006 Eur. Microw. Conf.*, 10-15 September 2006, Manchester, UK.
- Vaha-Heikkilä, T., Varis, J., Tuovinen, J. & Rebeiz, G. M. (2005) W-band RF MEMS double and triple-stub impedance tuners. *IEEE MTT-S Int. Microw. Symp. Digest 2005*, 17-17 June 2005, Long Beach, California, US
- Vähä-Heikkilä, T., Varis, J., Tuovinen, J. and Rebeiz, G. M. (2004) A 6-20 GHz Reconfigurable RF MEMS Impedance Tuner. *IEEE MTT-S Int. Microw. Symp. Digest*, Fort Worth, Texas, USA.
- Whatley, R.B., Zhou, Z. & Melde, K. L. (2006) Reconfigurable RF impedance tuner for match control in broadband wireless devices. *IEEE Trans. Antennas Prop.*, **54**: 470-478.
- Zhang, T., Che, W., Chen, H. and Xue, Q. (2018) Reconfigurable impedance matching networks with controllable phase shift. *IEEE Trans. Circ. Syst. II*, **65**: 1514-1518.
- Zhang, H.T., Gao, H. & Li, G.P. (2005) Broad-band power amplifier with a novel tunable output matching network. *IEEE Trans. Microw. Theory Tech.*, **53**: 3606–3614.

# EVALUATION OF THE EFFECT OF RADIO FREQUENCY INTERFERENCE (RFI) ON DUAL-FREQUENCY GLOBAL NAVIGATION SATELLITE SYSTEM (GNSS)

Dinesh Sathyamoorthy\*, Hafizah Mohd Yusoff, Ahmad Firdaus Ahmad Kazmar, Mohd Zuryn Mohd Daud & Maizurina Kifli

Science & Technology Research Institute for Defence (STRIDE), Ministry of Defence, Malaysia

\*Email: dinesh.sathyamoorthy@stride.gov.my

## ABSTRACT

*This paper is aimed at evaluating the effect of radio frequency interference (RFI) on the performance of a Garmin GPSMAP 66sr dual-frequency Global Navigation Satellite System (GNSS) receiver. This study is conducted via field evaluations for the GPS L1 coarse acquisition (C/A) and L5 signals, as well as Galileo E1 open service (OS) and E5a signals, for three conditions: 1) GPS only; 2) single frequency GPS L1 C/A and Galileo E1 OS; and 3) dual-frequency GPS L1 C/A and L5 as well as Galileo E1 OS and E5a. The findings of this study highlight the advantages of dual-frequency multi-GNSS in degraded environments, whereby it is able to provide lower probable errors as compared to the other modes, as the use of multiple frequency bands allows for more consistent tracklogs and improved positioning in challenging environments.*

**Keywords:** *Global Navigation Satellite System (GNSS) field evaluation; radio frequency interference (RFI); degraded environment; probable error; GNSS satellite geometry.*

## 1. INTRODUCTION

Global Navigation Satellite System (GNSS) refers to constellations of satellites providing signals from space that transmit positioning and timing data to GNSS receivers. It includes the four major global systems, which are Global Positioning System (GPS), Galileo, BeiDou and GLONASS, as well as regional systems such as Quasi-Zenith Satellite System (QZSS) and Navigation Indian Constellation (NAVIC). The advantage of having access to multiple satellites or multi-GNSS is for heightened accuracy, redundancy and availability. If the line of sight to satellites is obstructed, having access to multiple satellites ensures uninterrupted service provision. These GNSS systems employ multiple frequency bands, whereby GNSS receivers track more than one signal from each satellite on different frequencies, which allows for improved positioning in challenging environments (Knedlik, 2016; Kaplan & Hegarty, 2017; Jin *et al.*, 2022).

This paper is aimed at evaluating the effect of radio frequency interference (RFI) on the performance of a Garmin GPSMAP 66sr dual-frequency GNSS receiver. With the increasing threat of GNSS interference, the evaluation of the effect of RFI on GNSS performance has received significant attention (GPS World, 2019; Harrison *et al.*, 2020; Islam *et al.*, 2022).

The evaluated GNSS receiver is capable to observe GPS, GLONASS, Galileo and QZSS, as well as perform dual-frequency observations for GPS, Galileo and QZSS (Garmin, 2021). Based on the functionalities of the receiver, this study is conducted for the GPS L1 coarse acquisition (C/A) and L5 signals, as well as the Galileo E1 open service (OS) and E5a signals. The GPS L1 C/A and Galileo E1 OS signals have fundamental frequency of 1,575.42 MHz with code structures that modulate the signals over 2 and 4 MHz bandwidths respectively. The GPS L5 and Galileo E5a



signals have fundamental frequency of 1,176.45 MHz with code structures that modulate the signals over 20 MHz bandwidths (Kaplan & Hegarty, 2017; Povero, 2019; DOD, 2020; ESA, 2021).

This study is conducted via field evaluations for three conditions: 1) GPS only; 2) single frequency GPS L1 C/A and Galileo E1 OS; and 3) dual-frequency GPS L1 C/A and L5 as well as Galileo E1 OS and E5a. In our previous studies, field evaluations were used to study the effects of RFI on GPS performance (Dinesh *et al.*, 2010; Ahmad Norhisyam *et al.*, 2013).

## 2. METHODOLOGY

The tests in this study were conducted on 28 December 2022 at the Science & Technology Research Institute for Defence's (STRIDE) Block B bridge (Figure 1). While the chosen study area is not an ideal open space location for GNSS evaluation, the buildings and trees in the vicinity allow for evaluation of GNSS performance in the presence of line-of-sight obstructions and multipath.



**Figure 1: Test area located at N 2° 58.084' E 101° 48.638'**  
(Source: Screen capture from Google Earth)

The test setup employed is as shown in Figure 2. Interference signals are generated using an IFR 2023B signal generator (IFR, 1999) and transmitted via a Hyperlog 60180 directional antenna (Aaronia, 2009). An Advantest U3751 spectrum analyser (Advantest, 2009) is used to ensure that there are no external interference signals during the tests.

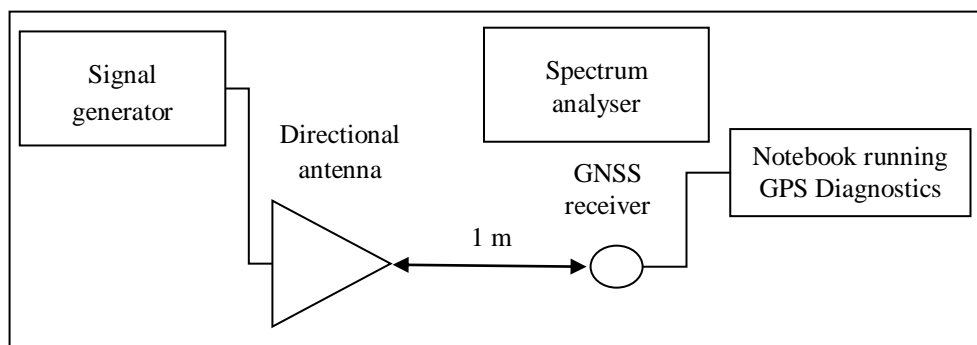


**Figure 2: Test setup employed for evaluation of the effect of RFI.**

The interference signal used is a frequency modulated (FM) signal with information frequency of 5 kHz and bandwidth of 2 MHz used. Interference signal transmission is started at power level of -140 dBm. The power level is increased by increments of 3 dBm at 1 min, and the corresponding values of horizontal probable error (HPE), vertical probable error (VPE) and estimate probable error (EPE) are recorded using GPS Diagnostics (CNET, 2008). The tests scenarios employed are shown in Table 1.

**Table 1: Test scenarios employed for the evaluation of the effect RFI.**

Scenario	Mode	Interference Signal
1	GPS only	L1 / E1
2	Single frequency multi-GNSS	L1 / E1
3	Dual-frequency multi-GNSS	
4		L1 / E1 (L5 / E5a jammed)
5		L5 / E5a (L1 / E1 jammed)
6		L1 / E1 and L5 / E5a

### 3. RESULTS & DISCUSSION

Based on the results obtained, as shown in Figures 3-8 and Table 2, the following observations can be made:

- 1) With increasing interference signal power level, probable error values increase due to decreasing carrier-to-noise density ( $C/N_0$ ) levels for GNSS satellites tracked by the receiver, which is the ratio of received GNSS signal power level to noise density. Lower  $C/N_0$  levels result in increased data bit error rate when extracting navigation data from GNSS signals, and hence, increased carrier and code tracking loop jitter. This, in turn, results in more noisy range measurements and thus, less precise positioning (USACE, 2011; Kaplan & Hegarty, 2017; DOD, 2020).
- 2) At lower interference signal power levels, Scenario 1 (GPS only, Figure 3) and Scenario 2 (single frequency multi-GNSS, Figure 4) have similar probable errors. However, at higher interference signal power levels, the higher number of GNSS satellites observed for the multi-GNSS mode allows it to have lower probable errors as compared to the GPS only mode.
- 3) For Scenario 3 (dual-frequency multi-GNSS, Figure 5) with increasing interference signal power levels for the L1 / E1 band (frequency of 1,575.42 MHz), no changes are observed in probable errors, as the L5 / E5a band (frequency of 1,176.45 MHz) is not affected by the interference signal. Lower probable errors are observed as compared to Scenarios 1 and 2, as the L5 / E5a signals have larger bandwidth and code length, higher chipping rate as well as stronger transmission power level, which increase its accuracy (Kaplan & Hegarty, 2017; Povero, 2019; DOD, 2020; ESA, 2021).
- 4) For Scenario 4 (dual-frequency multi-GNSS with the L5 / E5a band completely jammed, Figure 6), it is effectively a single frequency L1 / E1 band multi-GNSS mode, with similar probable errors to Scenario 2 for increasing interference signal power levels for the L1 / E1 band.
- 5) For Scenario 5 (dual-frequency multi-GNSS with the L1 / E1 band completely jammed, Figure 7), it is effectively a single frequency L5 / E5a band multi-GNSS mode. For increasing interference signal power levels for the L5 / E5a band, lower probable errors are observed as compared to the single frequency L1 / E1 band multi-GNSS mode in Scenarios 2 and 4, due to the robustness of the L5 / E5a signals.

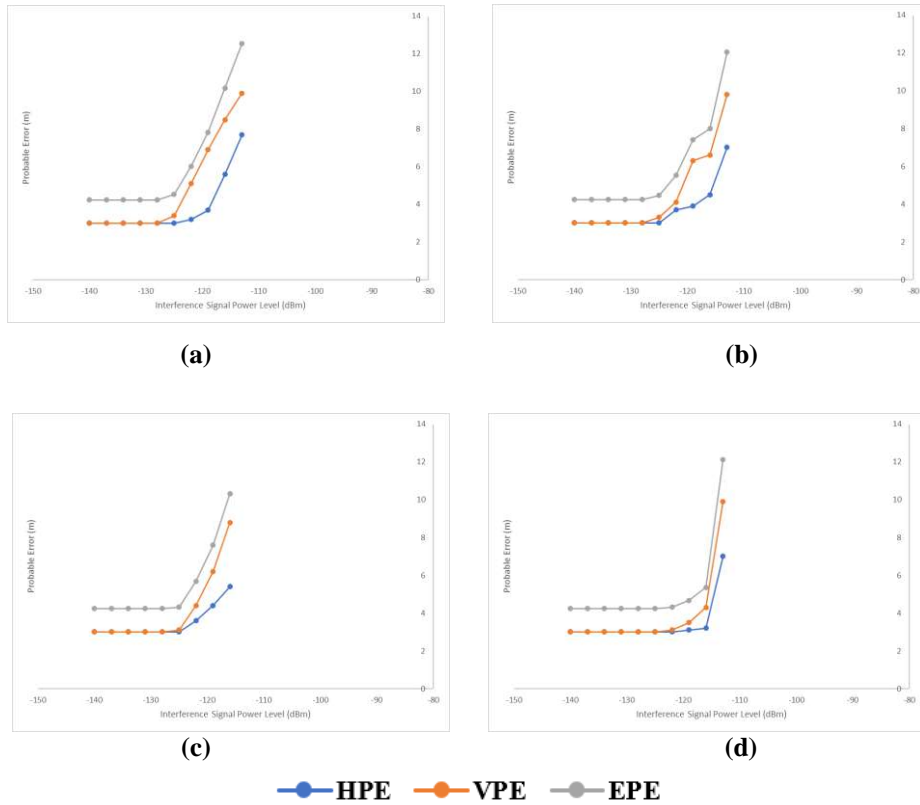


**Figure 3: Recorded probable error values for Scenario 1 (GPS only) for: (a) Reading 1 (b) Reading 2 (c) Reading 3 (d) Reading 4.**

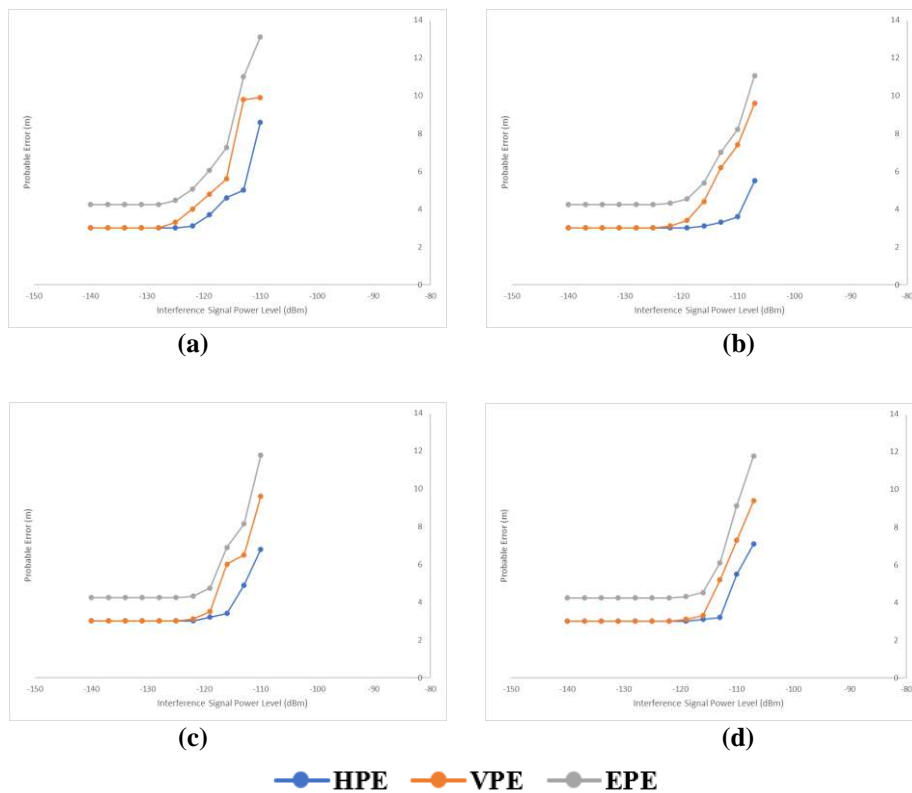


**Figure 4: Recorded probable error values for Scenario 2 (single frequency multi-GNSS) for: (a) Reading 1 (b) Reading 2 (c) Reading 3 (d) Reading 4.**

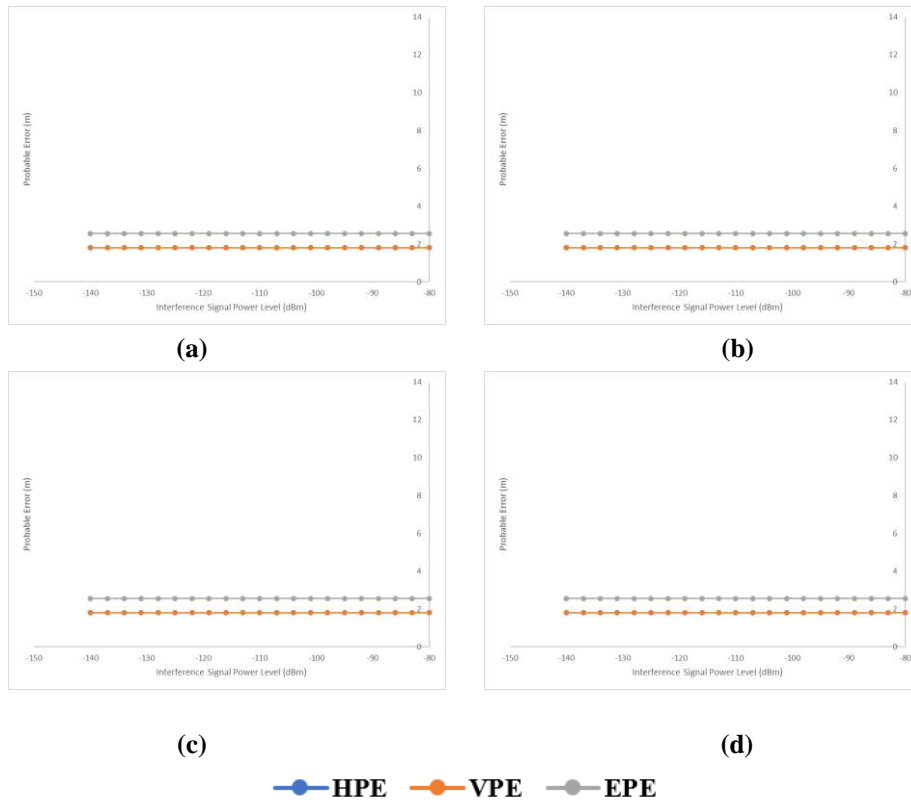


**Figure 5: Recorded probable error values for Scenario 3 (dual-frequency multi-GNSS) with increasing interference signal power levels for the L1 / E1 band for: (a) Reading 1 (b) Reading 2 (c) Reading 3 (d) Reading 4.**

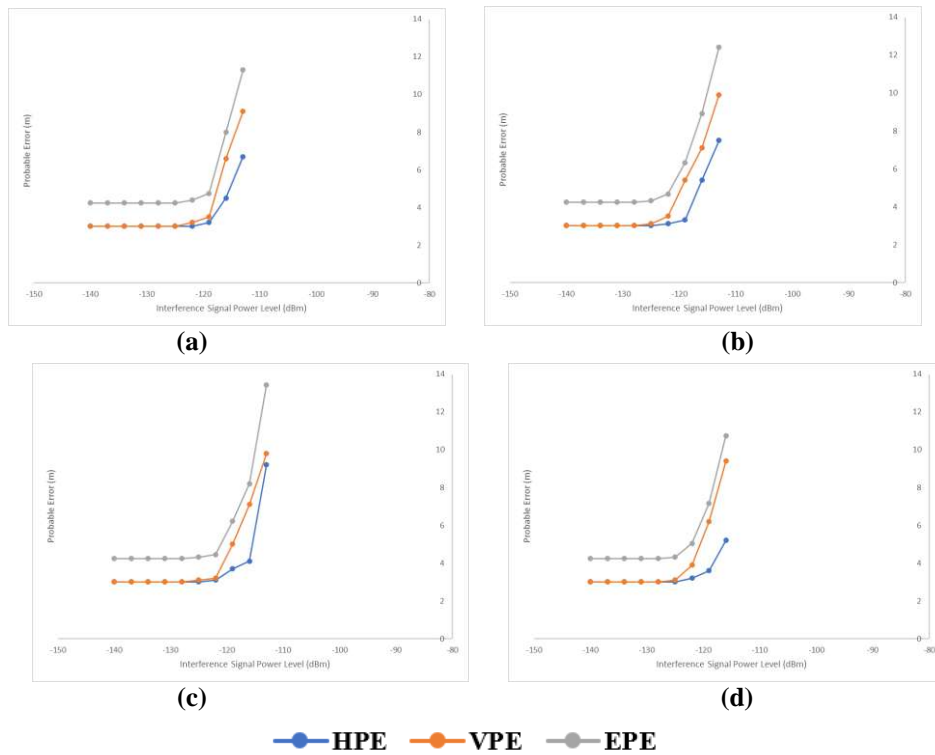


**Figure 6: Recorded probable error values for Scenario 4 (dual-frequency multi-GNSS with the L5 / E5a band completely jammed) with increasing interference signal power levels for the L1 / E1 band for: (a) Reading 1 (b) Reading 2 (c) Reading 3 (d) Reading 4.**

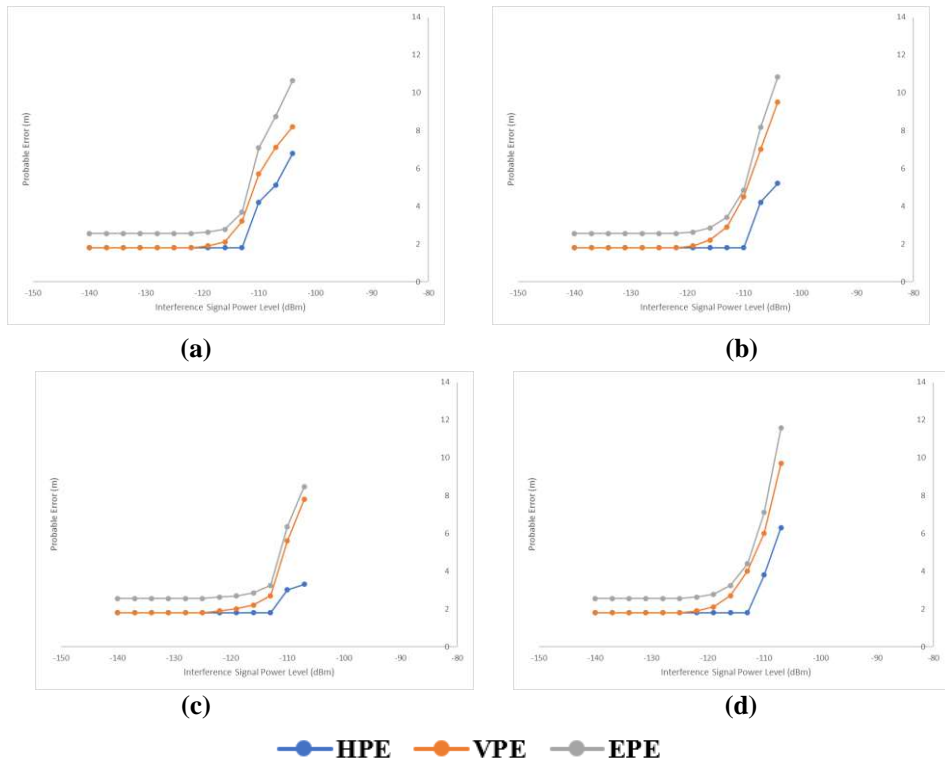


**Figure 7: Recorded probable error values for Scenario 5 (dual-frequency multi-GNSS with the L1 / E1 band completely jammed) with increasing interference signal power levels for the L5 / E5a band for: (a) Reading 1 (b) Reading 2 (c) Reading 3 (d) Reading 4.**

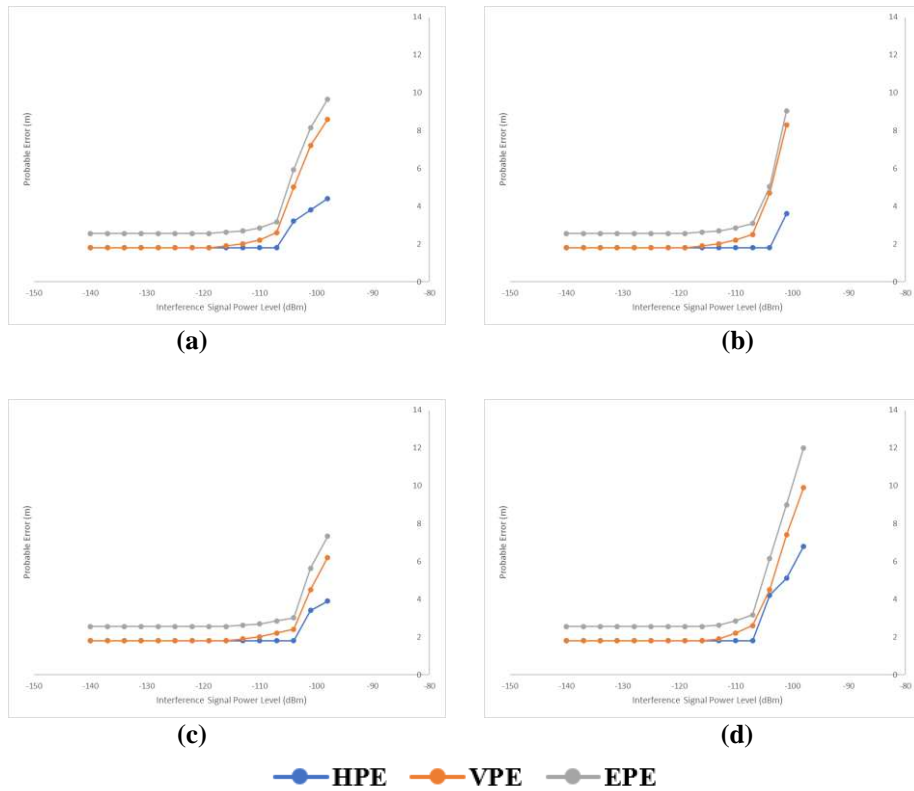


**Figure 8: Recorded probable error values for Scenario 6 (dual-frequency multi-GNSS) with increasing interference signal power levels for the L1 / E1 and L5 / E5a bands for: (a) Reading 1 (b) Reading 2 (c) Reading 3 (d) Reading 4.**

**Table 2: Interference signal power levels at which first degradation of accuracy is noticed and location fix is lost.**

Scenario	Mode	Interference Signal	Reading	Interference Signal Power Level (dBm)			
				First degradation of accuracy	Location fix lost		
1	GPS only	L1 / E1	1	-125	-110		
			2	-125	-110		
			3	-125	-113		
			4	-122	-110		
2	Single Frequency Multi-GNSS		1	-125	-107		
			2	-122	-104		
			3	-122	-107		
			4	-119	-104		
3	Dual-Frequency Multi-GNSS		1	-	-		
			2	-	-		
			3	-	-		
			4	-	-		
4		Dual-Frequency Multi-GNSS	L1 / E1 (L5 / E5a jammed)	1	-122	-110	
				2	-125	-110	
				3	-125	-110	
				4	-125	-113	
5			Dual-Frequency Multi-GNSS	L5 / E5a (L1 / E1 jammed)	1	-119	-101
					2	-119	-101
					3	-122	-104
					4	-122	-104
6	Dual-Frequency Multi-GNSS			L1 / E1 and L5 / E5a	1	-116	-95
					2	-116	-98
					3	-113	-95
					4	-113	-95

- 6) For Scenario 6 (dual-frequency multi-GNSS, Figure 8), for increasing interference signal power levels for the L1 / E1 and L5 / E5a bands, the lowest probable errors for all the readings are observed. This is due to the use of multiple frequency bands which allows for more consistent tracklogs and improved positioning in challenging environments, as well as correction of ionosphere errors. In addition, dual-frequency systems are better able to filter out multipath signals from obstacles, which in the case of this study are the buildings and trees in the test location (Kaplan & Hegarty, 2017; Povero, 2019; DOD, 2020; ESA, 2021). This highlights the advantages of multi-frequency GNSS in degraded environments.

It is observed that the interference signal power levels required to affect the GNSS signals in this study are lower as compared to previous studies conducted via field evaluation (Dinesh *et al.*, 2010; Ahmad Norhisyam *et al.*, 2013). This is due to the location of the study with buildings and trees that caused line-of-sight obstructions and multipath, which resulted in lower GNSS signal power level reaching the GNSS receiver, and thus, lower interference signal power level being required to affect it. Nonetheless, these interference signal power level thresholds are still higher than the expected GNSS signal strength (approximately -160 to -130 dBm). This is as the noise-like GNSS signal code structures allow for the signals to be received at low levels of interferences.

Varying probable error patterns are observed for each of the readings. This is due to the GNSS satellite constellation being dynamic, causing varying satellite geometry over time, resulting in GNSS accuracy being location / time dependent (USACE, 2011; Kaplan & Hegarty, 2017; DOD,

2020). Variation in other GNSS error parameters could have also resulted in the variation of probable error patterns.

In general, values of VPE are higher as compared to HPE for GNSS readings, as overhead satellites have higher  $C/N_0$  levels as compared to satellites above the horizon, resulting in GNSS height solution being less precise than the horizontal solution (USACE, 2011; Kaplan & Hegarty, 2017; DOD, 2020). However, for the evaluated GNSS receiver, at lower interference signal power levels, the values of VPE and HPE are similar, as the receiver's high receiver sensitivity allows for similar  $C/N_0$  levels for overhead satellites and satellites above the horizon. At higher interference signal power levels, the values of VPE become larger than HPE, due to significant reduction of  $C/N_0$  levels for satellites above the horizon as compared to overhead satellites.

The primary limitation of this study is that field evaluations are subject to various error parameters, such as ionospheric and tropospheric delays, GNSS satellite clock and ephemeris errors, GNSS satellite positioning and geometry, external RFI, as well as obstructions and multipath, which are uncontrollable by users. In this respect, the scope for future work is for the study to be conducted using GNSS simulation, which allows for the tests to be conducted with various repeatable conditions, as defined by the users. As the tests are conducted in controlled laboratory environments, they are not be inhibited by unintended signal interferences and obstructions (Pozzobon *et al.*, 2013; Arul Elango & Sudha, 2016; Bi & Yuan *et al.*, 2021; Emerick, 2022). In our previous studies, GNSS simulation was used to evaluate the vulnerabilities of GPS to RFI (Dinesh *et al.*, 2012a, 2017a, 2020), varying power levels (Dinesh *et al.*, 2012b, Dinesh, 2021), multipath (Dinesh *et al.*, 2013, 2014), GPS satellite clock error (Dinesh *et al.*, 2015a, 2019), varying speeds (Dinesh *et al.*, 2015b, 2022), power consumption (Dinesh *et al.*, 2016) and GPS antenna orientation (Dinesh *et al.*, 2017b). More recently, GNSS simulation was used to study the performance of single frequency L1 / E1 band multi-GNSS for varying GNSS signal power levels and RFI interoperability (Dinesh *et al.*, 2023). In addition, the performance of a wider range of multifrequency GNSS receivers should be evaluated.

#### 4. CONCLUSION

The findings of this study have highlighted the advantages of dual-frequency multi-GNSS in degraded environments. At higher interference signal power levels, the higher number of GNSS signals observed for the GPS + Galileo mode allows it to have lower probable errors as compared to the GPS only mode. The single frequency L5 / E5a band multi-GNSS mode is able to provide lower probable errors as compared to the single frequency L1 / E1 band multi-GNSS mode due to the robustness of the L5 / E5a signals. The dual-frequency multi-GNSS mode provides lower probably errors as compared to the other modes, as the use of multiple frequency bands allows for more consistent tracklogs and improved positioning in challenging environments.

#### REFERENCES

- Aaronia (2009). *Precompliance Test Antenna Series HyperLOG® 60xxx: Span 680 MHz to 18 GHz*. Aaronia AG, Strickscheid, Germany.
- Advantest (2009). *U3741/3751 Spectrum Analyzers*. Advantest Corporation, Chiyoda-ku, Tokyo, Japan.
- Ahmad Norhisyam, I., Dinesh, S. & Azman, M.S. (2013). Effect of radio frequency interference (RFI) on the performance of Global Positioning System (GPS) static observations. *9<sup>th</sup> IEEE Colloq. Signal Process. Appl. (CSPA 2013)*, 8-10 March 2013, Kuala Lumpur.
- Arul Elango, G. & Sudha, G.F. (2016). Design of complete software GPS signal simulator with low complexity and precise multipath channel model. *J. Electr. Syst., Inform. Tech.*, **3**: 161-180.
- Bi, Y. & Yuan, J. (2021). A portable GPS signal simulator design based on ZYNQ. *2<sup>nd</sup> Int. Symp. Comp. Eng. Intell. Comm. (ISCEIC 2021)*, 6-8 August 2021, Nanjing, China.

- CNET (2008). *GPSDiag 1.0*. Available online at: [https://download.cnet.com/GPSDiag/3000-2130\\_4-10055902.html](https://download.cnet.com/GPSDiag/3000-2130_4-10055902.html) (Last access date: 9 June 2022).
- Dinesh, S., Wan Mustafa, W.H., Mohd Faudzi, M., Kamarulzaman, M., Hasniza, H., Nor Irza Shakhira, B., Siti Robiah, A., Shalini, S., Jamilah, J., Aliah, I., Lim, B.T., Zainal Fitry, M.A., Mohd Rizal, A.K., Azlina, B. & Mohd Hasrol, H.M.Y. (2010). Evaluation of the effect of radio frequency interference (RFI) on Global Positioning System (GPS) accuracy. *Defence S&T Tech. Bull.*, **3**: 100-118.
- Dinesh, S, Mohd Faudzi, M. & Zainal Fitry, M.A. (2012a). Evaluation of the effect of radio frequency interference (RFI) on Global Positioning System (GPS) accuracy via GPS simulation. *Defence. Sci. J.*, **62**: 338-347.
- Dinesh, S., Mohd Faudzi, M., Rafidah, M., Nor Irza Shakhira, B., Siti Robiah, A., Shalini, S., Aliah, I., Lim, B.T., Zainal Fitry, M.A., Mohd. Rizal, A.K., & Mohd Hasrol, H.M.Y. (2012b). Evaluation of the effect of varying Global Positioning System (GPS) signal power levels on GPS accuracy. *Defence S&T Tech. Bull.*, **5**: 57-71.
- Dinesh, S., Shalini, S., Zainal Fitry, M.A. & Siti Zainun, A. (2013). Evaluation of the repeatability of Global Positioning System (GPS) performance with respect to GPS satellite orbital passes. *Defence S&T Tech. Bull.*, **6**: 130-140.
- Dinesh, S., Shalini, S., Zainal Fitry, M.A., Siti Zainun, A., Siti Robiah, A., Mohd Idris, I. & Mohd Hasrol Hisam, M.Y. (2014). Evaluation of the effect of commonly used materials on multipath propagation of Global Positioning System (GPS) signals via GPS simulation. *Adv. Mil. Tech.*, **9**: 81-95.
- Dinesh, S., Shalini, S., Zainal Fitry, M.A., Asmariah, J. & Siti Zainun, A. (2015a). Evaluation of the effect of Global Positioning System (GPS) satellite clock error via GPS simulation. *Defence S&T Tech. Bull.*, **8**: 51-62.
- Dinesh, S., Shalini, S., Zainal Fitry, M.A., Asmariah, J. & Siti Zainun, A. (2015b). Evaluation of the accuracy of Global Positioning System (GPS) speed measurement via GPS simulation. *Defence S&T Tech. Bull.*, **8**: 121-128.
- Dinesh, S., Shalini, S., Zainal Fitry, M.A., Asmariah, J. & Siti Zainun, A. (2016). Evaluation of trade-off between Global Positioning System (GPS) accuracy and power saving from reduction of number of GPS receiver channels. *Appl. Geomatics*, **8**: 67-75.
- Dinesh, S., Zainal Fitry, M.A. & Shahrudin, A.H. (2017a). Evaluation of Global Positioning System (GPS) adjacent band compatibility via GPS simulation. *Defence S&T Tech. Bull.*, **10**: 229 – 235.
- Dinesh, S., Shalini, S., Zainal Fitry, M.A., Mohamad Firdaus, A., Asmariah, J. & Siti Zainun, A. (2017b). Evaluation of the effect of Global Positioning System (GPS) antenna orientation on GPS performance. *Defence S&T Tech. Bull.*, **10**: 33-39.
- Dinesh, S., Zainal Fitry, M.A & Esa, S. (2019). Evaluation of the effectiveness of receiver autonomous integrity monitoring (RAIM) in Global Positioning System (GPS) receivers. *Defence S&T Tech. Bull.*, **12**: 295-300.
- Dinesh, S., Zainal Fitry, M.A, Esa, S., Shahrudin, E.S., Ahmad Firdaus, A.K & Zaherudin, Z. (2020). Evaluation of the vulnerabilities of unmanned aerial vehicles (UAVs) to Global Positioning System (GPS) jamming and spoofing. *Defence S&T Tech. Bull.*, **13**: 333-343.
- Dinesh, S. (2021). Evaluation of accuracy of Global Positioning System (GPS) receivers. *Defence S&T Tech. Bull.*, **14**: 211-216.
- Dinesh, S., Hafizah, M.Y., Ahmad Firdaus, A.K. Mohd Zuryn, M.D. & Maizurina, K. (202). Evaluation of performance of Global Positioning System (GPS) speed meters. *Defence S&T Tech. Bull.*, **15**: 222-227.
- Dinesh, S., Hafizah, M.Y., Ahmad Firdaus, A.K. Mohd Zuryn, M.D. & Maizurina, K. (2023). Evaluation of multi-GNSS performance via GNSS simulation. *Defence S&T Tech. Bull.*, **16**: 13-23.



- DOD (Department of Defence) (2020). *Global Positioning System Standard Positioning Service Performance Standard, Command, Control, Communications, and Intelligence, 5<sup>th</sup> Ed.* Department of Defence (DOD), Washington D.C.
- Emerick, M. (2022). *EUSPA to hold GNSS Signal Simulator Manufacturers Forum in December.* Available online at: <https://www.gpsworld.com/euspa-to-hold-gnss-signal-simulator-manufacturers-forum-in-december> (Last access date: 23 November 2022).
- ESA (European Space Agency) (2021). *European GNSS (Galileo) Open Service Signal-in-Space Interface Control Document.* European Space Agency (ESA), Paris, France.
- Garmin (2021). *GPSMAP 66 Owner's Manual.* Garmin International Inc., Olathe, Kansas.
- GPS World (2019). *Year-Long Ocean Cruise Finds GNSS Interference...Everywhere.* Available online at: <https://www.gpsworld.com/year-long-ocean-cruise-finds-gnss-interference-everywhere> (Last access date: 19 April 2020).
- Harrison, T., Johnson, K., Roberts, T.G. & Way, T. (2020). *Space Threat Assessment 2020.* Center for Strategic and International Studies (CSIS), Washington, D.C.
- IFR (1999). *2023A/B, 2025 Signal Generators.* IFR Americas Inc., Wichita, Kansas.
- Islam, S., Bhuiyan, M.Z.H., Thombre, S. & Kaasalainen, S. (2022). Combating single-frequency jamming through a multi-frequency, multi-constellation software receiver: A case study for maritime navigation in the Gulf of Finland. *Sensors*, **22**: 2294
- Jin, S., Qisheng, W. & Dardanelli, G. (2022). *A Review on Multi-GNSS for Earth Observation and Emerging Applications.* *Remote Sens.*, **14**: 3930.
- Kaplan, E.D. & Hegarty, C.J. (2017). *Understanding GPS: Principles and Applications.* Artech House, Norwood, Massachusetts.
- Knedlik, S. (2016). *Introduction to Satellite Navigation, Inertial Navigation, and GNSS/INS Integration.* Springer, Berlin, Germany.
- Povero, G. (2019). *GNSS Signals Introduction.* Links Foundation, Torino, Italy.
- Pozzobon, O., Sarto, C., Chiara, A.D., Pozzobon, A., Gamba, G., Crisci, M. & Ioannides, R. (2013). Developing a GNSS position and timing authentication testbed: GNSS vulnerability and mitigation techniques. *Inside GNSS*, **8**: 45-53.
- USACE (US Army Corps of Engineers) (2011). *Engineer Manual EM 1110-1-1003: NAVSTAR Global Positioning System Surveying.* US Army Corps of Engineers (USACE), Washington D.C.

# DEVELOPMENT OF FRAMEWORK FOR QUALITY INDEX MODEL OF DEFENCE AEROSPACE PRODUCTS

Manmeet Singh<sup>1,2,\*</sup> & Nilesh Ware<sup>1</sup>

<sup>1</sup>Department of Technology Management, Defence Institute of Advanced Technology, India

<sup>2</sup>Terminal Ballistics Research Laboratory, Defence Research and Development Organisation (DRDO), India

\*Email: ms\_pec@yahoo.com

## ABSTRACT

*Quantitative assessment of quality of defence aerospace products is required for comparison of the product quality of different products. The objective of this research is to develop a framework for quality index model (QIM) of defence aerospace products. Delphi study is carried out for ranking nine quality factors and their 36 sub-factors. This ranking is then used to evaluate weightage of the quality factors and sub-factors using equal weight (EW), rank sum weight (RSW), rank exponent weight (REW), rank reciprocal weight (RRW), rank order centroid weight (ROCW) and rank sum reciprocal weight (RSRW) methods. In addition, the focus group study is carried out to decide on the rating of quality factors and sub-factors for 10 existing defence aerospace products. Analysis of variance (ANOVA) is used to examine the regularity of the answers. The QIM is validated using data generated by a control group for the defence aerospace products.*

**Keywords:** *Quality index model (QIM); Delphi; analysis of variance (ANOVA); validation; focus group.*

## 1. INTRODUCTION

Defence aerospace products require excessive focus on quality and reliability because of their requirement of operation and availability is expected to be high. Presently the quality of a product cannot be quantified unless it is utilised for a specified time period. However, for comparison of the product before utilisation, there should be quantified parameters for quality apart from the technical specifications. The quantification of quality will help in associating minor characteristics linked to quality across a wide category of defence aerospace products. This will in turn facilitate in comparison, planning and decision making (Argotti *et al.*, 2019; Iorga *et al.*, 2022). In order to quantitatively assess quality, there is a requirement to develop a proper framework of quality index model (QIM) for defence aerospace products. The QIM will help in quantifying the quality of products during the design stage, and categorise them for their quality and customer satisfaction levels.

A comprehensive literature review has been carried out considering various index models to measure the quality of a product or service. The reliability improvement through failure root cause analysis has been done by Singh & Nandula (2020). The certification requirements for defence aerospace products were identified by Singh *et al.* (2022), and a comparison of quality and reliability practices by different public design centres in India was conducted by Singh & Ware (2023a). Landry *et al.* (1983) studied on model validation and related issues, while Raju *et al.* (2012) investigated on the performance measurement indices for maintenance of military aircrafts. A risk management system for rail construction projects was proposed by Qing *et al.* (2014) and unit cost life index for non-periodic preventive maintenance of a series parallel system was developed by Wang & Lin (2011). Raptis *et al.* (2015) proposed a methodology of power quality index for electric grids, while Cosco *et al.* (2015) validated a successful aging index for human beings. Wei (2009) constructed a service quality index

for banks and Deng *et al.* (2013) proposed a hotel customer satisfaction index to propose customer satisfaction level of tourists in international hotels. Temizer & Turkyilmaz (2012) developed and tested a student satisfaction index for higher education institutions. Employee satisfaction index model and quick discrimination index for adults were proposed by Hsu & Wang (2008) and Ponterotto *et al.* (1995) respectively. A framework for habitat suitability index for oyster habitation was developed and validated by Theuerkauf & Lipcius (2016), whereas Soniat & Brody (1988) field-tested the habitat suitability index for oysters. The quality indices for peach quality considering firmness, sugar content and acidity were proposed by Zhang *et al.* (2008). Crop specific drought index and nutrient rich foods index were developed and validated by Meyer *et al.* (1993) and Drewnowski (2013) respectively. Scott (1998) validated an environment accident index, while Ginoux & Torres (2003) developed and validated a total ozone mapping spectrometer aerosol index for dust plumes. A weighted arithmetic water quality index for studying the appropriateness of water for drinking was used by Satish Chandra *et al.* (2017), and Feng *et al.* (2015) proposed a dynamic water QIM for classifying the quality of river water. In addition, Parween *et al.* (2022) developed a quantitative approach to assess water quality of Mahananda river. Dengiz (2019) used weighted soil quality index to study rice cultivation in the plains of Turkey, while Zhan *et al.* (2018) proposed a geographical detector model using socio-economic and natural factors for air pollution alleviation in China. The research gap identified is that there is no QIM available in the literature for assessing the quality of defence aerospace products.

In the present work, a Delphi study is conducted to rank the nine quality factors and their 36 sub-factors, which were identified as quality impact indicators (QII) by Singh & Ware (2023b). After the Delphi study, a focus group study is carried out to develop the framework for QIM of defence aerospace products. The QIM is validated for the 10 defence aerospace products.

## 2. METHODOLOGY

This section will discuss on the methodologies for Delphi study for ranking and evaluating weights of QIIs, focus group study, and on the framework and validation of QIM.

### 2.1 Delphi Study

Delphi study is a qualitative method established by RAND Corporation, in which a structured questionnaire is used during numerous rounds to reach at a group agreement quantitatively. In the first round, the subjective questions are given in the survey form. In the further rounds, the experts can change their answers centred on the group agreement. Delphi study was used by Hasson *et al.* (2000), Okoli & Pawlowski (2004), Vogel *et al.* (2019) and Crawford & Wright (2016) for their studies. In the present Delphi study, the questionnaire for ranking of nine quality factors and their four sub-factors was forwarded to participants in two rounds. The selection of participants was done using selective sampling, where the participants were selected by following the criteria that participants should have more than 10 years of experience in defence aerospace. In Hasson *et al.* (2000), it was suggested to have number of participants ranging from 15 to 60. In the present study, 60 participants were invited. The participants were from three backgrounds, namely defence aerospace production, research and development (R&D) and users. For testing the consistency of the replies, analysis of variance (ANOVA) was used (Ostertagova & Ostertag, 2013; Sow, 2014). The null hypothesis is that no significant difference exists between population means. The  $p$ -value is calculated using  $F$ -value and the null hypothesis is recognised if  $p$ -value is more than 0.05. The minimum group consensus value for each questionnaire item is taken as 0.7. MATLAB was used for data analysis. Equations 1 to 3 show the formula used for ANOVA analysis:

$$S_{between}^2 = \frac{\sum n (\bar{x} - \bar{\bar{x}})^2}{k-1} \quad (1)$$

$$S_{within}^2 = \frac{\sum \sum (x - \bar{x})^2}{n-k} \quad (2)$$

$$F = \frac{S_{between}^2}{S_{within}^2} \quad (3)$$

where:

$\bar{x}$  = Sample mean

$\bar{\bar{x}}$  = Overall or Grand mean

$k$  = number of distinct samples

$n$  = number of items in sample

The questionnaire of Delphi study consisted of 36 QIIs that have to be ranked. The ranking is used to evaluate the weightage of the quality factors and their sub-factors using equal weight (EW), rank sum weight (RSW), rank exponent weight (REW), rank reciprocal weight (RRW), rank order centroid weight (ROCW) and rank sum reciprocal weight (RSRW) methods. With ranks of sub-factors being  $r_j$ ;  $j=1,2,\dots,n$  where  $n=4$ , and, ranks of quality factors being  $R_i$ ;  $i=1,2,3,\dots,m$  where  $m=9$ , the formulas for weights are shown in Equations 4 to 15.

#### **Equal Weight (EW)**

Weight of sub-factor for  $j=1, 2, \dots, n$ ;  $n=4$

$$w_j = \frac{1}{n} \quad (4)$$

Weight of quality factor for  $i=1, 2, 3, \dots, m$ ;  $m=9$

$$W_i = \frac{1}{m} \quad (5)$$

#### **Rank Sum Weight (RSW)**

Weight of sub-factor for  $j=1, 2, \dots, n$ ;  $n=4$

$$w_j = \frac{n - r_j + 1}{\sum_{k=1}^n (n - r_k + 1)} = \frac{2(n - r_j + 1)}{n(n+1)} \quad (6)$$

Weight of quality factor for  $i=1, 2, 3, \dots, m$ ;  $m=9$

$$W_i = \frac{m - R_i + 1}{\sum_{k=1}^m (m - R_k + 1)} = \frac{2(m - R_i + 1)}{m(m+1)} \quad (7)$$

#### **Rank Exponent Weight (REW)**

Weight of sub-factor for  $j=1, 2, \dots, n$ ;  $n=4$ ;  $p=0.5$

$$w_j = \frac{(n - r_j + 1)^p}{\sum_{k=1}^n (n - r_k + 1)^p} \quad (8)$$

Weight of quality factor for  $i=1, 2, 3, \dots, m$ ;  $m=9$ ;  $p=0.5$

$$W_i = \frac{(m - R_i + 1)^p}{\sum_{k=1}^m (m - R_k + 1)^p} \quad (9)$$

#### **Rank Reciprocal Weight (RRW)**

Weight of quality factor for  $i=1, 2, 3, \dots, m$ ;  $m=9$

$$W_i = \frac{1/R_i}{\sum_{k=1}^m (1/R_k)} \quad (10)$$

Weight of sub-factor for  $j=1, 2, \dots, n; n=4$

$$w_j = \frac{1/r_j}{\sum_{k=1}^n (1/r_k)} \quad (11)$$

**Rank Order Centroid Weight (ROCW)**

Weight of sub-factor for  $j=1, 2, \dots, n; n=4$

$$w_j = \frac{1}{n} \sum_{k=j}^n \frac{1}{r_k} \quad (12)$$

Weight of quality factor for  $i=1, 2, 3, \dots, m; m=9$

$$W_i = \frac{1}{m} \sum_{k=i}^m \frac{1}{R_k} \quad (13)$$

**Rank Sum Reciprocal Weight (RSRW)**

Weight of sub-factor  $j=1, 2, \dots, n; n=4$

$$w_j = \frac{1/\left(r_j + \frac{n-r_j+1}{n}\right)}{\sum_{k=1}^n \left[1/\left(r_k + \frac{n-r_k+1}{n}\right)\right]} \quad (14)$$

Weight of quality factor  $i=1, 2, 3, \dots, m; m=9$

$$W_i = \frac{1/\left(R_i + \frac{m-R_i+1}{m}\right)}{\sum_{k=1}^m \left[1/\left(R_k + \frac{m-R_k+1}{m}\right)\right]} \quad (15)$$

**2.2 Focus Group Study**

Focus group study is a group dialogue on specific subjects organised, guided, transcribed and monitored by a moderator for research purposes. Quinn (2002) and Gill *et al.* (2008) have used focus group study for their researches. In the present focus group study, selective sampling is conducted for participant selection by using pre-existing or pre-decided groups. The optimum group size suggested by Gill *et al.* (2008) is ranging from six to eight participants. This focus group study was conducted with eight experts from quality and reliability fields, with the details provided in Table 1. The objective of the focus group was to decide on the ratings of quality factors and sub-factors for 10 existing defence aerospace products, and to rate the quality index for the products. In order to avoid conflict of interest, the ten products are referred to as Products 1 to 10. These products have resemblance to aerospace vehicles of short and medium range.

**Table 1: Details of experts in the focus group study.**

Category	Number	Background
Quality and Reliability	Eight	Two have experience in design quality
		Four have experience in quality management
		One has experience in customer quality assurance
		One has experience in product utilization

### 2.3 QIM and Validation

The hierarchical table and flow diagram for the framework of QIM is shown in Figures 1 and 2 respectively. The following equation shows the formula of QIM:

$$QIM = \sum_{j=1}^n \left( \sum_{i=1}^m (w_{ji} * QIrating_{ji}) \right) \quad (16)$$

where:

$w_{ji}$  = Weightage of the  $i^{th}$  sub – factor of  $j^{th}$  quality factor

$QIrating_{ji}$  = Rating of the  $i^{th}$  sub – factor of  $j^{th}$  quality factor

$m$  = Number of sub-factors in each quality factor

$n$  = Total number of quality factors

The QIM was validated using the sum of square of errors (SSE) and  $R^2$  methods.

Input (Sub-factor rating)	Intermediate (Quality Factor)	Output (QI)
Organisational Support	Human Factor Management and Support	Quality Index
Knowledge		
Continual Improvement and Innovation		
Team Work		
Standards		
Proven Parts		
Policy / Guidelines		
Material Qualification		
Qualitative Requirements		
Technical Requirements		
Disruptive Technologies	Standardisation	
Customer Review/ Participation	Customer Requirements / Focus	
Quality Assurance Plan	Documentation	
Detailed Drawings	Quality Management	
Test Plan	Reliability Management	
User Manual with Technical Specifications	Airworthiness / Design Certification	
Configuration Management	Evaluation	
Design Review	Maintenance / Manual	
Software QA / IV&V		
Quality Improvement Techniques		
Reliability Prediction / Estimation		
Reliability Apportionment / Goal		
Reliability Improvement Techniques		
FRACAS		
Design Adequacy		
Test Adequacy		
System Safety		
System Testability		
Quality/ Design Evaluation		
Life Estimate		
HALT/HASS		
Design Verification and Validation		
Maintainability and Spare Parts availability		
Preventive/Dynamic Predictive Maintenance		
Corrective Maintenance		
Reliability Centred Maintenance		

Figure 1: Hierarchical table of QIM.

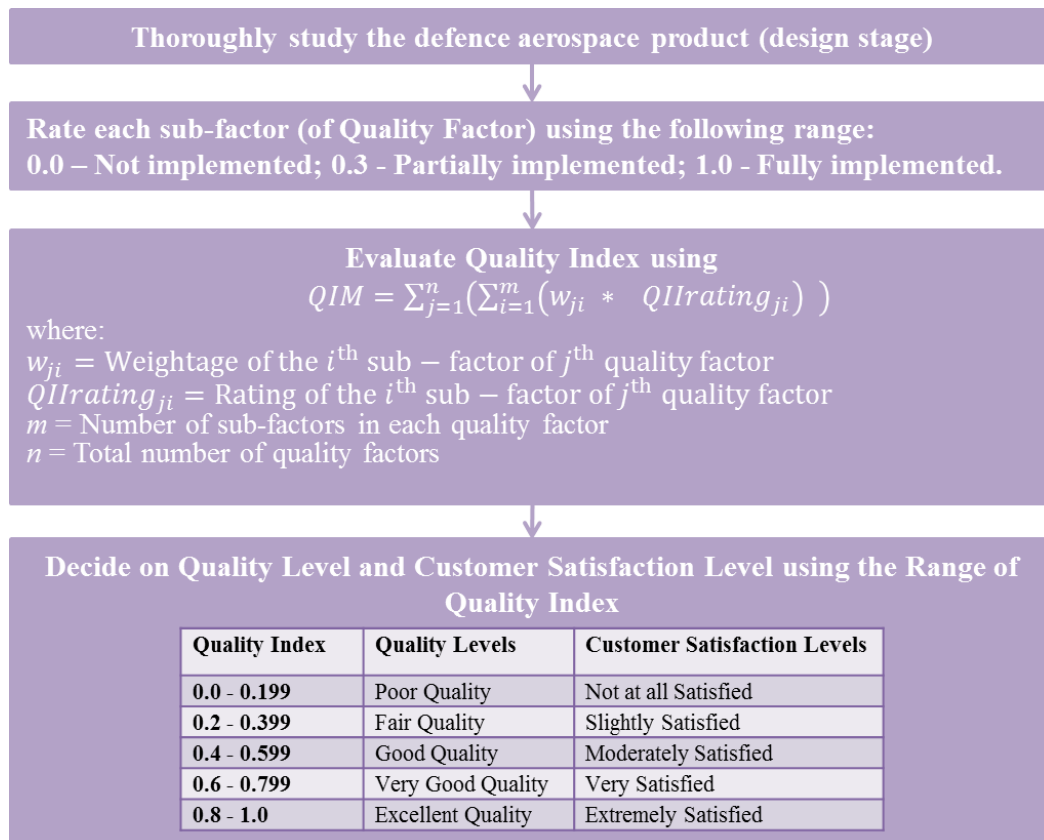


**Figure 2: Flow diagram for framework of QIM.**

### **3. RESULTS AND DISCUSSION**

#### **3.1 Ranking and Weightage of QII**

The 36 QIIs are divided into nine quality factors and further into four sub-factors for each quality factor. The participants were asked to rank the nine quality factors separately. The other questions asked the participants to rank the four sub-factors of each quality factor separately. The option of giving same rank to quality factors or sub-factors was given to the participants.

For participation in the Delphi Study to *Assign Weightage Using Ranking for Quality Impact Indicators in Defence Aerospace Industry*, around 60 prospective participants were approached, of which 33 participants replied in first round. In second round, 30 participants replied to the questionnaire. The Delphi study was concluded in 40 days. The consensus parameters for Rounds 1 and 2 of the study are given in Tables 2 and 3 respectively, while the ANOVA parameters are given in Table 4.

The weightage of the quality factors and their sub-factors were evaluated using the EW, RSW, REW, RRW, ROCW and RSRW methods. The rank and weightage of each QII is shown in Table 5.

**Table 2: Consensus parameters of Round 1.**

**Rank the quality factors and their sub-factors in the defence aerospace industry**

Quality Factors		Round 1	Ser (10)	Round 1	R&D(12)	Round 1	Prod(11)	Round 1	Overall (33)
		Rank	Consensus	Rank	Consensus	Rank	Consensus	Rank	Consensus
Human Factor Management and Support		1	0.5000	3	0.5833	3	0.4545	3	0.4242
Standardisation		3	0.4000	3	0.4167	3	0.3636	3	0.3939
Customer Requirements / Focus		1	0.5000	1	0.5000	1	0.5455	1	0.5152
Documentation		4	0.5000	4	0.5000	4	0.4545	4	0.4848
Quality Management		3	0.6000	3	0.4167	2	0.3636	3	0.4242
Reliability Management		2	0.7000	2	0.6667	2	0.5455	2	0.6364
Airworthiness / Design Certification		2	0.7000	2	0.7500	2	0.4545	2	0.6364
Evaluation		2	0.7000	2	0.6667	2	0.4545	2	0.6061
Maintenance / Manual		3	0.6000	3	0.6667	3	0.4545	3	0.5758
Quality Factors	Sub-Factors	Round 1	Ser (10)	Round 1	R&D(12)	Round 1	Prod(11)	Round 1	Overall (33)
		Rank	Consensus	Rank	Consensus	Rank	Consensus	Rank	Consensus
Human Factor Management and Support	(a) Organisational Support	2	0.7000	2	0.8333	2	0.8182	2	0.7879
	(b) Knowledge	3	0.7000	3	0.8333	3	0.7273	3	0.7576
	(c) Continual Improvement and Innovation	2	0.5000	1	0.5833	1	0.4545	1	0.4545
	(d) Team Work	1	0.7000	1	0.6667	1	0.7273	1	0.6970
Standardisation	(a) Standards	1	0.6000	1	0.7500	1	0.6364	1	0.6667
	(b) Proven Parts	1	0.5000	1	0.5833	1	0.4545	1	0.5152
	(c) Policy / Guidelines	1	0.5000	1	0.6667	1	0.5455	1	0.5758
	(d) Material Qualification	1	0.5000	1	0.6667	1	0.5455	1	0.5758
Customer Requirements / Focus	(a) Qualitative Requirements	1	0.7000	1	0.8333	1	0.7273	1	0.7576
	(b) Technical Requirements	1	0.8000	1	0.8333	1	0.8182	1	0.8182
	(c) Disruptive Technologies	2	0.6000	2	0.5833	2	0.7273	2	0.6364
	(d) Customer Review	2	0.6000	2	0.6667	2	0.6364	2	0.6364
Documentation	(a) Quality Assurance Plan	1	0.7000	1	0.8333	1	0.7273	1	0.7576
	(b) Detailed Drawings	1	0.5000	1	0.6667	1	0.5455	1	0.5758
	(c) Test Plan	2	0.7000	2	0.8333	2	0.7273	2	0.7576
	(d) User Manual with Technical Specifications	2	0.5000	2	0.6667	2	0.6364	2	0.6061
Quality Management	(a) Configuration Management	2	0.5000	2	0.6667	1	0.5455	2	0.5152
	(b) Design Review	1	0.5000	1	0.6667	2	0.4545	1	0.4848
	(c) Software QA / IV&V	1	0.7000	1	0.6667	1	0.8182	1	0.7273
	(d) Quality Improvement Techniques	2	0.5000	2	0.6667	2	0.6364	2	0.6061
Reliability Management	(a) Reliability Prediction / Estimation	1	0.4000	1	0.5833	1	0.4545	1	0.4848
	(b) Reliability Apportionment / Goal	1	0.7000	1	0.5833	1	0.6364	1	0.6364
	(c) Reliability Improvement Techniques	2	0.6000	2	0.7500	2	0.6364	2	0.6667
	(d) FRACAS	1	0.4000	1	0.5833	1	0.5455	1	0.5152
Airworthiness / Design Certification	(a) Design Adequacy	1	0.6000	1	0.7500	1	0.6364	1	0.6667
	(b) Test Adequacy	1	0.4000	1	0.5833	1	0.5455	1	0.5152
	(c) System Safety	1	0.4000	1	0.4167	1	0.4545	1	0.4242
	(d) System Testability	1	0.5000	1	0.7500	1	0.6364	1	0.6364
Evaluation	(a) Quality Evaluation	1	0.6000	1	0.8333	1	0.6364	1	0.6970
	(b) Life Estimate	2	0.6000	2	0.5833	2	0.6364	2	0.6061
	(c) HALT/HASS	1	0.5000	2	0.6667	2	0.6364	2	0.5758
	(d) Design Verification and Validation	1	0.7000	1	0.8333	1	0.7273	1	0.7576
Maintenance / Manual	(a) Maintainability	1	0.5000	1	0.6667	1	0.6364	1	0.6061
	(b) Preventive Maintenance	2	0.6000	2	0.7500	2	0.6364	2	0.6667
	(c) Corrective Maintenance	2	0.5000	3	0.5833	3	0.5455	3	0.4848
	(d) Reliability Centred Maintenance	1	0.7000	1	0.7500	1	0.6364	1	0.6970



**Table 3: Consensus parameters of Round 2.**

**Rank the quality factors and their sub-factors in the defence aerospace industry**

Quality Factors		Round 2 Ser (10)		Round 2 R&D(10)		Round 2 Prod(10)		Round 2 Overall (30)	
		Rank	Consensus	Rank	Consensus	Rank	Consensus	Rank	Consensus
Human Factor Management and Support		3	0.7000	3	0.8000	3	0.7000	3	0.7333
Standardisation		3	0.8000	3	0.7000	3	0.9000	3	0.8000
Customer Requirements / Focus		1	0.9000	1	0.8000	1	1.0000	1	0.9000
Documentation		4	0.8000	4	0.7000	4	0.7000	4	0.7333
Quality Management		3	0.7000	3	0.8000	3	0.8000	3	0.7667
Reliability Management		2	0.8000	2	0.7000	2	0.7000	2	0.7333
Airworthiness / Design Certification		2	0.8000	2	1.0000	2	0.7000	2	0.8333
Evaluation		2	0.7000	2	0.8000	2	0.7000	2	0.7333
Maintenance / Manual		3	0.7000	3	0.7000	3	0.8000	3	0.7333
Quality Factors	Sub-Factors	Round 2 Ser (10)		Round 2 R&D(10)		Round 2 Prod(10)		Round 2 Overall (30)	
		Rank	Consensus	Rank	Consensus	Rank	Consensus	Rank	Consensus
Human Factor Management and Support	(a) Organisational Support	2	1.0000	2	0.9000	2	0.9000	2	0.9333
	(b) Knowledge	3	0.9000	3	0.8000	3	0.9000	3	0.8667
	(c) Continual Improvement and Innovation	1	0.7000	1	0.7000	1	0.7000	1	0.7000
	(d) Team Work	1	0.7000	1	0.8000	1	0.8000	1	0.7667
Standardisation	(a) Standards	1	0.7000	1	0.8000	1	0.8000	1	0.7667
	(b) Proven Parts	1	0.8000	1	0.7000	1	0.7000	1	0.7333
	(c) Policy / Guidelines	1	0.8000	1	0.8000	1	0.9000	1	0.8333
	(d) Material Qualification	1	0.8000	1	0.7000	1	0.7000	1	0.7333
Customer Requirements / Focus	(a) Qualitative Requirements	1	0.7000	1	0.8000	1	0.8000	1	0.7667
	(b) Technical Requirements	2	0.7000	2	0.8000	2	0.7000	2	0.7333
	(c) Disruptive Technologies	3	0.8000	3	0.8000	3	0.7000	3	0.7667
	(d) Customer Review	1	0.7000	1	0.7000	1	0.8000	1	0.7333
Documentation	(a) Quality Assurance Plan	1	0.7000	1	0.8000	1	0.8000	1	0.7667
	(b) Detailed Drawings	1	0.8000	1	0.7000	1	0.7000	1	0.7333
	(c) Test Plan	2	0.7000	2	0.8000	2	0.8000	2	0.7667
	(d) User Manual with Technical Specifications	2	0.7000	2	0.7000	2	0.8000	2	0.7333
Quality Management	(a) Configuration Management	2	0.7000	2	0.8000	2	0.7000	2	0.7333
	(b) Design Review	1	0.8000	1	0.9000	1	0.8000	1	0.8333
	(c) Software QA / IV&V	1	0.7000	1	0.7000	1	0.8000	1	0.7333
	(d) Quality Improvement Techniques	2	0.7000	2	0.7000	2	0.8000	2	0.7333
Reliability Management	(a) Reliability Prediction / Estimation	2	0.7000	2	0.8000	2	0.7000	2	0.7333
	(b) Reliability Apportionment / Goal	2	0.8000	2	0.7000	2	0.7000	2	0.7333
	(c) Reliability Improvement Techniques	1	0.7000	1	0.9000	1	0.7000	1	0.7667
	(d) FRACAS	1	0.8000	1	0.7000	1	0.7000	1	0.7333
Airworthiness / Design Certification	(a) Design Adequacy	1	0.8000	1	0.7000	1	0.7000	1	0.7333
	(b) Test Adequacy	1	0.7000	1	0.7000	1	0.8000	1	0.7333
	(c) System Safety	1	0.7000	1	0.8000	1	0.7000	1	0.7333
	(d) System Testability	1	0.8000	1	0.7000	1	0.8000	1	0.7667
Evaluation	(a) Quality Evaluation	1	0.7000	1	0.8000	1	0.8000	1	0.7667
	(b) Life Estimate	2	0.7000	2	0.8000	2	0.7000	2	0.7333
	(c) HALT/HASS	2	0.8000	2	0.7000	2	0.7000	2	0.7333
	(d) Design Verification and Validation	1	0.7000	1	0.8000	1	0.8000	1	0.7667
Maintenance / Manual	(a) Maintainability	1	0.7000	1	0.8000	1	0.8000	1	0.7667
	(b) Preventive Maintenance	2	0.8000	2	0.8000	2	0.9000	2	0.8333
	(c) Corrective Maintenance	3	0.7000	3	0.8000	3	0.8000	3	0.7667
	(d) Reliability Centred Maintenance	1	0.8000	1	0.8000	1	1.0000	1	0.8667

**Table 4: ANOVA parameters for Round 2.**

No.	Quality Factors	Sub-Factors	$S_{between}^2$	$S_{within}^2$	F	p-value
1)	Human Factor Management and Support	(a) Organisational Support	0.1000	0.0667	1.5000	0.2411
		(b) Knowledge	0.0333	0.4185	0.0796	0.9237
		(c) Continual Improvement and Innovation	0.0333	1.0148	0.0328	0.9677
		(d) Team Work	0.1000	0.3741	0.2673	0.7674
2)	Standardisation	(a) Standards	0.0333	0.1963	0.1698	0.8447
		(b) Proven Parts	0.0333	0.4778	0.0698	0.9328
		(c) Policy / Guidelines	0.0333	0.1519	0.2195	0.8043
		(d) Material Qualification	0.0333	0.2148	0.1552	0.8570
3)	Customer Requirements / Focus	(a) Qualitative Requirements	0.1333	0.2815	0.4737	0.6278
		(b) Technical Requirements	0.0333	0.2148	0.1552	0.8570
		(c) Disruptive Technologies	0.0333	0.1963	0.1698	0.8447
		(d) Customer Review/ Participation	0.0333	0.2148	0.1552	0.8570
4)	Documentation	(a) Quality Assurance Plan	0.1000	0.7037	0.1421	0.8682
		(b) Detailed Drawings	0.1333	0.3852	0.3462	0.7105
		(c) Test Plan	0.0333	0.1963	0.1698	0.8447
		(d) User Manual with Technical Specifications	0.1333	0.4889	0.2727	0.7634
5)	Quality Management	(a) Configuration Management	0.0333	0.2148	0.1552	0.8570
		(b) Design Review	0.1333	0.3370	0.3956	0.6771
		(c) Software QA / IV&V	0.1333	0.3852	0.3462	0.7105
		(d) Quality Improvement Techniques	0.0333	0.2741	0.1216	0.8860
6)	Reliability Management	(a) Reliability Prediction / Estimation	0.0333	0.2741	0.1216	0.8860
		(b) Reliability Apportionment / Goal	0.0333	0.2148	0.1552	0.8570
		(c) Reliability Improvement Techniques	0.3000	0.3593	0.8351	0.4447
		(d) FRACAS	0.0333	0.4778	0.0698	0.9328
7)	Airworthiness / Design Certification	(a) Design Adequacy	0.1333	0.3852	0.3462	0.7105
		(b) Test Adequacy	0.0333	0.2148	0.1552	0.8570
		(c) System Safety	0.0333	0.2148	0.1552	0.8570
		(d) System Testability	0.0333	0.1963	0.1698	0.8447
8)	Evaluation	(a) Quality/ Design Evaluation	0.0333	0.1963	0.1698	0.8447
		(b) Life Estimate	0.0333	0.2148	0.1552	0.8570
		(c) HALT/HASS	0.0333	0.2148	0.1552	0.8570
		(d) Design Verification and Validation	0.1333	0.5444	0.2449	0.7845
9)	Maintenance / Manual	(a) Maintainability and Spare Parts availability	0.1333	0.5444	0.2449	0.7845
		(b) Preventive/ Dynamic Predictive Maintenance	0.0333	0.1519	0.2195	0.8043
		(c) Corrective Maintenance	0.1333	0.5444	0.2449	0.7845
		(d) Reliability Centred Maintenance	0.3000	0.3037	0.9878	0.3855

**Table 5: Ranking and weights of quality factors and their sub-factors.**

No.	Quality Factors	Sub-Factors	Rank QF	Rank SF	EW	RSW	REW	RRW	ROCW	RSRW
1)	Human Factor Management and Support	(a) Organisational Support	3	2	0.0278	0.0241	0.0262	0.0144	0.0097	0.0198
		(b) Knowledge	3	3	0.0278	0.0161	0.0214	0.0096	0.0039	0.0132
		(c) Continual Improvement and Innovation	3	1	0.0278	0.0321	0.0302	0.0288	0.0330	0.0317
		(d) Team Work	3	1	0.0278	0.0321	0.0302	0.0288	0.0330	0.0317
2)	Standardisation	(a) Standards	3	1	0.0278	0.0261	0.0270	0.0204	0.0199	0.0241
		(b) Proven Parts	3	1	0.0278	0.0261	0.0270	0.0204	0.0199	0.0241
		(c) Policy / Guidelines	3	1	0.0278	0.0261	0.0270	0.0204	0.0199	0.0241
		(d) Material Qualification	3	1	0.0278	0.0261	0.0270	0.0204	0.0199	0.0241
3)	Customer Requirements / Focus	(a) Qualitative Requirements	1	1	0.0278	0.0413	0.0342	0.0864	0.0850	0.0570
		(b) Technical Requirements	1	2	0.0278	0.0310	0.0297	0.0432	0.0250	0.0356
		(c) Disruptive Technologies	1	3	0.0278	0.0207	0.0242	0.0288	0.0100	0.0238
		(d) Customer Review/ Participation	1	1	0.0278	0.0413	0.0342	0.0864	0.0850	0.0570
4)	Documentation	(a) Quality Assurance Plan	4	1	0.0278	0.0256	0.0268	0.0204	0.0047	0.0245
		(b) Detailed Drawings	4	1	0.0278	0.0256	0.0268	0.0204	0.0047	0.0245
		(c) Test Plan	4	2	0.0278	0.0192	0.0232	0.0102	0.0016	0.0153
		(d) User Manual with Technical Specifications	4	2	0.0278	0.0192	0.0232	0.0102	0.0016	0.0153
5)	Quality Management	(a) Configuration Management	3	2	0.0278	0.0224	0.0250	0.0136	0.0099	0.0185
		(b) Design Review	3	1	0.0278	0.0299	0.0289	0.0272	0.0298	0.0297
		(c) Software QA / IV&V	3	1	0.0278	0.0299	0.0289	0.0272	0.0298	0.0297
		(d) Quality Improvement Techniques	3	2	0.0278	0.0224	0.0250	0.0136	0.0099	0.0185
6)	Reliability Management	(a) Reliability Prediction / Estimation	2	2	0.0278	0.0256	0.0268	0.0204	0.0194	0.0232
		(b) Reliability Apportionment / Goal	2	2	0.0278	0.0256	0.0268	0.0204	0.0194	0.0232
		(c) Reliability Improvement Techniques	2	1	0.0278	0.0341	0.0309	0.0408	0.0581	0.0371
		(d) FRACAS	2	1	0.0278	0.0341	0.0309	0.0408	0.0581	0.0371
7)	Airworthiness / Design Certification	(a) Design Adequacy	2	1	0.0278	0.0299	0.0288	0.0306	0.0387	0.0301
		(b) Test Adequacy	2	1	0.0278	0.0299	0.0288	0.0306	0.0387	0.0301
		(c) System Safety	2	1	0.0278	0.0299	0.0288	0.0306	0.0387	0.0301
		(d) System Testability	2	1	0.0278	0.0299	0.0288	0.0306	0.0387	0.0301
8)	Evaluation	(a) Quality/ Design Evaluation	2	1	0.0278	0.0341	0.0309	0.0408	0.0581	0.0371
		(b) Life Estimate	2	2	0.0278	0.0256	0.0268	0.0204	0.0194	0.0232
		(c) HALT/HASS	2	2	0.0278	0.0256	0.0268	0.0204	0.0194	0.0232
		(d) Design Verification and Validation	2	1	0.0278	0.0341	0.0309	0.0408	0.0581	0.0371
9)	Maintenance / Manual	(a) Maintainability and Spare Parts availability	3	1	0.0278	0.0321	0.0302	0.0288	0.0330	0.0317
		(b) Preventive/ Dynamic Predictive Maintenance	3	2	0.0278	0.0241	0.0262	0.0144	0.0097	0.0198
		(c) Corrective Maintenance	3	3	0.0278	0.0161	0.0214	0.0096	0.0039	0.0132
		(d) Reliability Centred Maintenance	3	1	0.0278	0.0321	0.0302	0.0288	0.0330	0.0317

### 3.2 QIM and Validation

The range of QIIs decided by the focus group is given in Table 6. The range of quality index was deliberated upon by the members for defence aerospace products based on their experiences and was quantified accordingly, as shown in Table 7.

**Table 6: Range of quality impact indicators.**

<b>Extent of implementation or presence of quality factor</b>	<b>Rating</b>
Fully implemented	1.0
Partially implemented (more than 50 percent but not complete)	0.3
Not implemented (less than 50 percent)	0.0

**Table 7: Range of quality index.**

<b>Quality Index</b>	<b>Quality Levels</b>	<b>Customer Satisfaction Levels</b>
0.0 - 0.199	Poor Quality	Not at all satisfied
0.2 - 0.399	Fair Quality	Slightly satisfied
0.4 - 0.599	Good Quality	Moderately satisfied
0.6 - 0.799	Very good Quality	Very satisfied
0.8 - 1.0	Excellent Quality	Extremely satisfied

The focus group gave ratings to 10 different defence aerospace products as shown in Tables 8 and 9.

The overall quality index of the products estimated using the Equation 5 is shown in Figure 3. For Products 8 and 10, the customers were extremely satisfied because of excellent quality. For Products 1, 2, 4, 6 and 7, the customers were very satisfied because of very good quality. For Product 3, the customers were moderately satisfied because of good quality. For Product 9, the customers were slightly satisfied because of fair quality. For Product 5, the customers were not at all satisfied because of poor quality.

The QIM is validated with data of the 10 defence aerospace products. The SSE and  $R^2$  of each weightage method are shown in Table 10. The values show good fit, with the best fit statistic of SSE = 0.011459 and  $R^2 = 0.980106$  being for the RSRW method.

**Table 8: Rating of Products 1 to 5 by the focus group.**

No.	Quality Factors	Sub-Factors	Rating				
			Product 1	Product 2	Product 3	Product 4	Product 5
1)	Human Factor Management and Support	(a) Organisational Support	1	1	1	1	1
		(b) Knowledge	1	1	1	1	0
		(c) Continual Improvement and Innovation	0	0	0	0	0
		(d) Team Work	1	1	1	1	1
2)	Standardisation	(a) Standards	1	1	1	1	0
		(b) Proven Parts	1	1	1	1	0
		(c) Policy / Guidelines	0	1	0	0	0
		(d) Material Qualification	1	1	1	1	0
3)	Customer Requirements / Focus	(a) Qualitative Requirements	1	1	1	1	1
		(b) Technical Requirements	1	1	1	1	0
		(c) Disruptive Technologies	0	0	0	0	0
		(d) Customer Review/ Participation	1	1	1	1	0
4)	Documentation	(a) Quality Assurance Plan	1	1	1	1	0
		(b) Detailed Drawings	1	1	1	1	0.3
		(c) Test Plan	1	1	1	0.3	0
		(d) User Manual with Technical Specifications	0.3	1	0	0.3	0.3
5)	Quality Management	(a) Configuration Management	1	1	1	1	0
		(b) Design Review	1	1	1	1	1
		(c) Software QA / IV&V	0.3	0.3	0	1	0
		(d) Quality Improvement Techniques	0	0	0	0	0
6)	Reliability Management	(a) Reliability Prediction / Estimation	0	0	0	0	0.3
		(b) Reliability Apportionment / Goal	0	0	0	0	0
		(c) Reliability Improvement Techniques	0.3	1	0.3	0	0
		(d) FRACAS	1	1	0.3	1	0
7)	Airworthiness / Design Certification	(a) Design Adequacy	1	1	0	1	0
		(b) Test Adequacy	1	1	1	1	0
		(c) System Safety	1	0	0	1	0
		(d) System Testability	1	1	0	1	0
8)	Evaluation	(a) Quality/ Design Evaluation	1	1	0.3	1	0
		(b) Life Estimate	0	0	0	1	0
		(c) HALT/HASS	0	0	0	0	0
		(d) Design Verification and Validation	1	1	0	1	0
9)	Maintenance / Manual	(a) Maintainability and Spare Parts availability	0.3	0.3	0.3	1	0
		(b) Preventive/ Dynamic Predictive Maintenance	0	0	0	0.3	0
		(c) Corrective Maintenance	1	1	1	1	0
		(d) Reliability Centred Maintenance	0	0	0	0	0
	Quality Index		0.7	0.7	0.5	0.7	0.1

**Table 9: Rating of Products 6 to 10 by the focus group.**

No.	Quality Factors	Sub-Factors	Rating				
			Product 6	Product 7	Product 8	Product 9	Product 10
1)	Human Factor Management and Support	(a) Organisational Support	1	1	1	1	1
		(b) Knowledge	0.3	1	1	0	1
		(c) Continual Improvement and Innovation	0	0.3	0.3	0	0.3
		(d) Team Work	1	1	1	1	1
2)	Standardisation	(a) Standards	1	1	1	0	1
		(b) Proven Parts	1	1	1	0	1
		(c) Policy / Guidelines	0	1	1	0	1
		(d) Material Qualification	1	1	1	1	1
3)	Customer Requirements / Focus	(a) Qualitative Requirements	1	1	1	1	1
		(b) Technical Requirements	1	1	1	0	1
		(c) Disruptive Technologies	0	0	0.3	0	0.3
		(d) Customer Review/ Participation	1	1	1	1	1
4)	Documentation	(a) Quality Assurance Plan	1	1	1	0	1
		(b) Detailed Drawings	1	1	1	1	1
		(c) Test Plan	1	1	1	1	1
		(d) User Manual with Technical Specifications	1	0	0.3	1	0.3
5)	Quality Management	(a) Configuration Management	1	1	1	0.3	1
		(b) Design Review	1	1	1	1	1
		(c) Software QA / IV&V	1	0	1	0	1
		(d) Quality Improvement Techniques	0	0	0.3	0	0
6)	Reliability Management	(a) Reliability Prediction / Estimation	1	1	1	0	1
		(b) Reliability Apportionment / Goal	0.3	0	1	0	1
		(c) Reliability Improvement Techniques	0.3	0	1	0	1
		(d) FRACAS	1	1	1	0	1
7)	Airworthiness / Design Certification	(a) Design Adequacy	1	1	1	0	1
		(b) Test Adequacy	1	1	0.3	0	1
		(c) System Safety	1	0.3	0.3	0	1
		(d) System Testability	1	1	1	0	1
8)	Evaluation	(a) Quality/ Design Evaluation	1	1	1	0.3	1
		(b) Life Estimate	0	0	0.3	0	1
		(c) HALT/HASS	0	0	0.3	0	1
		(d) Design Verification and Validation	1	1	1	0	1
9)	Maintenance / Manual	(a) Maintainability and Spare Parts availability	0	0	1	0	1
		(b) Preventive/ Dynamic Predictive Maintenance	0	0	1	0	1
		(c) Corrective Maintenance	1	1	1	0.3	1
		(d) Reliability Centred Maintenance	0	0	0	0	1
	Quality Index		0.7	0.7	0.9	0.3	0.9

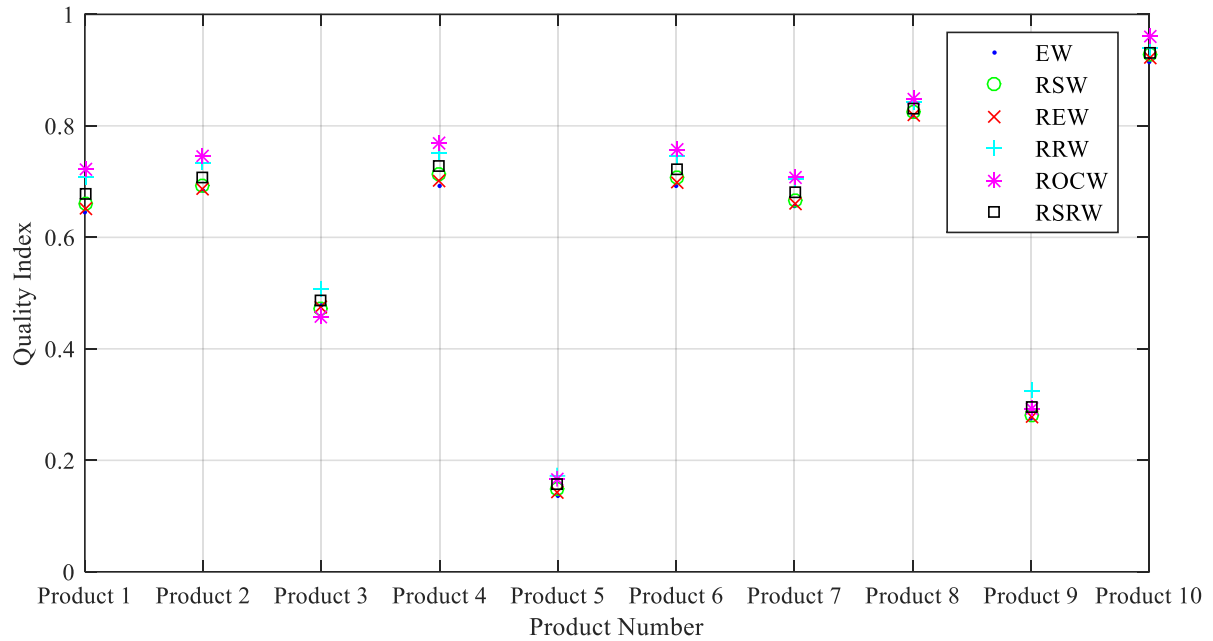


**Figure 3: Quality index of the 10 defence aerospace products.**

**Table 10: Goodness of fit statistics.**

Weightage method	SSE	$R^2$
EW	0.01479	0.9743
RSW	0.01301	0.9774
REW	0.01399	0.9757
RRW	0.01671	0.9710
ROCW	0.02294	0.9602
RSRW	0.01146	0.9801

#### 4. CONCLUSION

In this study, the Delphi study was performed in two rounds. A total of 33 out of 60 prospective participants responded to the questionnaire in the first round. The group consensus value was progressed to 33 participants and 30 responded to the questionnaire in second round. For consistency of ranking, ANOVA analysis was carried out for three types of participants, namely defence aerospace production, R&D and user.

QIM was validated with data of 10 defence aerospace products using SSE and  $R^2$ . It was found that the RSRW method had the lowest SSE and highest  $R^2$ . The proposed QIM with RSRW weightage can be used for estimating the quality of defence aerospace products during the design stage, so that corrective actions can be taken at this stage when the cost of design change is less.

The research implication is that a framework for QIM for defence aerospace products has been developed. This will help in quantification of quality of product during the design stage. The limitations of research are that the participants in the Delphi and Focus group studies are from India only. However, the proposed QIM can be a good estimate of quality of any defence aerospace product irrespective of the country of origin. Future studies can include the utilisation of the QIM for estimating the quality levels of numerous defence aerospace products (at the design stage) and improvement of the QIM based on feedback received.

## REFERENCES

- Argotti, Y., Baron, C., & Esteban, P. (2019). Quality quantification in systems engineering from the qualimetry eye. *2019 IEEE Int. Syst. Conf. (SysCon)*, 8-11 April 2019, Orlando, Florida, U.S..
- Cosco, T.D., Stephan, B.C. & Brayne, C. (2015). Validation of an a priori, index model of successful aging in a population-based cohort study: the successful aging index. *Int. Psychogeriatr.*, **27**: 1971 - 1977.
- Crawford, M. & Wright, G. (2016). *Delphi Method*. John Wiley & Sons, New Jersey, U.S.
- Deng W.J., Yeh, M.L. & Sung, M.L. (2013). A customer satisfaction index model for international tourist hotels: Integrating consumption emotions into the American Customer Satisfaction Index. *Int. J. Hosp. Manage.*, **35**: 133-140.
- Dengiz, O. (2020). Soil quality index for paddy fields based on standard scoring functions and weight allocation method. *Arch. Agron. Soil Sci.*, **66**: 301-315.
- Drewnowski, A. (2009). Defining nutrient density: development and validation of the nutrient rich foods index. *J Am. Coll. Nutr.*, **28**: 421S-426S.
- Feng, Y., Liu, L., Li, Y., Zhang, Y., Chen, M. & Xing, X. (2015). A dynamic water quality index model based on functional data analysis. *Ecol. Indic.*, **57**: 249–258.
- Gill, P., Stewart, K., Treasure, E. & Chadwick, B.. (2008). Methods of data collection in qualitative research: Interviews and focus groups. *Brit. Dent. J.*, **204**: 291-295.
- Ginoux, P. & Torres, O. (2003). Empirical TOMS index for dust aerosol: Applications to model validation and source characterisation. *J. Geophys. Res.*, **108**: 4534.
- Hasson, F., Keeney, S. & McKenna, H. (2000). Research guidelines for the Delphi survey technique. *J. Adv. Nurs.*, **32**: 1008-1015.
- Hsu, S.H. & Wang, Y.C. (2008). The development and empirical validation of the Employee Satisfaction Index model. *Total Qual. Manag. Bus.*, **19**: 353-366.
- Iorga, M., Ioana, A., Ene, B.C., Deonisie, D., Petcu, F.Ş, & Pollifroni, M. (2022). Aspects on the analysis and quantification of the quality of products, works and services (I). *Acta Tech. Napocensis, Ser. Appl. Math. Mech. Eng.*, **65**: 111-116.
- Landry, M., Malouin, J. & Oral, M. (1983). Model validation in operations research. *Eur. J. Oper. Res.*, **14**: 207-220.
- Meyer, Steven & Hubbard, Kenneth & Wilhite, Donald. (1993). A Crop-Specific Drought Index for Corn: I. Model Development and Validation. *Agron. J.*, **85**: 388-395.
- Okoli, C. & Pawlowski, S.D. (2004). The Delphi method as a research tool: an example, design considerations and applications. *Inf. Manag.*, **42**: 15-29.
- Ostertagova, E., & Ostertag, O. (2013). Methodology and application of one-way ANOVA. *Am. J. Mech. Eng.*, **1**: 256-261.
- Parween, S., Siddique, N.A., Diganta, M.T.M., Olbert, A.I. & Uddin, M.G. (2022). Assessment of urban river water quality using modified NSF water quality index model at Siliguri city, West Bengal, India. *Environ. Sustain. Indic.*, **16**: 100202.
- Ponterotto, J.G., Burkard, A., Rieger, B.P., Grieger, I., D'Onofrio, A., Dubuisson, A. & Sax, G. (1995). Development and initial validation of the Quick Discrimination Index (QDI). *Educ. Psychol. Meas.*, **55**: 1016-1031.
- Qing, L. I., Rengkui, L. I. U., Jun, Z. & Quanxin, S. U. N. (2014). Quality risk management model for railway construction projects. *Procedia Eng.*, **84**: 195-203.
- Quinn, P.M. (2002). *Qualitative Research and Evaluation Methods*. Sage Publications, London, U.K.
- Raju, V.R.S., Gandhi, O.P. & Deshmukh, S.G. (2012). Maintenance, repair, and overhaul performance indicators for military aircraft. *Defence Sci. J.*, **62**: 83-89.
- Raptis, T.E., Vokas, G.A., Langouranis, P.A. & Kaminaris, S.D. (2015). Total power quality index for electrical networks using neural networks. *Ener. Proc.*, **74**: 1499-1507.
- Satish Chandra D., Asadi, S.S. & Raju, M.V.S. (2017). Estimation of water quality index by weighted arithmetic water quality index method: a model study. *Int. J. Civil Eng. Tech.*, **8**: 1215–1222.
- Scott, A. (1998). Environment–accident index: Validation of a model. *J. Hazard. Mater.*, **61**: 305-312.
- Singh, M. & Nandula, S. (2020). Reliability improvement of single-shot device. In Varde, P., Prakash, R. & Vinod, G. (Eds.), *Reliability, Safety and Hazard Assessment for Risk-Based Technologies*. Springer, Singapore, pp. 153-158.



- Singh, M., Ware, N. & Singh, R. (2022). Processes required for certification of an engineering equipment. In Singari, R.M., Jain, P.K. & Kumar, H. (Eds.), *Advances in Manufacturing Technology and Management*. Springer, Singapore. pp. 48-54.
- Singh, M. & Ware, N. (2023a). SWOT and AHP analysis for Quality and Reliability culture in public design centers of India. *Int. J. Indian Cult. Bus. Manag.*, In press.
- Singh, M. & Ware, N. (2023b). *Determine the Quality Impact Indicators in Defence Aerospace Industry using Delphi Technique*. Department of Technology Management, Defence Institute of Advanced Technology, India [Manuscript submitted for publication].
- Soniat, T.M. & Brody, M.S. (1988). Field validation of a habitat suitability index model for the American oyster. *Estuaries*, **11**: 87-95.
- Sow, M. T. (2014). Using ANOVA to examine the relationship between safety & security and human development. *J. Int. Bus. Econ.*, **2**: 101-106.
- Temizer, L. & Turkyilmaz, A. (2012). Implementation of student satisfaction index model in higher education institutions. *Procedia Soc.*, **46**: 3802-3806.
- Theuerkauf, S.J. & Lipcius, R.N. (2016). Quantitative validation of a habitat suitability index for oyster restoration. *Front. Mar. Sci.*, **3**: 64.
- Vogel, C., Zwolinsky, S., Griffiths, C., Hobbs, M., Henderson, E. & Wilkins, E. (2019). A Delphi study to build consensus on the definition and use of big data in obesity research. *Int. J. Obesity*, **43**: 2573-2586.
- Wang, C.H. & Lin, T.W. (2011). Minimisation of non-periodic preventive maintenance cost in series-parallel systems. *Defence Sci. J.*, **61**: 44-50.
- Wei, K.K. (2009). Service quality index: A study on Malaysian banks. *Contemp. Manag. Res.*, **5**: 109-124.
- Zhan, D., Kwan, M. P., Zhang, W., Yu, X., Meng, B. & Liu, Q. (2018). The driving factors of air quality index in China. *J. Clean. Prod.*, **197**: 1342-1351.
- Zhang, H., Chang, M., Wang, J. & Ye, S. (2008). Evaluation of peach quality indices using an electronic nose by MLR, QPST and BP network. *Sens. Actuators B: Chem.*, **134**: 332-338.